“This I choose to do. If there is a price, this I choose to pay. If it is my death, then I choose to die. Where this takes me, there I choose to go. I choose. This I choose to do.”

— Terry Pratchett, *Wintersmith*

University of Alberta

Blown Away: The Shedding and Oscillation of Sessile Drops by Cross Flowing Air

by

Andrew James Barnabas Milne

A thesis submitted to the Faculty of Graduate Studies and Research
in partial fulfillment of the requirements for the degree of

Doctor of Philosophy

Department of Mechanical Engineering

Spring 2013
Edmonton, Alberta

To my wife, Sarah Andrea Milne. A wonderful woman whom I love and thank very much.

Abstract

For drops sessile on a solid surface, cross flowing air can drive drop oscillation or shedding, based on the balance and interaction of aerodynamic drag force (based on drop size/shape and air speed) and adhesion/capillary forces (based on surface tension and drop size/shape). Better understanding of the above has applications to, e.g., fuel cell flooding, airfoil icing, and visibility in rain.

To understand the basic physics, experiments studying individual sessile drops in a low speed wind tunnel were performed in this thesis. Analysis of high speed video gave time resolved profiles and airspeed for shedding. Testing 0.5 μl to 100 μl drops of water and hexadecane on poly(methyl methacrylate) PMMA, Teflon, and a superhydrophobic surface (SHS) yielded a master curve describing critical airspeed for shedding for water drops on all surface tested. This curve predicts behavior for new surfaces, and explains experimental results published previously. It also indicates that the higher contact angle leads to easier shedding due to decreased adhesion and increased drag.

Developing a novel floating element differential drag sensor gave the first measurements of the microNewton drag force experienced by drops. Forces magnitude is comparable to gravitational shedding from a tilted plate and to simplified models for drop adhesion, with deviations that

suggest effects due to the air flow. Fluid properties are seen to have little effect on drag versus airspeed, and decreased adhesion is seen to be more important than increased drag for easing shedding. The relation between drag coefficient and Reynolds number increases slightly with liquid-solid contact angle, and with drop volume. Results suggest that the drop experiences increased drag compared to similarly shaped solid bodies due to drop oscillations aeroelasticly coupling into the otherwise laminar flow.

The bulk and surface oscillations of sessile drops in cross flow was also studied, using a full profile analysis technique to determine mode shapes. Oscillation frequency/mode shape is similar for cross flow and quiescent drops. The highest order models collected from the diffuse literature are seen to be reasonably accurate, except at maximum and minimum ranges of contact angle.

Acknowledgements

There are many to whom I owe debts of thanks for their help to me in completing this thesis, starting with those who have advised, supervised, and examined my work. To my main supervisor, Professor Alidad Amirfazli, who has provided much help, support, and guidance (both academic and not) over the years of my PhD and MSc work. Also to my co-supervisor, Professor Brian Fleck, for sharing his knowledge, support, and wisdom as well. Finally, to my entire supervision and advisory committee (the above, as well as Professors Subir Bhattacharjee, Morris Flynn, and Janet Elliott), who have provided countless hours of thought provoking discussions over the last five years.

Next, to the woman I have dedicated this thesis to, my wife, (Sarah) Andrea Milne. Without you, I would not be the person I am, and I owe you much for your love and support throughout the time I have taken to complete my degrees.

To family and friends, in Edmonton, South-Western Ontario, and around the world, for their support and encouragement. To my friends in the Surface Engineering and Instrumentation Lab (especially David Barona and Javed Ally), for all the help and support. Even now, with the lab dispersing, I consider you all friends and look forward to whatever work and relationships we may have together in the future. To all the office, IT,

and machine shop staff at the University of Alberta (especially Bernie Faulkner), for you dedication to your jobs, and your help in making mine possible. Also to all the visiting researchers and summer students who contributed ideas and effort to the work of this thesis.

I wish to thank the Natural Science and Engineering Research Council of Canada (NSERC), Alberta Innovates Technology Futures, and The Killam Trusts for their financial support of my work. I also thank the University of Alberta International Office Research in Germany Award and the Centre for Smart Interfaces at the Technical University of Darmstadt for financial assistance in conducting research in Darmstadt and Bordeaux.

To all those who have helped in my past schooling, especially Bruce Cameron at S.M.H., Kitchener, and Professors Beth Weckman, Gord Stubley and Royden Fraser at the University of Waterloo. I wouldn't be here if it weren't for you.

Finally, to all the people I've missed. Thank you.

Table of Contents

List of Tables

List of Figures

List of Symbols, Nomenclature, Abbreviations

a – drop exposed surface area

A – reference area of drop, taken as cross sectional area of the axisymmetric drop measured in quiescent conditions

c_w – mass concentration of drop's vapour at the surface

C – unitless factor of 0.852.

CAH– Contact Angle Hysteresis

C_D – Drag Coefficient

$C_{D\,crit}$ – drag coefficient at point of incipient motion

CFD – Computational Fluid Dynamics

d – drop initial contact diameter

D – diffusion coefficient of the drop's vapour in air

f_{ml} – ordinary frequency (in Hz) of an oscillation mode of degree l and order m

$f_{n,\gamma g}$ – ordinary frequency (in Hz) of an oscillation of 'mode n'

F_D – drag force

FEA – Finite Element Analysis

FFT – Fast Fourier Transform

g – gravitational acceleration

GDM – Gas Diffusion Membrane (frequently called a gas diffusion layer)

h – drop height

h_{ave} – a measure of average drop height

j – one half the number of nodes along the the arc length of a profile view of a drop, $n = 2j - 1$

l – degree number of oscillation

m – order number of oscillation

$\dot{M}$ – rate of mass transfer

n – integer number of half wavelengths dividing the arc length of a profile view of a drop

PMMA – poly(methyl methacrylate)

$r_{substrate}$ – radius of the floating element sensor surface, 9 mm

R – spherical cap radius of the axisymmetric drop measured in quiescent conditions

R_a – average roughness

Re_d – Reynolds number based on d

Re_h – Reynolds number based on h

Re_R – Reynolds number based on R

R_p – minor axis of an ellipsoid approximating the shape of a sessile drop

S – surface area of an ellipsoid approximating the shape of a sessile drop

Sc – Schmidt number

SHS – Superhydrophobic Surface

U_{crit} – critical air velocity for incipient motion (i.e. for the onset of drop motion), measured upstream in Chapter 2 (see U_{up}) and two centimeters above the streamlined body in Chapters 3 and 4 (see U_∞).

U_{up} – air velocity measured upstream of the streamlined body used in tests

U_{∞} – free stream air velocity

V – volume of the drop/bubble

VOF – Volume of Fluid (a CFD Technique)

x – streamwise distance from front of streamlined body to location of drop placement

γ – surface tension

θ – contact angle

θ_a – advancing contact angle

θ_{max} – maximum contact angle (seen at downstream side of air sheared drop)

θ_{min} – minimum contact angle (seen at upstream side of air sheared drop)

θ_r – receding contact angle

$\lambda_{ml,\gamma}$ – eigenvalue of a surface tension based drop oscillation mode of degree l and order m

$\lambda_{ml,g}$ – eigenvalue of an gravity based drop oscillation mode of degree l and order m

$\lambda_{n,\gamma g}$ – eigenvalue of a sessile drop oscillation of 'mode n'

µl – *microliter*

μ – viscosity of air

ρ – air density

ρ_1 – density of the inner fluid of drop/bubble

ρ_2 – density of the fluid outside of a drop/bubble

1-D – one dimension(al) (spatial dimension)

2-D – two dimension(al) (spatial dimensions)

3-D – three dimension(al) (spatial dimensions)

Chapter 1: Introduction

1.1 Conceptual Example

This thesis considers some of the interactions between sessile drops and shearing air flow, specifically, drop oscillation and the onset of shedding. Consider, as a conceptual example, an automobile after a rainstorm. Water drops sit (are sessile) on the car body. As the car accelerates, air velocity increases over the surface (and the drops on it). As the air velocity increases, there will be advection enhanced evaporation of the drop and an internal circulation set up. Further increasing the velocity, the drop will deform from its axisymmetric shape and may begin to oscillate under the airflow. At higher velocities still, the point of incipient motion will be reached and the drop will start to shed (run back) along the surface, possibly being broken up, or (re)entrained into the airflow.

The above list can be termed as the interaction of a sessile drop with shearing flow, and is not limited to the conceptual example given. The phenomena directly apply to controlling fuel cell flooding, decreasing airfoil icing, and improving visibility in rainy driving/flight conditions. Results can also be applied to driers, condensers, pesticide use, and medical aerosols. Enhanced oil recovery/floatation/detergency are also applications, if one considers a system where flowing liquid shears sessile oil drops/bubbles/particles, respectively, rather than systems where flowing air shears sessile liquid drops. Liquid-liquid and liquid-solid

particle systems will not be considered in this thesis, so the author will generally write of sessile drops and shearing air, but the reader should keep in mind that shearing liquids and/or sessile bubbles/solid particles are possible.

From an investigative standpoint, it is fortunate that many of the above interactions of sessile drops with shearing airflow can be separated and studied individually. For example, evaporation can be studied separately from shedding by keeping the air velocity lower than the critical air velocity for incipient motion. Likewise, evaporation of the drop can be removed from other examinations either by controlling the relative humidity (RH) of the airflow, or by conducting the test quickly enough to limit evaporation. As a counter example, the oscillation, deformation, internal circulation and shedding of a drop are generally linked, or at least concurrent. However, one could remove shedding by using a low enough air velocity, and similarly, some drops could be shed with little to no oscillation, deformation, or internal circulation depending on the properties of the fluid and solid.

The interactions between sessile drops and shearing flow will obviously depend on both drop and shear flow fluid properties such as density and viscosity. The interactions also depend on surface properties such as the surface tension between drop and shearing fluid, and the contact angle between the drop and surface. The contact angle, denoted θ, is the angle

measured from the interface under the drop to the tangent of the liquid-vapor interface at each point along the three phase contact line. The three phase contact line describes the extents of the drop's contact on the surface where liquid, vapor, and solid phases meet. In this thesis, systems for which the contact angles are below 90° (indicating a less than hemispherical drop shape) are termed hydrophilic. Systems for which the contact angles are between 90° and 150° (drop shape more than hemispherical) are termed hydrophobic. Systems for which the contact angles are above 150° (nearer to spherical drop shape) are termed superhydrophobic, with the surfaces terms to be superhydrophobic surfaces (SHS)[1].

Contact angle hysteresis (CAH) must also be considered in its effects on sessile drop/shear flow interactions. CAH is the difference between the maximum contact angle occurring where part of a drop advances across a surface and the minimum contact angle occurring where part of a drop recedes across a surface. These contact angles are commonly termed 'advancing' and 'receding' (θ_a and θ_r, respectively), though some clarification must be made as to under what conditions the measurements are performed since the contact angles are history and measurement condition dependent[1]. The difference in contact angles due to CAH leads to an adhesion force between drop and surface that resists motion of the drop along the surface, and can lead to non-axisymmetric drop shapes.

For the chosen areas of concentration in this thesis (force versus air velocity up to the point of incipient motion and drop oscillations before this point) the interactions of sessile drops with shearing flow depend mainly on the balance of drag force with adhesion/surface tension forces. Shedding begins when the drag force overcomes adhesion force. Drag depends, at least, on drop size, drop shape and air speed/density. Adhesion depends, at least, on drop size, drop shape and liquid-vapour surface tension. Drop shape is based on contact angle, CAH and deformation/oscillation of the drop. Oscillation will depend on the driving force (drag) and its interactions with the restoring force (based on surface tension and the shape of the deformable drop).

In the following pages, the literature of sessile drop interactions with shearing flow will be reviewed. The focus is on the chosen topics of incipient motion and drop oscillation, and a rationale for these choices will be given. Though not in the scope of this thesis, evaporation and breakup/(re)entrainment are also reviewed for the sake of completeness. The methodology, scope, and outline of the thesis are then presented.

1.2 Literature Review

1.2.1 Shedding: Incipient Motion

For a sessile drop under shear flow, when air drag overcomes the total force of adhesion between the drop and the surface the point of incipient

motion is reached and the drop is shed (starts to undergo runback) along the surface. Adhesion and drag are therefore both important in the study of shedding. As illustrated in Figure 1-1, the force from adhesion is the summation of surface tension forces acting around a complex and usually unknown contact line shape, in a varying direction given by an again unknown distribution of contact angle[2]. In shedding by shear flow, the applied force is aerodynamic drag. The pressure drag component depends on the distribution of air velocity over the drop shape, while the shear drag component would depend on air velocity and the drop internal circulation (see 5.III in Clift et al. and the thesis by G. Minor[3,4]). As a reminder, the drop could be oscillating under the airflow. This oscillation could affect the drag force over the drop through perturbations to the wake (see Figure 7.2 of Clift et al, and Lin and Peng[3,5]), and also lead to an oscillation in the adhesion force by changing the local contact angle around a fixed or partially oscillating contact line.

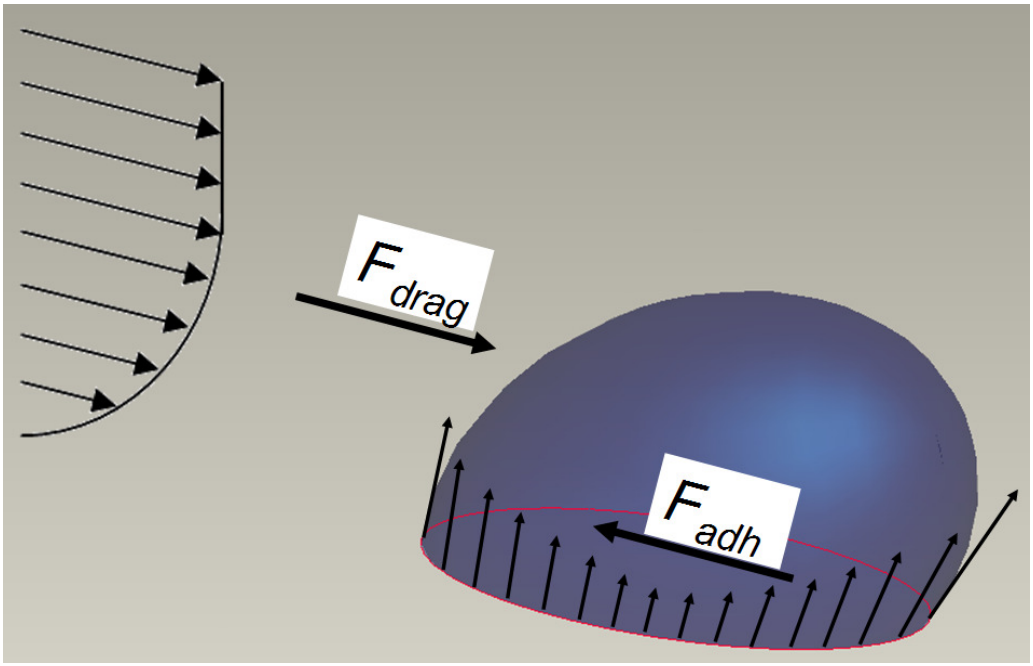

Figure 1-1: Schematic of a sessile drop showing the distribution of contact angles around the contact line. This distribution helps determine the force due to adhesion which opposes the force of drag caused by the non-steady perturbation of the drop by the boundary layer.

The topic of shedding of sessile drops is of interest for applications since it is quite ubiquitous, existing anywhere one has a fluid on a surface under another shearing fluid. This means it has applications to automobiles in rain[6], airplanes or wind turbines[7,8], fuel cells[4,9,10], oil recovery/detergency[11–13] , condensers, etc.

Shedding by shear flow has been widely modeled. Models have progressed from the deformation of drops with fixed contact line[14], up to models involving, e.g., runback (flow) of the drop along the surface[15–18], drop breakup and re-entrainment[16,17,19], and oscillation of the drop[5,15]. The models put forth above are advanced, but lack experimental data for basic understanding of the phenomena, as well as validation and calibration of

the models. Also, the models are often limited to lower Reynolds numbers of the drop (ranging from 1-80) and other simplifications (e.g. simplified flow fields, two dimensional simulations, small density differences between drop and surrounding fluid). They also consider only simplified models of adhesion[20], meaning their application is suspect. Finally, each were performed considering a single system of fluid and solid, so a systematic study of the effects of liquid and solid is needed. This is especially important since as noted above, both adhesion and drag depend on contact angles and drop area/shape (i.e. wetting properties of the system).

In terms of experimental studies, for internal (channel) flow, the work of Mahé *et al.*[11] is of note as one of the early studies of shedding of various oil drops by water flow. In that work, they found critical shear rates for detachment, but the study was largely phenomenological. It also cannot be directly applied to this thesis since the shearing liquid was water rather than air as in the present case. This would impact shedding since the different viscosity and density ratios between water and oil versus air and water would change the characteristics of momentum transfer from the shearing flow to the drop.

More recently, interest in fuel cells, and the concomitant requirements of managing the water produced by them, has increased. This has led to several papers examining (with experiments and models) shedding of

drops placed on a fuel cell gas diffusion membrane with small channel geometries[4,9,10,19,21–24] (see Chapter 2 for a more detailed discussion of most of these works). The work of Esposito *et al.*[22], which was not published at the time of publication of Chapter 2, is a fairly good work, but performs little analysis of the criterion for shedding, forcing the fit to be a simple power law. They also studied only a limited range of volumes on only one surface).

Of the other above mentioned works, that of Theodorakakos *et al.*[24] is perhaps the best, finding good comparison between their Volume of Fluid (VOF) CFD model and experimental results. However, the experimentally measured contact angles were required as inputs to the model, with a sinusoidal distribution assumed between the upstream and downstream measured values, so the model is somewhat 'tuned' to the experiment. They tested three different types of gas diffusion membrane, and found that drops shed at the lowest airspeed for the membrane with the lowest contact angle hysteresis (CAH). They also found that smaller drops required a higher air velocity to shed, explaining this as the effect of decreased drag due to a decreased obstruction to the flow (interestingly, they found a recirculation zone downstream of the drop for all tests, regardless of the decreased obstruction). They performed a good parametric study of factors such as flow rate of water into the drop, temperature, pressure, location of drop etc., but found that the main controlling parameter is the contact angle hysteresis (CAH) of the surface.

Lacking in the work is a simple predictive model. Each simulation of each drop size required 2-3 days, and resulted in three separate curves for three separate surfaces. Therefore, the difficulty in developing separate models for multiple systems and multiple drop volumes at higher Reynolds numbers and the computation cost of running CFD for all of these would likely be prohibitive. Considering the range of solid surfaces that could be used in applications, attempts should be made to find simpler predictive curves explaining the shedding of drops across a range of volumes and on a variety of surfaces.

Minor[4], is also an interesting preliminary work giving criteria for drop shedding. It is also one of only two works found measuring internal circulation in the drop. Unfortunately, due to difficulties in the design process only limited analysis of results was performed, and only a small range of volumes was tested on a single surface. Further, distortion limited the internal velocity measurements to be in the less interesting core region of the drop, instead of the more important interface region. Minor[4] found that the maximum internal velocity measured is approximately 2 orders of magnitude lower than the free stream velocity and that increasing air flow velocity has a diminishing effect on internal velocity. A similar result was presented in a conference by Njifenju et al [25], who managed measurements closer to the interface and found that maximum internal velocities are at most approximately 3 orders of magnitude lower than the free stream. These results indicate that the internal velocity of the drop is likely a

minor contributor to the shedding behavior of sheared sessile drops. It is thus neglected in this thesis.

As a reminder, all of the above experimental works on fuel cells (therefore excepting Njifenju et al.[25]) looked only at a small range of surfaces (various types of gas diffusion membrane, GDM). Thus they have examined only a limited range of surface properties (just the porous surface of the GDM, lacking tests of surface with other hydrophobicities/topographies). So, more work is needed examining drop shedding from different types of solid surfaces. Also, the channel flow geometry used in fuel cell work could result in different aerodynamic forces on the drop due to blockage effects unless the drop was much smaller than the channel, so tests in external flow are required.

Aside from the work of the author (see Chapters 2-4, or the literature[1]), external flow has been studied by others. Bico *et al.* and Njifenju *et al.* [6,25] presented in conferences an examination of both aerodynamic and adhesion characteristics for water and silicone oil drops on a RainX® (water repelling) coated surface. They studied volumes from 3-500 μl, finding that above 100 μl the critical air velocity and runback behavior was independent of volume, a result they attributed to their drops elongating into a 'sausage' shape with the long axis perpendicular to the airflow direction. This would effectively make the airflow and adhesion forces independent of volume by making the problem quasi-two dimensional.

Conversely, over a small range of drop volumes (~10-30 μl), they found that a critical Weber number (constant for the range of volumes) was the criteria for drop shedding (incipient motion). They also attempted to measure drag force on the drop by tilting the surface while flowing air upward along it[25]. As discussed in Chapter 3, this technique is of limited use since it confounds the measurement of drag by introducing gravitational force and its effects to distort the drop.

Also considering external flow, White and Schmucker[7] studied a system of water on smooth aluminum, finding the critical runback volume for three different turbulent air velocities. They performed advanced aerodynamic analysis, but did not consider wetting and adhesion in great depth. In order to avoid confusion, it is important when reading the literature to note that in this thesis, as in our previous work[1], incipient motion is defined as the instant of initial motion of the drop's entire contact line downstream, which is different than the meaning that White and Schmucker[7] put forth (i.e. a runback of the drop for a short distance, followed by a stop). This confusion in terminology is unfortunate, but it is felt that the term 'incipient motion' is the correct term to use in the work of this thesis, in keeping with its definition in drop shedding by gravity[2].

Schmucker and White more recently published another work[26], in which they studied 15-450μl water drop shedding from rough (average roughness R_a = 3.25μm) aluminum surfaces (θ_a = 63.5°±3.7°, θ_r = 8.2°±1.5°). They

tested level surfaces in a 25 mm by 50 mm working section wind tunnel, and also tilted the wind tunnel to have gravity and air shear complement each other to shed drops at lower air velocities (i.e. the opposite case to Njifenju et al [25]). They also used a speckle technique[26,27] to partially reconstruct the drop's 3-D surface contours.

Schmucker and White[26] found that increasing the tilt of the surface decreased the critical air velocity, and changed the drop shape compared to level surface tests, meaning that combined gravity-shear tests should not be taken to be representative of situations in which shear stress alone acts. They also found a constant Weber number of 8 as the threshold for level surfaces in the large volume limit (where drops should deform into 'sausage' shapes for which adhesion force is largely independent of volume). At lower drop volumes, the critical Weber number seems to decrease with increasing volume. Finally, they used their speckle technique to attempt a reconstruction of the contact line shape and contact angle distribution as illustrated in Figure 1-1. Measurement error (specifically in determining advancing contact angle) prevented high accuracy in the reconstruction, but adhesion force (related to drag force up to the point of incipient motion) was seen to be of the same order of magnitude as the force for shedding drops in quiescent conditions by tilting the surface.

In summary, the field of incipient motion and runback of sheared sessile drops has certainly been opened, but is still a fertile area for study. Missing (except in the work of the present author) is a systematic investigation of drop shedding for a variety of systems (with varying contact angles and fluid properties) and a large range of drop volumes. Such a study would give fundamental experimental knowledge and be useful to modelers. Importantly, given that the contact angles are an important parameter[24], surfaces with different hydrophobicities should be compared, and the use of superhydrophobic surfaces (SHS) to promote drop shedding should be investigated. Also missing in the above is individual study of the adhesion and drag forces on the drop. Since these forces are coupled at the point of incipient motion they are generally not studied separately. Decoupling adhesion and drag and studying each will provide increased understanding of shedding. Considering that this field is open, and that the point of incipient motion is the fundamental state leading to subsequent sheared sessile drop interactions such as breakup and (re)entrainment, the study of incipient motion has been chosen as the main focus of this thesis.

1.2.2 Drop Oscillation

The oscillation of sessile drops has applications to areas such as drop actuation and mixing in microfluidics[28–34], as well as transitions between the Cassie and Wenzel wetting states on rough surfaces[35,36]. It can also decrease/overcome the energy barriers responsible for contact angle

hysteresis and thereby decrease CAH[37–43], which can lead to easier shedding of drops due to decreased adhesion force. It is also expected to affect the wake downstream of a sessile drop under shear flow, affecting the drag on the drop (see Figure 7.2 of Clift et al, and Lin and Peng[3,5]).

The oscillation of free drops (those not constrained by contact with a solid surface) in a quiescent atmosphere has been investigated extensively. It seems Plateau first reported[44] observing drop oscillations in 1843, with Rayleigh forming the first models to explain them[45,46]. Constrained drops (either sessile, pendant, or otherwise constrained by a solid body) are a more recent field of study, but again have been studied for the quiescent case both for axisymmetric[47–52] ('longitudinal'), and non-axisymmetric[50–54] ('lateral') modes of oscillation. The oscillation of air sheared drops are little studied, however, with only four papers on the topic[5,15,22,55]

The body of literature on quiescent drop oscillations is large. In conducting the oscillation work of this thesis, it was found that several of the diffuse works on the subject seem to be little used by other researchers. Also it seems some confusion exists as to the precise physics governing drop and bubble oscillations. Specifically, confusion seems apparent as to what models exist to describe oscillations and how such models should be applied (especially for non-axisymmetric oscillations). We believe the source of this confusion is twofold: first, due to misunderstanding of bulk (i.e. center of mass) oscillation and surface oscillation of drops and their

connection to each other; and second, due to a lack of appreciation for the complexities of non-axisymmetric wave shapes and the three-dimensional character of the drop surface. Given its extent, much greater discussion of the literature is given in Chapter 5, while the basics of drop oscillation and the four works on sheared sessile drop oscillation are given here.

The oscillation of drops is described generally by (axisymmetric or non-axisymmetric) spherical harmonics and the related associate Legendre polynomials. Models (for surface tension restored oscillations) take the form of:

$$f_{ml} = \frac{1}{2\pi}\sqrt{\frac{\gamma}{\rho_1 V \lambda_{ml,\gamma}}} \qquad \text{Equation 1-1}$$

where f_{ml} is the ordinary frequency (in Hz) of an oscillation mode of degree l and order m; γ is surface tension; ρ_1 is the density of the drop/bubble; V is the volume of the drop; and $\lambda_{ml,\gamma}$ is the eigenvalue of a surface tension based drop oscillation mode of degree l and order m (a mode *m-l* oscillation described by a spherical harmonic of the same degree and order). The concept of oscillation eigenvalues is used since most models for drop/bubble oscillation follow the same general form. Various eigenvalues are possible, depending on degree and order numbers as well as drop shape. Closed form first principles solutions for the eigenvalue exist for, e.g. free drops and bubbles[56], while infinite series or approximate equations are necessary to determine the eigenvalue for constrained

(sessile) drop oscillation[48–52,54]. Various models for the eigenvalue/oscillation are considered in Chapter 5, and tested in comparison to measured data for sheared sessile drop oscillation and data for quiescent sessile drop oscillation collected from the literature.

As stated before, there is very little experimental research on the oscillation of sessile drops by shear flow. The only exceptions to this are a translated Chinese language paper[55] and another more recent work[22]. The first work[55] studied a small range of water volumes (2-6 μl) on rough and smooth copper with a high speed camera. They found lateral and longitudinal modes of decreasing frequency with increasing volume, and a slight inverse effect of airspeed on frequency. However, they did not attempt to linearize their data and performed little analysis of it. Further, the single system tested (water on copper) means that they only considered a small range of contact angles. Contact angle was also not reported/considered, but was approximately 80° based on images given in their paper. Finally, their analysis technique (which seemed limited to visually counting frames from high speed videos) means their frequency measurements are imprecise. The second work[22] was studying shear shedding and oscillation of sessile drops. They only studied a small range of water volumes on a single surface (proton exchange membrane for a fuel cell, water contact angle of approximately 130°). They found a dependence similar to Equation 1-1 for lateral modes, but did not gather sufficient data to fit longitudinal modes. Neither did they attempt any first

principles models, nor consider the effects of contact angle. They found no dependence of frequency on air speed. Aside from these papers, in most of the shear shedding works to date, there has been no time resolved observation of the drop, so high speed drop motions such as oscillation have been lost. However, in examining the figures of several of the other works, one can see blurred outlines of the drop, suggesting oscillation.

In terms of modelling, only Zhang *et al.*[15] and Lin *et al.*[5] have reported observations of drop oscillation under shear flow. Zhang *et al.* did not analyze the oscillations in any way. Lin *et al.* used a simplified two dimensional CFD model for a single volume. They found that the oscillation coincides with a pair of vortices inside the drop, and that each oscillation coincides with a vortex shed from the exterior of the drop, supporting the idea that sessile drop oscillations will interact with the flow over the drop and could affect the drag force on a drop under cross flow.

In summary, the oscillation of sessile drops by cross flow is a very new field, and one that could be related to shedding both in its interactions with wake drag, and as a cause of drop motion in its own right. Further, as little/no consideration has been given as to the effects of contact angle on sheared sessile drop oscillation, and as confusion exists in the literature as to the models for sessile drop oscillation, a study of these topics would also be of fundamental interest. As such, drop oscillation under cross flow has been chosen as a secondary area of study for this thesis.

1.2.3 Evaporation

The evaporation of sessile drops has applications to areas such as internal combustion engines[57], drying[58], pesticides[59], and chemical weapons[60–62]. Evaporation of free floating drops in a quiescent atmosphere is diffusion limited and has a well known analytic solution giving the 'd^2 law' where the instantaneous squared diameter of the drop varies linearly with time. For sessile drops, high[57,58,63–68] (including superhydrophobic[58,64,68]) and low[59,61,62,66,67,69,70] contact angle drops have been tested. A similar diffusion limited process exists when a sessile drop evaporates in quiescent conditions, though the distortion caused by the solid surface to both the drop and the concentration field must be taken into account[63].

One must also account for the possible change in drop shape as a sessile drop evaporates. Drops have been observed to evaporate with fixed contact radii and decreasing contact angles, and/or with fixed contact angles and decreasing contact radii[63]. These two regimes lead to different evaporation rates. Mixed modes of evaporation have also been observed and studied[71]. With the further complication of cross flow over the drop, the problem is advection controlled rather than diffusion limited, and more advanced analysis is required. This analysis has been performed both in 2-D[60] and 3-D[59,66], and confirmed with more recent experiments[61,69], though the relations derived appear to have been only confirmed for drops of low

contact angle, in the linear portion of the boundary layer. The non-dimensionalized relation for sessile drop evaporation in cross flow is[61]:

$$Sh_d = \frac{\dot{M}d}{Ac_w D} = C \cdot Sc^{1/3} \mathrm{Re}_d^{2/3} \qquad \text{Equation 1-2}$$

In Equation 1-2, $\dot{M}$ is the rate of mass transfer, d is the drop's initial contact diameter, A is the drop's exposed surface area, c_w is the mass concentration of the drop's vapour at the surface, D is the diffusion coefficient of the drop's vapour in the air, and C is a unitless factor of 0.852. Sc is the Schmidt number and Re_d is the Reynolds number based on d. Equation 1-2 is only valid for constant contact area (i.e. pinned contact line) evaporation, though corrections for constant contact angle evaporation are given in the literature[61]. Also, Equation 1-2 requires knowledge of the initial rate of mass transfer.

Altogether, though the field is not closed (for example, the need for an initial measure of mass transfer), it was decided that the evaporation of sessile drops under cross flow would not be a focus of this thesis. The reasons for this were twofold. First, the field is already more researched than other interactions of sessile drops in a cross flow. Second, the applications of study of the other fields were of greater interest to the author. Throughout the work reported in this thesis, evaporation effects

have been mitigated by conducting tests in a short enough time scale that evaporation effects are negligible.

1.2.4 Runback, Breakup and (Re)Entrainment

The runback, breakup and (re)entrainment of a sessile drop under cross flow can be thought of as advanced cases of shedding. That is, they would tend to occur after the point of incipient motion. Breakup would occur if the drag forces on the drop were sufficient to overcome the cohesive forces of the drop. (Re)entrainment can occur in two ways. First, if the airflow generates sufficient lift force on the drop to completely remove a part or all of it from the surface the drop will be lifted into the airflow and (re)entrained. Second, if a drop runs back to the end of a solid and the air flow removes it from the surface it may be (re)entrained. Considering the more complex nature of these phenomena, few works examine them. The works that were found are discussed below.

Jones *et al.*[16] simulated oil drops in a water flow, using a Dissipative Particle Dynamics approach. They found that drops of varying contact angle reached incipient motion at a sufficient flow rate, and ran back along the surface. Further, drops with high contact angles (~150°) tended to lift off the surface after a period of runback if the flow rate was increased sufficiently beyond the point for incipient motion. Finally, drops with lower contact angles (≤120°) tended to form necks and breakup into smaller drops (which were either entrained or fell back to be sessile on the

surface) when the flow rate was increased sufficiently beyond the point for incipient motion/runback.

Similar to Jones *et al.*[16], Zhu *et al.*[17] also performed numerical simulations, this time with a 2-D VOF technique for drops with a continuous input of water to their base. They found a recirculation zone behind the drop/rivulet, with pressure drag being the main force causing shedding. They observed that sometimes the drops would breakup, but did not investigate this thoroughly. They also found that multiple drops could coalesce, and that this led to easier shedding due to the larger drop size/increased channel blockage. Similar to Theodorakakos *et al.*[24] they found that smaller drops required a larger air velocity for shedding. As a caveat on the results of Zhu *et al.*[17], it appears that they did not properly account for contact angle hysteresis in their model, which would explain their incongruous results for drops not connected to a continuous input of water.

Golpaygan and Ashgriz have also studied drop breakup with a 2-D VOF technique for drops with pinned contact lines on a gas diffusion membrane[10]. They found that drops would assume an equilibrium shape if air velocity was low enough, and that drops would breakup at higher air velocities. They considered the effects of fluid properties on the threshold for breakup, but since they pinned the contact line of their drops in all

cases, they could not determine at what point the drop would start to run back before/after breakup.

Experimentally, Theodorakakos *et al.*[24] have given phenomenological evidence of blow off, reporting that drops 'flew' off the gas diffusion membrane they considered, and confirming that the same result occurred with their VOF model.

Bico *et al.* and Njifenju *et al.*[6,25] also presented work in conferences looking at runback, finding that drop speed increases with air velocity (with drop speed on the order of 10^{-4} times lower than air velocity. They also found a roughly linear relation between the capillary number based on drop speed and the Weber number based on air velocity.

So runback, breakup, and blow off/(re)entrainment seem to be largely untouched areas for research. They are therefore open, but it has been decided that the wiser course is to gain a firm grasp on the fundamental, and still largely unexplored/unexplained, area of incipient motion before investigating more advanced aspects of shedding. As such, runback, breakup, blow off, and (re)entrainment are not fields of study for this thesis.

1.2.5 Summary

Summarizing Sections 1.2.3-1.2.4, for the interaction of sessile drops with a cross flow, oscillation, incipient motion, runback, breakup, and (re)entrainment are all largely open topics. Since incipient motion is the fundamental point leading to all subsequent shedding behaviours, it has been chosen as the main topic of this thesis. Oscillation has been chosen as a secondary topic because it is an area in which fundamental knowledge can be gained, and as it can have an effect on shedding. Also, oscillations can be researched with the same data collected for shedding tests. Air has been chosen as the cross flowing fluid because it is more common in the applications of interest. External flow has been chosen since it is less researched than channel flow.

1.3 Goals of this Thesis

Considering the state of present knowledge, and the open fields chosen for study, the goals of this thesis are to:

1) Understand the relation between drop size and critical airflow at the point of incipient motion for different liquid-solid systems under laminar airflow.
2) Gain fundamental knowledge regarding the individual effects of drag and adhesion forces acting on sessile drops in a cross flow by measuring each.

3) Investigate the scarcely studied field of sessile drop oscillations in cross flow and how these oscillations increase or decrease the ease of shedding.

1.4 Principal Methodologies

Wishing to study incipient motion in its purest form, we choose to study individually placed sessile drops. This avoids complications due to wake interactions between multiple drops. The point of incipient motion is determined by slowly increasing the air velocity until the drop has moved 210 μm downstream along the surface. A slow increase in velocity has been shown[24] to allow for the precise identification of the critical air velocity for incipient motion without undesirable dynamic effects, while the distance of 210 μm was chosen as a suitably small but still discernable distance signaling the onset of motion.

A wind tunnel was used as the experimental apparatus. High speed optical monitoring of the drop is the main measurement technique, along with image processing, a pitot static tube to monitor airspeed, and a floating element wall shear sensor to measure forces on the drop. Experimental apparati are discussed in more detail in the following chapters.

Understanding that shedding and oscillation are controlled by fluid properties and surface hydrophobicity, smooth hydrophilic and hydrophobic surfaces, as well as rough etched and coated

superhydrophobic surfaces were tested. Two different fluids (water and hexadecane) were used to form drops, to investigate the effects of surface tension, density, and viscosity. A range of drop volumes were used to test the relation between drop size and critical air velocity for incipient motion. Analysis of results has been informed by considering and balancing basic equations for drag and adhesion forces, as well as first principles models for constrained drop oscillation.

1.5 Outline of Remaining Thesis Chapters

This thesis is presented in 'Mixed-Paper' format. Chapter 2 is a published paper, while Chapters 3-5 are draft manuscripts that will be submitted for publication in peer reviewed journals. For readers of this thesis who wish to also read the peer reviewed publications, they will be listed with Milne, A. J. B., and Amirfazli, A. as authors on all papers, and titles will be similar to the chapter headings.

Chapter 2 contains an investigation of the critical air velocity necessary to shed sessile drops by cross flowing air, considering the effects of contact angle and surface tension and finding a normalized curve to explain behavior on multiple systems. It also investigates the differences between contact angles seen in a cross flowing air test compared to a tilted plate or quasistatic advancing/receding test.

Chapters 3 and 4 relate to the measurement of drag force on sessile drops. Chapter 3 introduces the novel measurement technique that was developed, based on a floating element wall shear sensor, combined with a differential drag measurement technique. The specifics of sensor design, and the challenges addressed in implementing the technique in a low speed wind tunnel are discussed. Chapter 4 presents the first ever measurements of drag force on sessile drops in cross flow and considers their implications on adhesion and shedding. Chapter 4 also shows the non-dimensionalization of the drag versus airspeed curve, finding similarities to and differences from standard drag curves for solid bodies which are hypothesized to relate to the oscillating drop coupling with the wake to increase drag.

Chapter 5 begins with a preface considering the effects (or rather, lack of effect) of external tunnel vibrations on the cross flow induced shedding of sessile drops. Further analyzing the drop oscillation results, it was found that there were misunderstandings and gaps in the literature. As such, Chapter 5 presents a unifying framework for drop/bubble oscillation and reviews the literature with an eye toward what models exist to understand drop oscillations. It also uses full profile oscillation analysis to identify the frequencies and mode shapes of sessile drop oscillations. It then combines the newly generated data with collected literature data, giving a wider range of contact angles, and allowing for multiple literature models to be

tested for their ability to account for the effects of contact angle on sessile drop oscillation.

Chapter 6 summarizes the thesis and presents conclusions regarding the oscillation and incipient motion of sessile drops in a cross flow. It also suggests future studies that can be performed, including further liquids and solid surfaces that could be tested, and experiments that could be performed, to better understand nuances of sessile drop shedding and oscillation in a cross flow. Other tests using the floating element differential drag measurement technique are also discussed.

Following Chapter 6, the Appendix gives details of experimental methods, etc. not fully discussed in previous chapters, including, e.g., illustrative images from the image processing routines used, and annotated image of the wind tunnel. Letters of permission for copyrighted material (used in Chapters 4 and 5) are also contained in the Appendix.

References for Chapter 1

(1) Milne, A. J. B.; Amirfazli, A. *Langmuir* **2009**, *25*, 14155–14164.
(2) Antonini, C.; Carmona, F. J.; Pierce, E.; Marengo, M.; Amirfazli, A. *Langmuir* **2009**, *25*, 6143–6154.
(3) Clift, R.; Grace, J. R.; Weber, M. E. In *Bubbles, drops, and particles*; Dover Publications: Mineola N.Y., 2005.
(4) Minor, G. Experimental Study of Water Droplet Flows in a Model PEM Fuel Cell Gas Microchannel. MASc, University of Victoria, 2007.
(5) Lin, Z.; Peng, X. *Heat Transfer-Asian Research* **2009**, 485–491.
(6) Bico, J.; Basselièvre, F.; Mermigier, M. In *Bulletin of the American Physical Society*; American Physical Society: Chicago, IL, 2005.
(7) White, E. B.; Schmucker, J. A. *Journal of Fluids Engineering* **2008**, *130*, 061302.
(8) Lee, S.; Bragg, M. B. *J Aircraft* **1999**, *36*, 844–850.
(9) Zhang, F. Y.; Yang, X. G.; Wang, C. Y. *Journal of The Electrochemical Society* **2006**, *153*, A225.
(10) Golpaygan, A.; Ashgriz, N. *International Journal of Energy Research* **2005**, *29*, 1027–1040.
(11) Mahé, M.; Vignes-Adler, M.; Adler, P. M. *Journal of Colloid and Interface Science* **1988**, *126*, 329–336.
(12) Schleizer, A. D.; Bonnecaze, R. T. *Journal of Fluid Mechanics* **1999**, *383*, 29–54.
(13) Thoreau, V.; Malki, B.; Berthome, G.; Boulange-Petermann, L.; Joud, J. C. *Journal of Adhesion Science and Technology* **2006**, *20*, 1819–1831.
(14) Li, X.; Pozrikidis, C. *Journal of Fluid Mechanics* **1996**, *307*, 167–190.
(15) Zhang, J.; Miksis, M. J.; Bankoff, S. G. *Physics of Fluids* **2006**, *18*, 072106.
(16) Jones, J. L.; Lal, M.; Ruddock, J. N.; Spenley, N. A. *Faraday Discussions* **1999**, *112*, 129–142.
(17) Zhu, X.; Sui, P. C.; Djilali, N. *Journal of Power Sources* **2007**, *172*, 287–295.
(18) Rothmayer, A. P.; Tsao, J. C. *AIAA Paper No. 2001-676* **2001**.
(19) Golpaygan, A.; Ashgriz, N. *International Journal of Computational Fluid Dynamics* **2008**, *22*, 85–95.
(20) Chang, C.; Criscione, A.; Jakirlic, S.; Tropea, C.; Amirfazli, A. In *Bulletin of the American Physical Society*; American Physical Society: San Diego, CA, USA, 2012; Vol. Volume 57, Number 17.
(21) Yang, X. G.; Zhang, F. Y.; Lubawy, A. L.; Wang, C. Y. *Electrochemical and Solid-State Letters* **2004**, *7*, A408.
(22) Esposito, A.; Montello, A. D.; Guezennec, Y. G.; Pianese, C. *Journal of Power Sources* **2010**, *195*, 2691.
(23) Kumbur, E. C.; Sharp, K. V.; Mench, M. M. *Journal of Power Sources* **2006**, *161*, 333–345.

(24) Theodorakakos, A.; Ous, T.; Gavaises, M.; Nouri, J. M.; Nikolopoulos, N.; Yanagihara, H. *Journal of Colloid and Interface Science* **2006**, *300*, 673–687.
(25) Njifenju, K.; Bico, J.; Andrès, E.; Jenffer, P.; Fermigier, M. In *Bulletin of the American Physical Society*; American Physical Society: Minneapolis, MN, 2009; Vol. Volume 54, Number 19.
(26) Schmucker, J. A.; White, E. B. *Journal of Fluid Mechanics* **2013**, *In Revisions*, 26 pages.
(27) Schmucker, J. A.; Osterhout, J. C.; White, E. B. *Experiments in Fluids* **2011**, *52*, 123–136.
(28) Beyssen, D.; Lebrizoual, L.; Elmazria, O.; Alnot, P. *Sensors and Actuators B: Chemical* **2006**, *118*, 380–385.
(29) Noblin, X.; Kofman, R.; Celestini, F. *Physical Review Letters* **2009**, *102*, 194504–1–194504–4.
(30) Dong, L.; Chaudhury, A.; Chaudhury, M. K. *The European Physical Journal E* **2006**, *21*, 231–242.
(31) Daniel, S.; Sircar, S.; Gliem, J.; Chaudhury, M. K. *Langmuir* **2004**, *20*, 4085–4092.
(32) Mettu, S.; Chaudhury, M. K. *Langmuir* **2011**, *27*, 10327–10333.
(33) Daniel, S.; Chaudhury, M. K.; De Gennes, P.-G. *Langmuir* **2005**, *21*, 4240–4248.
(34) John, K.; Thiele, U. *Physical Review Letters* **2010**, *104*, 107801–1–107801–4.
(35) Bormashenko, E.; Pogreb, R.; Whyman, G.; Bormashenko, Y.; Erlich, M. *Applied Physics Letters* **2007**, *90*, 201917–1–201917–2.
(36) Boreyko, J. B.; Chen, C.-H. *Physics of Fluids* **2010**, *22*, 091110.
(37) Della Volpe, C.; Maniglio, D.; Morra, M.; Siboni, S. *Colloids and Surfaces A: Physicochemical and Engineering Aspects* **2002**, *206*, 47–67.
(38) Montes Ruiz-Cabello, F. J.; Rodríguez-Valverde, M. A.; Cabrerizo-Vílchez, M. A. *Langmuir* **2011**, *27*, 8748–8752.
(39) Meiron, T. S.; Marmur, A.; Saguy, I. S. *Journal of Colloid and Interface Science* **2004**, *274*, 637–644.
(40) Decker, E. L.; Frank, B.; Suo, Y.; Garoff, S. *Colloids and Surfaces A: Physicochemical and Engineering Aspects* **1999**, *156*, 177–189.
(41) Andrieu, C.; Sykes, C.; Brochard, F. *Langmuir* **1994**, *10*, 2077–2080.
(42) Smith, T.; Lindberg, G. *Journal of Colloid and Interface Science* **1978**, *66*, 363–366.
(43) Rodríguez-Valverde, M. A.; Montes Ruiz-Cabello, F. J.; Cabrerizo-Vílchez, M. A. *Soft Matter* **2011**, *7*, 53.
(44) Plateau, J. In *Annual report of the Board of Regents of the Smithsonian Institution*; Government Printing Office: Washington, D. C., 1865; Vol. 1864.
(45) Rayleigh, J. W. S., Baron In *The theory of sound*; Dover: New York, 1945; Vol. 2.
(46) Rayleigh, L. *Proceeding of the Royal Society of London* **1879**, *29*, 71–97.
(47) Rodot, H.; Bisch, C.; Lasek, A. *Acta Astronautica* **1979**, *6*, 1083–1092.
(48) Strani, M.; Sabetta, F. *Journal of Fluid Mechanics* **1984**, *141*, 233–247.

(49) Lyubimov, D. V.; Lyubimova, T. P.; Shklyaev, S. V. *Physics of Fluids* **2006**, *18*, 012101.
(50) Bauer, H. F.; Chiba, M. *Journal of Sound and Vibration* **2004**, *274*, 725–746.
(51) Chiba, M.; Miyazawa, T.; Baoyin, H. *Journal of Sound and Vibration* **2006**, *298*, 257–279.
(52) Chiba, M.; Michiue, S.; Katayama, I. *Journal of Sound and Vibration* **2012**.
(53) Bisch, C. *Comptes rendus de l'Académie des sciences Paris - Série II* **1981**, *293*, 107–110.
(54) Lyubimov, D. V.; Lyubimova, T. P.; Shklyaev, S. V. *Fluid Dynamics* **2004**, *39*, 851–862.
(55) Lin, Z.; Peng, X.; Wang, X. *Heat Transfer—Asian Research* **2006**, *35*, 13–19.
(56) Lamb, H. *Hydrodynamics*; 6th ed.; Cambridge University Press: Cambridge, England, 1932.
(57) Li, G.; Flores, S. M.; Vavilala, C.; Schmittel, M.; Graf, K. *Langmuir* **2009**, *25*, 13438–13447.
(58) Aruga, D.; Kaneko, A.; Moronuki, N. *Journal of Advanced Mechanical Design, Systems, and Manufacturing* **2008**, *2*, 773–782.
(59) Baines, W. D.; James, D. F. *Industrial & Engineering Chemistry Research* **1994**, *33*, 411–416.
(60) Cain, B. *A 2-D Analysis of Evaporation in Laminar Flow (U)*; Defence Research Establishment Ottawa, 1991; p. 27.
(61) Danberg, J. E. *Mass Remaining During Evaporation of Sessile Drop*; Science Applications International Corp Abingdon, MD, 2008.
(62) Amin, M.; Navaz, H. K.; Kehtarnavaz, N.; Dabiri, D. *Food Bioprocess Technol* **2008**, *3*, 276–287.
(63) Erbil, H. Y.; McHale, G.; Newton, M. I. *Langmuir* **2002**, *18*, 2636–2641.
(64) Bhushan, B.; Jung, Y. C.; Koch, K. *Philosophical Transactions of the Royal Society A: Mathematical, Physical and Engineering Sciences* **2009**, *367*, 1631–1672.
(65) Rowan, S. M.; Newton, M. I.; McHale, G. *The Journal of Physical Chemistry* **1995**, *99*, 13268–13271.
(66) Coutant, R. W.; Penski, E. C. *Industrial & Engineering Chemistry Fundamentals* **1982**, *21*, 250–254.
(67) Bourges-Monnier, C.; Shanahan, M. E. R. *Langmuir* **1995**, *11*, 2820–2829.
(68) Jung, Y. C.; Bhushan, B. *Journal of Microscopy* **2008**, *229*, 127–140.
(69) Weber, D.; Molnar, J.; Shuely, W. *Environmental Fate of Toxic Chemicals on Surface Materials in Laboratory Wind Tunnels: Measured and Computed Wind Speeds and Flow Fields*; U.S. Army Edgewood Chemical Biological Center Aberdeen Proving Ground, MD, 2003.
(70) Joyce, M. J.; Todaro, P.; Penfold, R.; Port, S. N.; May, J. A. W.; Barnes, C.; Peyton, A. J. *Langmuir* **2000**, *16*, 4024–4033.
(71) Chini, F. Drop Removal from solid surfaces: Shedding and Evaporation. PhD, University of Alberta: Edmonton, Alberta, 2013.

Chapter 2: Drop shedding by cross flow for hydrophilic to superhydrophobic surfaces[a]

2.1 Introduction

When a drop rests (is sessile) on a substrate and is exposed to airflow, the drop will be shed (move) if the adhesion force of the drop to the surface is overcome by the external drag forces on the drop. The point at which the drop starts to move is referred to as the point of incipient motion and after this the drop is said to undergo runback (i.e., move downstream along the surface). The adhesion to (or mobility of) a drop on a surface is controlled by surface tension, contact angle, and contact line shape/size (broadly speaking, the wetting characteristics). Sometimes wetting characteristics from one type of test (e.g. simple advancing contact angle tests, or usually quasi-static advancing and receding experiments) are used in application to other setups (such as shedding by tilted plate or airflow). As will be discussed in this paper, this is not always suitable for airflow shedding, as others have pointed out for tilted surfaces[1,2]. The drag forces on the drop are based upon air velocity, and upon drop area/shape (both functions of contact angle), so both adhesion and drag forces are dependent on wetting characteristics.

[a] A version of this chapter has been published. Milne, A. J. B.; Amirfazli, A. "Drop Shedding by Shear Flow for Hydrophilic to Superhydrophobic Surfaces", *Langmuir* **2009**, 25, 14155–14164.

Shedding of sessile drops by airflow has many applications, including but not limited to the avoidance of airfoil icing/efficiency of wind turbines[3,4], and water management in fuel cells[5,6]. The more general case of drop shedding by fluid flow also has applications to enhanced oil recovery[7,8] and cleaning[9]. The results of this study will be most applicable to the first three examples given. The results could also be applied to driers, condensers, pesticide use and medical aerosols. Since limited experimental insight into the fundamentals of drop shedding by airflow exists in the literature, as a first attempt this study aims to elucidate the underlying parameters that influence drop shedding. Specifically missing in the literature is a study of drop shedding from superhydrophobic surfaces (SHS). SHS have shown promise in promoting drop shedding (e.g. on tilted surfaces) and this issue will also be investigated in the presence of cross flowing air.

Considering the many applications, numerous attempts have been made at numerical/analytical modeling of drop shedding by fluid flow. Models have progressed from the deformation of drops with fixed contact line[10], up to models involving, e.g., runback (flow) of the drop along the surface[11-14], drop breakup and re-entrainment[11,13] , and oscillation of the drop[12,13]. The models put forth above are advanced, but lacking is experimental data for basic understanding of the phenomena, as well as validation and calibration of the models. Also, the models are often limited to lower Reynolds numbers and other simplifications (e.g. simplified flow fields, two dimensional simulations, small density differences between drop and

surrounding fluid). Finally, all are performed considering a single system of fluid and solid, so a systematic study of the effects of liquid and solid is needed. This is especially important since as noted above, both adhesion and drag depend on contact angles and drop area/shape (each functions of contact angles, i.e. wettability).

In terms of experimental studies, the work of Mahé *et al.*[7] is of note as one of the early studies. In this work, they found critical shear rates for the detachment of various oil drops by water flow, but the study was largely phenomenological. It also cannot be directly applied to this study since the cross flowing liquid was water rather than air in the present case. More recently, interest in fuel cells, and the concomitant requirements of managing the water produced by them, has increased. This has led to several papers examining (with experiments and models) shedding of drops placed on a fuel cell gas diffusion membrane with small channel geometries. However, the knowledge is incomplete. For example, one reference[15] is an observational study, giving locations of drop creation and growth, without data on necessary airflow to shed. Zhang *et al.*, 2006 does present information on the critical airflow for a given drop diameter[6]. Two works[16,17] are similar, and provide critical flow rates, but the models do not match results well. This is likely due to the assumption made that the fully developed flow upstream of the drop remains intact over the drop in a channel with a high blockage ratio. Also, one work[16] uses a poor model of adhesion that assumes a circular contact line and a stepwise distribution

with the advancing and receding contact angle on the downstream and upstream halves, respectively. As an improvement, the other[17] introduces a linear distribution, but still assumes a circular contact line. Finally, both works[16,17] neglect the shear stress that exists on the side walls of the control volumes used to develop the models. Theodorakakos *et al.*, 2006 has found good comparison between a CFD model and experimental results[18], but it would be difficult to develop separate models for multiple systems and multiple drop volumes at higher Reynolds numbers. Additionally, the computation cost of running CFD for all of these would likely be prohibitive. Minor 2007 gave criteria for drop shedding and also measured internal velocities in the drop[5]. However, the range of volumes was limited, and the internal velocity measurements were far from the interface.

As a reminder, all of the above experimental works on fuel cells only looked at a single type of surface (gas diffusion membrane). Thus, they have examined only a limited range of surface hydrophobicities. Further, the adhesion to a porous membrane surface such as a gas diffusion membrane would be expected to differ from a solid surface since water can penetrate into a porous surface. Also, the channel flow geometry used in fuel cell work may result in different aerodynamic forces than would be found in external flow. Thus more work is needed examining drop shedding from solid surfaces of differing hydrophobicities, and also for drops exposed to external (instead of channel) flow.

White and Schmucker[3] studied external flow over a system of water on smooth aluminum, finding the critical runback volume for three different turbulent air velocities. They performed advanced aerodynamic analysis, but did not consider wetting and adhesion in great depth. They only studied a single system. Bico *et al.* presented[19] an examination of both aerodynamic and adhesion characteristics for water on a RainX® (water repelling) coated surface. They studied volumes from 3-500 μl, finding that above 100 μl the critical air velocity and runback behavior was independent of volume. Over a small range of drop volumes (~10-30 μl), they found that a critical Weber number (constant for the range of volumes) was the criteria for drop shedding (incipient motion). Note that here, incipient motion is defined as the instant motion of the drop downstream, which is different than the meaning that White and Schmucker put forth[3] (i.e. a runback of the drop for a short distance, followed by a stop).

The understanding provided by the above studies is somewhat sporadic and narrow in scope. Missing is a systematic investigation of the criteria for drop shedding (runback) for a variety of systems for a large range of drop volumes. Such a study would give fundamental experimental knowledge on drop shedding and be useful to modelers. Especially, given that contact angle is an important parameter, surfaces with different

hydrophobicities should be compared, and the use of SHS to promote drop shedding should be investigated.

Thus, we present here results and analysis for the shedding of water drops from hydrophilic poly(methyl methacrylate) PMMA, hydrophobic Teflon, and superhydrophobic Teflon coated etched aluminum, as well as shedding of hexadecane drops from Teflon. Drops ranged in volume from 0.5 to 100 μl. The goal of this work is not a detailed study of the fluid mechanics of drop shedding, but instead to use fundamental fluid mechanics principles in conjunction with fundamental wetting and adhesion principles to perform a first encompassing examination of the problem. In the pages that follow, a theoretical formulation for incipient motion/runback is first developed, followed by a description of the experimental setup and procedure. Following this, results are discussed and analyzed to show the influence of adhesion/drop mobility on shedding. The special behavior of SHS is explained, and normalization of the results to self-similar curves is performed. Finally, airflow tests are compared to tilted plate experiments and quasi-static advancing and receding tests on the same systems to examine drop shape and contact angles between test types. The differences found impact drop adhesion calculations and the implications of this are stressed.

2.2 Scaling Analysis

The aim below is to develop a theoretical understanding that can be used to investigate drop shedding by cross flowing air. In order to do this, one must use experimentally accessible parameters such as upstream velocity, and measurements of the drop (such as contact base length, height, and cross sectional area) in the undeformed (quiescent) condition. Thus we use these parameters to derive our formulation. The exception to this statement is in the measurement of contact angles. As will be shown in the discussion, it is necessary that the measurement of contact angle be performed at or after the threshold for drop runback.

As stated in the introduction, shedding by airflow is controlled by the balance of adhesion and drag forces. The adhesion force of the drop is controlled by surface tension, contact angles, and the shape and length of the contact line[20]. Specifically, the force is the integration of the surface tension acting in the direction of the local contact angle around the three phase contact line. This issue is discussed in more detail in our recent study[20], where it is shown that the force of adhesion (F_{adh}) for the drop is given by:

$$F_{adh} = -\gamma \int_0^L \cos\theta(l)\cos\psi(l)\cdot dl \qquad \text{Equation 2-1}$$

with γ being the surface tension, dl runs from 0 at the downstream contact point of the contact line counter-clockwise around the length of the contact line, L. The function $\psi(l)$ describes the distribution of the angle

between the unit normal of the contact line in the plane of the solid surface and the unit vector pointing in the upstream direction. Meanwhile, $\theta(l)$ describes the distribution of the contact angle around the contact line. The contact angle is assumed to vary from a maximum value at the downstream end of the drop to a minimum value at the upstream end. This distribution impacts the force of adhesion and points to the importance of using measures of drop mobility in predicting shedding, rather than simply relying on repellency/hydrophobicity (measures of the advancing contact angle).

It is difficult to determine $\psi(l)$ and $\theta(l)$ terms in Equation 2-1 for this study, both because it is a dynamic experiment and because the drop profile is observed from a fixed perspective normal to the airflow. As such, one can only observe and measure minimum (θ_{min}) and maximum (θ_{max}) contact angles at upstream and downstream locations, respectively. Therefore, to make progress in the formulation, a parameter, k, is introduced (similar to Furmidge's[21] model) to partly account for the distribution of the contact angle, $\theta(l)$. The factor k (effectively a fitting parameter), along with the length of the drop base as viewed in profile (L_b), also partially captures the shape of the non-circular contact line $\psi(l)$ integrated along L in Equation 2-1. Considering this, Equation 2-2 can be derived as a simplified model of adhesion:

$$F_{adh} = k \cdot L_b \cdot \gamma \cdot \left(\cos\theta_{\min} - \cos\theta_{\max}\right) \qquad \text{Equation 2-2}$$

Whereas Equation 2-2 requires the use of a parameter, k, it provides a tractable solution for our purposes. It is important to note that the general form of Equation 2-1 would hold both for a drop being shed by airflow and a drop being shed by gravity in a tilted plate experiment. Potential differences in the value of F_{adh} would come about based on the shape of the contact line, $\psi(l)$, and the distribution of the contact angle, $\theta(l)$ between airflow and tilted plate experiments. Considering that k is meant to account for $\psi(l)$ and $\theta(l)$, airflow and tilted plate experiments could also be expected to result in different k's.

For a drop exposed to airflow, assuming that there are no net body forces on the drop (gravity being balanced by normal surface reaction force, and no other body forces), the only forces acting to shed the drop are aerodynamic skin and pressure drags. These can be captured using the drag coefficient at the point of incipient motion (C_{Dcrit}[b]) as:

$$F_{drag} = \tfrac{1}{2} \cdot \rho \cdot U_{up}^{\ 2} \cdot A \cdot C_{Dcrit} \qquad \text{Equation 2-3}$$

where ρ is the density of air, U_{up} is the upstream air velocity, and A is the frontal area of the deformed drop (here represented by the measurement of the side area of the un-deformed drop, which is axisymmetric). The area, A, and perhaps C_{Dcrit}, will depend on contact angles since different contact angles will lead to different drop shapes. Thus, the hydrophobicity

[b] As a note, in the original publication, the symbol C_D rather than C_{Dcrit} was used. It will likewise be used through the rest of this chapter to indicate the coefficient drag at the critical air velocity for incipient motion, while in subsequent chapters it will refer more generally to the coefficient of drag as it varies with air velocity/Reynolds number.

of the surface controls both the adhesion and drag characteristics of drop shedding by airflow.

It is plausible that there is viscous dissipation within the drop, but neglecting this for now, the drop will be shed (run back) when the drag force (increasing with airflow) equals the adhesion force (a force, like solid-solid friction, which increases to a point to prevent motion). Equating Equations 2-2 and 2-3 and re-arranging, results in:

$$U_{crit} = \sqrt{\frac{2 \cdot k \cdot L_b \cdot \gamma \cdot (\cos\theta_{\min} - \cos\theta_{\max})}{\rho \cdot A \cdot C_{Dcrit}}} \qquad \text{Equation 2-4}$$

From Equation 2-4, one can see that for smaller drops (corresponding to larger $(A/L_b)^{1/2}$), a larger critical air velocity, U_{crit}, is expected. Further, one sees that the critical air velocity for incipient motion should depend upon L_b and the contact angle distribution (i.e. it should depend on the mobility of the drop).

Equation 2-4 would be a linear function of $(L_b/A)^{1/2}$ if C_{Dcrit} and $k\cdot(cos\theta_{min}-cos\theta_{max})$ were constant for a given system. However, whereas observations show that $(cos\theta_{min}-cos\theta_{max})$ remains constant with volume, for a given system (see Table 2-1), there is no guarantee that k, or especially C_{Dcrit} does so. Thus, the ratio of k/C_{Dcrit} is viewed as a variable. It is assumed that if k changes, it only depends on the changes in drop shape as size changes. At the time of original publication of this section, no literature

data could be found for C_D of drops on surfaces for any Reynolds number, nor for solid caps in the Reynolds number range of this study (see Chapter 4 for such measurements on drops). Based on the literature available for solid hemispheres on a surface, the drops in this study (with Reynolds numbers ranging from 2900 to 3500) are below the critical Reynolds number of $<\sim 5 \cdot 10^4$ for the turbulent drag crisis[22]. Also, based on a 2-D analysis[23], hemicylinder results follow the same trends for cylinders in a free stream up to a Reynolds number of 400, where C_D begins to settle to a constant value. At the time of original publication of this section, it was therefore hypothesized that the drops are in the range for which C_D is constant with respect to Reynolds number, and further hypothesized that any changes in C_{Dcrit} with volume should only be due to changing drop shape[c]. Therefore both k and C_D should depend only on drop shape. Since drop shape changes with drop size, it is hypothesized that U_{crit} should be a (perhaps non-linear) function of $(L_b/A)^{1/2}$. This is because $(L_b/A)^{1/2}$ is both a variable in Equation 2-4 and a variable describing drop size.

[c] The first hypothesis proved false (see Chapter 4), while the second (that C_D should change with drop volume) proved correct.

Table 2-1: Comparison of maximum and minimum contact angles for airflow and tilted plate induced shedding tests, as well as advancing and receding contact angle measurements performed by quasi-static volume increase/decrease of a drop sessile on a smooth, flat, level substrate of the same material as airflow/tilted plate tests. Values were seen to apply for all drop volumes.

	Average Max/Adv Contact Angle (degrees)	Standard Deviation (degrees)	Average Min/Rec Contact Angle (degrees)	Standard Deviation (degrees)	θ_{max}-θ_{min} or Contact Angle Hysteresis (Degrees)
HD-Teflon					
Air Flow	66.7	1.5	53.6	3.3	13.1
Tilted Plate	63.9	1.3	54.1	1.5	9.8
Quasi-Static	68.7	0.4	62.1	0.3	6.6
Water-PMMA					
Air Flow	76.3	3.3	53.1	3.8	23.2
Tilted Plate	71.4	2.3	52.6	2.2	18.8
Quasi-Static	73.6	0.7	58.2	1.3	15.4
Water-Teflon					
Air Flow	124.3	0.7	108.2	3.4	16.1
Tilted Plate	124.2	1.4	110.2	2.4	14
Quasi-Static	126.0	0.6	111.2	1.0	14.8
Water-SHS					
Air Flow	161.4	0.8	129.8	8.9	31.6
Tilted Plate	164.4	1.6	144.4	5.5	20
Quasi-Static	160.5	2.0	154.9	2.0	5.6

2.3 Experimental Methods and Setup

2.3.1 Wind Tunnel Tests

Experiments were performed in the 215.9 mm by 469.9 mm test section of a low-speed wind tunnel capable of 0-30 m/s flow[d]. Set into this section is

[d] An annotated picture of the setup is contained in Appendix A.1.

a symmetric, level streamlined body with a front section in the shape of a semiellipse (major axis 68.58 mm, minor axis 34.29 mm) (see Figure 2-1), followed by a flat section of 50.8 mm length into which the surface under test is mounted flush. The back of the body tapers at 19° to prevent flow separation and ensure a complication-free flow where the drop was placed. Use of tell tales on the surface of the body have confirmed that no flow separation occurs on the body.

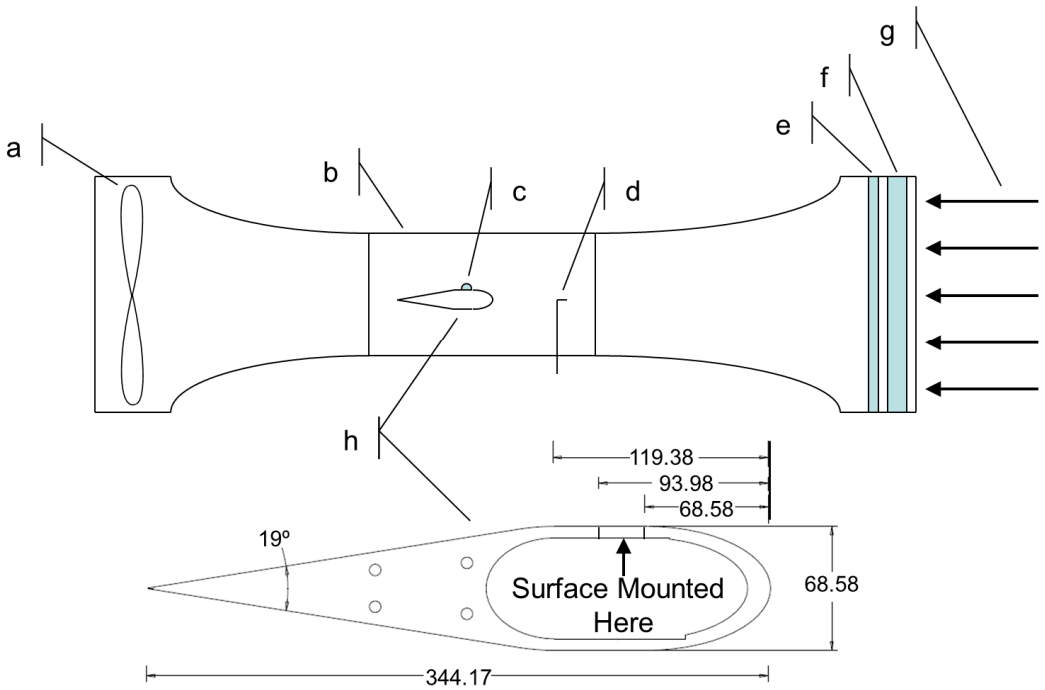

Figure 2-1: Side view schematic of wind tunnel with detail image of streamlined body used for tests of drop shedding by a cross flow, a) fan, b) working section (469.9mm (h) x 927.1mm (l) x 215.9 mm (d)), c) drop on surface mounted in streamlined body, h, d) pitot tube, e) screen, f) flow straighteners, g) airflow, h) stream lined body and detail image of same. All linear dimensions in mm. Cut out through center of body allows access for inserting and removing surface sample and adjusting it to maintain flush top surface. Camera view is into the page and light is mounted behind the tunnel pointing out of the page.

A Phantom v4.3 high speed camera (Vision Research Inc.) operating at 100 frames per second captured images of the drop in side view through a set of telecentric Navitar lenses (part numbers 1-50694, 1-50993, 1-62831

and 1-6010, Navitar Inc.) operating at a magnification of 0.56. This magnification resulted in a resolution of 42 μm/pixel. The drop is backlit by a cold diffuse light source and upstream velocity is measured by a pitot-static tube upstream of the body connected to a pressure transducer (Setra, 0-5 inH_2O range) that is connected to a DAQ board (National Instruments).

For each test: a background image without the drop was taken; a drop was placed manually on a dry surface using a digital micropipette (Fisher Scientific); and data acquisition was initiated (acquiring timed traces of voltage from the pressure transducer, and voltage across the camera trigger switch during the test). While capturing images, the airflow was slowly and uniformly increased until drop movement was observed.

2.3.2 Boundary Layer and Reynolds Number Calculations

For the maximum flow speed possible (30 m/s), the Reynolds number for the body at the location of drop placement (approximately 10 cm downstream of the leading edge) is ~$2 \cdot 10^5$, well below the Reynolds number for turbulent transition of either a flat plate or a cylinder in a free stream. Thus, we surmise that the drop is exposed to a laminar boundary layer. The drop Reynolds number based on upstream velocity and drop diameter is on the order of 3000. The assumed boundary layer characteristics have been calculated based on the results Schlichting

presented[24] for laminar flow over a cylinder. The major and minor axis of the front section of the body have been averaged and taken as the radius for boundary layer calculation. The drop is placed on the surface just after the semielliptical front section and so the results for the front half of a cylinder have been calculated. Based upon these calculations, and measurements determined from image analysis, the drop height ranged from approximately 0.9 to 2.5 times the boundary layer height. Thus the drop is exposed to both the boundary layer and the free stream above the streamlined body.

2.3.3 Surface Preparation and Liquid Types

Three different surfaces and two liquids were used in tests. Teflon surfaces were prepared by taking a glass microscope slide as received, dicing it to size, and cleaning it thoroughly with ethanol and acetone. Approximately 200 μl of Teflon solution (5:1 v:v FC-75 (3-M):Teflon AF (Dupont)) was pipetted onto the surface and spread using a spin coater. The surface was then placed under vacuum for at least one hour to drive off solvent, leaving a Teflon film. PMMA surfaces were prepared the same way, except the solution was 1% w:w of PMMA dissolved in dry toluene. Confocal Scanning Microscope (Zeiss, magnification 100x, line profile 150 μm length) images give measures of the average roughness[e] of both smooth surfaces to be Ra

[e] The average roughness (R_a) values presented here are a correction to the erroneous values reported in the original work (see footnote 'a' for reference). The erroneous values reported previously (0.016 μm for smooth glass and 0.589 μm for etched aluminum) were due to a miscalibration of the machine by its manufacturer, but do not affect analysis since the corrected

= 0.063 μm. The SHS was prepared using an in-house recipe as follows: Aluminum (6061-T6, Aircraft Spruce and Specialty Co., Corona, CA) was cleaned thoroughly with ethanol and acetone, and etched for approximately 1.5 minutes in a 36% solution of hydrochloric acid in de-ionized (DI) water. The aluminum surface was then removed from the acid, quenched in a beaker of DI water, rinsed thoroughly in DI water, and dried in a clean dry nitrogen stream. The surface was then coated with Teflon in the same way as the glass slide described above. This process resulted in a rough microtexture and superhydrophobic behavior of the surface with water. Confocal Scanning Microscope images analyzed in the same way give measures of the average roughness of the SHS to be Ra = 3.244 μm, significantly rougher than the smooth surfaces.

Two liquids were tested on the three surfaces described above. Hexadecane (Sigma Aldrich) was taken as received and tested on Teflon coated glass (this system is labeled as HD-Teflon). DI water was tested on PMMA coated glass, Teflon coated glass, and the superhydrophobic surface. The three water systems are labeled water-PMMA, water-Teflon, and water-SHS, respectively.

Drops of volumes 0.5, 2.1, 3.8, 13, 30, 58, and 100 μl were tested for each system, with additional tests of 1 μl drops on water-PMMA and water-

---

results still show that the etched superhydrophobic aluminum surface is significantly rougher than the coated glass surfaces.

Teflon. At least 3 tests of a given drop volume were performed for each system, with suitable repeatability seen. The exception to this was the 0.5 μl drop on water-SHS, due to the great difficulty in placing such a small drop on a SHS, only one test was performed.

2.3.4 Post Processing and Analysis

The Drop Snake program[25] was used to find downstream (θ_{max}) and upstream (θ_{min}) contact angles for images of the moving drops after the point of incipient motion (see Figure 2-2). From the high speed video and the pressure trace, time resolved data on drop shape, drop oscillations, drop base length and critical air velocity for shedding were determined using an image processing routine developed by students (including the thesis author and several summer students) in the Surface Engineering and Instrumentation Lab at the University of Alberta. The routine was coded in Matlab and performed image registration, inversion, background subtraction, edge finding (using the Sobel algorithm), and boundary tracing[f]. From the traced boundary, the position of the upstream and downstream contact points (see Figure 2-2) can be plotted as a function of time (see Figure 2-3). The air velocity (taken from the pressure trace using Bernoulli's equation) was synchronized to the position measurement by means of a trigger switch closure, which was recorded by both the DAQ and the camera. From the combined time trace of drop contact point

[f] Illustrative images from the processing routine are contained in Appendix A.2.

positions and air velocity, the critical air velocity can be determined as illustrated in Figure 2-3 and discussed below.

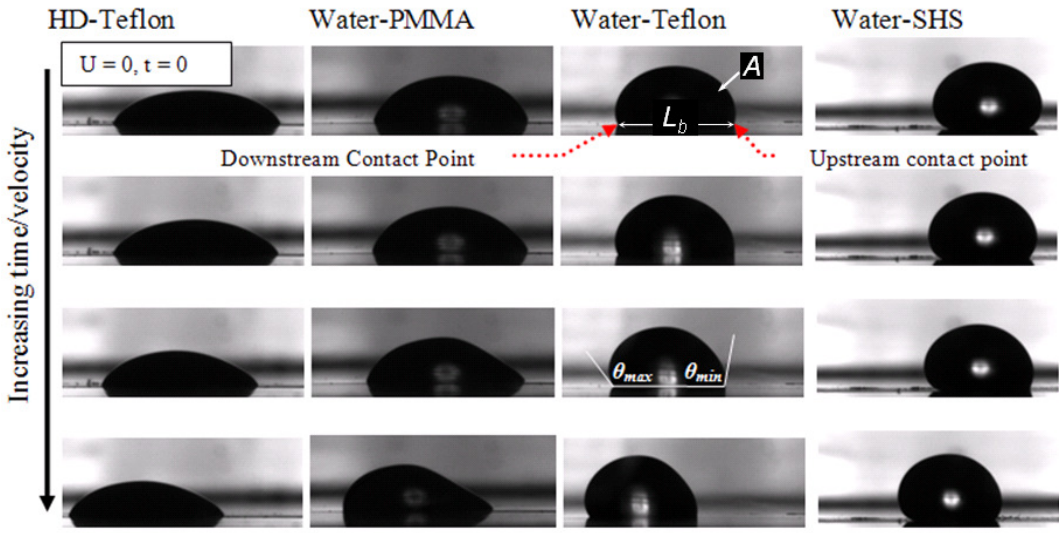

Figure 2-2: Typical progression of drop deformation and motion (airflow right to left) – all drops 100 µl in volume; each column represents a given system of liquid-solid as listed above the column. Upstream and downstream contact points, baselength (L_b), Area (A), θ_{max} and θ_{min} labeled for water-Teflon. Initially axisymmetric drop (1st row, quiescent conditions) deforms as air velocity increases (2nd row). At the critical air velocity the point of incipient motion has been reached (3rd row) and runback commences (4th row).

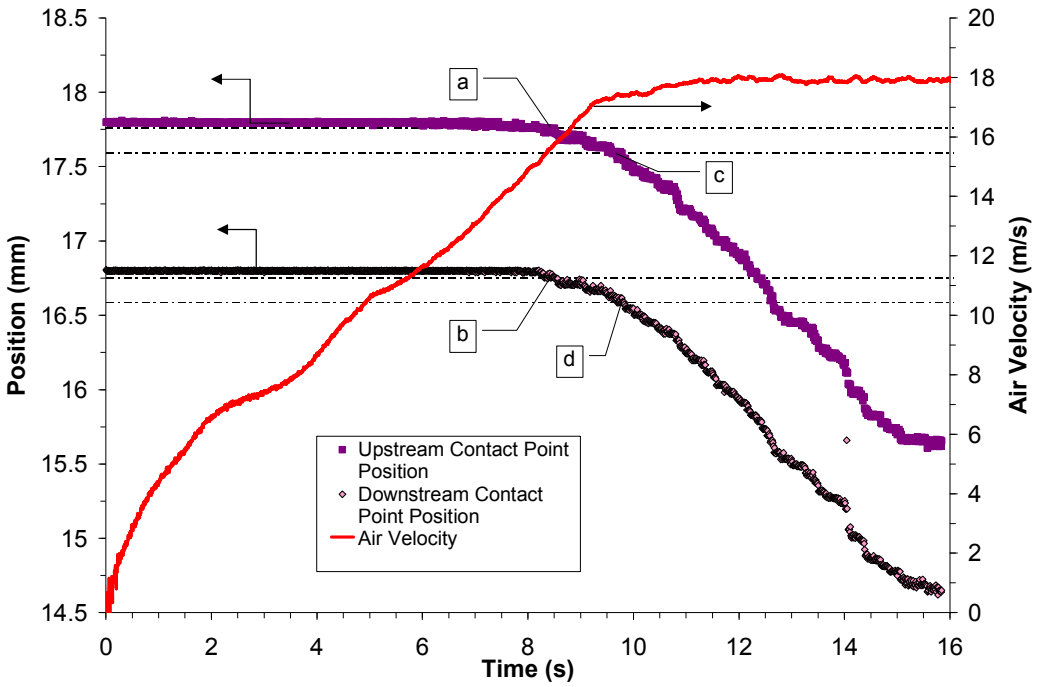

Figure 2-3: Typical test result – water-Teflon – 0.5 µl. Horizontal lines denote 42 and 210 µm (i.e. 1 and 5 pixels, respectively) displacements of both upstream and downstream points from their position for quiescent conditions. Labeled point 'a' marks time that upstream contact point passes 42 µm threshold, 'b' marks slightly later time that downstream contact point passes 42 µm threshold and is thus taken as the time for incipient motion of 42 µm drop displacement. Likewise, 'c' and 'd' mark times for upstream and downstream contact points to cross 210 µm threshold, respectively. Points 'c' and 'd' mark approximately the same time, taken as the time for incipient motion of 210 µm drop displacement.

2.4 Experimental Results and Discussion

Typical pictures of 100 µl drops are shown in Figure 2-2, along with a schematic showing values such as contact angle and baselength used in the formulation developed in Section 2.2. Smaller volume drops also deformed into similar shapes as those shown depending on the system. The slight differences seen in drop shape and drop size changes may have an effect on k and C_D values as discussed in Section 2.2 and Section 2.4.3. It can be seen in Figure 2-2 that for all the drops, the initially axisymmetric drop (1st row, quiescent conditions) deforms into a streamlined shape for the two lower contact angle systems (HD-Teflon,

water-PMMA), and into deformed spheroids for the higher contact angle systems (water-Teflon, water-SHS) as air velocity increases (2nd row). At the critical air velocity the point of incipient motion has been reached (3rd row) and runback commences (4th row).

2.4.1 Typical Test Results for Incipient Motion

A typical example of the processed results of a single test is shown in Figure 2-3. In this test the air velocity was increased relatively uniformly from 0 to 18 m/s over the course of several seconds. The position of the upstream and downstream contact points (see Figure 2-2) on the contact line (determined by the Matlab code) is plotted on the same time scale. The horizontal lines represent the thresholds for 42 and 210 μm displacements (1 and 5 pixels) of the upstream and downstream points. The critical air velocity for incipient motion was defined as the air velocity measured when both the upstream and downstream contact point had moved a prescribed distance downstream. In general, this threshold was crossed by both upstream and downstream contact points at similar times (within 0.05 - 0.55 s), however using the temporal resolution of the high speed camera, the instance of shedding was selected when the latter of the contact points crossed the threshold. Prescribed distances of 42 and 210 μm were used initially (1 and 5 pixels based on optical magnification) to investigate the effect of this choice on results. After the test was stopped, the drop was observed to generally continue traveling downstream until it

reached the end of the test surface (approximately 25 mm), so runback of the drop occurred after the point of incipient motion.

Figure 2-4, shows the results of shedding tests for a range of drop volumes of hexadecane on Teflon. Graphs for the other system show the same trend. All the data supports the observation based on Equation 2-4 that critical air velocity should increase with decreasing volume. Further, Figure 2-4 also shows that the results for the two markers of incipient motion (i.e. 42 and 210 μm (1 and 5 pixels) displacement) are very similar in trend (again, this is the case for the other systems). Considering questions regarding the ability to reliably distinguish one pixel of motion from background noise, it was decided to use the 210 μm (5 pixels) definition of incipient motion from this point forward in this paper.

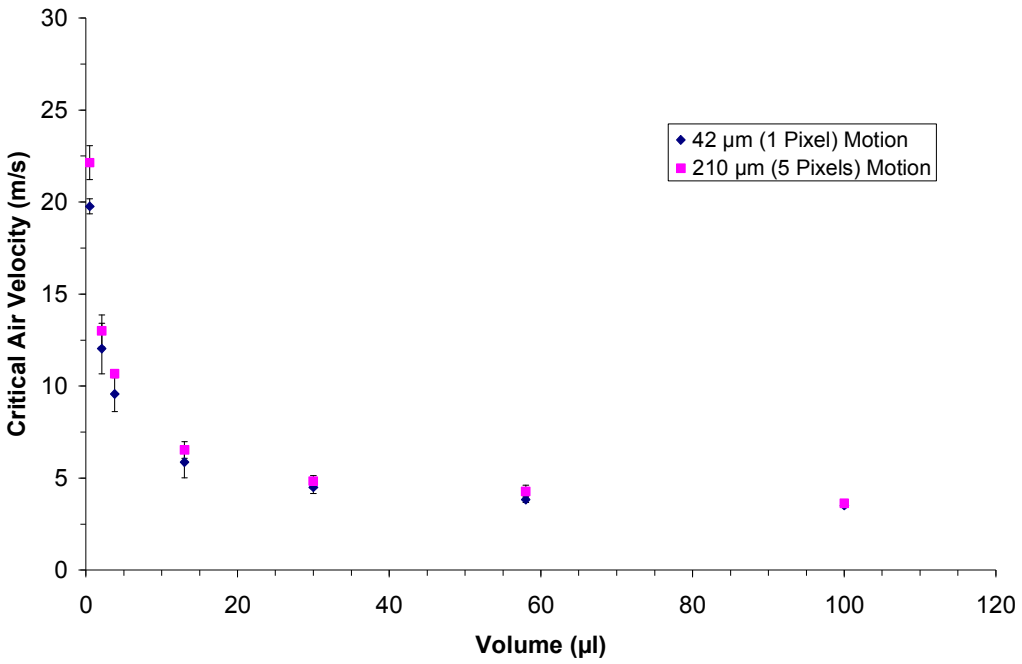

Figure 2-4: Typical results for critical air velocity for incipient motion versus volume for HD-Teflon surface. Note that critical air velocity increases as volume decreases, and that the results for the two definitions of incipient motion (1 and 5 pixels, (i.e. 42 and 210 µm, respectively)) are similar in trend. Error bars denote one standard deviation; for larger volumes, the error bars are smaller than the symbol size.

2.4.2 Effects of Adhesion on Shedding

Equation 2-4 suggests that critical air velocity should depend on adhesion. That this is so can be seen in Figure 2-5 (HD-Teflon left off to simplify the graph). Looking across volumes (dotted lines), $cos\theta_{min}$-$cos\theta_{max}$ is constant for a given system so that the data could be simplified to leave L_b on the horizontal axis. Since L_b is simply a proxy of drop volume for a given system, it gives similar curves to Figure 2-4. However, comparing the three different systems in Figure 2-5 it is seen that for each volume (solid lines), as $L_b \cdot (cos\theta_{min}$-$cos\theta_{max})$ decreases, so does the necessary air velocity for drop shedding. The decrease in $L_b \cdot (cos\theta_{min}$-$cos\theta_{max})$ is related to the

reduction in drop adhesion (see Equation 2-2) across the three systems. This shows the important relation between adhesion and shedding, and reinforces the idea that systems with greater mobility (lower adhesion) shed drops more easily, with superhydrophobic surface shedding them most easily.

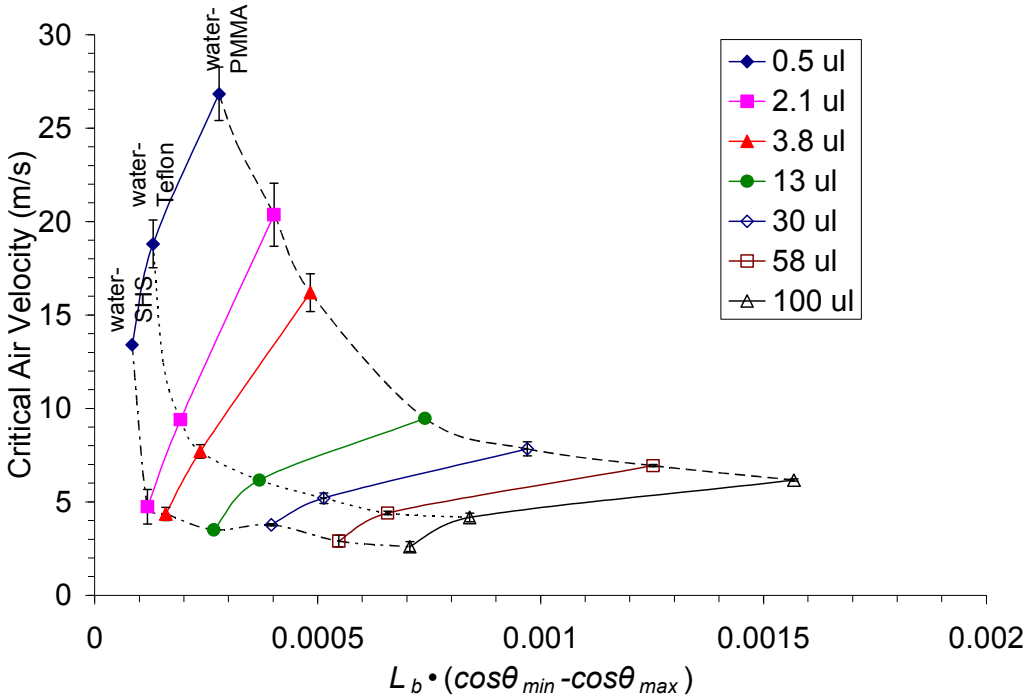

Figure 2-5: Critical air velocity for incipient motion versus $L_b \cdot(\cos\theta_{min}-\cos\theta_{max})$ (a measure of drop adhesion). Each symbol type denotes the three systems at a given volume, for all volumes, critical air velocity increases with $L_b \cdot(\cos\theta_{min}-\cos\theta_{max})$, for all volumes, the order of the systems is water-SHS, water-Teflon, and water-PMMA from left to right, as labeled for the 0.5 µl drops. Error bars denote one standard deviation; for larger volumes, the error bars are smaller than the symbol size. Solid lines (given by cubic splines) guide the eye along systems for a given volume; dashed lines (given by cubic splines) guide the eye along volumes for a given system.

Regarding the meaning of adhesion and application of measured contact angles, in the past, some researchers have associated repellency (high advancing contact angle) with low adhesion. As an improvement, more recently the trend has been to associate high contact angle hysteresis

(CAH, advancing contact angle minus receding contact angle, defined traditionally in a quasi-static measurement) with adhesion. In the case of drop shedding by airflow it is not suitable to use CAH and instead (θ_{max}-θ_{min}) could be used. Considering this definition one would expect water-SHS to show high critical air velocities since it shows the highest (θ_{max}-θ_{min}) value of the four systems (see Table 2-1). However, water-SHS shows the lowest critical air velocity for runback. This is due to the increased A (increasing drag) and decreased L_b (in principle decreasing adhesion) of the water drops on the SHS. Thus the factor $L_b \cdot (cos\theta_{min} - cos\theta_{max})$ is the best readily accessible measure of ease of shedding. Considering the factor $L_b \cdot (cos\theta_{min} - cos\theta_{max})$, one should note that L_b is itself a function of contact angle and volume, so the wetting and adhesion characteristics of a system play several important roles in shedding (runback) of drops by airflow.

Also in Figure 2-5, the data for water-SHS is seen to be flatter for intermediate and large volumes (an increase of 35% between 100 μl and 13 μl) compared to the other systems that show a gradual increase for decreasing volume (increases of 48% and 54% for water-Teflon and water-PMMA, respectively between 100 μl and 13 μl). The relative flatness of the water-SHS data is due to the shift of the curve down and to the left in Figure 2-5 as a consequence of the relationship between A and L_b, as will be discussed in the next section, and does not hold at the lowest volumes. For the range in which it holds, however, this result means that drops of many different sizes (say in a cloud, or spray situation) would be expected

to shed similarly, a useful simplification for both models and design calculations. It is worth repeating here that A is measured in quiescent conditions from a side view of the sessile drop. In such conditions the drop is axisymmetric and the measurement gives a measure of the frontal area of the drop.

2.4.3 Self Similarity of Results

Plotting the results for the four systems it is seen that all are non-linear with respect to $(L_b/A)^{1/2}$, confirming the observation made regarding Equation 2-4 that k/C_D changes with volume (specifically, that k/C_D is itself a non-linear function of $(L_b/A)^{1/2}$). We consider that this variability in k/C_D is due to changes in drop shape with drop size (Section 2.2), due to flattening of the drop by gravity. Since the ratio k/C_D, the critical air velocity and the drop size are related by Equation 2-4, the ratio cannot be separately examined at this time. The present analysis will thus continue using the experimental observation that the non-linearity introduced in Equation 2-4 by the ratio k/C_D can be captured using a fitting equation. As shown in Figure 2-6 the relationship of critical air velocity to $(L_b/A)^{1/2}$ is of the exponential form given by Equation 2-5, meaning that the data appear linear in the semi-log plot.

$$U = a \cdot e^{b \cdot \left(\frac{L_b}{A}\right)^{1/2}} \qquad \text{Equation 2-5}$$

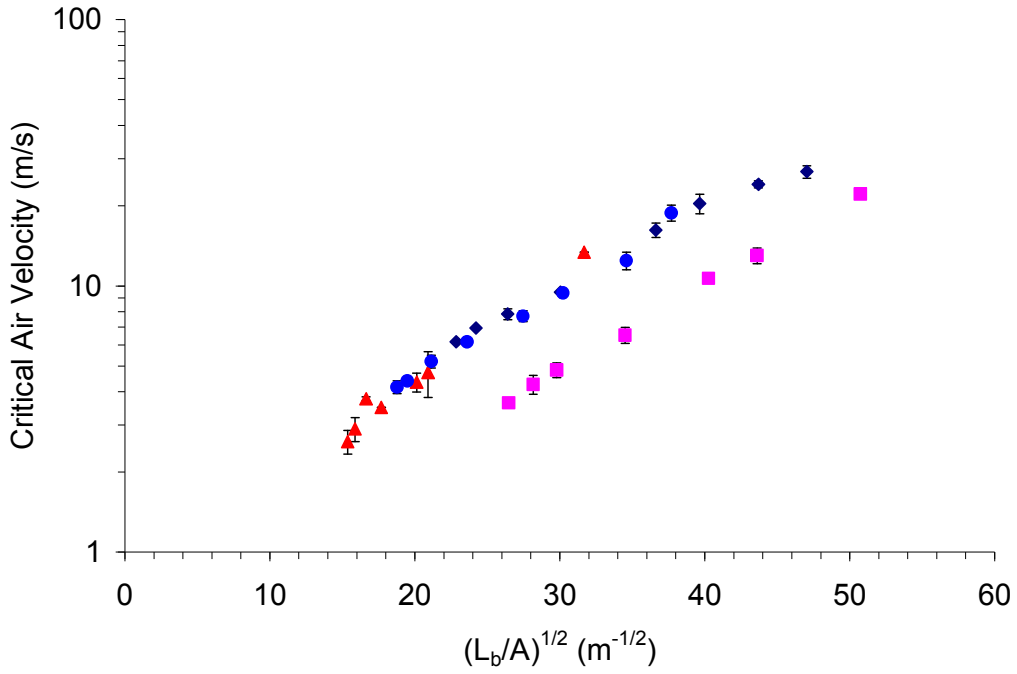

Figure 2-6: Critical air velocity for incipient motion for HD-Teflon (squares), water-PMMA (diamonds), water-SHS (triangles) and water-Teflon (circles). Error bars denote +/- one standard deviation and are often small enough that they cannot be seen. Note that water-SHS shows the lowest values of $(L_b/A)^{1/2}$ for the systems tested, reinforcing the arguments presented earlier regarding the benefit of SHS over other surfaces for shedding.

The data presented in Figure 2-6 can be used to interpolate critical air velocities for runback for drop volumes between those tested. Extrapolating the results to larger and smaller volumes is not recommended. At larger volumes (lower $(L_b/A)^{1/2}$) a point would be reached where the drop deforms under airflow into a sausage shape[19], changing both drag and adhesion and therefore shedding. At smaller volumes, the drop size would shrink and the drag would become dominated by shear stress[14], again changing the shedding behavior.

Figure 2-6 also demonstrates the particular benefit to shedding that SHS provide. The water-SHS data points show the lowest $(L_b/A)^{1/2}$ values, and

the lowest critical air velocities for runback. The low $(L_b/A)^{1/2}$ are due to the superhydrophobic nature of the surface causing the water drops to bead up, and leading to both decreased adhesion and increased drag. This combination in turn leads to lower critical air velocities compared to the other systems.

The data for the three water systems in Figure 2-6 can be fit by three equations (each with different parameters) of the type given by Equation 2-5. However, by normalizing the results from Figure 2-6 the versatility of the fitting can be increased. Normalizing by the critical airflow velocity and $(L_b/A)^{1/2}$ for the largest drop, the curves collapse into one master curve as shown in Figure 2-7. Normalization with respect to other drop volumes (i.e. largest drop versus smallest drop) yields the same self similar outcome. A similar curve can also be generated using the inverse square root of the drop height or the inverse sixth root of drop volume as the controlling parameter, since these are both proxy measurements of $(L_b/A)^{1/2}$.

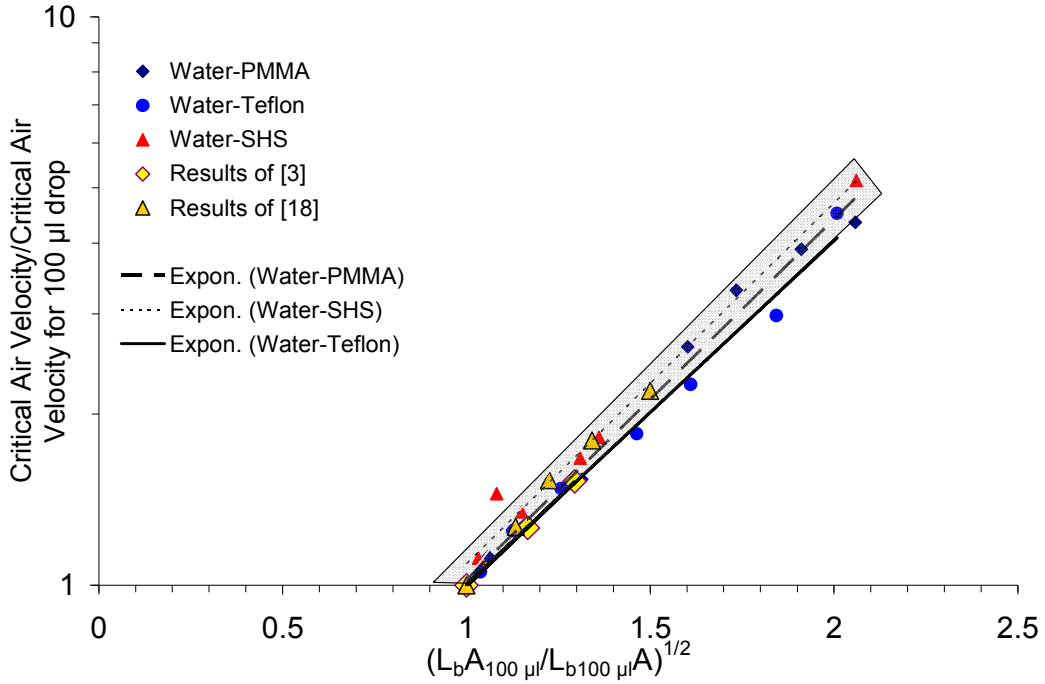

Figure 2-7: Normalized critical air velocity versus normalized $(L_b/A)^{1/2}$ for the three water systems tested. Normalized in the same manner, some previous results[3],[18] fall within the band of the other water systems, whereas others[19] do not (left off graph for clarity). Exponential fits are displayed for each system (see Table 2-2). Grey band denotes the range of values given by taking the average of the fitting parameters for water on the three surfaces +/- one standard deviation of the fitting parameters for water on the three surfaces (average and standard deviation given in Table 2-2) and results for HD-Teflon deviate from this band. Error bars left off this graph for clarity.

The fitting coefficients from the curves in Figure 2-7 are given in Table 2-2. The fitting coefficients for HD-Teflon are also included; but this data was omitted from Figure 2-7 for clarity since it does not collapse onto the master curve for water systems. HD-Teflon data will be dealt with in Section 2.4.4. The low standard deviations of the mean parameters for the water data show that, when normalized, all the systems tested with water show similar results. The average of these parameters is used in Figure 2-7 to draw the grey band showing the range of values for water on the three systems tested. As noted above, the average curve should not be

extrapolated back to its intersect (a value) since this would correspond to very large drop volumes. Similarly, extrapolation to small volumes is also questionable (see Section 2.4.2). The value of b on the other hand describes how normalized U_{crit} changes with normalized $(L_b/A)^{1/2}$, describing therefore the non-linearity of critical air velocity with $(L_b/A)^{1/2}$.

Table 2-2: Parameters for Equation 2-5 of normalized critical air velocity versus normalized $(L_b/A)^{1/2}$ for the four systems tested. R^2 values are goodness of fit measures for the exponential fit.

System Tested	HD-Teflon	Water-PMMA	Water-Teflon	Water-SHS
a (m/s)	0.1448	0.2373	0.25	0.2532
b ($m^{1/2}$)	1.9542	1.4606	1.3852	1.4612
R^2	0.999	0.989	0.989	0.980
Average +/- standard deviation for three water systems		a	0.2468 +/- 0.0084	
		b	1.4609 +/- 0.0437	

The use of the average parameters in Table 2-2 greatly simplifies the prediction of shedding behavior for water drops on a wide range of surfaces due to the self similarity of the systems. For any surface on which water contact angles are between those on PMMA and the superhydrophobic aluminum (i.e. ~ 76° to 161° advancing and ~ 53° to 130° receding), one could perform tests for airflow induced shedding at a single volume (say, 100 μl), and with confidence extrapolate the results to volumes ranging down to 0.5 μl. Only the undisturbed drop shape at a given untested volume would be needed to calculate the critical airflow at that volume. The undisturbed drop shape is itself just a function of contact angle, drop size, and gravity, and can be calculated by solving Laplace's

equation using a program such as that described elsewhere[26]. Thus again the importance of the wetting characteristics of a system are shown, as they will control both the undisturbed drop shape and the normalizing air velocity (see Figure 2-5). Thus wetting parameters determine how the normalized curve of Figure 2-7 is transformed to the behavior for a specific system. Specifically, it determines if the curve is transformed into one with a long, flat tail such as that for water-SHS or into one with an increase in critical air velocity across all volumes such as that for water-PMMA (see Figure 2-5). Figure 2-7 also reinforces the importance of wetting characteristics on drop shedding by showing a somewhat universal dependence of critical air velocity on the parameter $(L_b/A)^{1/2}$.

In support of the above comments regarding the self similarity of the water systems, the results from White and Schmucker[3] have also been plotted on Figure 2-7. From their stated process of calculating drop height using the spherical cap assumption, drop volume, and from this, L_b and A values, can be calculated. Normalizing the results by dividing by the U_{crit} and $(L_b/A)^{1/2}$ values for the largest drop, the results[3] for water on smooth aluminum (θ = 70 +/- 5) fall within the same band for the three water systems tested here. The results in that reference[3] are for a turbulent flow, rather than the laminar flow presented here. This suggests that the self similarity arguments presented above may have application to turbulent flow systems as well. Also, in that work[3] tests were conducted at a number of set air velocities, placing drops of increasing volume on the surface and

observing the critical volume for runback. The results of their process compare well with our converse process of placing drops of a specified volume on a surface and increasing air velocity. This insensitivity of results to the method of conducting tests suggests that both methods are investigating the fundamental process of incipient motion/runback. Speaking to our results, we have observed that if air velocity is increased at a high rate (~ 10 m/s^2), drop shedding is affected. It is therefore important if following the protocol in this paper to increase air velocity over the course of many seconds (~ 0.5 m/s^2). The results of Theodorakakos *et al.*[18] and Bico *et al.*[19] have also been compared to Figure 2-7. The results of Theodorakakos *et al.*[18] (for water drops on a proton exchange membrane with in channel flow) match relatively well, while those of Bico *et al.*[19] do not. It is difficult to tell from the conference presentation slides[19] how exactly tests were conducted, so no attempt is made to explain this discrepancy.

2.4.4 Extension of Self Similarity Arguments to Systems with Different Liquids

Table 2-1 and Figure 2-2 show that HD-Teflon and water-PMMA have similar but not identical drop shapes and contact angles. This is also supported by Figure 2-8, which shows that over the range of volumes tested, HD-Teflon and water-PMMA have similar values for a variety of measures of drop shape such as drop height, baselength, aspect ratio and the ratio $(L_b/A)^{1/2}$. Considering this, one can assume that the two systems

would have similar k and C_D values. Thus, drag forces will be similar, and adhesion forces (see Equation 2-2) will depend only on surface tension values for hexadecane versus water and on the slightly different value of $cos\theta_{min}$-$cos\theta_{max}$. Considering this, and referring to Equation 2-4, the critical air velocity for the two systems should differ by a simple multiplicative factor, MF, as shown in Equation 2-6:

$$MF = \frac{U_{HD-Teflon}}{U_{water-PMMA}} = \sqrt{\frac{\gamma_{HD-Teflon} \cdot (\cos\theta_{\min} - \cos\theta_{\max})_{HD-Teflon}}{\gamma_{water-PMMA} \cdot (\cos\theta_{\min} - \cos\theta_{\max})_{water-PMMA}}} \qquad \text{Equation 2-6}$$

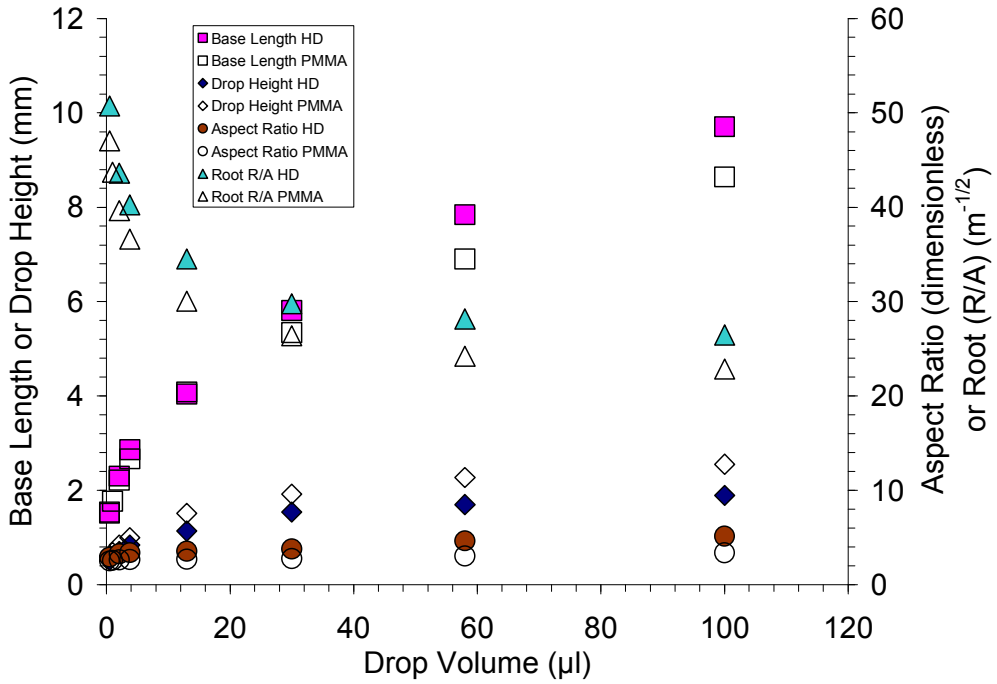

Figure 2-8: Various drop size and shape parameters versus volume for HD-Teflon (closed symbols) and water-PMMA (open symbols). Size and shape parameters are similar for the two systems over the range of volumes shown. Standard deviations have been omitted because they fit within the symbol size.

Taking contact angle values from Table 2-1 and using surface tensions for water and hexadecane of 72.8 and 27.47 mJ/m^2, respectively, Equation 2-

6 gives a factor of 0.452. Applying this factor to the results for water on PMMA produces Figure 2-9.

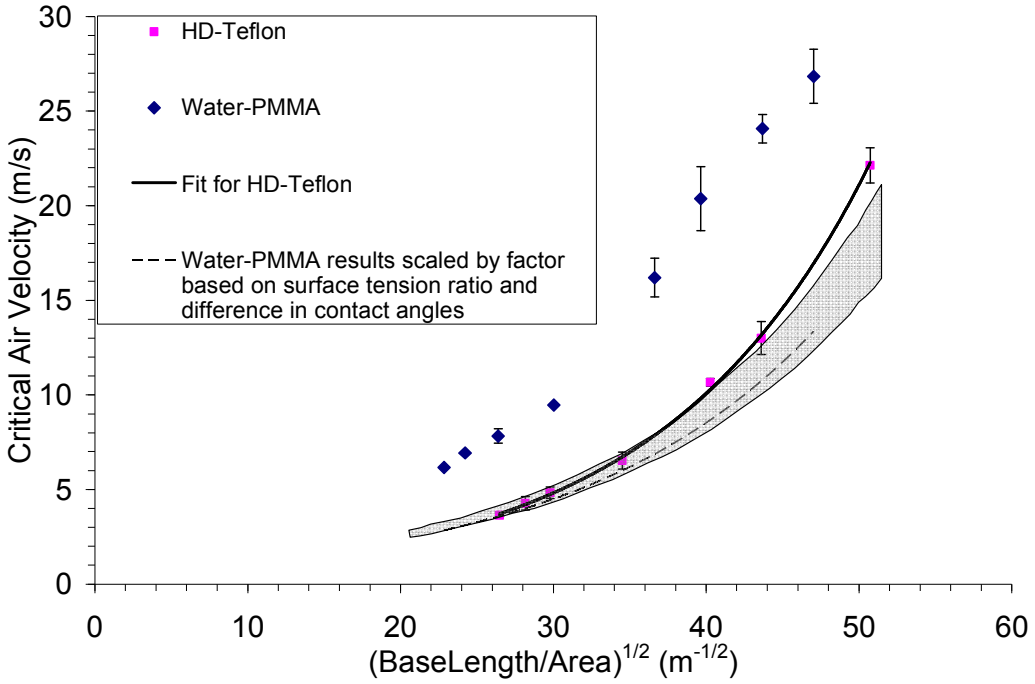

Figure 2-9: Critical air velocity versus $(L_b/A)^{1/2}$ for HD-Teflon and water-PMMA, as well as results of applying multiplicative factor to water-PMMA results to correct for differences in surface tension and $\cos\theta_{min}$-$\cos\theta_{max}$ between the two systems. Grey band denotes the range of values given by Table 2-2 after applying the same multiplicative factor as was applied to water-PMMA results to correct for differences in surface tension and $\cos\theta_{min}$-$\cos\theta_{max}$. Error bars denote +/- one standard deviation and are often small enough that they cannot be seen.

Figure 2-9 shows that multiplication by the corrective factor given by Equation 2-6 (in this case, 0.452) has brought the results for the two systems closer together. The differences still seen between the shifted values for water-PMMA versus HD-Teflon in Figure 2-9 are likely due to the slight variations in drop shape (see Figure 2-2 and Figure 2-8). The success of using the multiplicative factor to generalize results from one system to another allows one to conceptualize how hexadecane would behave on a surface for which it showed high contact angles (say, one like

or better than the surface reported on by Chen *et al.*[27] for which advancing and receding contact angles with hexadecane were 140° and 125°, respectively). Applying the same idea of a multiplicative factor to the results for water-SHS, one can conceptualize the airflow induced shedding behavior of hexadecane on a surface such as that described by Chen *et al.*[27] to be as shown in Figure 2-10.

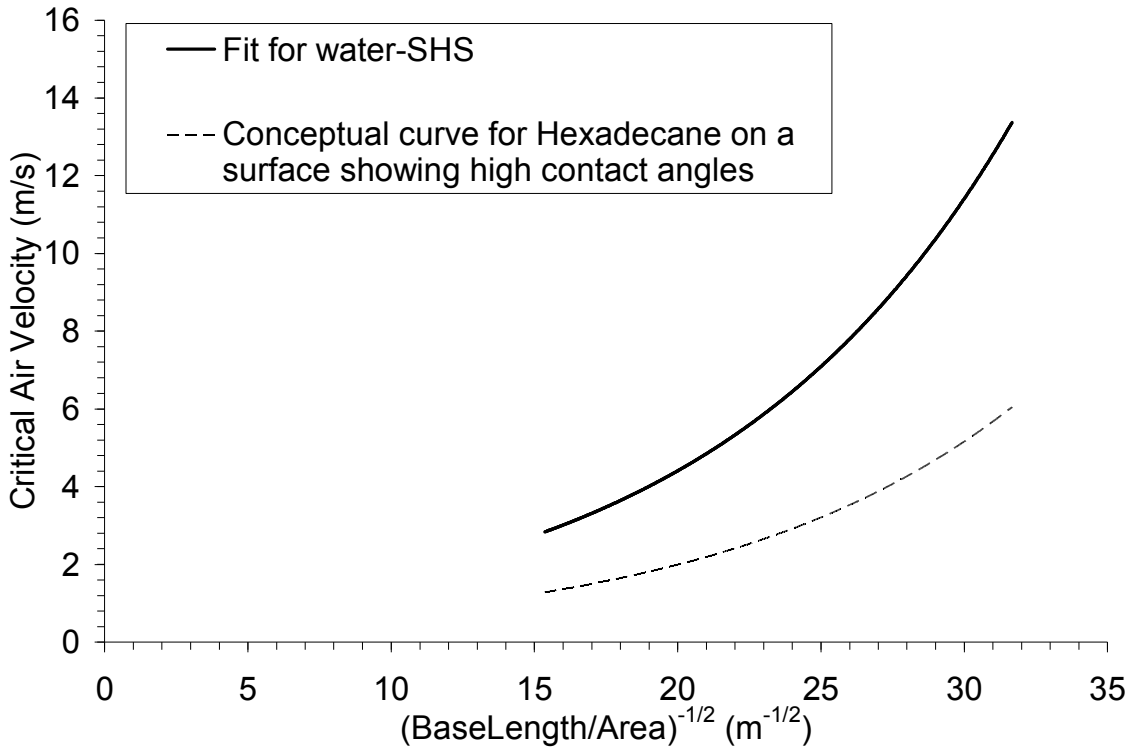

Figure 2-10: Fitted critical air velocity for water on SHS and predicted critical air velocity of hexadecane on a superlyophobic surface for which advancing and receding contact angles are very high such as for the surface of Chen *et al.*[27].

Figure 2-10 shows that one would expect hexadecane drops, when exposed to airflow, to shed very easily from a surface with very high contact angles. Combining this technique of applying a multiplicative factor with the self similar results shown in Figure 2-7 increases the utility of the equations presented here since first order predictions can be performed for a wide

range of systems, instead of only focusing on systems of water drops on various surfaces.

2.4.5 Drop Shape and Contact Angle Variation Between Test Types

ElSherbini and Jacobi[28] suggested that no difference exists between contact angles measured in a standard advancing/receding test and the maximum and minimum contact angles taken by a drop as it is shed from a tilted plate by gravity. Other researchers[1,2] have argued to the contrary that the style of testing (advancing/receding versus tilted plane) does make a difference in contact angle measurements. To investigate this in the context of airflow induced shedding, presented below is a comparative discussion of contact angles found via airflow shedding, tilted plate shedding, and traditional quasi-static advancing/receding tests for the four systems presented in this paper.

Immediately after drop movement, contact angle measurements were made using side view images. Though difficult to show in the static pictures of Figure 2-2, the top part of the drops oscillated in the airflow (though the contact line position remained fixed). Larger oscillations were seen for larger drops, and for water compared to hexadecane. This observation conforms to the predictions of Thoroddsen[29], relating the natural frequency of drop vibration to density, surface tension, and drop size.

Since the contact angles varied within a range due to the oscillation, several representative images were analyzed to give average values of the contact angles. The measured contact angles are shown in Table 2-1. Also in Table 2-1 are values of maximum and minimum contact angle measured in tilted plate experiments similar to previous 'placed from above then tilted' tests[2], and quasi-static advancing and receding contact angle data. The advancing and receding data for hexadecane and water on Teflon are taken from literature[30]. Advancing and receding contact angle were measured in the usual way (i.e. profile analysis of drops sessile on a flat level surface by the quasi-static addition or reduction of volume through a small hole drilled in the surface[30]).

It can be seen in Table 2-1 that the maximum/advancing contact angles are relatively similar, considering the standard deviation, for all three tests for a given system. On the other hand, minimum contact angles are usually similar for airflow versus tilted plate tests, but are not necessarily similar to the receding contact angle measured by quasi-static volume reduction (the traditional way of measuring advancing and receding contact angles). This supports the observations made previously[1,2], that transferring contact angle information amongst various applications is not in general permitted and suggests that care must be taken in applying the results of a quasi-static advancing and receding test to other situations. Further, examining the last column of Table 2-1 it is seen that the difference

between θ_{max} and θ_{min} for air flow experiments seems larger than that for tilted plate experiments. This suggests that the method of forcing the drop (surface applied drag forces for airflow tests versus body applied gravitational force for tilted plate tests) can have an impact on the distribution of contact angles around the drop (which would change $\theta(l)$ in Equation 2-1, and therefore k in Equation 2-2). This would mean that the adhesion force of a drop in an airflow experiment could be different from that of a drop in a tilted plate experiment. This is contrary to the finding of Bico *et al.*[19], and means that contact angles obtained from one type of test should be used with care (or not at all) in modeling the behavior of another test type.

2.5 Conclusions

Shedding of sessile drops by laminar airflow has been investigated for hexadecane on Teflon, as well as water on PMMA, Teflon, and superhydrophobic surfaces. Drops ranged in volume from 0.5 to 100 μl. For the range of volumes tested, the contact angles were not seen to change significantly for a given system.

Wetting properties are seen to have a major influence on drop shedding by airflow. Specifically, they affect drop adhesion and cross sectional area (and therefore drag). Adhesion is seen to be an especially strong influencing parameter of shedding, with the lowest adhesion (highest mobility) SHS showing the lowest critical air velocities for shedding of the

systems tested. The water-SHS system also shows a uniform critical air velocity over a range of volumes, meaning that in situations where multiple drop sizes will be present (e.g. clouds or sprays) the shedding behavior can be assumed to be constant. This is understood as a manifestation of the wetting characteristics of the SHS (i.e. L_b and A).

For a given system, critical air velocity is well fit by an exponential relation with $(L_b/A)^{1/2}$ (both measured for the undeformed drop), meaning that k/C_D is a non-linear function of $(L_b/A)^{1/2}$. Critical air velocity data for water drops on any of the three surfaces can be collapsed to self similar curves. With a corrective factor based on the ratio of surface tensions and a function of contact angles, the results for hexadecane can be matched to water results relatively well. Together with the self similar curves, this further increases the predictive power of the presented results to systems involving non-aqueous pure liquid.

The self similar curves match external turbulent flow shedding and laminar channel flow shedding results of other researchers. This shows that the method of testing (increasing air velocity for a set volume versus increasing volume for a set air velocity), does not affect results. It further suggests that shedding behavior may be independent of flow conditions, meaning that the predictive powers of the normalized results may be applicable to other flow conditions.

Finally, contact angle measurements have been compared between air flow shedding tests, tilted plate shedding tests, and quasi-static advancing/receding tests. It was found that the three test types result in different contact angles, and therefore different measures of adhesion. Therefore, it is suggested that models for drop shedding should always use contact angles measured using a suitable experimental methodology (i.e. one that mimics the expected model conditions).

References to Chapter 2

(1) Krasovitski, B.; Marmur, A. *Langmuir* **2005**, 21, 3881.
(2) Pierce, E.; Carmona, F. J.; Amirfazli, A. *Colloids and Surfaces A* **2008**, 323, 73.
(3) White, E. B.; Schmucker, J. A. *Journal of Fluids Engineering* **2008**, 130, 061302.
(4) Lee, S.; Bragg, M. B. *J. Aircraft* **1999**, 36, 844.
(5) Minor, G. MASc Thesis, University of Victoria, Victoria, 2007.
(6) Zhang, F. Y.; Yang, X. G.; Wang, C. Y. *Journal of the Electrochemical Society* **2006**, 153, A225.
(7) Mahé, M.; Vignes-Adler, M.; Adler, P. M. *Journal of Colloid and Interface Science* **1988**, 126, 329.
(8) Schleizer, A. D.; Bonnecaze, R.T. *Journal of Fluid Mechanics* **1999**, 383, 29.
(9) Thoreau, V.; Malki, B.; Berthome, G.; Boulange-Petermann, L.; Joudi, J. C. *J. Journal of Adhesion Science and Technology* **2006**, 20, 1819.
(10) Li, X; Pozrikidis, C. *Journal of Fluid Mechanics* **1996**, 307, 167.
(11) Jones, J. L.; Lal., M.; Ruddock, N.; Spenley, N. A. *Faraday Discuss*. **1999**, 112, 129.
(12) Zhang, J.; Miksis, M. J.; Bankoff, S. G. *Physics of Fluids* **2006**, 18, 072106.
(13) Zhu, X.; Sui, P.C.; Djilali, N. *Journal of Power Sources* **2007**, 172, 287.
(14) Rothmayer, A. P.; Tsao, J. C. AIAA Paper No. 2001-676, **2001**.
(15) Yang, X. G.; Zhang, F. Y.; Lubawy, A. L.; Wang, C. Y. *Electrochemical and Solid-State Letters* **2004**, 7, A408.
(16) Chen, K. S.; Hickner, M. A.; Noble, D. R. *International Journal of Energy Research* **2005**, 29, 1113.
(17) Kumbur, E. C.; Sharp, K. V.; Mench, M. M. *Journal of Power Sources* **2006**, 161, 333.
(18) Theodorakakos, A.; Ous, T.; Gavaises, M.; Nouri, J. M.; Nikolopoulos, N.; Yanagihara, H. *Journal of Colloid and Interface Science* **2006**, 300, 673.
(19) Bico, J.; Basselièvre, F.; Fermigier, M. "Windswept droplets " (oral presentation), *APS-Division of Fluids Dynamics Meeting*, Chicago, November 20-22, 2005. accessed online: http://www.pmmh.espci.fr/~jbico/wind.pdf (8-April-2009)
(20) Antonini, C.; Carmona, F. J.; Pierce, E.; Marengo, M.; Amirfazli A. *Langmuir*, DOI 10.1021/la804099z, **2009**.
(21) Furmidge, C. G. L. *Journal of Colloid Science* **1962**, 17, 309.
(22) Savory, E.; Toy, N. *Journal of Wind Engineering and Industrial Aerodynamics*. **1986**, 23, 345.
(23) Kiya, M.; Arie, M. *Journal of Fluid Mechanics* **1975**, 69, 803.
(24) Schlichting, H. (Translated Kestin, J.) *Boundary Layer Theory*, 6th ed.; McGraw-Hill Book Co.: USA, 1968; Figure 9.6, pg 160.
(25) Stalder, A.F.; Kulik, G.; Sage, D.; Barbieri, L.; Hoffmann, P. *Colloids and Surfaces A* **2006**, 286, 92.

(26) del Rio, O. I.; Neumann, A. W. *Journal of Colloid and Interface Science* **1997**, 196, 136.
(27) Chen, W.; Fadeev, A. Y.; Hsieh, M. C.; Oner, D.; Youngblood, J.; McCarthy, J. *Langmuir* **1999**, 15, 3395.
(28) ElSherbini, A. I.; Jacobi, A. M. *Journal of Colloid and Interface Science* **2006**, 299, 841.
(29) Thoroddsen, S. T.; Etoh, T. G.; Takehara, K. *Annual Review of Fluid Mechanics* **2008**, 40, 257.
(30) Milne, A. J. B., MSc Thesis, University of Alberta, Alberta, 2008.

Chapter 3: A floating element differential drag system to measure the force of drag on sessile drops in cross flowing air[g]

3.1 Introduction

The interaction of sessile (wall constrained) drops or bubbles with a cross flow is ubiquitous in nature, with applications to, e.g., airfoil icing, fuel cell flooding, enhanced oil recovery, froth floatation, condensers, visibility through glass in rainy conditions, pesticide use, and fluid manipulation in reduced gravity[1–8]. In essence, it is important anywhere a discrete fluid phase is in contact with a solid and in relative motion with a dispersed fluid phase. The interaction can accelerate evaporation/dissolution, induce internal motion and mixing, drive oscillation, or cause the drop/bubble to shed (be blown along or off the surface or be broken into smaller drops/bubbles). Internal circulation, oscillation and shedding are the result of the drag force of the flow over the drop/bubble. Circulation is set up by shear (and perhaps pressure) forces[5]. Oscillation results from a flutter like instability[9] (see Chapter 5). Shedding occurs when drag forces (based on drop shape, velocity, and drop/air properties) overcome the adhesion force of the drop to the surface (based on drop shape/contact angle and surface tension)[1–7].

---

[g] A version of this chapter will be published, with co-authors A. J. B. Milne, B. Fleck, A. Amirfazli. B. Fleck and A. Amirfazli acted as supervisors, making the thesis author the main contributing author in terms of data collection, reduction, analysis, and writeup.

Given the importance of the drag force, it surprisingly has never been explicitly measured. The measurement is challenging due to the small magnitude of the force (on the order of tens of microNewtons) and the signal's variance in time due to drop oscillation. It is also challenging due to difficulties in measuring force on an object (such as a drop/bubble) which is lightly adhered to a surface, but free to deform and move on the surface if contact angle hysteresis can be overcome. Unlike a solid body, for a drop there is 'nothing to attach to', one cannot fix a drag balance to a drop, nor can one measure pressure distribution across its surface by means of pressure taps. So, in this chapter, we present a technique giving the first measurements of drag on sessile drops under airflow. We first discuss the limited preexisting related works and the requirements of a measurement device designed to measure drag force of weakly adhered bodies such as sessile drops. We then detail our design based on a novel combination of the floating element technique and the concept of differential drag measurements. The unique challenges of adapting the floating element technique for this work are then discussed. Finally, proof of concept is given by showing raw measurements of drag versus airspeed for drops of varying sizes on both a hydrophilic and a hydrophobic surface.

To the best of our knowledge our technique is novel, and while we focus on sessile drops due to our previous work on the topic[1], it can easily be extended to bubbles, and to drag measurements for other deformable and/or movable objects loosely

adhered to a surface (such as, e.g., vesicles, foams, bacterial/biofilms, and granular deposits such as dust or snow).

3.2 Previous Studies

Njifenju et al. presented on sessile drops in a cross flow in 2009[7]. They considered a sessile drop on a vertical plate, balancing the downhill component of gravity with an uphill component of drag force due to air flowing up the plate. This gives measurements (reported only as Cd ≈ 0.22) of use in applications such as windshields, where gravitational and drag forces both act to move the drop. However, expanding the results to other cases is difficult because the opposing forces of gravity and drag act to compress the drop, changing its shape and therefore the drag force acting upon it. The opposing forces also make the role of drop adhesion uncertain, since it is possible that drag and gravity could balance with or without some contribution of adhesion force. Drop shape would also be changed by the compressing effects of drag and gravity, affecting adhesion force. Further, the gravitational component shifts the bulk of the drop downhill/upwind, as shown in Figure 3-1a. This is contrary to the drop shapes normally seen for drops on a more horizontal surface (Figure 3-1b), meaning a change in drag force.

a

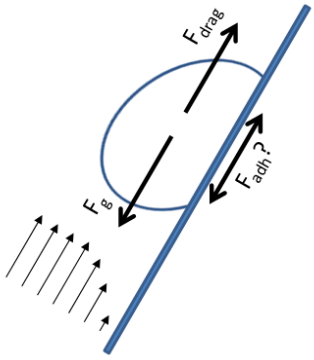

b

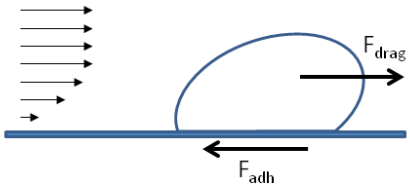

Figure 3-1: Showing drop shape and pertinent drag, adhesion, and gravitational forces affecting drops on a) a tilted surface with air flowing up the plate, and b) a level surface with air flowing along the surface. Note the difference in drop shape with respect to the direction of air flow.

Njifenju et al. also reported only a single value of drag coefficient, while it is expected to vary with airspeed (see Figure 7.2 of Clift et al.[10]). Finally, the work of Njifenju et al. considered only a single system of liquid and solid (silicone oil on a fluoropolymer coated glass surface), i.e. they only considered a single set of drop contact angles. Contact angle is defined as the angle between the base of the drop and the tangent of the liquid-vapour interface at the three-phase contact line where liquid, vapour, and solid meet. Advancing, or maximum, contact angle (θ_a or θ_{max}) is observed where the contact line is advancing across the surface, and receding, or minimum, contact angle (θ_r or θ_{min}) vice versa. Contact angle and drop shape are interrelated and affect drag, and the difference between advancing and receding contact angles (contact angle hysteresis, CAH), or more precisely

the difference in their cosines, affects drop adhesion to the surface[11] (determining the drag force necessary to overcome adhesion and shed the drop[1]). For Njifenju et al.[7], θ_a =55° and θ_r = 47°, indicating drops shapes well less than a hemisphere, with relatively low CAH.

Große et al. have used micropillars to measure wall shear, and have also examined the drag force of small bubbles attached to the end of a micropillar[12]. This technique is limited to near-wall, rather than on-wall measurements, and further limited in that higher flow velocities would introduce flow disturbances due to the presence of the pillar. Also, sessile drop drag measurements should be conducted in a way which allows the drop to deform along the surface, with its contact line moving from the quiescent circular shape as the drop adopts shapes maximizing adhesion force in opposition to drag. This precludes the use of micropillar techniques since the limited extents of the pillar top would pin the drop edges.

Aside from the above, Muthanna et al. have measured drag force on microparticles attached to AFM cantilevers[13]. However, to replicate common conditions, sessile drop drag measurements must be performed on a substrate which is largely continuous and flat around the drop to avoid flow disturbances. This precludes AFM measurement techniques since the design and orientation of the horizontal cantilever leaves relatively large and irregular gaps around the cantilever. The installation of an AFM in a well-conditioned wind tunnel is also challenging. Finally, the cantilever technique would also not allow drops to

deform freely on the tip of the catilever, similar to the restriction of micropillar techniques.

Instead of measuring drag, one could attempt to measure adhesion, since adhesion is a proxy measurement for drag up to (at at) the point of incipient motion[1]. Adhesion force calculation requires a knowledge of the surface tension and the three dimensional interface of the drop[11]. The deformation and oscillation of the drop make this strategy more difficult for drops in cross flow than for quiescent drops, but Schmucker and White have developed a speckle shift technique for 3-D drop imaging and applied it to sessile drops in cross flowing air[14]. However, they found that difficulties in finding the contact angles (especially the advancing contact angle) lead to unavoidable errors in calculating adhesion force. Further, their system is limited to a small range of contact angles due to limits of the optical system to find speckle shift near the edges of the drop for high and low contact angles. Altogether, this means that while they can find qualitative trends for drop/contact line shape and contact angle distribution, they can only confirm that adhesion force for drops in cross flowing air is in the same order of magnitude as adhesion force for drops on a tilted plate without giving specific values of force. They have also used their technique to confirm and expand on the previous finding[1] that drops shapes are different for tilted plate versus cross flow shedding, indicating the importance of studying the latter separately.

Aside from experiments, there is also a dearth of models for sessile drop drag. No general analytic results exist, as drop shape, oscillation, and internal flow conspire to make the governing equations intractable for realistic choices of drop shape/size and properties of the fluids. Numeric results are also currently limited to simplified cases in terms of contact angle, low Reynolds numbers, similar properties between the fluids etc[6,15–19]. The models that exist and those to be developed also lack experimental data for comparison, a problem the experimental technique we outline here can address.

3.3 Measurement System

To overcome the deficiencies in previous measurement efforts, we introduce here a novel measurement system which relies on the floating element technique and differential drag measurements.

The floating element technique is a long known technique for directly measuring localized shear force on part of a surface. An element of the surface is allowed to float (i.e. is mounted flush to, but separated by a gap from the rest of the surface) and connected to a shear force measurement device. Floating element techniques have commonly been used in the past to measure wall shear, generally in turbulent boundary layers[20–25]. As such, researchers have worked toward decreasing the size of the elements in order to improve spatial resolution, whereas the present application requires a surface large enough to hold a typical drop. Numerous works exist discussing variations of the technique, its benefits, challenges and shortcomings[26–35]. Specifics of the measurement setup used in

this work are discussed below, along with the challenges inherent in adapting the floating element technique to incorporate differential drag measurement of a deformable, movable drop.

The differential drag technique is a concept we have adapted from solid body drag measurements. In the past, differential drag has commonly been used, e.g., to measure the drag on some solid body held in a free stream by a strut, by taking a reference measurement of drag on the strut by itself, and a composite system measurement of drag on the strut and the body combined, with the drag on the body being the difference between the two (accounting for some interference drag caused by the mutual interference of the strut on the flow over the body, and vice versa)[36–39].

For drag measurements on sessile drops, we take a reference measurement over the floating element surface without any drop present, and a composite system measurement of the same surface with a sessile drop on it. As illustrated in Figure 3-2, the difference between the two measurements (corrected by the relative areas of the surface exposed during the two measurements and neglecting interference drag for simplicity) gives an estimate of the force of drag on the drop alone. To our understanding, this is the first time that differential drag measurements have been made using a floating element as the reference to measure the drag on adhering particles such as sessile drops.

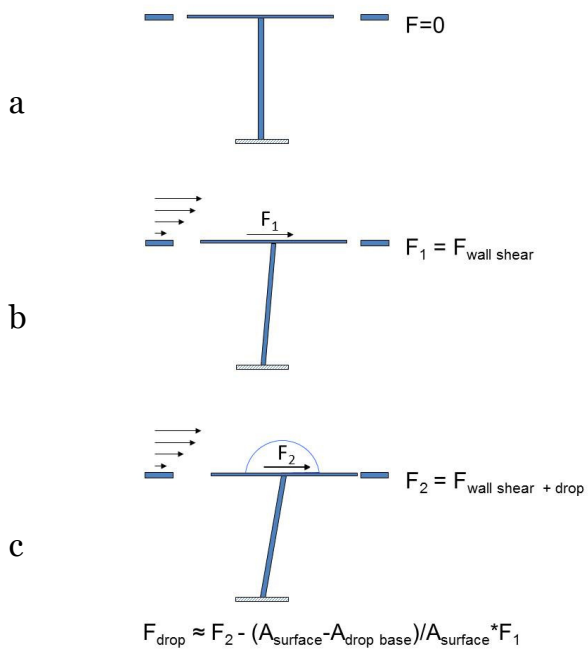

Figure 3-2: A schematic of the floating element sensor (not to scale) showing: a) no deflection in quiescent conditions, b) some deflection under airflow due to the force, F_1, which corresponds to wall shear with the drop absent, and c) some greater deflection under airflow with the drop present due to the force, F_2, which corresponds to drop drag, wall shear over the uncovered portion of the sensor, and any interference effects (assumed negligible). The force of drag on the drop (F_{drop}) is thus the difference between F_2 and F_1, accounting for the contact area of the drop.

The sensor used for this work is based on a single vertical cantilever shear force sensor—custom manufactured by Novatech Measurements Limited, St Leonards on Sea, UK—based on their F301 model low range stylus shear loadcell. It consists of a slim flexible metal cantilever, ~ 20 mm long, ~0.5 mm wide, and ~2.5 mm thick, with a rigid plastic beam of length ~140 mm and diameter ~8 mm attached to its top to provide a mechanical advantage to increase sensitivity. The cantilever is instrumented with a full Wheatstone micro strain gauge bridge circuit, excited and read by a custom circuit (Mantracourt Electronics Ltd., Exeter, UK). As constructed, it can measure forces linearly in the range of +/- ~20 mN with a resolution of 1 μN, and was calibrated by the manufacturer using

dead weights. The sensor is enclosed in a protective outer cylinder, limiting its range to +/- ~12 mN. The outer cylinder also shrouds the system from drag along its length, confirmed in wind tunnel tests with the cylinder exposed and the tip of the sensor shrouded. A schematic of the sensor and its installation is shown in Figure 3-3

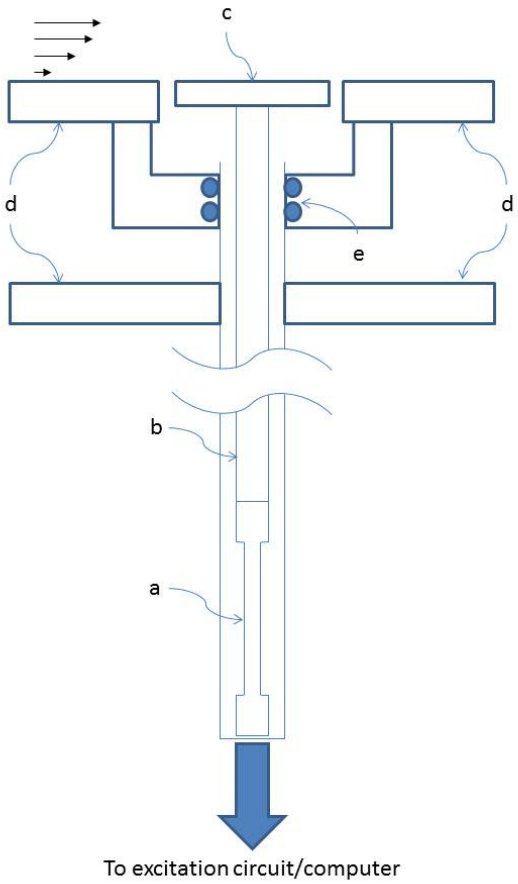

Figure 3-3: Schematic of the sensor (not to scale) showing: a) thin flexible metal beam, clacantilevered at its base (instrumented by full Wheatstone bridge, not shown), b) rigid plastic beam providing mechanical advantage, c) 9 mm diameter surface installed for testing, mounted flush and with a 1 mm clearance from, d) The walls of the streamlined body installed in the wind tunnel (see previous literature[1] for details of streamlined body). Sensor is sealed from external environment via e) a solid enclosure sealed to the top wall of the streamlined body with two o-rings at the point of entry by the sensor casing.

Surfaces of 9 mm radius were attached to the top of the sensor shaft, with the sensor mounted vertically through a symmetric, streamlined body, which in turn

is mounted in a laminar 0-30 m/s suckdown wind tunnel of 215.9 mm x 469.9 mm working section. The wind tunnel and streamlined body are described in detail elsewhere[1], with two pertinent differences noted in this paper. One such difference is that a hole was drilled through the bottom of the streamlined body to accommodate the sensor, and that the top of the streamlined body was modified to contain a 10 mm radius hole. The sensor was mounted so the 9 mm radius surface was flush with the flat, level portion of the streamlined body around it, and double o-ring seals were used to prevent infiltration of outside air past the sensor. Contrary to the usual goal (for wall shear measurements) of minimizing element size to improve spatial resolution, the surface was set at 9 mm radius to allow sufficient area for drops to be placed atop the surface such that their three phase contact lines were far from the edge of the surface (leaving the drops free to deform/move, signaling the onset of shedding and simulating the general conditions for sessile drops in a cross flow). The 1 mm gap between the surface and the streamlined body limits the gap's impact on the external flow field, while allowing a sufficient range for the sensor of +/- ~1 mN, without changing its resolution.

As constructed, and with a typical surface of, e.g., 2 mm thick glass attached to its tip, the sensor had a resonant frequency of ~5 Hz, and a settling time on the order of minutes. The settling time of the as-manufactured sensor resulted in too noisy a signal when operated in the wind tunnel. To correct this, the space between the sensor's outer protective cylinder shell and inner shaft was filled with silicone oil. Silicone oils of different viscosities were tested; a 10 cSt oil

(Sigma-Aldrich) was settled on as it provided a sufficiently reduced settling time (on the order of a second) without decreasing the natural frequency noticeably. Given the low natural frequency of the sensor, time resolved measurements of the variation in force due to drop oscillation are not possible, and this paper will generally report results measured at 20 Hz, and bin averaged to give a 2 Hz measurement rate.

3.4 Preliminary Testing

Preliminary tests with the sensor (both un-damped and damped with silicone oil) installed in the tunnel gave unexpected results in that the sensor moved *upstream* with increasing airflow. Drops were still shed downstream, confirming that the bulk flow was in the downstream direction, and the sensor gave positive differential drag measurements, (i.e. giving negative readings of force for reference tests of the surface alone, and less negative readings for composite system tests with the drop present). Several possible causes[27,33] of such an incongruous result were considered, including a recirculation zone over the surface, leaks from the ambient into the tunnel past the gap around the surface, inequality in the gap thickness around the surface, failure to mount the surface flush to the streamlined body, and failure to level the surface. Oil streak visualization confirmed that surface velocities were in the downstream direction, eliminating consideration of recirculation. The sensor was sealed from ambient pressure (confirmed by the absence of bubbles arising in the silicon oil filling the interior of the sensor, and over filled to cover the o-rings), which precluded either ambient pressure effects or secondary flows caused thereby. Misalignment was

ruled out by purposefully biasing the sensor position to leave larger or smaller gaps at various azimuthal positions without effect. Likewise, purposefully mounting the sensor so that the surface was either sunk into or projected from the streamlined body gave no effect. The effects of levelness were ruled out by rotating the surface and/or sensor such that any non-level mounting/imperfections would change their location and effect.

The negative force readings were ultimately determined to be due to an adverse pressure gradient along the streamlined body's surface[31]. The blockage caused by the streamlined body causes acceleration of the air flow near the surface at the nose of the streamlined body. This higher momentum is diffused upward as the flow attempts to equilibrate as it flows down the body. The diffusion away from the surface leads to a deceleration near the surface in the direction of flow, as shown previously for flow over ellipsoidal cylinders[40,41], generally at or before the point of maximum cross sectional width. This deceleration leads to an increase in pressure (see Figure 8.5 of White[40] or Chapter 10c and d of Schlichting[41]. This effect was confirmed with pressure taps located near the floating element, but laterally displaced ~32 mm, and spaced ~15 mm apart, also shown in Figure 3-4. An adverse pressure gradient of ~100 Pa was measured over 15 mm at ~27 m/s airspeed (see Figure 3-5) using the pressure taps. This gradient would cause a pressure force on the side walls of the sensor, and also cause a secondary flow under the sensor[27], as shown in Figure 3-6. Disconnecting the sensor shaft from the surface, and fixing the surface in place, the secondary flow over the shaft of the sensor alone was found to cause a force of ~ -300 μN at ~27 m/s. This, along

with pressure forces and secondary flow shear forces on the underside of the sensor surface could easily overwhelm the expected drop drag force (and composite measure of wall shear and sessile drop drag) on the order of 10-200 μN.

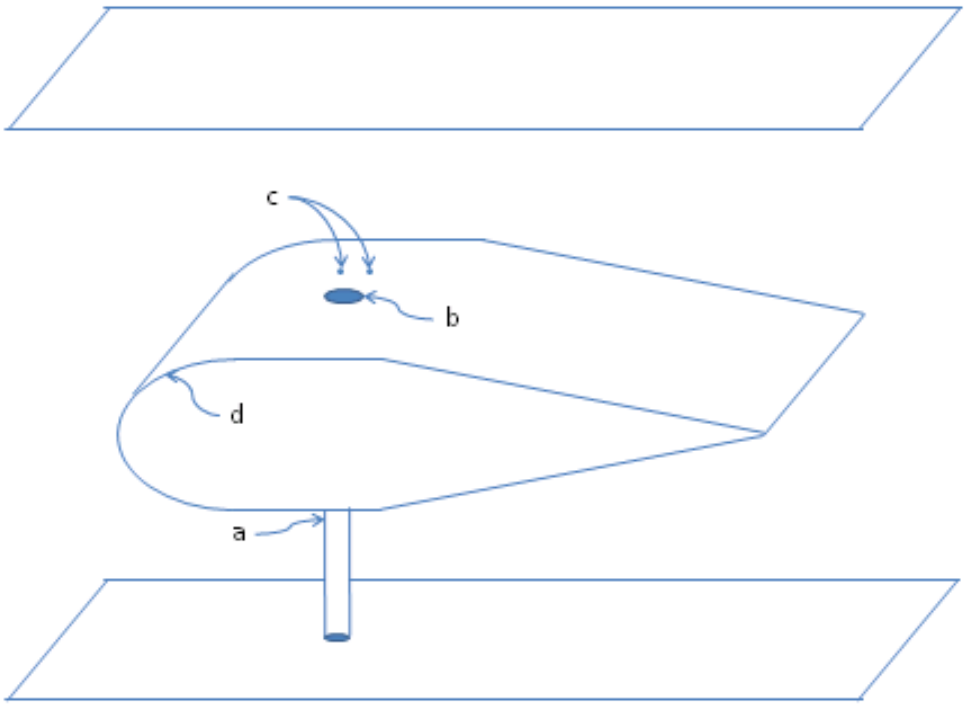

Figure 3-4: Schematic (not to scale) explaining adverse pressure gradient over sensor installed in wind tunnel showing: a) outer shell of sensor penetrating floor of wind tunnel, b) surface mounted flush in streamlined body, c) pressure taps used to measure pressure gradient, and d) nose of streamlined body which causes blockage effect and accelerates the flow over the nose. The deceleration of this flow as it travels down the body leads to an adverse pressure gradient.

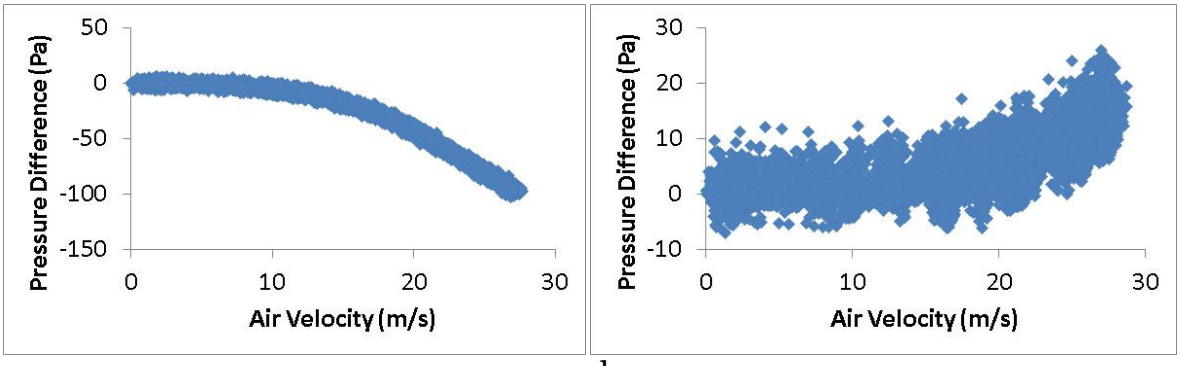

a b

Figure 3-5: Pressure gradients measured a) without and b) with the side walls angled to correct the flow as shown in Figure 3-7.

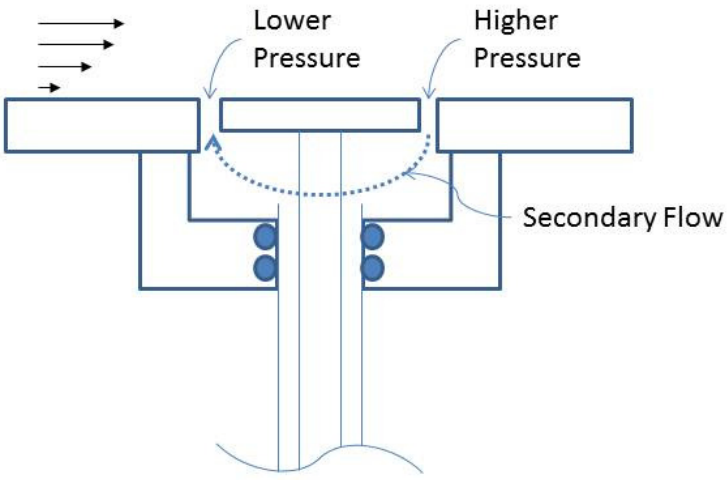

Figure 3-6: Schematic (not to scale) showing how an adverse pressure gradient can cause negative (upwind directed) forces on the sensor. The gradient would apply a pressure force to the edges of the surface (not shown) and also set up a secondary flow under the surface. This flow would cause shear and pressure drag forces on the underside of the surface as well as over the shaft of the sensor.

While differential drag measurements still gave positive drags on the drop, it was deemed desirable to remove the adverse pressure gradient since the secondary flow could theoretically re-enter the main flow through the gap upstream of the sensor and change the flow over the drop. To remove the adverse pressure gradient, the side walls of the tunnel over the streamlined body were modified (the second of two pertinent modifications compared to the previous setup[1]) to give them an inward tilt of ~5 degrees each as shown in Figure 3-7. This contraction counteracted the surface deceleration (confirmed by measuring a favorable pressure gradient of ~10-20 Pa over 15 mm at ~27 m/s airspeed, as shown in Figure 3-5). Given that the drops tested typically shed at much lower airspeeds[1], this result was considered acceptable, especially considering that the differential drag measurement technique relies upon relative, rather than absolute, measures of drag. The tunnel, with the modified angled walls, was

characterized by means of a pitot tube trace with measurement locations varying vertically from 1 cm above the streamlined body to near the roof of the tunnel, and laterally from the centerline to approximately 5.7 cm. The pitot trace indicated that the flow was largely two-dimensional, varying with height but not varying greatly with lateral location as shown in Figure 3-8. With angled walls, the sensor read positive force values near to the predicted values for a flat plate section, and higher positive forces with the drop present, as discussed below.

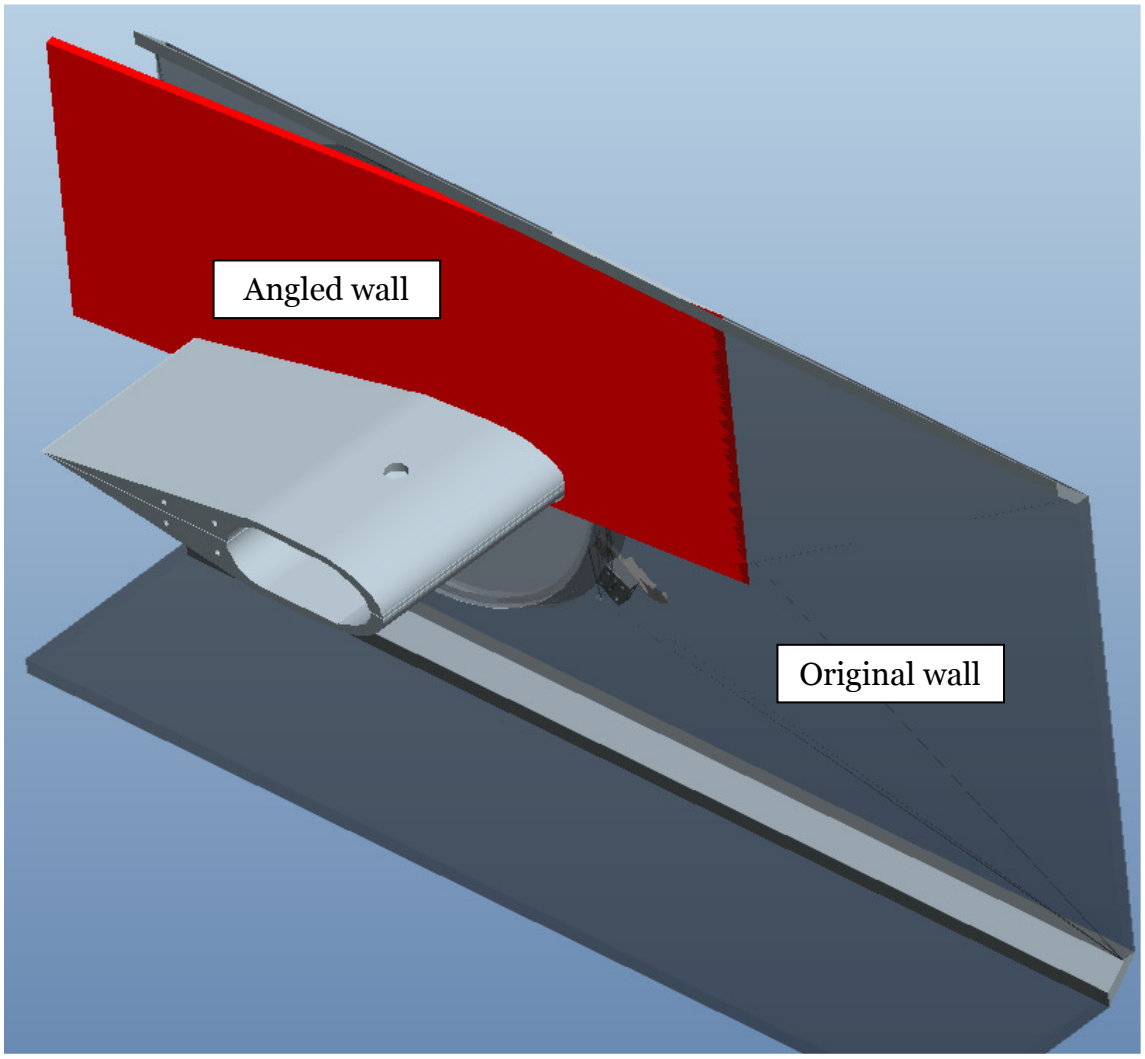

Figure 3-7: Schematic showing the angling of one of the tunnel side walls over the working section of the wind tunnel to counteract the adverse pressure gradient caused by flow deceleration along the surface due to boundary layer development. The other angled side wall, original wall/roof of tunnel, and the upstream and downstream portions of the wind tunnel are hidden for the sake of clarity.

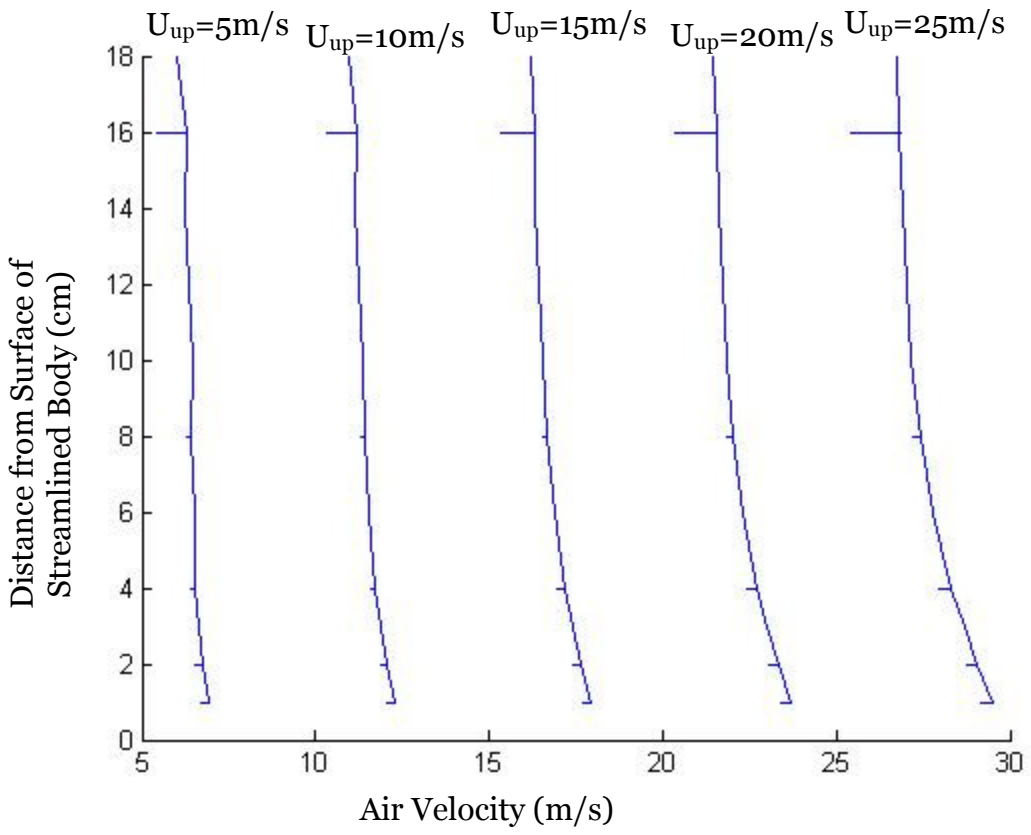

Figure 3-8: Results of pitot tube trace showing two-dimensionality of air velocities around the drop. The horizontal bars shown at heights 1, 2, 4, 8, and 16 cm show the variation in air velocity as position varies from the center line to approximately 5.7 cm lateral displacement. Labels above each curve correspond to the air velocity measured upstream of the streamlined body, abscissa shows air velocities measured above streamlined surface at the streamwise location of drop placement, but laterally displaced several centimeters. Air velocities reported in Chapters 3 and 4 as U_∞ were taken at 1 cm above the streamlined body's surface. The lowest measurements reported in this graph were taken at 1 cm above the surface of the streamlined body, meaning this graph does not show the boundary layer.

3.5 Proof of Concept

To prove the utility of the sensor to measure drag force on sessile drops in a cross flow, a series of tests were performed. This section describes the experimental setup of these tests, then discusses the use of the sensor in making wall shear (reference) measurements as well as system measurements leading to measurements of drag on sessile drops.

3.5.1 Experimental Setup

Proof of concept tests were performed for drops of water on PMMA-coated glass (denoted 'PMMA' in this chapter), and Teflon-coated glass (denoted 'Teflon'). This gives different values of contact angle for the drops (and therefore different drop shapes), with average downstream (advancing side) and upstream (receding side) contact angles of[1] $\theta_{water\text{-}PMMA\_Downstream}/\theta_{water\text{-}PMMA\_Upstream} = 76.3°/53.1°$, $\theta_{water\text{-}Teflon\_Downstream}/\theta_{water\text{-}Teflon\_Upstream} = 124.3°/108.2°$. Drops of 100, 58, 30, 13, 4, and 2 μl were tested to find the limits of resolution of the sensor.

Considering the size of drops and the air velocities at which they shed, the flat plate Reynolds number at the location of the sensor and drop was less than or equal to $2x10^5$, suggesting laminar flow. The Reynolds number based on free stream air velocity and drop spherical cap radius was less than or equal to 2000, again suggesting that flow over the drop would start in a laminar state, though likely with a destabilized wake. Air velocity was measured by pitot tubes, and the values reported in this section were taken with a tube mounted 1 cm above the sample at the same location as the drop, but displaced laterally by several centimeters. Tests were recorded by a Phantom v4.3 high speed camera (Vision Research, Wayne, NJ), operating at 200 fps and recording each drop and its surrounding at a resolution of 42 μm/pixel.

3.5.2 Reference Measurements

Before each set of sessile drop shedding tests on a given surface, reference measurements must be made of the force measured by the sensor without any

drop placed on it. Figure 3-9 shows the power law fit of the aggregated results of several of these reference measurements for the water-Teflon tests, with the error bars in the graph indicating the highest and lowest extent of individual reference measurements. The individual reference measurement results are shown in Appendix A.3. It is seen that the actual dependence on air velocity is quite similar to the flat plate shear drag (also shown in Figure 3-9), given by the formula presented as Equation 7.25 by White[40]:

$$F = 0.332\left(\frac{\rho\mu}{x}\right)^{1/2} U_{\infty}{}^{1.5}\pi r_{substrate}{}^{2} \qquad \text{Equation 3-1}$$

where x is the distance measured along the streamlined body from its nose to the location of drop placement, and $r_{substrate}$ is the radius of the floating element surface under the drop (i.e 9 mm).

The discrepancies between Equation 3-1 and the composite fit shown in Figure 3-9 are likely due to the fact that the sensor is not, in fact, installed in a flat plate. The overall good agreement indicates that the floating element wall shear sensor is working correctly to measure the reference force of air shear on the installed surface. It also suggests that the floating element is not unduly affecting the flow over the streamlined body. The other tests showed similar reference measurements. Variations within the error bars of Figure 3-9 (corresponding to the variation between individual runs as shown in Appendix A.3) are likely due to misalignments of the sensor for individual tests[27]. Their net result should be insignificant, however, since the differential drag measurement technique will be

exposed to similar deviations for both the reference and composite measurements. Further, composite system tests are unlikely to pass approximately 10 m/s, based on the critical air velocity for shedding of most drops (see previous works[1], as well as Chapters 2 and 4).

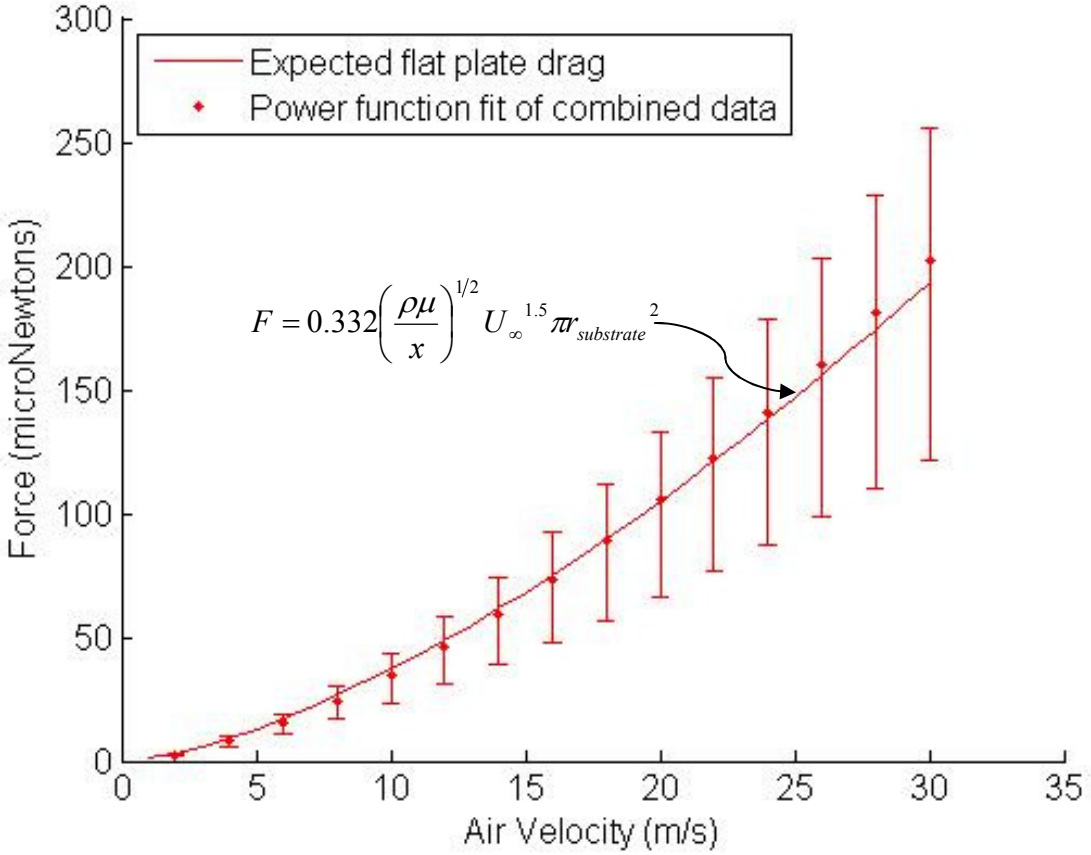

Figure 3-9: Power law fit of force measured by the floating element shear sensor (without drop present) versus airspeed measured 1 cm above surface for the composite results of five different reference tests. Also included is the expected force for flat plate drag theory. Error bars denote the highest and lowest extent of individual reference measurements, with the individual reference measurements show in Appendix A.3.

3.5.3 Introduction Effects

Before considering composite system force measurements, the introduction of the tilted walls and the sensor was also investigated for its effects on the critical

airflow for incipient motion (i.e. for the onset of shedding). The critical airflow was measured in the same way as previously[1]. Briefly, using image processing techniques, high speed videos of the drop can be analyzed to determine the frame showing incipient motion (defined as motion of at least 210 μm of the upwind and downwind contact points of the drop on the surface). Synchronized measurements of airspeed give the corresponding critical airspeed for incipient motion, which can be averaged between repetitions for a given volume of drop and liquid-solid system. Figure 3-10 shows results for the present tests with tilted side walls and the sensor installed for both systems, along with results for the same system taken without the side walls tilted and without the sensor installed[1] (i.e. with an immobile surface in the location of the drop, with no gap in the streamlined body).

As can be seen, the critical air velocities for incipient motion are similar in trend for the two cases, with a general bias toward lower velocities for shedding for the present tilted-wall case. This is likely due to the positive pressure gradient that the walls introduce, and indicate that direct comparisons of, e.g., velocity between the previous and present experiments should be done with caution. The similarity in trend and magnitude, however, indicates that the tilted side walls and sensor do not introduce unacceptable changes to the drop shedding behavior.

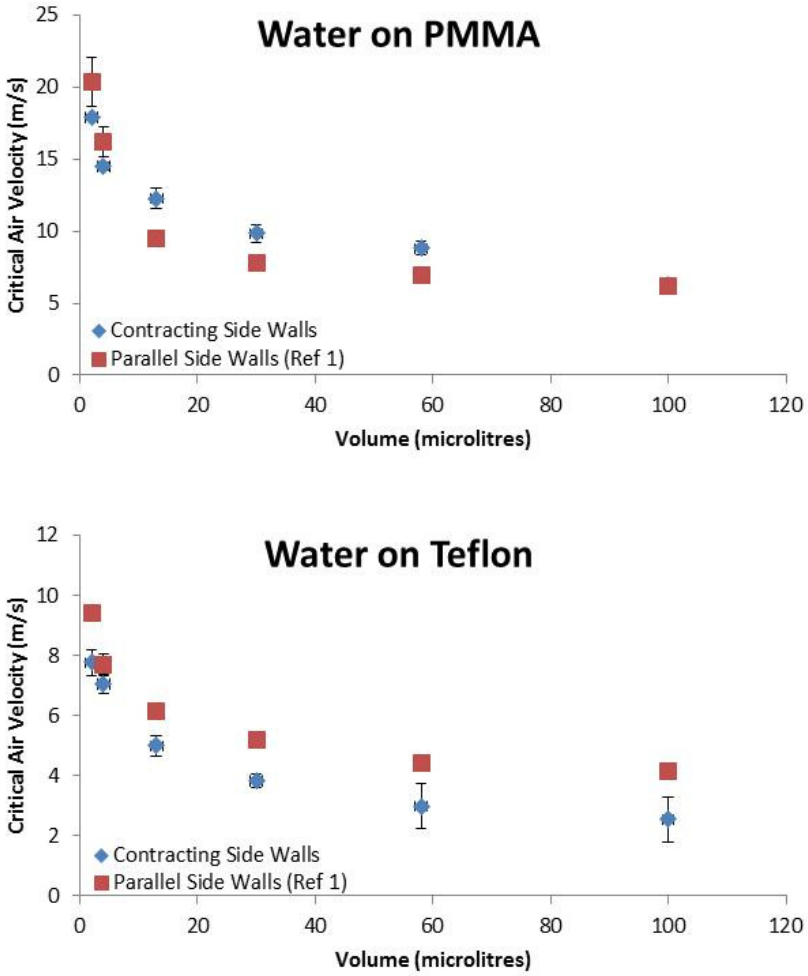

Figure 3-10: Critical air velocity for incipient motion of sessile drops in a cross flow versus drop volume for both systems, for the tests presented in this paper, and tests conducted previously[1] without the floating element differential drag sensor or tilted wind tunnel side walls installed. Error bars denote one standard deviation.

Since the trends for the present tests are similar to those seen previously, the same observations can be made[1]. First, larger drops are shed more easily. It is also seen that higher surface hydrophobicity lead to easier shedding of drops.

3.5.4 Composite System Measurement, Uncertainty Estimation, and Drag Measurements

Confident that the floating element sensor can measure wall shear in the absence of drops, and that drops are shed at similar air speeds compared to previous tests[1], it remains to consider composite systems measurements. Figure 3-11 shows representative reference and composite force measurements for both surfaces at the highest and lowest volumes tested. The composite signal is generally higher than the reference signal in all cases, all intermediate volumes showed signals in between the ranges shown in Figure 3-11.

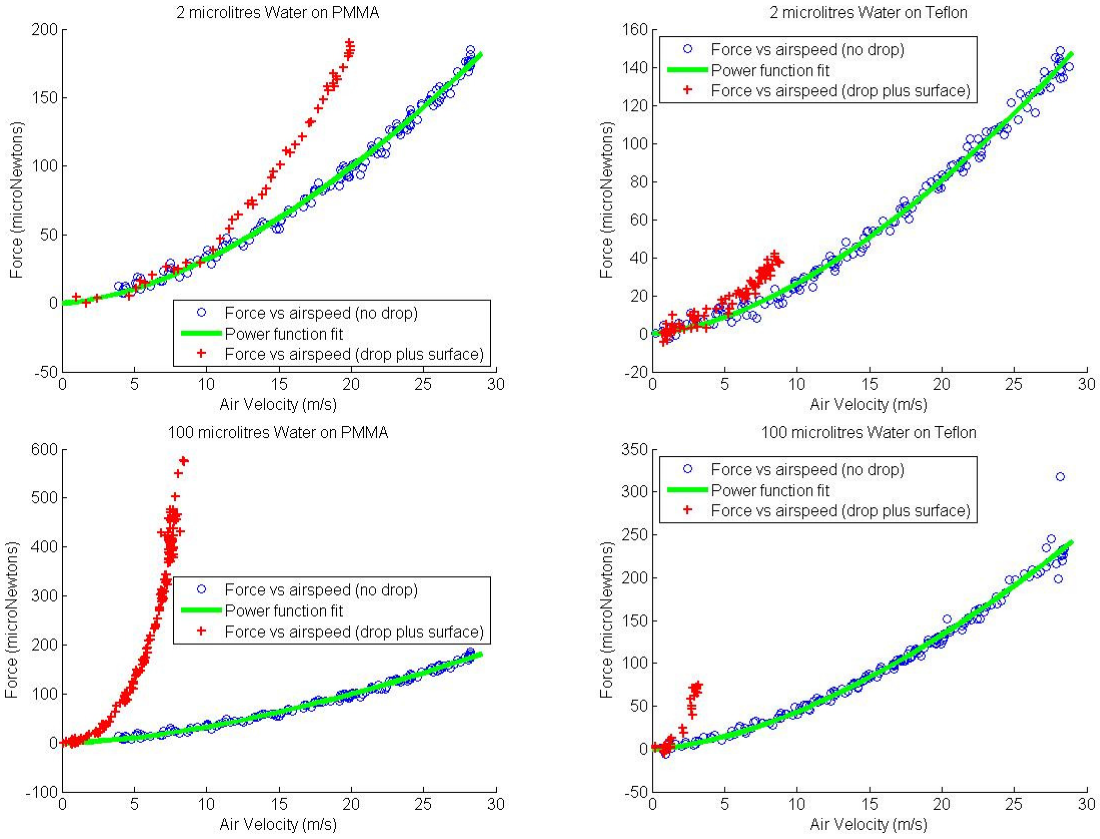

Figure 3-11: Representative reference (no drop) and composite system (drop plus surface) measurements versus air velocity for a 2 and 100 µl drops of water on PMMA and Teflon.

As stated above, the composite system measurement is generally noticeably higher than the reference measurement for both the largest and smallest volumes tested on both hydrophobic (Teflon) and hydrophilic (PMMA) surfaces. At lower air velocities, there is an uncertainty in measurement as reference and composite measurements are similar. However, it is known that the drops experience zero force and zero velocity, and a measurable force at some sufficiently high velocity, so the precise dependence of force on air velocity in the intermediate range is not of great consequence. As seen in Figure 3-11, the range of air velocities for which this uncertainty exists depends on the system and volume, with the smallest drops of water on PMMA displaying the largest uncertainty range (from 0 m/s to ≤ ~10 m/s) and the largest drops of water on Teflon displaying the smallest range (from 0 m/s to ≤ ~1.5 m/s). Outside of this range of uncertainty, larger drops, which present more area to the flow, show larger signal differences, while smaller drops show smaller differences. It can also be seen that drops on Teflon, which adopt a more spherical shape and therefore present more of a blunt face to the flow, experience larger forces at any given airspeed compared to water on PMMA. As a note, the composite system measurements in Figure 3-11 terminate at different values of air velocity, with each termination corresponding roughly to the point at which the drop began to shed and at which point the test was stopped.

With drag signals clearly distinguishable, questions remain as to the resolution and error inherent in the measurements. The sensor, as constructed, has a precision of 1μN if used in a vibration free environment. A floating element in a

wind tunnel obviously does not provide such an environment, so the resolution of the measurement system is limited by the uncertainty due to vibrational noise. Assuming a Gaussian distribution of noise, the standard deviations for reference and composite systems measurements are, on average, ~8.95 and ~4.49 μN, respectively. Since reference and composite systems are subtracted in the differential drag technique, the combined standard deviation is determined to be 10.01 μN by the standard process of taking the square root of the summed squared standard deviations. This indicates that the 1 μN resolution of the sensor is overwhelmed by an approximately 10 times higher standard deviation in measurements. Regardless, a 10 μN uncertainty is sufficient for determining the drag forces on sessile drops.

With the precision and uncertainty determined for the sensor, accuracy is now considered. Here, a comparison to expected values of the drag force to shed drops will be made to test the sensor's accuracy. For differential drag calculations, the power law fit of the reference signals in Figure 3-11, corrected for the area of the surface covered by the drop and evaluated at each value of airspeed, is subtracted from the composite system measurement. This assumes, for the sake of simplicity at this time, negligible interference drag (changes in drag due to the mutual interference of the drop and surface on the flow over each other) in the composite signal.

The point of incipient motion is determined from the high speed video, after which the calculations of differential drag force, taken at a lower sampling rate,

can be interpolated to determine the force required for shedding (interpolation, rather than extrapolation, can be used since the motion of the drop is quite minor about the point of incipient motion). Figure 3-12 shows averaged drag force for each volume and system along with the gravitation force needed to overcome the adhesion of a drop on a tilted plate for the same systems and similar volume ranges[1] without airflow present. It can be seen that the forces measured by the floating element differential drag sensor are of a similar magnitude to the expected adhesion force. Some differences are seen in the exact values of force, and in the way force changes with volume, but this is expected based on previous work[1,14] that has seen that drop shape (and therefore adhesion and drag forces) are different between cross flow and gravity shed drops. The differences are examined in more detail in Appendix A.4, but nevertheless, the excellent agreement in order of magnitude between the measurement of drag forces on sessile drops in cross flow and the gravitational force for tilted plate experiments indicates that the sensor is measuring drag with good accuracy, and that the assumption of negligible interference drag is reasonable at this time.

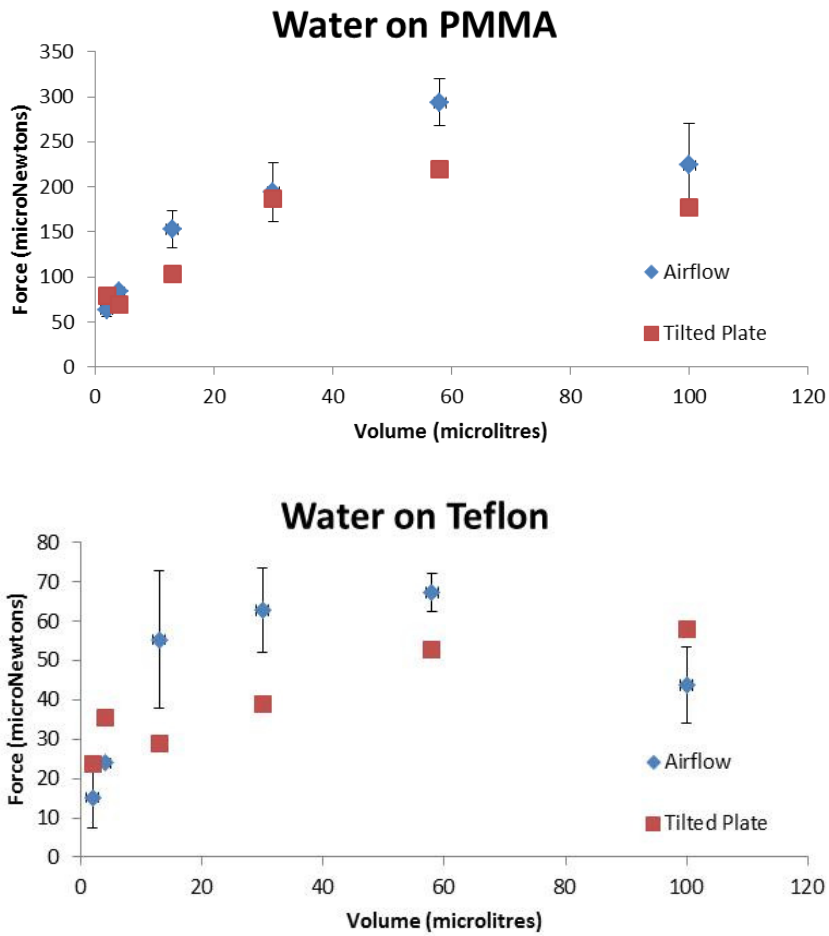

Figure 3-12: Force to shed a drop versus drop volume for the two systems tested. Diamond symbols show air drag measured in the present work, while squares are the gravitational force needed to shed a drop from a tilted plate measured previously for the same systems[1]. Error bars denote one standard deviation.

3.6 Summary

A novel measurement technique has been developed, based on differential drag measurements taken with a floating element shear sensor that is modified to allow for the placement of sessile drops on its surface element. Due to the long settling time of the high sensitivity cantilever, the sensor was damped with silicone oil. Initial tests read negative values of force for the reference (drop absent) measurement, and less negative values for the composite system (drop on surface) measurement. Recirculation zones, leaks, and other causes were ruled out and the source of the negative readings was found to be an adverse pressure gradient along the surface, causing a secondary flow underneath it and along the sensor shaft, as well as pressure forces along the surface's edge. The adverse pressure gradient was removed by modifying the side walls of the tunnel to prevent the flow from decelerating over the sensor surface, leading the sensor to read positive values. The modifications were seen not to greatly affect the shedding of drops by cross flowing air.

Initial tests show that the floating element sensor does not appreciably alter the flow around the sessile drops placed on top of it. Reference measurements give forces close to the prediction for flat plate drag, and composite system measurements show a clear increase in signal for drops of 2 and 100 μl of water on hydrophilic PMMA and hydrophobic Teflon coated glass. The clear signal, with a low uncertainty, permits the first direct measurements of the drag force on sessile drops to be reported in this paper. The values of drag force to shed drops

by a cross flow is shown to be of the same order of magnitude as the gravity force to shed similar drops from tilted surfaces. This indicates that the floating element differential drag sensor has good accuracy as well, and can be used to measure the force of drag on sessile drops and other weakly surface adhered particles.

References for Chapter 3

(1) Milne, A. J. B.; Amirfazli, A. *Langmuir* **2009**, *25*, 14155–14164.
(2) White, E. B.; Schmucker, J. A. *Journal of Fluids Engineering* **2008**, *130*, 061302.
(3) Bico, J.; Basselièvre, F.; Mermigier, M. In *Bulletin of the American Physical Society*; American Physical Society: Chicago, IL, 2005.
(4) McAlister, G.; Ettema, R.; Marshall, J. S. *Journal of Fluids Engineering* **2005**, *127*, 257.
(5) Minor, G. Experimental Study of Water Droplet Flows in a Model PEM Fuel Cell Gas Microchannel. MASc, University of Victoria, 2007.
(6) Theodorakakos, A.; Ous, T.; Gavaises, M.; Nouri, J. M.; Nikolopoulos, N.; Yanagihara, H. *Journal of Colloid and Interface Science* **2006**, *300*, 673–687.
(7) Njifenju, K.; Bico, J.; Andrès, E.; Jenffer, P.; Fermigier, M. In *Bulletin of the American Physical Society*; American Physical Society: Minneapolis, MN, 2009; Vol. Volume 54, Number 19.
(8) Antonini, C.; Innocenti, M.; Horn, T.; Marengo, M.; Amirfazli, A. *Cold Regions Science and Technology* **2011**, *67*, 58–67.
(9) Milne, A. J. B.; Defez Garcia, B.; Cabrerizo-Vílchez, M.; Amirfazli, A. *In revisions with co-authors* 55 pages.
(10) Clift, R.; Grace, J. R.; Weber, M. E. In *Bubbles, drops, and particles*; Dover Publications: Mineola N.Y., 2005.
(11) Antonini, C.; Carmona, F. J.; Pierce, E.; Marengo, M.; Amirfazli, A. *Langmuir* **2009**, *25*, 6143–6154.
(12) Große, S.; Schröder, W.; Brücker, C. *Measurement Science and Technology* **2006**, *17*, 2689.
(13) Muthanna, C.; Nieuwstadt, F. T. M.; Hunt, J. C. R. *Experiments in Fluids* **2005**, *39*, 455–463.
(14) Schmucker, J. A.; White, E. B. *Journal of Fluid Mechanics* **2013**, *In Revisions*, 26 pages.
(15) Li, X.; Pozrikidis, C. *Journal of Fluid Mechanics* **1996**, *307*, 167–190.
(16) Jones, J. L.; Lal, M.; Ruddock, J. N.; Spenley, N. A. *Faraday Discussions* **1999**, *112*, 129–142.
(17) Zhang, J.; Miksis, M. J.; Bankoff, S. G. *Physics of Fluids* **2006**, *18*, 072106.
(18) Zhu, X.; Sui, P. C.; Djilali, N. *Journal of Power Sources* **2007**, *172*, 287–295.
(19) Rothmayer, A. P.; Tsao, J. C. *AIAA Paper No. 2001-676* **2001**.
(20) Chandrasekharan, V.; Sells, J.; Meloy, J.; Arnold, D. P.; Sheplak, M. *Journal of Microelectromechanical Systems* **2011**, *20*, 622–635.
(21) Jiang Zhe; Modi, V.; Farmer, K. R. *Journal of Microelectromechanical Systems* **2005**, *14*, 167–175.
(22) Amili, O.; Soria, J. *Experiments in Fluids* **2011**, *51*, 137–147.
(23) Ayaz, U.; Ioppolo, T.; Ötügen, M. *Measurement Science and Technology* **2011**, *22*, 075203.
(24) Schmidt, M. A.; Howe, R. T.; Senturia, S. D.; Haritonidis, J. H. *IEEE Transactions on Electron Devices* **1988**, *35*, 750 –757.

(25) Shajii, J.; Ng, K.-Y.; Schmidt, M. A. *Journal of Microelectromechanical Systems* **1992**, *1*, 89 –94.
(26) Hanratty, T. J.; Campbell, J. A. In *Fluid mechanics measurements*; Hemisphere Pub. Corp., 1983.
(27) Kiewicki, J. C.; Saric, W. S.; Marusic, I.; Eaton, J. K. In *Springer handbook of experimental fluid mechanics*; Tropea, C.; Yarin, A. L.; Foss, J. F. (Eds. ., Eds.; Springer: Berlin, 2007; pp. 871–902.
(28) Gad-El-Hak, M. *MEMS Applications: The MEMS Handbook*; CRC Press, 2006.
(29) Barlian, A. A. Microfabricated Piezoresistive Shear Stress Sensors for Underwater Applications. PhD, Stanford University: Stanford, California, 2009.
(30) Hirt, F.; Zurfluh, U.; Thomann, H. *Experiments in Fluids* **1986**, *4*, 296–300.
(31) Frei, D.; Thomann, H. *Journal of Fluid Mechanics* **1980**, *101*, 79–95.
(32) Vakili, A. D. *Experiments in Fluids* **1992**, *12*, 401–406.
(33) Allen, J. M. *NASA STI/Recon Technical Report N* **1976**, *77*, 11339.
(34) Acharya, M.; Bornstein, J.; Escudier, M. P.; Vokurka, V. *AIAA Journal* **1985**, *23*, 410–415.
(35) Winter, K. G. *Progress in Aerospace Sciences* **1979**, *18*, 1–57.
(36) Tucker, V. A. *Journal of Experimental Biology* **1990**, *154*, 439–461.
(37) Abbott, I. H. *NACA Annual Report* **1932**, *17*, 583–604.
(38) Pope, A.; Harper, J. J. In *Low Speed Wind Tunnel Testing*; John Wiley & Sons Inc: New York, 1966; pp. 126–191.
(39) Desmond, G. L.; McCrary, J. A. *NACA Technical Note* **1935**, *536*, 21.
(40) White, F. M. *Fluid Mechanics*; 5th ed.; McGraw-Hill, 2003.
(41) Schlichting, H. (Translated Kestin, J.) *Boundary Layer Theory*, 6th ed.; McGraw-Hill Book Co.: USA, 1968.

Chapter 4: Measuring the force of drag on sessile drops in cross flowing air[h]

4.1 Introduction

The interactions of sessile (wall constrained) drops or bubbles with an external cross flow is important anywhere a discrete fluid phase is in contact with a solid and in relative motion with a dispersed fluid phase. These interactions can accelerate evaporation/dissolution, induce internal motion and mixing, drive oscillation, or cause the drop/bubble to shed (be blown along or off the surface or be broken into smaller drops/bubbles). As such, understanding of sessile drop/cross flow interactions has applications to airfoil icing, fuel cell flooding, enhanced oil recovery, froth floatation, condensers, visibility through glass in rainy conditions, pesticide use, and fluid manipulation in reduced gravity, etc.[1–8] Internal circulation, oscillation and shedding all depend in part on the drag force experienced by the drops.

Surprisingly, drag force has not been well measured in literature. The sole previous work measuring drag depended on balancing gravitation and drag forces[7] (which has the draw back of distorting drop shape and therefore drag (see Chapter 3)). Alternatively, researchers have attempted to measure the full three dimensional shape of the drop interface to determine adhesion force[9] (a proxy of

[h] A version of this chapter will be published, with co-authors A. J. B. Milne, B. Fleck, A. Amirfazli. B. Fleck and A. Amirfazli acted as supervisors, making the thesis author the main contributing author in terms of data collection, reduction, analysis, and writeup.

drag force before the point of incipient motion that leads to drop shedding[1]) using an innovative speckle shift technique. The current state of the art of the technique is limited, however, to a small range of contact angles, and even within that range, the technique can only give qualitative trends rather than highly accurate quantitative measurements of contact angle and adhesion[9]. Contact angle is measured between the base of the drop and the tangent of the liquid-vapour interface at the three-phase contact line where liquid, vapour, and solid meet. Advancing contact angle (θ_a) is observed where the contact line is advancing across the surface, and a lower receding contact angle (θ_r) vice versa. For sessile drops in a cross flow, θ_{max} and θ_{min}, respectively, replace the advancing and receding nomenclature since 'advancing' and 'receding' are generally used for quasi-static volume addition/removal tests in quiescent conditions and it was found (in literature[1] and Chapter 2) that drops in cross flow can display different values of contact angle. Contact angle and drop shape are interrelated and should affect drag by impacting the flow around the drop. The difference between advancing and receding contact angles (contact angle hysteresis, CAH) affects drop adhesion to the surface[10] (determining the drag force necessary to overcome adhesion and shed the drop[1]).

Models for sessile drop drag are also lacking. No general analytic results exist, as drop shape, oscillation, and internal flow make the governing equations intractable for realistic conditions. Numeric results are also limited to, e.g., extremely low contact angle, low Reynolds numbers, similar properties between

the fluids, etc.[6,11–15] The models that exist also lack experimental data for comparison, a problem we address here.

The measurement of sessile drop drag force is challenging due to its tens of microNewtons magnitude, and the signal's variance in time due to drop oscillation. It is also difficult due to the drop's fluid nature and light adherence to the surface (making it free to deform and move on the surface). To overcome these difficulties and address the lack of measurements in the literature, we developed and proved a technique based on a combination of the floating element technique and differential drag measurements in Chapter 3. We seek here to use our floating element differential drag sensor to understand how the drag necessary to shed the drop varies with drop volume, surface properties/hydrophobicity, and fluid properties. We also seek to understand how drag is related to Reynolds number and the airflow conditions around, and affected by, the drop.

While we focus on sessile drops due to our previous work on the topic[1], the techniques we use to measure/analyze drag in this work can easily be extended to bubbles, and to drag measurements for other deformable and/or movable objects loosely adhered to a surface (such as, e.g., vesicles, foams, bacterial/biofilms, and granular deposits such as dust or snow).

4.2 Experimental Methods and Materials

The sensor system design and characterization, and its implementation in the wind tunnel used, are discussed in detail in Chapter 3, with only a brief discussion here. To measure drag force on sessile drops we adapt the differential drag technique. Differential drag on solid bodies is determined from measurements of the drag on the body held in a free stream by a strut, and of drag on the strut by itself. The drag on the body is then the difference between the two measurements (accounting for interference drag caused by the mutual interference of the strut on the flow over the body, and vice versa)[16–19]. For sessile drops, a reference measurement is taken over a floating element surface without any drop present. Then a composite system measurement is taken of the same surface with a sessile drop on it. As shown in Figure 4-1, the difference in the measurements (corrected by the relative areas of the surface exposed during the two measurements and neglecting interference drag for simplicity) gives a measure of the force of drag on the drop alone.

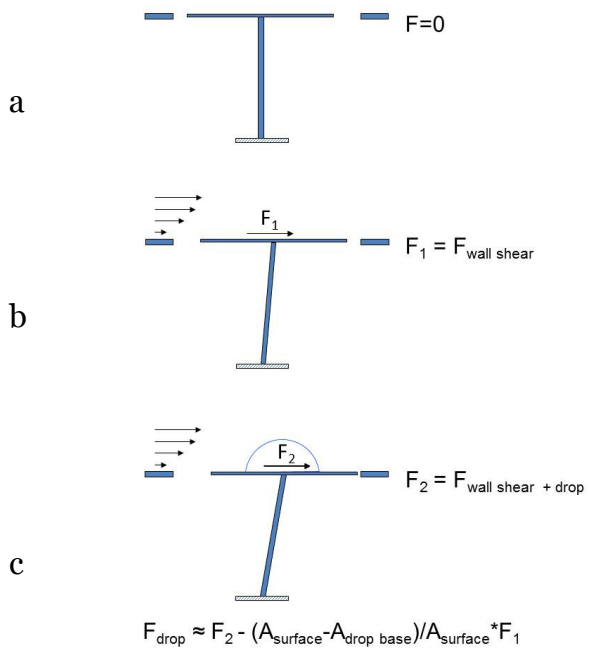

Figure 4-1: A schematic of the floating element sensor (not to scale) mounted flush with the surrounding body showing: a) no deflection in quiescent conditions, b) some deflection under airflow due to the force, F_1, which corresponds to wall shear with the drop absent, and c) some greater deflection under airflow with the drop present due to the force, F_2, which corresponds to drop drag, wall shear over the uncovered portion of the sensor, and any interference effects (assumed negligible). The force of drag on the drop (F_{drop}) is thus the difference between F_2 and F_1, accounting for the contact area of the drop.

Our sensor is based upon a modified single cantilever shear force sensor (Novatech Measurements Limited, St Leonards on Sea, UK). This cantilever is mounted vertically in an aerodynamic body in a laminar wind tunnel (0-30 m/s suckdown wind tunnel of 215.9 mm x 469.9 mm working section). The wind tunnel and streamlined body are described in detail elsewhere[1], with modifications described in Chapter 3. As implemented, the sensor has an uncertainty of ~10 μN, and a range of +/- ~1 mN. The sensor has a resonant frequency of ~5 Hz, meaning higher time resolution measurements of force are not possible. This paper will generally report results measured at 20 Hz, and bin averaged to give a 2 Hz measurement rate.

Sessile drop shedding tests were performed for drops of water on PMMA-coated glass (denoted 'PMMA' here), Teflon-coated glass (denoted 'Teflon'), and a superhydrophobic surface (denoted 'SHS') of Teflon-coated, etched aluminum. Details on the surface preparation and characterization are given[i] in Chapter 2. Drops of hexadecane (denoted 'HD') were also tested on Teflon-coated glass. The different liquids and surfaces were used to study the effects of contact angle (controlling drop shape) on sessile drop drag force. Average downstream (advancing side) and upstream (receding side) contact angles for the systems were[1] $\theta_{max\_HD\text{-}Teflon}/\theta_{min\_HD\text{-}Teflon}$=66.7°/53.6°, $\theta_{max\_water\text{-}PMMA}/\theta_{min\_water\text{-}PMMA}$=76.3°/53.1°, $\theta_{max\_water\text{-}Teflon}/\theta_{min\_water\text{-}Teflon}$=124.3°/108.2°, $\theta_{max\_water\text{-}SHS}/\theta_{min\_water\text{-}SHS}$=161.4°/129.8°. It can be seen that the contact angles (and therefore drop shape) are similar for the HD-Teflon and water-PMMA systems, a fact that will be exploited to study the effects of surface tension and other fluid properties. Drops of 100, 58, 30, 13, 4, and 2 μl (deviations on volume ranging from 1.5 to 0.2 μl for the largest and smallest volumes, respectively) were tested to study the effects of drop size, with three or more repetitions of each volume for each liquid-surface system.

Considering the size of drops and the air velocities necessary to shed them, the flat plate Reynolds number at the location of the sensor and drop was less than or

[i] It should be noted that due to a manufacturer's calibration error, the previously stated roughness values[1] are incorrect. The correct average roughness (R_a) values for the previous and present work are R_a = 0.063 μm and 3.244 μm, for the smooth coated glass and rough etched coated aluminum, respectively, as measured by white light confocal microscopy. This does not change previous conclusions[1] since the roughness values still show that the coated glass surfaces are significantly smoother than the SHS.

equal to $2x10^5$, suggesting laminar flow. The Reynolds number based on free stream airspeed and drop spherical cap radius was less than or equal to 2000, again suggesting that the flow over the drop would start of in a laminar regime, but it will be seen that the wake and flow is likely destabilized by drop oscillations. As discussed previously[1] and in Chapter 2, the assumed boundary layer characteristics have been calculated based on laminar flow over a cylinder. Based upon these calculations, and measurements determined from image analysis, the drop height ranged from approximately 0.9 to 2.5 times the boundary layer height. As such, the drop is largely exposed to velocities at or near the free stream. While ideally a full characterization of the boundary layer would be made to calculate an effective air velocity 'felt' by the drop, the free stream velocity will be used as it is a more accessible measurement to all users, and since the drop does 'feel' the free stream over a large portion of its surface. Free steam air velocity was measured by pitot tubes, with a tube mounted 1 cm above the sample at the same location as the drop, but displaced laterally by several centimeters. Tests were recorded by a Phantom v4.3 high speed camera (Vision Research, Wayne, NJ), operating at 200 fps and recording each drop and its surrounding at a resolution of 42 μm/pixel.

4.3 Force to Shed Drops

As noted in Chapter 3, the drag force to shed drops is similar in order of magnitude to the gravitational force to shed drops from a tilted plate in quiescent conditions. Appendix A.4 contains a discussion/analysis of this comparison, as

well as discussion/comparison to the Furmidge[20] model for adhesion as a proxy model for cross flow shedding.

4.4 Force versus Air Velocity

Figure 4-2 shows drag force versus free stream air velocity for a selection of volumes for each system, with power law fits of individual and combined data. The data for all volumes is given in graphs in Appendix A.5. In Figure 4-2, it can be seen that the differential drag measurements are generally well fit by power law relations. Additionally, it can be seen that larger drops experience greater drag forces at lower airspeeds compared to smaller drops, confirming previous hypotheses[1]. This partially explains why larger drops, which have higher adhesion forces due to their longer contact lines, are shed at lower airspeeds than smaller drops[j].

In comparing the results for various systems to each other, the data in Figure 4-2 can be considered in two ways. One is to consider the forces experienced at the point of incipient motion, the other is to consider the force at any given airspeed for each system. Considering the force at shedding (as is done in more detail in Appendix A.4), it is seen that water-PMMA experiences the highest forces,

[j] As a note, the maximum force and air velocity values shown in Figure 4-2 are roughly equivalent to the force and critical airspeed for shedding. However, Figure 4-2 also shows some data taken after the drop began to shed, but before it moved far enough for its weight to appreciably shift and affect the force measurement of the sensor. The force to shed the drops is discussed in Appendix A.4.

followed by water-Teflon, with water-SHS experiencing the lowest forces of the water systems. HD-Teflon experiences slightly higher forces than water-SHS.

Considering the forces experienced at a given airspeed for each system, for water drops it is seen that the water-Teflon and water-SHS systems generally experience similar forces, and that the water-PMMA and HD-Teflon systems also generally experience similar, but smaller magnitude, forces. This can be seen by plotting just the power law fits for each of the systems on the same graph for matching ranges of air velocities as is done in Figure 4-3. The range of air velocities in Figure 4-3 is limited to those for which all drops are pinned (i.e. limited to the critical air velocity for the water-SHS system). While some measurements of force or differences between curves in Figure 4-3 are below the 10 μN uncertainty of the sensor, the fact that the fits average in general at least three tests each improves this resolution. There is also the possibility of uncertainty in the measurement of composite versus reference measurements for the smallest drops of water on PMMA (and HD on Teflon) as discussed in Section 3.5.4, but as discussed there, the trends in Figure 4-3 should be correct, even if the exact shape of the curves may not be.

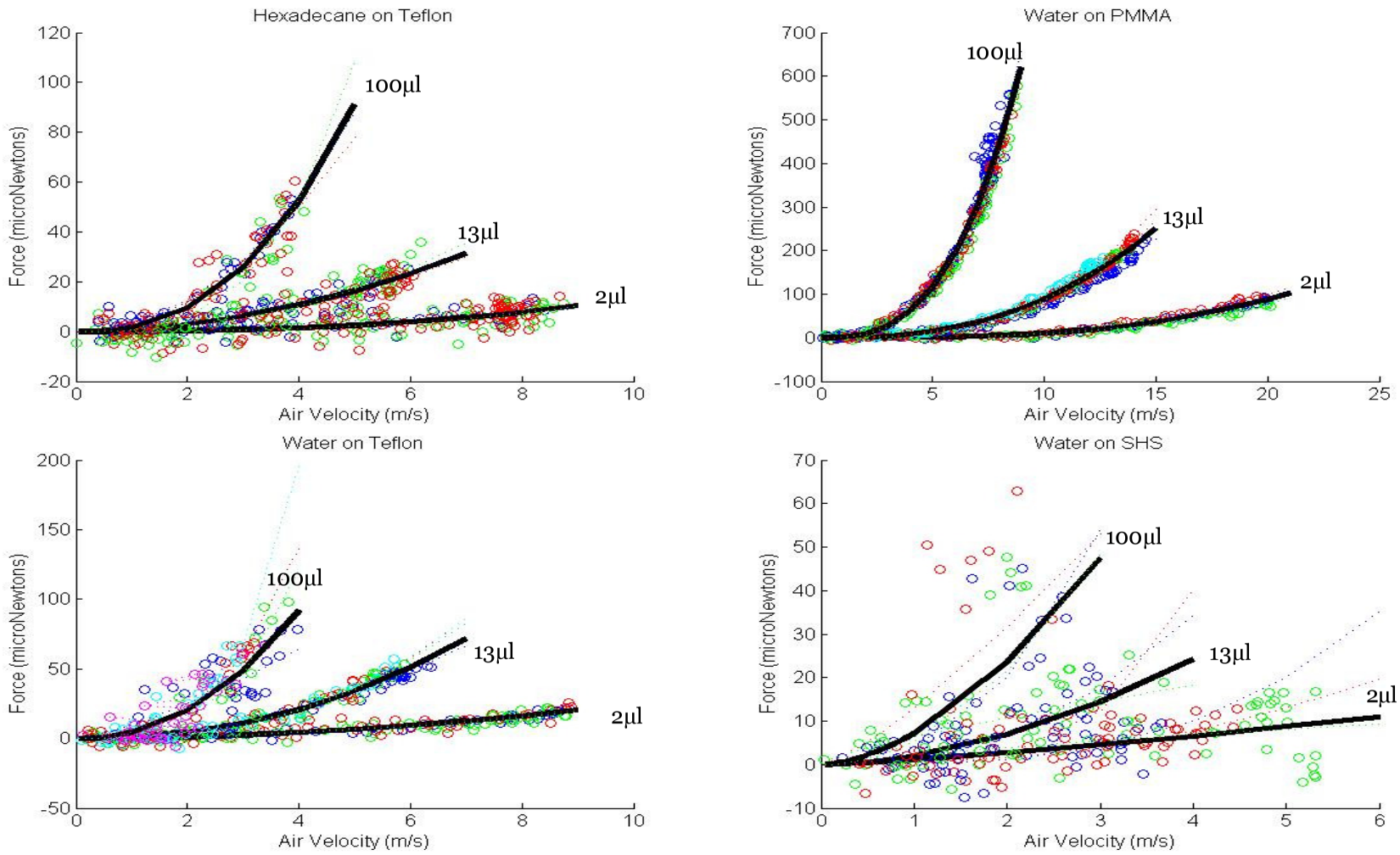

Figure 4-2: Force versus air velocity for different drop volumes for each system calculated using the differential drag technique (i.e. corrected to remove the drag on the surface). The differently coloured data points (available in the electronic version) denote different repetitions of the tests. Dotted lines are power law fits to individual tests, solid lines are fits to the collected data for each volume. Negative readings of force are a result of measurement scatter due to tunnel vibration.

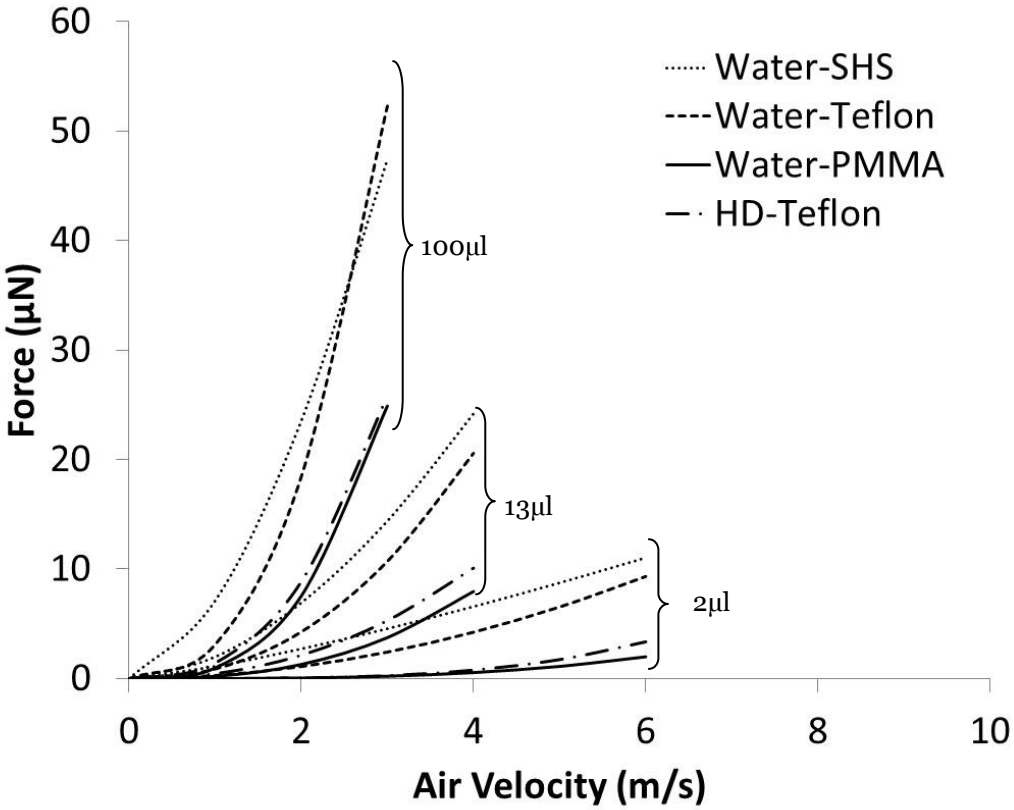

Figure 4-3: Power law fits for water volumes of 100, 13, and 2 µl on the four systems for matching ranges of air velocities for which all drops are pinned. Scatter in individual measurement is at most ~10µN, the composite fits shown achieve a higher resolution through averaging in general at least three tests.

Considering Figure 4-3, the drops for water-PMMA and HD-Teflon do not sit as high in the boundary layer as drops for the other systems, and also present a flatter, more streamlined shape (See Figure 2-2). This suggests that they would disturb the flow less and experience less force. They also present less frontal area to airflow than drops of water on more hydrophobic surfaces, as illustrated in Figure 4-4. Drops for water-SHS and water-Teflon are closer to spherical in shape, meaning that they sit higher in the boundary layer, they also present more cross sectional area and more of a blunt face for any given volume (see Figure 4-4). The fact that water drops are shed at lower air velocities from SHS, while

experiencing similar forces compared to water drops on Teflon, suggests that it is the lower adhesion force for the water-SHS that eases shedding. The effects of the differences in exposed area will be explored in the next section by consideration of the drag coefficient.

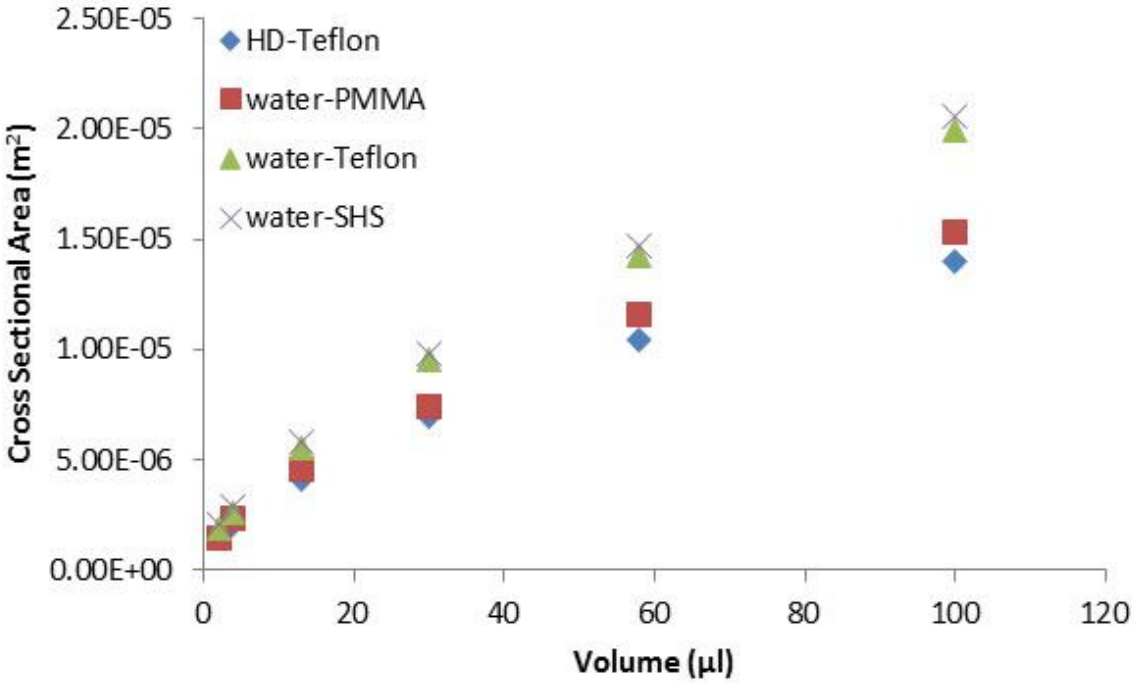

Figure 4-4: Cross sectional area versus drop volume for the four systems tested. Note the similar, higher values of area for water-SHS and water-Teflon, and the similar, lower areas for water-PMMA and hexadecane on Teflon. Standard deviations are within symbol size

4.5 Coefficient of Drag

Non-dimensionalizing the relationship between drag force and air velocity can give insight into the separate effects of drop size and drop shape/contact angle, and give indications as to the effects of fluid properties. We use the usual relations for coefficient of drag and Reynolds number here. The coefficient of drag, C_D, is defined by:

$$F_D = \frac{1}{2}\rho U_\infty{}^2 C_D A \qquad \text{Equation 4-1}$$

where F_D is the drag force, ρ is air density, U_∞, is the free stream air velocity, and A is a reference area of the drop (here taken to be the cross sectional area of the axisymmetric drop measured in quiescent conditions). The Reynolds number is defined by:

$$\mathrm{Re}_h = \frac{\rho U_\infty h}{\mu} \qquad \text{Equation 4-2}$$

where h is the axisymmetric drop height measured in quiescent conditions and μ is the viscosity of air. As a reference length, the drop height is used rather than the more fundamental choice of spherical cap radius for two reasons. First, spherical cap radius is non-unique in that each drop with a contact angle above 90° by some value will have a related, smaller volume drop with an identical spherical cap radius and a contact angle below 90° by that same value. A more unique length scale for sessile drops then is the drop height, which when specified along with drop volume is unique for each contact angle as long as gravitational effects are negligible. The second reason for choosing drop height as a length scale is that this choice better collapses data between systems, as will be seen. The analysis and discussion of drag coefficient versus Reynolds number based on spherical cap radius can be found in Appendix A.6.

In Equations 4-1 and 4-2, quiescent measurements of cross sectional (equal to frontal) area and drop height are used. As air velocity increases, however, the drop deforms, changing its area and height. Further, it is uncertain if frontal area

(related to form drag) or total surface area (related to shear drag) is a more appropriate choice of reference area (both reference choices would change as the drop deforms). Quiescent measurements are used (as discussed in Chapter 2), since they are experimentally accessible, and furthermore, since they can be calculated a priori based on a knowledge of contact angle and drop volume/fluid properties. Time resolved measurements of the shape/area of the drop might prove more useful in non-dimensionalizing force, but are not experimentally accessible, and further, would result in a reference area that changes over time, somewhat defeating the idea of a reference. Regarding the uncertainty in the importance of frontal versus total area, since quiescent measurements are used in calculating area, cross sectional area is equal to frontal area, and related to total surface area by known relations for a spherical cap. This means that the use of one reference area should capture the effect of the other. For the interested reader, measurements and calculations of drop properties are included in Appendix A.6.

Considering Equations 4-1 and 4-2, it is immediately apparent that neither accounts for drop properties (surface tension, density, viscosity), nor do the equations explicitly account for contact angle, nor for the oscillation of the drops, their internal circulation, and the deformation of drops away from axisymmetric as velocity increases from quiescent. Drop properties are constant between all the water systems. Contact angle is approximately constant with volume for each system considered separately, and similar for HD-Teflon and water-PMMA. This means that some study of the effects of changing drop properties can be made by

comparing HD-Teflon and water-PMMA, but the different contact angles between the three water systems makes any other direct comparisons difficult. Differences in deformation, oscillation, and internal circulation within a system should manifest as differences in the relationship between coefficient of drag and Reynolds number for different drop volumes in the same system.

Figure 4-5 presents drag coefficient versus Reynolds number for all drop volumes for the four systems tested, for Reynolds numbers corresponding to the range of near quiescent to just past incipient motion (similar to Figure 4-2). Given that the force versus airspeed relations were well fit by power laws, the drag coefficient versus Reynolds number relations could be found from the power law fits. However, this would make each relation appear as a single straight line on the log-log graphs. This line would effectively present an averaged relationship between drag coefficient and Reynolds number, similar to an averaged slope of a function over some interval compared to instantaneous tangents of the same function. This averaging would limit knowledge of how drag coefficient changes with Reynolds number. Instead, discrete values of force and airspeed were considered for each drop volume and each repetition of the tests, resulting in a richer demonstration of the relationship, at a tradeoff of slightly noisier signals.

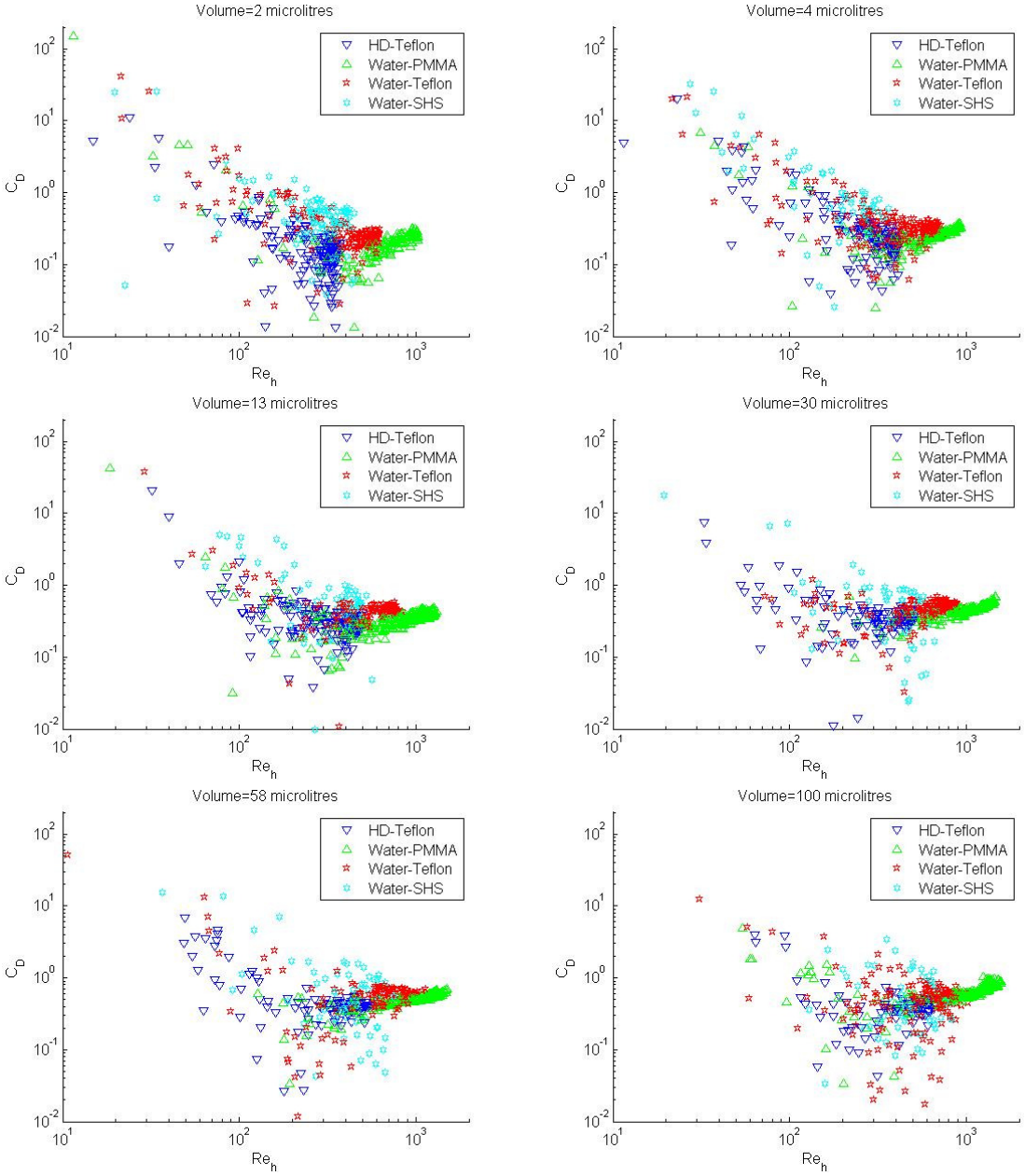

Figure 4-5: Coefficient of drag versus Reynolds number based on drop height for sessile drops under cross flowing air for the four liquid-on-solid-surface systems tested and various volumes. An alternative plot showing all volumes together for each individual system is given in Appendix A.6.

Considering Figure 4-5 in total, all four systems show roughly similar behaviours to each other, and over all volumes. These general similarities might be behind the self similar curves for shedding found previously[1] and discussed in Chapter 2. Considering the curves in more detail, it is seen that drag coefficient does not generally level off with Reynolds number, with most relations showing either a roughly linear decrease, or more often a decrease followed by brief leveling and then an increase in drag coefficient with Reynolds number. The roughly linear decrease can be ascribed to Stokesian drag behavior for the drops. The fact that all four systems, with different fluid properties, contact angles, and volumes, show similar slopes in this region suggests that it is indeed the Stokesian regime, in which the exact shape of objects is generally not important. However, the linear regimes shown in Figure 4-5 do not follow the 24/Re relation common for Stokes drag over solid bodies in free space, instead showing higher drag coefficients. The difference is likely due to the presence of the solid wall changing the airflow conditions/introducing vorticity in the incoming boundary layer, which has been suggested to increase drag coefficient for solid bodies on surfaces modeled for a range of Reynolds numbers from 0.1 to 100[21].

The increase in drag coefficient at higher Reynolds numbers is contrary to the behavior of solid bodies, which tend to show drag coefficients which level off from the Stokesian regime with increasing Reynolds number (up to the turbulent drag crisis). We hypothesize that the increase can be understood by drawing an analogy to the behavior of free drops (e.g. drops floating/falling freely in air, not in contact with a surface), which also show an increase in drag coefficient versus

Reynolds number as shown in Figure 4-6. The increase in drag for free drops is ascribed to an aeroelastic coupling, in that flow over the drop causes the drop to oscillate, which in turn causes vortex shedding/increased wake drag, which in turn reinforces the drop oscillations. In this way, drop oscillations destabilize the wake and increase drag force[22], a phenomenon which has been suggested to exist for sessile drops as well[23]. Oscillation of the drops, which based on the work of Chapter 5 is certainly observed at higher air velocities, could therefore explain the general increase in coefficient of drag at higher Reynolds number. The increase in drag coefficient occurs at lower Reynolds numbers for the sessile drops studied in this chapter (~500 to 700) compared to free drops (for which the increase is seen above Reynolds number of 1000, see Figure 4-6). However, sessile drops oscillate more easily and at lower frequencies than free drops, due to the constraint imposed by the surface (see Chapter 5), suggesting that oscillations would have a greater effect at lower Reynolds numbers for sessile compared to free drops.

Another possible cause of the increased drag at higher Reynolds numbers is boundary layer thinning. As free stream velocity increases, the height of the boundary layer decreases, exposing the drop to a higher mean velocity across the extent of its height. The effect of boundary layer thinning tends to plateau, however, as the boundary layer becomes thinner and thinner, meaning that the shape of the curve would be concave downward. Conversely, the increase seen at higher Reynolds numbers in Figure 4-5 seems to be concave upward (increasing more so as Reynolds number increases, rather than plateauing), which leads us to propose drop oscillation as the cause of the increase.

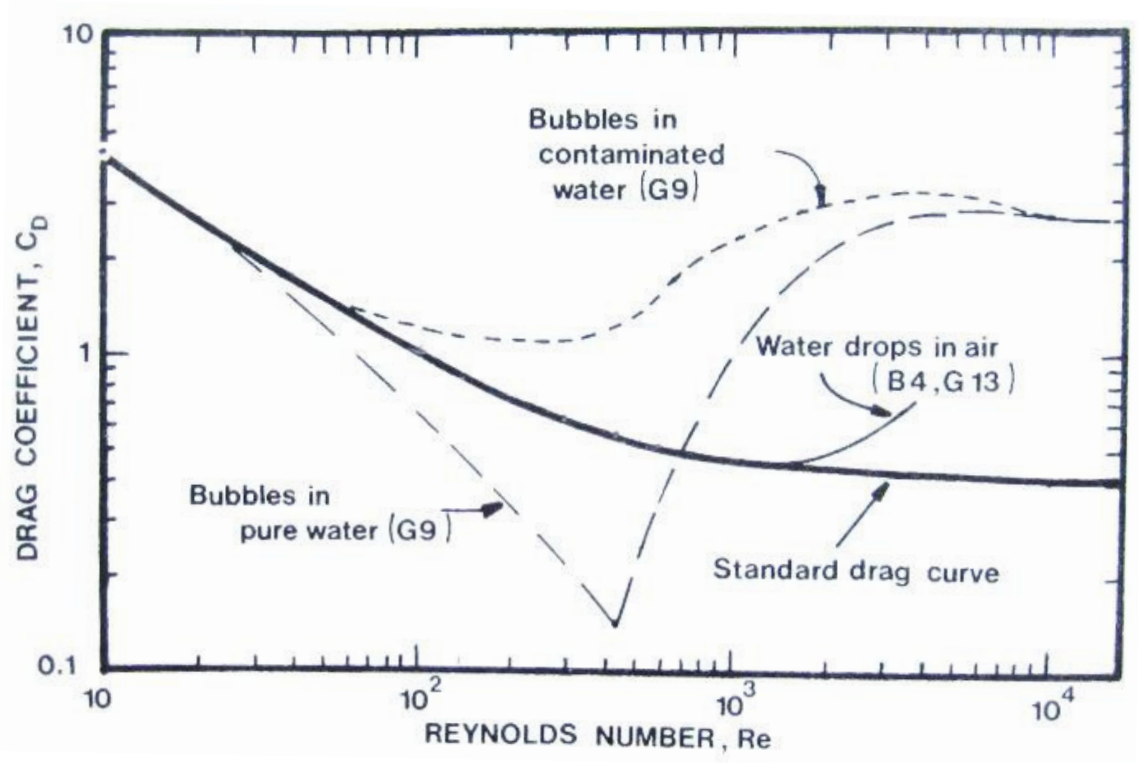

Figure 4-6: A reproduction of Figure 7.2 from Clift et al.[22], describing the drag coefficient versus Reynolds number for free (not in contact with a surface) drops, and solid spheres. Note the increase in drag coefficient for water drops in air (compared to solid spheres), which is due to oscillations of the drop causing vortex shedding/increased drag in the wake through an aeroelastic instability. Permission for use of this copyrighted work was given by the publishers, as noted in Appendix A.7.

Further to the above, within each system shown in Figure 4-5, different volumes present similar curves, but generally show a shift to higher drag coefficients for larger drop volumes (most clearly seen for the water-PMMA system, but also seen in general for the other systems). Increasing volume also slightly increases the Reynolds number at which drag coefficient begins to increase. Considering volume changes, the deformation of smaller versus larger drops seems similar[1], which indicates the difference seen in Figure 4-5 is due to some changing effect of internal circulation or oscillation with drop volume. It was certainly seen during the work of Chapter 5 that larger drops underwent larger magnitudes of oscillation, which could increase drag force beyond the effects of increased drop

size alone, explaining the observed results. Determining the exact effects and implications for shedding of these changes can be aided with measurements of drag force using the floating element differential drag technique.

Considering comparisons between systems, HD-Teflon and water-PMMA systems have similar drop shapes, meaning that the effects of drop shape on coefficient of drag should be similar. Surface tension, while affecting the maximum adhesion opposing shedding, should not affect drag except perhaps in terms of its effects on oscillation, likewise for drop viscosity. It is seen that the HD-Teflon and water-PMMA curves are practically identical for the range of Reynolds numbers they share. This can be seen more clearly in Figure 4-7, which plots the data for a limited range of Reynolds number. This similarity indicates that the three-fold variation in viscosity, and surface tension, and the slight change in density, do not greatly affect the coefficient of drag for the two systems in the Stokesian and level drag coefficient regions. However, since HD-Teflon drops are shed at lower Reynolds number, higher Reynolds numbers are untested for HD-Teflon. Changes might be seen at higher Reynolds numbers if drops remained pinned to the surface, and greater changes in fluid properties might also show a larger effect, but no great effect of fluid properties is seen in the present data leading up to the point of incipient motion.

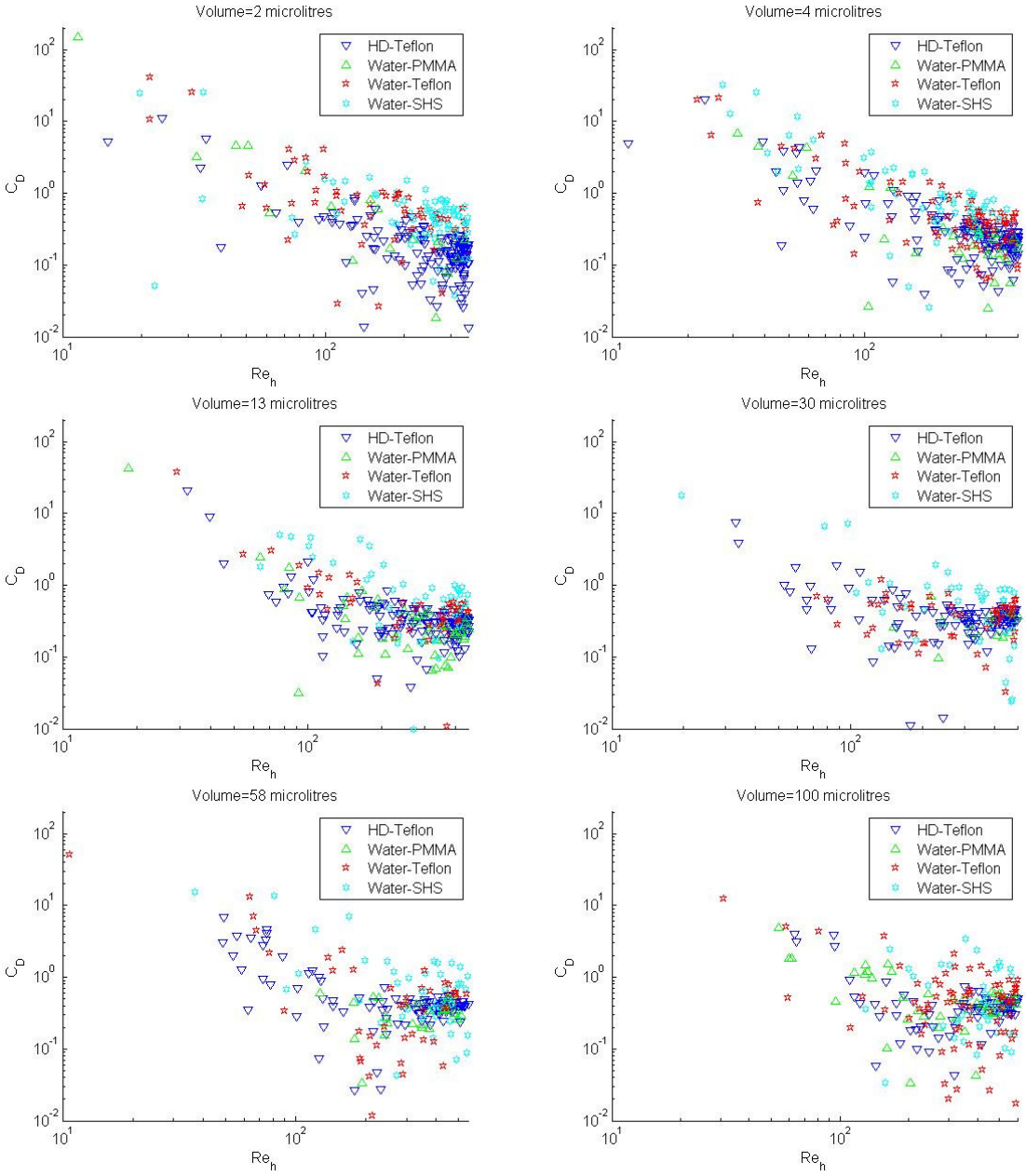

Figure 4-7: Coefficient of drag versus a limited range of Reynolds number based on drop height for sessile drops in cross flowing air for the four liquid-on-solid-surface systems tested and various volumes.

In further comparing systems, it is seen that Figure 4-5 does not completely collapse the data. While the order of magnitude and rough curve shape for all the systems are similar for all volumes, water-Teflon routinely shows slightly higher

drag coefficients than water-PMMA and HD-Teflon, and water-SHS shows slightly higher drag coefficients than water-Teflon. These subtle differences indicate some additional effect of drop shape not capture by the non-dimensionalization by drop height. In comparing water-Teflon and water-SHS, each show a similar slope in the Stokesian region (see Figure 4-7). However, the water-SHS systems remains in the Stokesian regime without showing much of a leveling/increase in drag coefficient, meaning that any possible differences in water-SHS behavior at higher Reynolds numbers cannot be probed with the present data.

4.5.1 Coefficient of Drag for Incipient Motion

The drag coefficient experienced by drops at their point of incipient motion can be determined by analyzing the high speed video to find the point at which the drop starts to move as described in Chapter 2 and previous literature[1]. Also, in Chapter 2 and the previous literature[1], scaling analysis and experimental results were used to determine that the critical air velocity for incipient motion depends exponentially on the ratio $(L_b/A)^{1/2}$. The variable L_b is the base length of the drop measured from the side view for the quiescent drop (meaning it is equivalent to the same measurement taken from a frontal view); it is a variable in a standard proxy model from drop adhesion[1,20]. The scaling analysis/results also indicated that the ratio $(k/C_D)^{1/2}$ must also vary in an exponential way with $(L_b/A)^{1/2}$, where k is a fitting parameter in the same proxy model. As discussed in more detail in Appendix A.4, the fact that the force for shedding by cross flow is similar to the

force for shedding by tilted plate indicates that k is roughly constant with volume. This means k is roughly constant with $(L_b/A)^{1/2}$, indicating that the drag coefficient at the point of shedding should vary exponentially with $(L_b/A)^{1/2}$. Figure 4-8 shows that this is indeed the case generally. Figure 4-8 shows the reciprocal square root of the drag coefficient versus $(L_b/A)^{1/2}$ along with exponential fits for the HD-Teflon, water-PMMA, and water-Teflon systems. It can be seen that for these systems, the relationship generally appears to be exponential. The water-SHS system does not show an identifiable relationship, likely because the forces measured are closer to the sensor's threshold, and noisier, as seen in Figure 4-2. Strategies for improving the resolution of the sensor are discussed at the end of Chapter 6. In fitting the exponential relationships in Figure 4-8, the second largest volume of HD-Teflon was neglected as an outlier, as was the largest volume of water-Teflon, as discussed in Appendix A.4.

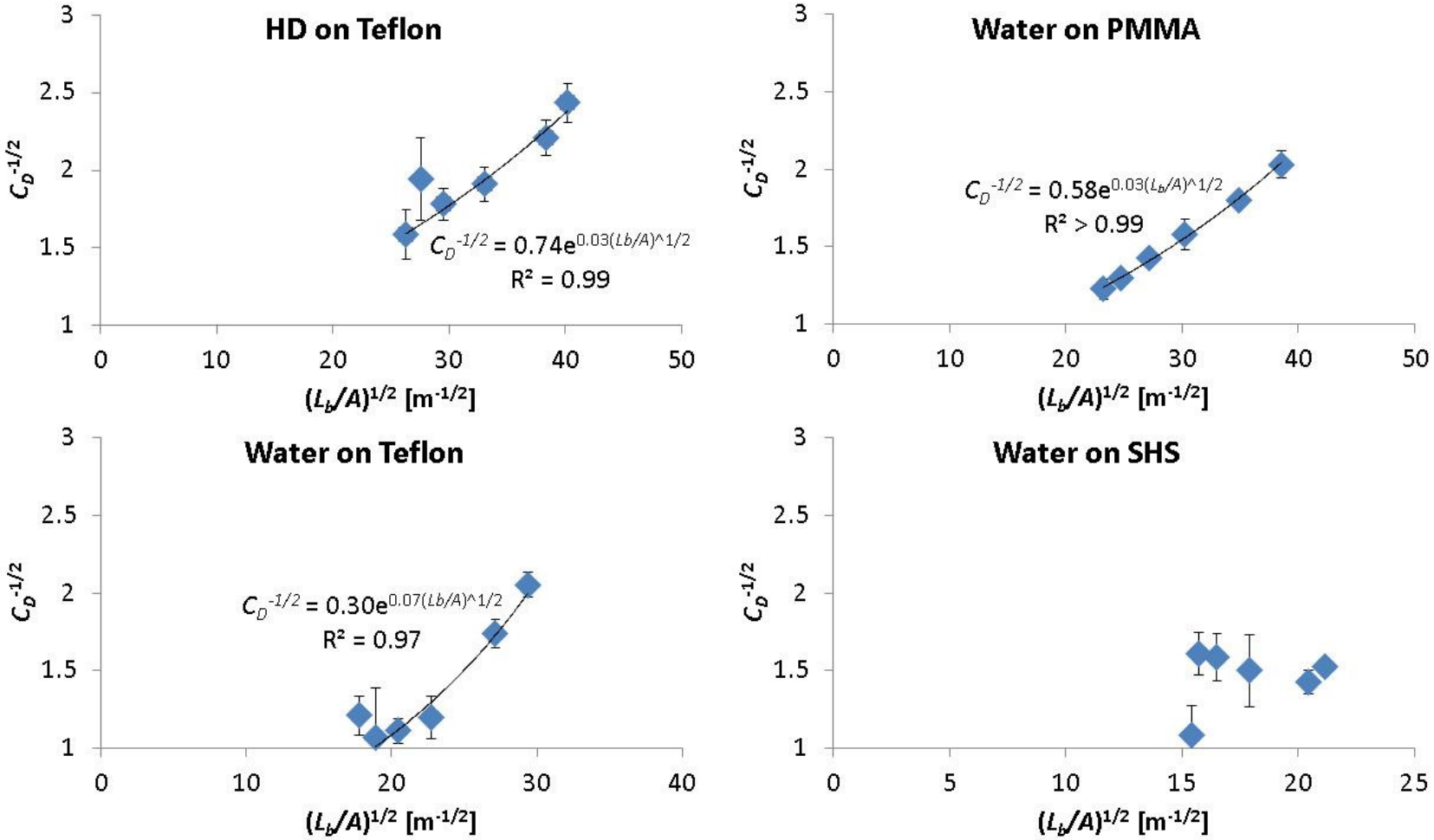

Figure 4-8: The reciprocal of the square root of drag coefficient versus the square root of the ratio of drop baselength over area, showing the generally exponential relation between the two for at least three out of four of the systems tested.

In further considering the drag coefficient at incipient motion, it is seen in Figure 4-5 and Figure 4-8 that water-SHS sheds drops at approximately the same drag coefficient compared to water-Teflon or water-PMMA, while showing slightly higher drag coefficients at any given value of Reynolds number. As discussed previously, for a given value of air velocity water-SHS drops experience similar forces compared to water-Teflon drops (see Figure 4-3), while requiring lower forces for shedding (see Figure 4-2 and Appendix A.4). The combination of similar drag force with generally higher drag coefficients, and shedding at similar values of drag coefficient/lower forces indicates that the water-SHS system drops are more easily shed due to the decrease in adhesion force (rather than an increase in drag force). The other water systems require higher drag forces at incipient motion due to the larger adhesion forces that must be overcome.

4.6 Conclusions

Using a novel floating element differential drag sensor, the first direct measurements of the drag force on sessile drops of water and hexadecane on surfaces of PMMA, Teflon, and an etched superhydrophobic surface have been analyzed.

Drag force versus air speed is seen to be well fit by power law relations. Interestingly, it is seen that drops of water on Teflon and water-SHS experience similarly high forces for a given airspeed, even though drops shed most easily from the superhydrophobic surface. Calculations show similar/higher coefficient of drag for drops on the superhydrophobic surface, indicating that it is the

decreased contact line length/adhesion of drops on the superhydrophobic surface which lead to easier shedding.

The best non-dimensionalization is found by scaling the Reynolds number with the drop height, rather than the drop spherical cap radius. Non-dimensionalizing data, it is seen that drag coefficient does not level off with Reynolds number, as is typical for solid bodies, but instead shows a decrease similar to Stokes drag at lower Reynolds numbers and an increase of drag coefficient at higher Reynolds numbers. It is hypothesized that the increasing drag coefficient is due to oscillations of the drop interacting with the wake and increasing drag through aeroelastic coupling, similar to the behavior seen for free drops. The drag coefficient versus Reynolds number relation also generally increases slightly with drop volume for a given liquid-solid system, indicating that drop size effects on, e.g. oscillation and internal circulation, are affecting drag coefficients and drag forces in a way which cannot be accounted for by standard non-dimensionalization strategies.

References for Chapter 4

(1) Milne, A. J. B.; Amirfazli, A. *Langmuir* **2009**, *25*, 14155–14164.
(2) White, E. B.; Schmucker, J. A. *Journal of Fluids Engineering* **2008**, *130*, 061302.
(3) Bico, J.; Basselièvre, F.; Mermigier, M. In *Bulletin of the American Physical Society*; American Physical Society: Chicago, IL, 2005.
(4) McAlister, G.; Ettema, R.; Marshall, J. S. *Journal of Fluids Engineering* **2005**, *127*, 257.
(5) Minor, G. Experimental Study of Water Droplet Flows in a Model PEM Fuel Cell Gas Microchannel. MASc, University of Victoria, 2007.
(6) Theodorakakos, A.; Ous, T.; Gavaises, M.; Nouri, J. M.; Nikolopoulos, N.; Yanagihara, H. *Journal of Colloid and Interface Science* **2006**, *300*, 673–687.
(7) Njifenju, K.; Bico, J.; Andrès, E.; Jenffer, P.; Fermigier, M. In *Bulletin of the American Physical Society*; American Physical Society: Minneapolis, MN, 2009; Vol. Volume 54, Number 19.
(8) Antonini, C.; Innocenti, M.; Horn, T.; Marengo, M.; Amirfazli, A. *Cold Regions Science and Technology* **2011**, *67*, 58–67.
(9) Schmucker, J. A.; White, E. B. *Journal of Fluid Mechanics* **2013**, *In Revisions*, 26 pages.
(10) Antonini, C.; Carmona, F. J.; Pierce, E.; Marengo, M.; Amirfazli, A. *Langmuir* **2009**, *25*, 6143–6154.
(11) Li, X.; Pozrikidis, C. *Journal of Fluid Mechanics* **1996**, *307*, 167–190.
(12) Jones, J. L.; Lal, M.; Ruddock, J. N.; Spenley, N. A. *Faraday Discussions* **1999**, *112*, 129–142.
(13) Zhang, J.; Miksis, M. J.; Bankoff, S. G. *Physics of Fluids* **2006**, *18*, 072106.
(14) Zhu, X.; Sui, P. C.; Djilali, N. *Journal of Power Sources* **2007**, *172*, 287–295.
(15) Rothmayer, A. P.; Tsao, J. C. *AIAA Paper No. 2001-676* **2001**.
(16) Tucker, V. A. *Journal of Experimental Biology* **1990**, *154*, 439–461.
(17) Abbott, I. H. *NACA Annual Report* **1932**, *17*, 583–604.
(18) Pope, A.; Harper, J. J. In *Low Speed Wind Tunnel Testing*; John Wiley & Sons Inc: New York, 1966; pp. 126–191.
(19) Desmond, G. L.; McCrary, J. A. *NACA Technical Note* **1935**, *536*, 21.
(20) Furmidge, C. G. . *Journal of Colloid Science* **1962**, *17*, 309–324.
(21) Kiya, M.; Arie, M. *Journal of Fluid Mechanics* **1975**, *69*, 803–823.
(22) Clift, R.; Grace, J. R.; Weber, M. E. In *Bubbles, drops, and particles*; Dover Publications: Mineola N.Y., 2005.
(23) Lin, Z.; Peng, X. *Heat Transfer-Asian Research* **2009**, 485–491.

Preface to Chapter 5

This chapter gives a review of the literature on oscillating drops and bubbles, focusing on models to predict the frequency of different modes of oscillation, giving a unifying framework for the analysis and understanding of the topic, presenting a full profile analysis technique for drop oscillation studies, and testing literature models with experimental data. As outlined in the thesis introduction, the oscillation of sessile drop exposed to airflow was expected to possibly affect shedding, both because drop oscillation can lead to shedding in its own right[1–7], and because the oscillation of drops could impact wake drag (see Figure 7.2 of Clift et al, and Lin and Peng[8,9]). Chapter 5 does not strictly deal with either of these topics, since it became obvious that the first point is not important in the present set of experiments, and since the second cannot be sufficiently investigated with the techniques available for this thesis. The above two issues relating oscillation to shedding are discussed below, prior to the body of Chapter 5.

The techniques to analyze the oscillation of sessile drops in cross flow are discussed in more detail in Chapter 5. Briefly, from the profile measurements discussed in Chapter 2, a trace of centroid position with time can be made, as can measurements of the instantaneous deformation of the surface away from its equilibrium profile. Fast Fourier transforms (FFT) of either signal can give measurements of the frequency and (for profile measurements) mode shape of

drop oscillations. The frequencies of centroid (roughly speaking, centre of mass) oscillations for the HD-Teflon, water-PMMA, and water-Teflon systems discussed in Chapter 2 are given in Figure P5-1 (they are also given in the main body of Chapter 5).

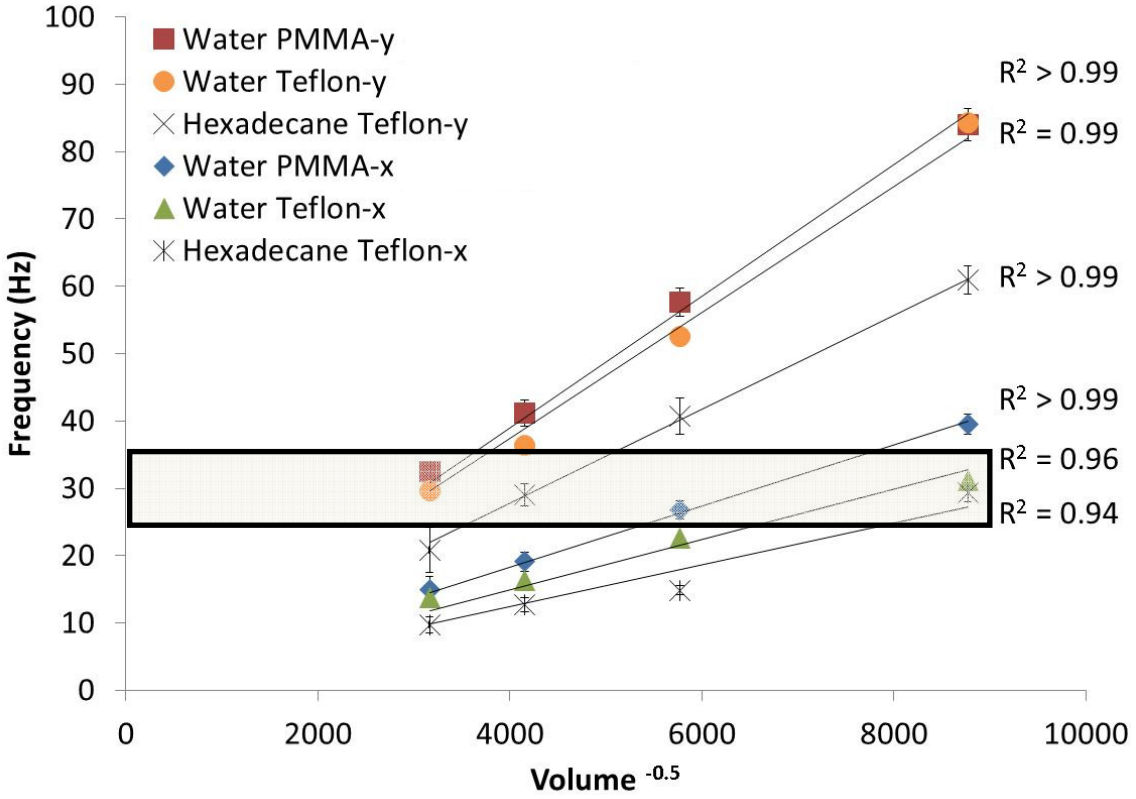

Figure P5-1: Bulk oscillation frequency versus the inverse root of volume for systems of drops of water on PMMA and Teflon, and hexadecane on Teflon under cross flowing air, with the direction of bulk (centroid) motion denoted in the legend (*x* denoting lateral (horizontal) motion, *y* denoting longitudinal (vertical) motion relative to the flat surface). Volumes shown (from left) are 100, 58, 30, and 13 µl. Error bars denote one standard deviation. Grey band is a 10 Hz window centered around 30 Hz, since 30Hz is the dominant vibrational frequency of the wind tunnel in which tests were conducted.

Also shown in Figure P5-1 is a 10 Hz wide band centered about 30 Hz. The tunnel was observed to vibrate with a dominant natural frequency of 30 Hz. As can be seen, high, medium, and low volumes of drops for all of the systems show natural frequencies close to 30 Hz. If the oscillation of the tunnel were to have an effect

on the shedding of drops, it would be most likely to affect those drops with similar frequencies. Figure P5-2 is adapted from Chapter 2 and shows the critical air velocity for incipient motion versus the inverse sixth root of volume (chosen since this dependence linearizes the curves on the semi-log plot shown). The drops with natural frequencies near 30 Hz are distinguished in Figure P5-2 by unfilled symbols, and it can be seen that the six drop volumes in question (two for each system) display critical air velocities for shedding in line with drops for which the natural frequency of oscillation is far from the tunnel's vibration frequency of 30 Hz. This indicates that the ambient tunnel vibrations do not affect drop shedding. Higher amplitude and/or frequency of forcing may affect shedding[10], but it was decided that such energy intensive, large disturbances to the environment of the drop would not be investigated in this thesis.

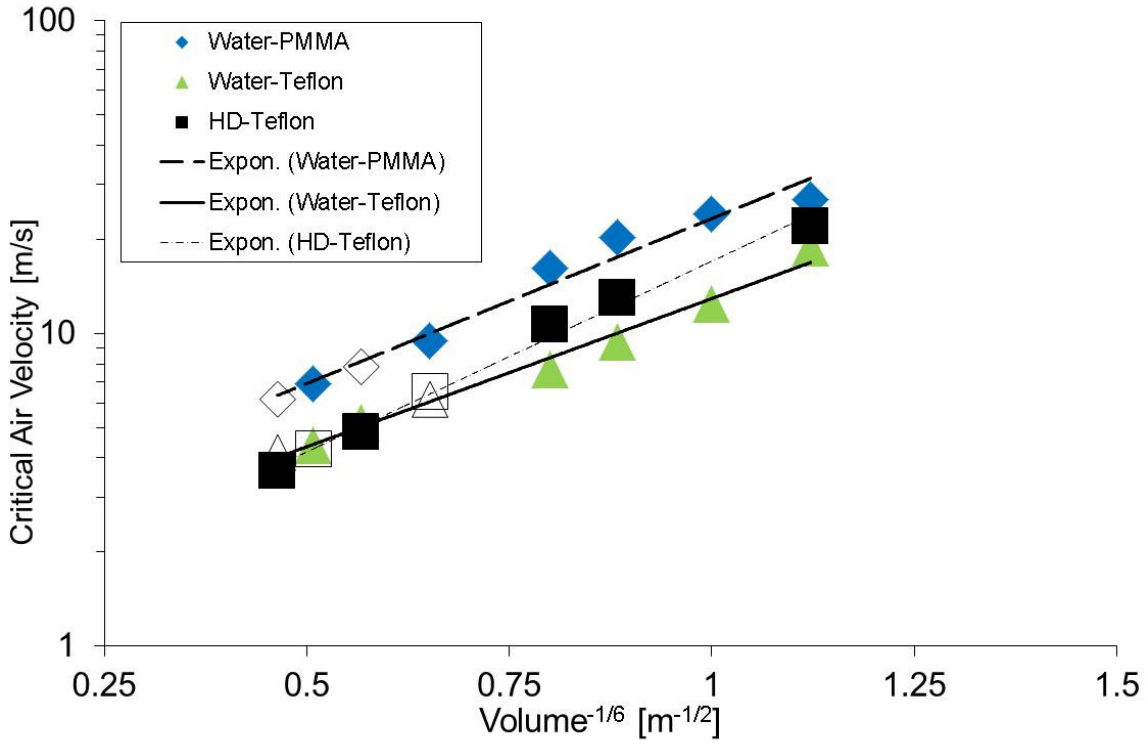

Figure P5-2: Critical air velocity for incipient motion versus inverse 6th root of volume. Data adapted from Chapter 2. Unfilled symbols indicate volumes for which drops of that system have natural frequencies of oscillation near the tunnel's dominant vibrational noise at 30 Hz. Volumes shown (from left) are 100, 58, 30, 13, 3.8, 2.1, 1, and 0.5 µl. Standard deviation within symbol size.

The other direct influence of sessile drop oscillation on incipient motion and shedding by cross flow is the possible coupling of the oscillating drop into the wake, increasing wake drag (see Figure 7.2 of Clift et al, and Lin and Peng[8,9]). The water-PMMA system showed the most marked increase in drag coefficient with Reynolds number (an indication of oscillations affecting wake drag, as discussed in Chapter 4). While the Reynolds number for the onset of drop oscillation does seem to correspond to the Reynolds number at which drag coefficient increases for water-PMMA, the lack of multiple systems to test, and uncertainties in the data as to the exact point of onset for oscillations means that no concrete conclusions can be drawn. This topic will therefore be left for future work, which

should be undertaken in a wind tunnel with decreased vibrational noise to allow for an unambiguous determination of the onset of oscillation. Tests could also be undertaken with drops pinned to the surface with chemical heterogeneities/roughness to increase the Reynolds number range of tests, thereby allowing for more observation of the increase in drag coefficient with Reynolds number (see Chapter 4).

In order to prepare for these future tests, a better understanding of the oscillation of sessile drops in cross flowing air is desired in terms of frequencies, mode shapes, and effects of fluid properties and contact angle. In analyzing the present results, it was found that some confusion existed in the literature as to the physics governing sessile (or more generally, surface constrained) drops and bubbles. It was also found that much of the literature is diffuse and does not seem to be known to others in clear terms. Therefore, a review of literature models and the creation of a framework for understanding them was undertaken, as well as the creation of a full profile oscillation analysis technique that may be useful in the proposed future tests. These tasks are discussed in the body of Chapter 5.

Chapter 5: Understanding bubble/drop oscillations: a framework for diffuse literature, application to sessile drops in cross flowing air, and comparison of literature models[k]

5.1 Introduction

Consider a drop or bubble; as common as a drop of rain or a pot of boiling water, with applications as diverse as aerosolized medicines or floatation of metal ores. Under the influence of surface tension, drops and bubbles adopt spherical shapes if free from constraint and external forces. In contact with a surface the constrained drop or bubble forms a shape similar to a spherical cap.

Now consider the oscillations of a drop or bubble. Deformed and/or displaced, the drop/bubble is driven back towards equilibrium by a restoring force such as surface tension, gravity, etc. As will be discussed shortly, the analytic works on drop/bubble oscillation have mainly focused on wave shapes that are axisymmetric about either an arbitrary axis for a free drop/bubble, or about the normal of the solid surface for a constrained drop/bubble. Recently, the pace of applied research in drop oscillations has increased, especially for the case of

[k] A version of this chapter will be published, with co-authors A. J. B. Milne, B. Defez Garcia, M. Cabrerizo-Vílchez, A. Amirfazli. B. Defez Garcia contributed to image analysis algorithm development, M. Cabrerizo-Vílchez, A. Amirfazli acted as supervisors, making the thesis author the main contributing author in terms of data collection, reduction, analysis, and writeup. Letters of permission and support are included in Appendix A.7.

sessile drops. Perhaps due to the more rapid pace, some confusion seems apparent as to the precise physics governing drop and bubble oscillations, what models exist to describe them, and how such models should be applied (especially for non-axisymmetric oscillations). We believe the source of this confusion is twofold: first, due to misunderstanding of bulk (i.e. center of mass) oscillation and surface oscillation of drops and their connection to each other; and second, due to a lack of appreciation for the complexities of non-axisymmetric wave shapes and the three-dimensional character of the drop surface.

The literature on drop/bubble (especially sessile drop) oscillation is also diffuse, with no publication giving a categorizing framework for its understanding. Considering the diffuse nature of the literature available, and the different possible cases of drop/bubble oscillation, this chapter first presents an overview of the present understanding of drop and bubble oscillations, including mathematical models proposed to predict resonant frequencies. This overview is categorized in terms of free versus constrained drops, and in terms of axisymmetric versus non-axisymmetric oscillations, with an emphasis on sessile (surface constrained) drops. A framework for summarizing, categorizing and understanding drop/bubble oscillations is then given. A full profile processing tool for the study of free or constrained drop/bubble oscillation is introduced and its use illustrated in analyzing new experimental results for sessile drops in cross flowing air. These new results are finally combined with those from literature to test various models given in literature.

5.2 Status of Understanding in Literature

The new experimental work presented in this chapter focuses on the surface and bulk oscillations of sessile (i.e. constrained) drops driven by cross flowing air and restored by surface tension, since it is an area of interest to the authors[11]. As such, this literature review will focus on the surface oscillations of drops opposed by surface tension. Little literature was found on oscillations opposed by gravity, though what was found will be reviewed. No works were found studying pure bulk oscillations of either free or constrained drops/bubbles, likely due to their uncommon nature as will be discussed below.

5.2.1 Axisymmetric and Non-Axisymmetric Surface Oscillations of Free Drops

The oscillation of free drops (those falling/floating freely in their surroundings) has been studied since at least 1843, when Plateau reported observing them following the breakup of falling fluid streams[12]. Lord Rayleigh considered drops in vacuum, balancing surface tension and inertial forces to arrive at a formula for the frequency of axi-symmetric capillary wave oscillations of spherical drops[13]. Lord Kelvin[14] and Lamb[15] both considered oscillations balancing inertia and gravity. Gravity waves are less predominant than capillary waves for small drops as evidenced by the low Bond number (~0.14 for a 1 mm drop of water in air). Lamb also expanded the capillary analysis to drops or bubbles in an infinite medium of arbitrary density[16], and to viscous drops[15], finding that for low viscosities there is no effect on frequency. Finally, Landau and Lifshitz[17] and (briefly) Lamb[15] have considered non-axisymmetric waves. In terms of frequency,

mathematical models can be categorized by whether the restoring force for oscillations is surface tension or gravity based. For surface tension restored oscillations, drop/bubble oscillation models take the form of:

$$f_{ml} = \frac{1}{2\pi}\sqrt{\frac{\gamma}{\rho_1 V \lambda_{ml,\gamma}}} \qquad \text{Equation 5-1}$$

where f_{ml} is the ordinary frequency (in Hz) of an oscillation mode of degree l and order m, γ is surface tension, ρ_1 is the density of the drop/bubble, V is the volume of the drop, and $\lambda_{ml,\gamma}$ is the eigenvalue of a surface tension based drop oscillation mode of degree l and order m (a mode m-l oscillation). We give Equation 5-1 in terms of volume here, since the radius of the drop is poorly defined for a non-spherical (cap) drop shape, and to allow comparison of frequencies for constrained drops of the same volume with different contact angles.

The concept of oscillation eigenvalues will be used throughout this paper since most models for drop/bubble oscillation follow the same general form. The eigenvalue technique acknowledges the similar physics governing drop/bubble oscillations in multiple cases, and facilitates comparison between the models. The eigenvalue depends on degree and order number, as stated, and can also depend on fluid properties, contact angle or constraint type for constrained drops and bubbles. The eigenvalue does not depend on surface tension, γ. The subscripted γ in Equation 5-1 instead denotes the deformations are restored by a surface tension derived force.

For free drops/bubbles undergoing small amplitude oscillations about a spherical shape, eigenvalues are given by[16,18]:

$$\lambda_{ml,\gamma} = \frac{3\left(\left(l+1\right)+\left(\rho_2/\rho_1\right)l\right)}{4\pi\ l\left(l-1\right)\left(l+1\right)\left(l+2\right)} \qquad \text{Equation 5-2}$$

where ρ_2 is the density of the fluid surrounding the drop/bubble. Equations 5-1 and 5-2 combined return the formulae originally derived for drops[13,15–17] and bubbles[16] by substituting $\rho_2 = 0$ and $\rho_1 = 0$, respectively.

Equation 5-2 is derived from first principles by considering each oscillation mode as a spherical harmonic and using the properties of the related associated Legendre polynomials. Non-axisymmetric modes correspond to non-axisymmetric (i.e. tesseral or sectoral) spherical harmonics, resulting in parts of the drop oscillating non-axisymmetrically. As Equation 5-2 shows, these non-axisymmetric modes are degenerate, in that they have the same frequency as the axisymmetric (zonal spherical harmonic) oscillations (i.e. the eigenvalue does not depend on order, m). Equation 5-2 also shows that mode m-0 is not allowed for drops since it would equate to volume change of an incompressible fluid; it is, conversely, allowed for bubbles. Mode m-1 is not allowed for either free drops or free bubbles since it would amount to movement of the bulk of the drop without any surface distortion, and therefore without any restoring force. It can thus be stated that surface oscillation of a free drop/bubble is generally decoupled from oscillation/motion of the bulk of the drop/bubble.

Subsequent researchers have advanced the field with consideration of higher viscosity inner and outer fluids (see, e.g., Morrison et al.[19] and Miller and Scriven[20], the references therein, and references in Bauer and Chiba[21]). Others have examined the combined effects of capillarity and electromagnetism[13,19], indicating that electromagnetic forces can affect (generally decreasing) the restoring force of oscillations. Non-spherical (but still axisymmetric) equilibrium drop shapes have also been considered[22–24]. Finally, large amplitude (non-linear)[24–27] axisymmetric and non-axisymmetric drop oscillations have been researched. It is suggested, at least at higher oscillation magnitudes, that the axisymmetric mode shapes are unstable, tending toward non-axisymmetric modes[27]. Natarajan and Brown[26,27] have also studied resonant energy transfer between different axisymmetric and non-axisymmetric modes of oscillation, something which in general depends on the higher order (non-linear) terms describing drop oscillation.

Consider now when gravity is the restoring force for oscillations. Then free oscillation models take the form of[14,15]:

$$f_{ml} = \frac{1}{2\pi}\sqrt{\frac{g}{R}\frac{1}{\lambda_{ml,g}}} \qquad \text{Equation 5-3}$$

where g is gravity, R is the radius of the sphere/spherical cap made by the drop, and $\lambda_{ml,g}$ is the eigenvalue of an gravity based drop oscillation mode of degree l and order m, which depends on contact angle/constraint type for constrained drops. The subscript, g, indicates that gravitational forces are involved in the

oscillations, but does not imply a functional dependence of the eigenvalue on the magnitude of the gravitational acceleration. For free drops oscillating axisymmetrically, the eigenvalues are given by:

$$\lambda_{ml,g} = \frac{2l(l-1)}{2l+1} \qquad \text{Equation 5-4}$$

Equation 5-4 is again derived from first principles by considering spherical harmonics. Non-axisymmetric modes have been very briefly considered[15], with the indication being that they are degenerate (meaning that Equation 5-4 should be valid for any value of m). Again, one can see in Equation 5-4 that modes m-0 and m-1 are forbidden for free drops. Equation 5-4 was derived for drops in a vacuum. No works have been found for gravitationally restored oscillating bubbles, nor have many further works been found considering free, or constrained, oscillation of drops restored by gravity. This is likely because gravitational forces are not usually important for drops or bubbles, as indicated by the generally low Bond number.

Regardless of the governing model, in terms of applications, researchers have considered shifts in scattered electro-magnetic radiation from oscillating drops[28], and generation of electro-magnetic radiation by oscillating charged drops[29]. Oscillating drops have also been used as a means of measuring viscosity[30] and surfactant concentration/dynamic surface tension[31], to give but two examples. Considering the long history of their study, and the advancements that have been made in studying ranges of viscosities, densities, and magnitudes of oscillations, the understanding of free drop and bubble oscillations can be considered

advanced at this point, and will be left at this stage for the remainder of this chapter.

5.2.2 Axisymmetric Surface Oscillations of Constrained Drops

While the oscillation of free drops has a long history, the study of constrained drop oscillations is significantly younger. In 1979, Rodot et al. seem to have been the first to report observations for a drop constrained to the end of a rod, forced to oscillate axisymmetrically in a fluid of matched density to remove the effects of gravity and study pure surface tension restored oscillations[32]. They did not attempt to present a mathematical model for their results.

No closed form, analytic, first principles eigenvalues equations exist in literature for constrained drops. Several researchers[18,21,33–39] have produced infinite summation formulae to calculate eigenvalues and frequencies for various modes (including non-axisymmetric modes[34–37]) and various contact angles/kinds of drop constraints. Frequencies and/or eigenvalues are tabulated/graphed in the original references[18,21,33–39] and by Smithwick and Boulet[40] and Yamakita[41]. These results will not be repeated here, but the works will be reviewed below, first in terms of their combined findings, followed by reviews of their individual works. Their models will be compared to experimental results in Section 5.5.

All previous researchers[18,21,33–40] found that constraining the drop increases the frequency of oscillation for each mode compared to a free drop (as long as the

drop is not a hemisphere with a completely free contact line as in Chiba et al.[35]). The amount of increase is dependent on contact angle and mode. The solid support also allows a lower frequency mode of oscillation equivalent to the forbidden first harmonic for free drops and bubbles. This is because, for constrained drop/bubble oscillation, surface oscillation is generally coupled to oscillation of the center of mass. This can be understood conceptually by simplifying a constrained drop to a cup of liquid. As illustrated in Figure 5-1, for such a system all modes of surface oscillation must displace the bulk of the liquid. Thus, as the surface modes oscillate with their characteristic frequencies, the bulk of the liquid mass will oscillate with the same frequency. This generally holds for all modes, indicating that for constrained drops and bubbles, bulk and surface oscillations are generally coupled.

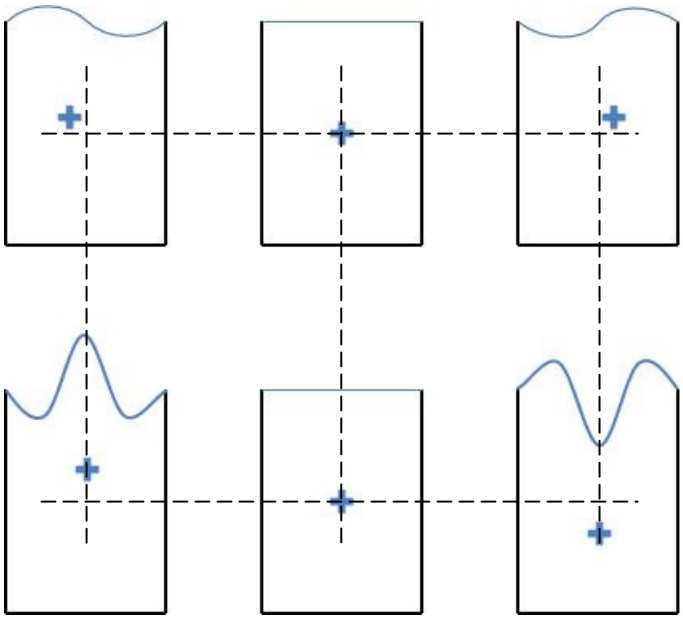

Figure 5-1: Illustration of oscillations occurring in a cup of liquid. The surface oscillation modes all require an oscillation of the center of mass, at the same frequency as the surface oscillation.

All previous researchers[18,21,33–40] also found that each mode of a constrained drop corresponds to a summation of multiple Legendre polynomials[37,38]. This is in contrast to the oscillation of free drops, for which each mode corresponds to a single Legendre polynomial. Below, we review the abovementioned works individually.

Strani and Sabetta were the first to perform a mathematical analysis of constrained drop oscillations, producing an analytic model of Rodot et al.'s work by balancing capillarity and inertia in a similar manner to Rayleigh for spherical drops, oscillating axisymmetrically, but constrained by solid spherical cap bowls of the same radius as the unperturbed drop[18]. Changing the bowl angle thus simulates different contact angles of a drop on a flat surface, though with an extra mass of liquid in the depression of the bowl and a different boundary condition from that which would exist if there was a flat surface beneath the drop. Strani and Sabetta's analytic model agreed well with Rodot et al.'s, experimental results. They found the same relation for drop oscillations as given in Equation 5-1. Also, the infinite series solution they presented for the eigenvalue simplifies to Equation 5-2 for the case of 0° bowl angle (180° contact angle, i.e. a free drop). Watanabe produced a similar model for the axisymmetric oscillation of drops on flat surfaces[33] which also showed good agreement with Rodot et al. and gave very similar results to the model of Strani and Sabetta. This indicates that models for constrained drop oscillations may be insensitive to the precise geometry (e.g. bowl or flat) of the solid under the drop.

One should note that there is a slight typographic error in Strani and Sabetta, which Smithwick and Boulet corrected[40]. Smithwick and Boulet also tabulated approximate results of the infinite summations outlined in Strani and Sabetta and found good agreement between calculated and measured frequencies for mercury drops sessile on flat surfaces, within a small range of contact angles from 128.6° to 139.1°.

Further advancements have been made by Bauer and Chiba[34] and Chiba et al.[37], who performed a similar analysis to Strani and Sabetta, but for many more types of geometric constraints on the drop such as paired spherical bowls, drops surrounding a spherical shell, and most recently[37] drops constrained with their centers of curvature at the apex of conical solid bodies or conical valleys. Drop shapes from some of their models are thus somewhat similar to the range seen for sessile drops on flat surfaces, but with either valleys or protrusions through what would be the solid flat base of a sessile drop on a flat surface. They did not compare any of their models to experimental results. Further, Bauer and Chiba's results for axisymmetric oscillations of a drop in a single spherical bowl seem suspect since they predicted practically identical frequencies for non-axisymmetric oscillations of the same system. This contradicts their later work[37] and, as will be discussed in Section 5.2.3, is unlikely to be correct.

A selection of images from Chiba et al[37] are reproduced in Figure 5-2. The leftmost (mode 0-1) illustrates the first axisymmetric mode. The middle image (mode 1-1) illustrates the first non-axisymmetric mode (a so called 'bending'

mode described by Lyubimov[36], to be discussed in more detail in Section 5.2.3). The rightmost (mode 2-1) is another non-axisymmetric mode which we will later argue is observed in our experimental data. It can be seen in Figure 5-2 that each surface oscillation shown would correspond to a bulk oscillation of the drop's center of mass, as illustrated previously in Figure 5-1.

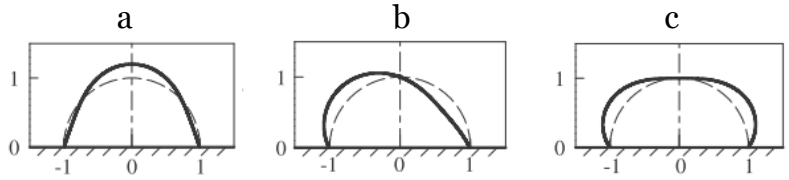

Figure 5-2: Oscillation modes of, (a) degree 0 and order 1, (b) degree 1 and order 1, and (c) degree 2 and order 1. Diagrams are taken from Figures 5, 7, and 9, respectively, of Chiba et al.[37], with permission for use of this copyrighted work given by the publisher as noted in Appendix A.7.

The above reviewed studies considered purely surface tension restored axisymmetric oscillation of constrained drops. However, only three sets of data have been used to test these models[32,40,41]. The first data set[32] considers a wide range of contact angles, but only for the case of drops in a matched density fluid (which, based on Equation 5-2, would be expected to change frequencies significantly compared to drops in air). The agreement between this data set and the models adjusted to the matched density system it represents is reasonable, but not perfect[18,33]. The later experimental works[40,41] each consider small ranges of contact angles. They each found good agreement with the model developed by Strani and Sabetta[18], expressed for drops in a vapor. Thus, while the evidence suggests at least one of these models is accurate, they should still be tested against larger combined data sets for drops in air/vapor to ensure that the model of Strani and Sabetta was applied correctly. Futher, the models should be compared against each other in order to validate them. Neither the Bauer and

Chiba[34] nor Chiba et al.[37] models seem to have been tested experimentally in any way, nor have they been tested against other proven models.

Notwithstanding the need for further validation, the advanced state of modeling of constrained simple inviscid drops and bubbles has led researchers to advance their analysis to the more complex cases of viscous drops, higher amplitude oscillations, and moving contact lines, as discussed below. It should be noted that calling drops with mobile contact lines 'constrained' is perhaps not completely accurate since the contact lines can move, but the term shall be retained here to denote that the drops still interact with a solid body over part of their surface.

Strani and Sabetta have expanded their analysis to include mild viscous effects, finding little effect on frequency and mode shapes, but effects on the damping of oscillations[38]. Bauer and Chiba also expanded their analysis by considering the effects of viscosity[21], with similar findings to Strani and Sabetta. Other researchers have studied the effects of larger viscosity with finite element analysis FEA[42–44]. The first study[42] compared their FEA results with experimental runs, finding good agreement. The last two studies[43,44] also examined large amplitude oscillations, finding changes in the oscillating frequency for large viscosities and/or amplitudes. Large amplitude sessile drop oscillations have also been studied experimentally[45], with findings that as the forcing amplitude increases, the contact line becomes unpinned and oscillates, and that non-axisymmetric modes of surface oscillation appear, eventually leading to the breakup of the drop.

The group of Chiba et al. have also considered the coupled system of a drop on an oscillating cantilever, numerically solving an eigenvalue problem to study inviscid hemispherical drops with contact lines that are free to move[35]. The discussion of drop-cantilever coupling is beyond the scope of this chapter, but their findings of drop oscillations matched theory for free drops closely (since an inviscid hemispherical drop with a free contact line is a precise model of half of a free drop). More advanced research has included contact line dynamics by means of the Hocking condition[39,46], but again only for hemispherical inviscid drops. It was found that a moving contact line decreases the oscillation frequency, and changes mode shapes. The stick-slip behavior of a contact line undergoing Hocking-like motion was also seen to dissipate energy from an oscillating drop even in the inviscid case.

Despite the relatively advanced state of knowledge of axisymmetric constrained drops oscillations, full models still require the use of infinite series to calculate eigenvalues. Because of this, other researchers have made various simplifications to present closed form models for drop oscillation[47–49]. Perez et al. modeled the first axisymmetric mode for a sessile drop, flattened by gravity, with a free "contact line"[47] caused by levitating the drop on a gas layer. Thus the mode should correspond to mode 0-1 with a slipping contact line. They presented an empirical relation for the eigenvalue as:

$$\lambda_{01,\gamma} = \frac{1}{6} f(R) \qquad \text{Equation 5-5}$$

where $f(R)$ is an ad hoc function of the various radius measurements of the deformed drop and the factor of 1/6 is a fitting parameter, ensuring excellent agreement with experiment. They also presented a model based on a variational approach, namely:

$$\lambda_{01,\gamma} = \frac{1}{\partial^2 S / \partial R_p^{\,2}} \approx \frac{5}{16\pi} \qquad \text{Equation 5-6}$$

where S is the surface area of an ellipsoid approximating the drop shape, and R_p is the minor axis of the ellipsoid. Neglecting higher order terms allowed them to approximate this function as $\lambda_{01,\gamma} \approx \frac{5}{16\pi}$ for nearly spherical drops. Equation 5-6 was found to fit data fairly well when accounting for the higher order terms at large volumes, but poorly at low volumes. Further, neither Equation 5-5 nor 5-6 can in fact be used as a general model, since a levitated drop has a contact angle of 180° while in general a constrained drop can take any contact angle. Perez et al. did not allow for a dependence on contact angle in their model.

Noblin et al. have considered drops sessile on flat surfaces, excited longitudinally[48,49]. They have developed a theory based on the planar 1-D gravity-capillary wave formula, using an assumed average wavelength found by dividing the arc length of a profile view of the drop into an integer number, n, of half wavelengths. Considering both pinned and freely oscillating contact lines they found reasonable agreement in the limited range of contact angles considered. They found poorer agreement for lower mode number, and better agreement for higher modes; however, as Vukasinovic noted[45], any model (even Equation 5-2 of

Lamb for free drops) will give reasonable results for constrained drops as mode number increases. The relation Noblin et al. gave[48,49] can be expressed as the eigenvalue function:

$$\lambda_{n,\gamma g} = \frac{1}{\left[\frac{ng\pi\rho V}{2\gamma\theta R} + V\left(\frac{n\pi}{2\theta R}\right)^3\right]\tanh\left[\frac{n\pi}{2R\theta}h_{ave}\right]}$$

$$f_{n,\gamma g} = \frac{1}{2\pi}\sqrt{\left[\frac{ng\pi}{2R\theta} + \frac{\gamma}{\rho}\left(\frac{n\pi}{2R\theta}\right)^3\right]\tanh\left[\frac{n\pi}{2R\theta}h_{ave}\right]} \qquad \text{Equation 5-7}$$

$$R = \left(\frac{3V}{\pi\left(\cos^3\theta - 3\cos\theta + 2\right)}\right)^{1/3}$$

where $\lambda_{n,\gamma g}$ is the eigenvalue of an oscillation mode of 'mode n' and θ is contact angle. The hyperbolic tangent term exists to attempt to account for the finite height of the drop (captured by some average height, h_{ave}). Equation 5-7 is given with respect to drop spherical cap radius, R, rather than only volume, V since the equation in terms of volume is needlessly complex. The equation for ordinary frequency, $f_{n,\gamma g}$ (in Hz) is given for clarity. Equation 5-7 is also given in terms of n, while Noblin et al. originally derived their equation with respect to j, one half the number of nodes along the drop profile[48,49]. The use of n (with $n = 2j - 1$) follows Sharp et al.[50], who performed a similar analysis to Noblin et al., but for non-axisymmetric oscillations. The work of Sharp et al.[50] will be discussed with other non-axisymmetric models in Section 5.2.3.

Neither the use of n nor j as a mode numbering scheme completely accounts for the three-dimensional nature of oscillations. As discussed earlier, non-

axisymmetric oscillations involve both a degree and order number (l and m, respectively), which cannot be mapped to values of n. There is thus a fundamental concern regarding the applicability of Equation 5-7. However, the experimental work to be presented in this paper will be used to test Equation 5-7 in the manner prescribed in the original works[48–50] (i.e. determining n directly from consideration of the profile view).

In summary, the axisymmetric oscillation of constrained drops is relatively well understood. It has advanced far enough, for example, that recent research looks at systems of pendant and sessile drops coupled by a hole through a surface[51] (with the anticipated application of fast variable focus lenses for cameras). Further research applying drop oscillations include measuring contact angle[41,52] or evaporation rate[53] using axisymmetric oscillations of sessile drops. Forcing sessile drops (or Whilhelmy plate menisci) to oscillate to relax them into their most stable contact angle has also been investigated[1–3,5–7,54], as has oscillating drops to transition them between the Wenzel and Cassie states[55,56]. One major application of oscillating sessile drops is promoting or inducing motion of the drop along the surface either by axisymmetric[57] or non-axisymmetric[57–59] oscillations of a drop on a surface with an incline[58] or a surface energy gradient[57,59], or by means of non-symmetric wave forms along a surface without a surface energy gradient[57,58,60–62]. Considering all of the above, the understanding of axisymmetric constrained drop oscillations is considered relatively advanced in this paper. Regardless, the models will be tested against each other, and against experimental data.

5.2.3 Non-Axisymmetric Surface Oscillations of Constrained Drops

Concomitant to the study of constrained drop axisymmetric oscillations has been a (less vigorous) study of non-axisymmetric oscillations (i.e. those with non-zero order number). These were first observed by Bisch in 1981, who laterally forced a rod on which a drop was suspended in a matched density liquid[63]. He thus considered surface tension restored oscillations with the effects of gravity 'canceled' by buoyancy. He found that non-axisymmetric modes have lower oscillation frequencies compared to the axisymmetric modes he also observed[63]. Bisch did not present a mathematical model.

Compared to the models for axisymmetric oscillations, there have been fewer research groups[34–37] that have produced first principles infinite summation formulae to calculate eigenvalues and frequencies for non-axisymmetric modes of constrained drop oscillation. Similar to axisymmetric models, values are graphed and tabulated in the references[34–37]. These models will be compared to experimental data in Section 5.5, but the works will be discussed now. Lyubimov et al.[36] modeled the non-axisymmetric spherical harmonic oscillations of an inviscid hemispherical drop (i.e. equilibrium shape contact angle fixed at 90°) on a flat surface with a contact line constrained by the Hocking condition. They found a breaking of the degeneracy of non-axisymmetric modes for pinned or partially pinned contact lines (i.e. they found that non-axisymmetric oscillation frequencies depended on the order number (the amount of non-axisymmetry)).

This differs from free drops and bubbles, for which non-axisymmetric modes had the same frequencies as axisymmetric modes. For fully free contact lines, Lyubimov et al.[36] found that non-axisymmetric modes were degenerate. This is not surprising since a drop with 90° contact angle and a free contact line behaves precisely like half of a free drop. They also found a low order mode (the first non-axisymmetric mode of degree one and order one (mode 1-1, see Figure 5-2)) which they termed a "bending" mode. This mode was present for sufficiently pinned contact lines, but absent for free contact lines since it would equate to lateral motion of the drop without any surface deformation/restoring force. This is a similar concept to the low frequency mode for axisymmetric constrained drops first found by Strani and Sabetta[18], which is absent for free drops for the same reason. In the case of Lyubimov et al., however, the "bending" oscillation is at an even lower frequency, and is itself a non-axisymmetric subset of the mode found by Strani and Sabetta that requires both contact on a solid body and a sufficiently pinned contact line. Lyubimov et al. did not compare their model to experimental data.

Bauer and Chiba advanced the theory of non-axisymmetric constrained drop oscillations by considering drops in spherical bowls of arbitrary half-angle, oscillating both non-axisymmetrically and axisymmetrically for various mode numbers[34]. Their model gave frequencies practically identical for non-axisymmetric and axisymmetric modes. This unexpected result[36,37,40,63] contradicts their later work, and other works, and is thus suspect. Chiba et al. also studied the oscillation of hemispherical drops with free contact lines coupled

to an oscillating beam[35]. Similar to Lyubimov et al., Chiba et al[35] found that the non-axisymmetric modes were degenerate, not surprisingly since the hemispherical drops have a free contact line and are thus effectively half of a free drop. One should note in reading Chiba et al[35] that they follow a different numbering scheme for their modes, which, for example, means that the bottom row of their Figure 2 (labled as the first mode) displays modes 0-2, 1-1 and 2-2 according to the numbering used in this chapter. They present three dimensional simulations in their Figure 2, showing some possible non-axisymmetric mode shapes. Neither model has been compared to experimental data.

Most recently, Chiba et al. have modeled drops with a 90° contact angle, constrained with their centers of curvature at the apex of a conical solid body with either a pinned or freely moving contact line[37]. The half-angle of the cone was varied from near 0° (a deep valley filled with liquid) to near 180° (a tall thin spike with the nearly spherical drop centered on its apex). Drop shapes are thus somewhat similar to the range seen for sessile drops on flat surfaces, but with either a conical valley or spike instead of a flat surface. They allowed their drops to oscillate axisymmetrically or non-axisymmetrically. They followed the same numbering scheme for modes as Chiba et al[35], finding that the lowest mode of nonaxisymmetric drop oscillation has a frequency ~1/2 lower than the corresponding axisymmetric oscillation (though the ratio depended on contact angle). This can be taken as confirmation and expansion of Lyubimov's finding[36] that the degeneracy of the non-axisymmetric modes is broken for all cases of

pinned contact line, and all cases of slipping contact line except for 90° contact angle on a flat plate.

Chiba et al.'s 2012 findings[37] for a slipping contact line on a 90° half-angle cone (i.e. a flat plate with 90° contact angle) matched their 2006 work[35]. The similar cases of pinned oscillations on the cone structure[37] and the spherical cap bowl structure[34] gave similar, but not identical frequencies for non-axisymmetric modes. However, there is a discrepancy with the same work[34] for axisymmetric modes (which found practically identical frequencies for non-axisymmetric versus axisymmetric oscillations[34] compared to frequencies ~1/2 lower[37]). This may be due to the difference in geometry, but is more likely a mathematical error in the earlier work[34]. The 2012 model of Chiba et al.[37] was again not compared to experimental measurements.

Perhaps due to the dearth of first principles models, their limited range of applicable contact angles[35,36], or the problems inherent in some of them[34], several research groups have searched for simpler models of surface tension restored drop oscillations. Another possible reason for researchers seeking for simpler models might be the relative obscurity of the works[34–37]; the fact that they have been little referenced in the literature suggests that researchers are not aware of their existence/applicability, which this present review will hopefully address. Regardless of the cause, researchers have attempted to form simpler models of non-axisymmetric constrained drop oscillation as discussed below.

Smithwick and Boulet found similar results to Bisch[63], i.e. lowered frequencies for non-axisymmetric versus axisymmetric oscillations, for their experimental study of microscopic drops of mercury condensed inside an evacuated cuvette[40]. They tried to explain their non-axisymmetric results using a simplified form of the polygonal oscillation theory presented by Takaki and coworkers[64–68]. Smithwick and Boulet noted that the application of this theory is non-ideal due to the extreme deformation of the drops studied by Takaki and coworkers[64–68]. In addition, they arbitrarily considered the difference in frequencies instead of the frequencies themselves to improve the fit of the model across part of the small range of contact angles studied (128.6° to 139.1°). Also, the model was simplified to the point that the eigenvalue consisted of a simple constant factor that increased with mode number independent of contact angle. Considering that the model of Takaki and coworkers is designed for extremely large (up to 1.7 cm diameter), and extremely deformed 'puddles' of liquid (with mobile[64–67] or pinned[68] contact lines), their models will not be considered in this paper. If one attempts to expand their analysis to non-flattened drops, additional terms containing the drop radius are needed. This violates the ultimate dependence of frequency on drop size/volume (as seen in Equation 5-1), and may explain some of the errors Smithwick and Boulet[40] found in applying the model. Takaki and co-workers themselves noted that their model should only be applied to gravity flattened 'puddles'.

Instead of modeling the dynamics of constrained drop oscillations, Celestini and Kofman took a different approach to modeling 'lateral' (non-axisymmetric)

sessile drop oscillations[69]. Looking only at the lowest frequency 'bending' mode (mode 1-1), they modeled dynamic drop motions as equivalent to the static drop deformations caused by changing the direction of gravity (i.e. by tilting the plate on which the drop rests). They found reasonable agreement for various drop sizes within a small range of contact angles around 130°, but did not investigate how their model (presented for contact angles between 90° and 180°) performed for drops of different contact angle. Their model for the eigenvalues is:

$$\lambda_{11,\gamma} = \frac{1}{2\pi(1-\cos\theta)h(\theta)} \qquad \text{Equation 5-8}$$

where $h(\theta)$ is a function (graphed in their paper[69]) of the contact angle of the drop. The additional term involving the contact angle, θ, comes from the equations for the surface area and volume of a spherical cap.

Similar to the model of Noblin et al. for axisymmetric oscillations[48,49], Sharp et al. have modeled sessile drops oscillating in mode 1-1, comparing their model to drops excited by a laterally directed single pulse (a puff) of air[50]. They experimentally tested a wide range of contact angles, but did not consider the effects of gravity. As with Noblin et al.[48,49], Sharp et al.[50] approximated the three dimensional drop oscillation (fully three dimensional in this case due to the non-axisymmetry) using the one-dimensional wave equations and an average wavelength assumed to be equal to the arc length of the drop divided into a number of half-wavelengths. With an additional fitting parameter, they claimed good agreement between experiment and model, but as will be examined in Section 5.5, this model does not fully capture the behavior of the drops.

Moving further from the basis of the capillary wave equation, Esposito et al.[70] formed a model based on a simple oscillator formula for water drops on a model fuel cell gas diffusion membrane. They found reasonable agreement in terms of trend, but did not apply their model to drops with different contact angles or modes of oscillation. Esposito et al. supposed that the eigenvalue would be based on the drop curvature[70]. Approximating the curvature of the drop by measuring the cross sectional curvature and approximating the out of plane component based on the surface area to arc length ratio for a sphere, they proposed (for a single value of contact angle) that mode 1-1 follows:

$$\lambda_{11,\gamma} = \frac{1}{3.12}$$ Equation 5-9

Attempting to expand Equation 5-9 to different values of contact angle (by considering the curvature of drops with different contact angles, one discovers that additional terms containing the drop radius are introduced. This would change the ultimate dependence of frequency on drop size/volume (violating the assumption of surface tension restored drops). This in turn means that the model of Esposito et al., while perhaps tuned to their single value of contact angle, cannot be applied in general.

Finally, perhaps unaware of the models that exist, several groups[58,59,62,71,72] have attempted to use Lamb's model for the axisymmetric oscillation of a free drop for sessile drops undergoing non-axisymmetric (or sometime axisymmetric) oscillations. Not surprisingly, they have found that the trend (a dependency on

the square root of surface tension divided by density and drop size) is correct. Otherwise, the application of Lamb's model to these cases is uncalled for due to the differences in geometry and oscillation modes, and the effects of contact angle. This criticism is not meant to diminish the excellent CFD[58], experimental work[71], measurement technique developement[72], and application to 'ratcheting' drops along surfaces[58,59,62] outlined in the respective papers. Some of the above works noted the approximations inherent in their approach to modeling.

To summarize, the oscillation of constrained drops excited laterally is somewhat understood, but the non-axisymmetry introduces new complexities related to the 3-D nature of the drop, which are not fully explored. Specifically lacking is a model similar to Chiba et al.'s[37] for a drop of arbitrary contact angle on a flat surface (which will not be attempted here). There has also been no study of non-spherical cap equilibrium drop shapes/an investigation of possible effects of type of forcing. Most previous works have considered mechanically excited surfaces/deformed drops. One work investigated sessile drops in a cross flow[70], and this field is one of the authors main areas of interest[11], but it is uncertain if the forcing by airflow and deformation of the equilibrium shape would change oscillation behavior.

Further, none of the first principles[34–37], semi-empirical[69,73], or low order[40,48–50,70] models available have been tested with rigorous experiments for a wide range of contact angles, fluid properties, etc. There is also some confusion in the literature as to the fact that constrained drop oscillations that involve surface deformations

must involve center of mass displacement for each mode. There is further confusion as to the relation between axisymmetric and non-axisymmetric oscillations of free and constrained drops in that some researchers have tried to use a given model in situations where it is not applicable.

As a final note, like all drops and bubbles, constrained drops undergoing oscillations can be restored by forces other than surface tension. Gravity has been considered as the restoring force for non-axisymmetric constrained drop oscillations. Moon et al.[73] exposed a pendant drop to an *external* gravitational field and acoustically driven oscillations. The drop swung like a pendulum, with the same $\sqrt{g/R}$ dependence as for Equation 5-3 (which considered free drops undergoing self-generated gravity restored oscillations). An eigenvalue for the situation studied by Moon et al. can be expressed as:

$$\lambda_{ml,g} \approx 0.151 \qquad \text{Equation 5-10}$$

In Moon et al.[73], the frequency of oscillation was found to be even lower than that of surface tension restored oscillations of the same drop (which they also investigated somewhat). However, the ranking of frequencies, in general, would depend on surface tension, density, and drop shape. The gravity restored oscillations of Moon et al. are of further interest since they illustrate a case of constrained drops undergoing mostly bulk oscillation as opposed to the more commonly observed surface oscillations linked with bulk oscillations (see Figure 5-1). For extremely small solid constraint areas, a pendant system oscillating as a

pendulum could almost completely decouple bulk oscillation from surface oscillation. However, as Chiba et al. explained[37], for a pinned contact line even infinitesimal constraints on the drop can cause a slight but not vanishing deviation in the frequency and mode shape of a constrained drop which is approaching the free state. In other words, as the constraint size approaches zero, the limit of the constrained drop oscillation is not the same as free drop oscillations, at least for some modes of oscillation. In general then, a constrained drop should be thought of as having bulk and surface oscillations coupled, as Dong et al. acknowledge[58].

Having reviewed the literature, we next present a framework for categorizing and understanding free and constrained drop/bubble oscillation. We then introduce in Section 5.4 a full profile measurement technique which we think is useful since in all of the works discussed above (with a few exceptions[43,45,49]), experimental measurements have largely been limited to point measurements (e.g. the center of mass, or the apex position) instead of full profile measurements. This is despite the fact that oscillations generally involved surface deformations and the related motion of the center of mass. Collected literature data and the new experimental data are then compared to literature models to test their effectiveness.

5.3 Conceptual Framework

The framework is shown graphically in Figure 5-3. To begin considering drop/bubble oscillations, one first needs to consider the source of the oscillation. The oscillation can be driven (forced) by an oscillating body force and/or an

oscillating surface force. Alternatively, natural oscillations can be due to drop/bubble displacement from an equilibrium position (e.g. motion away from a potential minimum in a gravitational, electromagnetic, or acoustic pressure field) or due to drop/bubble deformation from an equilibrium shape. One also needs to consider the restoring forces, whether they be surface tension, gravity, etc.

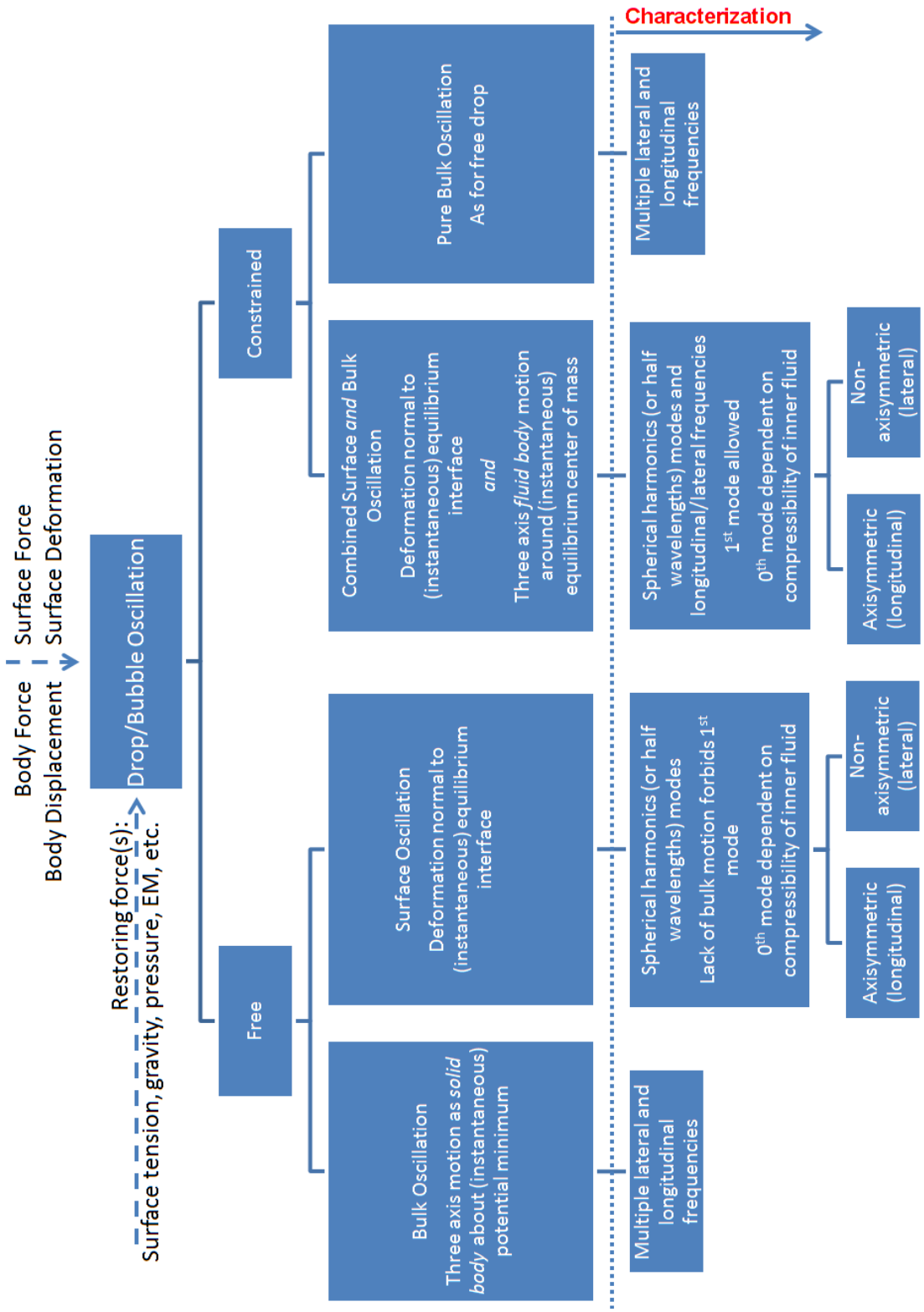

Figure 5-3: Graphical representation of a framework for understanding the oscillation of drops or bubbles.

Of importance also is the state of the drop/bubble, either free of constraint or constrained by a surface. For a free drop/bubble, the aforementioned sources of oscillation can give rise to an oscillation of the bulk or an oscillation of the surface. For pure bulk oscillation, there is no surface deformation and the drop/bubble moves in bulk with motion in cardinal directions about the potential minimum. An example would be an acoustically levitated drop which 'wobbles' about the pressure minimum of the levitator without any appreciable surface oscillation (because of, e.g., high viscosity). If the potential minimum shifts, the drop/bubble would oscillate about this moving point. For pure surface oscillation, there is no motion of the center of mass and the drop/bubble deforms, its surface oscillating normal to some equilibrium shape with restoring forces (surface tension, and/or gravity, commonly) attempting to restore the equilibrium shape. The equilibrium shape can be as simple as a sphere, or more complicated if the free drop/bubble undergoes some external steady forcing, such as in a cross flow. Similarly, the shape of the equilibrium interface can change over time if the drop/bubble undergoes changing forces (e.g. a cross flow of varying intensity). Examples of free drop/bubble surface oscillations are diverse, including falling raindrops and rising bubbles.

The connection (if any) between bulk and surface oscillations depends on the situation. For free floating drops and bubbles, oscillations of the bulk and of the surface are generally decoupled since oscillations of the surface cannot move the center of mass of the drop/bubble. On the other hand, in the example given above, a drop in an acoustic levitator would likely undergo surface oscillations as

its bulk was driven to oscillate, with the surface oscillations caused by instabilities introduced by imperfections in the levitator's force distribution.

For constrained drops/bubbles, the situation is different. Here bulk and surface oscillations are generally linked since the constraint leads most changes of center of mass to result in a change of surface shape (and vice versa). As a result, one sees a mixture of the behaviors seen for pure bulk and surface oscillation, in that the surface oscillates about the instantaneous equilibrium profile and the center of mass oscillates about the instantaneous equilibrium center of mass. The bulk oscillation is fluid however (i.e. not all portions of the drop will oscillate at the same magnitude and there may be internal circulation) in comparison to a solid body like motion of pure bulk oscillation. An example (studied in this paper) is a sessile water drop exposed to airflow, such as raindrops on the windshield of a moving car. Pure bulk oscillation of constrained drops/bubbles is also possible, with a similar definition as for free drops/bubbles. Examples would be a drop with no contact angle hysteresis rolling or sliding about the bottom of a curved bowl or a drop help pendant by an infinitely small constraint (though the second example is imperfect, as discussed in Section 5.2.3).

In terms of characterizing the oscillations, one can consider multiple bulk modal frequencies along each axis. If an orienting force (e.g. gravity) or direction is present, then oscillations along this axis can be termed 'longitudinal' while those about the remaining axis can be termed 'lateral'. It is also possible that the

drop/bubble could be undergoing rotational oscillations in which case the 'lateral axes' would be rotational (i.e. azimuthal and possibly inclination angles).

For surface oscillations, there are likewise multiple surface modes, each corresponding to harmonics of the equilibrium shape. The zeroeth mode (the degree zero spherical harmonic corresponding to volume expansion and contraction) is generally forbidden for drops (as it relies on compressibility) while it is allowed for bubbles. The first mode is forbidden for free drops or bubbles because it would amount to motion of the drop without surface deformation. It would thus be pure bulk oscillation, requiring different driving and restoring forces. The first mode is allowed for constrained drops due to the link between surface and bulk motions for constrained drops.

Most researchers have considered axisymmetric surface oscillations of a spherical (cap) shaped drop/bubble. For free drops/bubbles, these modes are described by axisymmetric spherical harmonics and the associated Lengendre polynomials, each defined by a distinct degree (commonly called mode) number. Each mode corresponds basically to an integer number of half-wavelengths across the surface of the drop. Constrained drops and bubbles are also defined by degree number for axisymmetric oscillations, but as discussed in Section 5.2.2 the spherical harmonic mathematics are more complex, and the number of half-wavelengths across the drop changes compared to the same mode for free drops/bubbles. This last point suggests that defining/modeling drop/bubble

oscillations by simply counting half-wavelengths is insufficient, a point that will be expanded on throughout this paper.

Non-axisymmetric oscillations of a spherical (cap) shaped drop are again described by spherical harmonics, in this case non-axisymmetric. Due to the non-axisymmetry, the mode shape is fully three dimensional, requiring both an order and degree number to define them. Similarly though, in any profile through the drop a mode will again correspond to an integer number of half-wavelengths measured along the equilibrium profile of the drop. The number of half-wavelengths may not be constant for each profile for a given mode, however, again casting doubt on the use of this technique for modeling oscillations.

Finally, if the drop does not have a spherical (cap) shaped equilibrium surface, then the modes should still correspond to (axisymmetric or non-axisymmetric) non-spherical harmonics[65]. These, however, would in general be mathematically intractable.

Regardless of the exact nature of the oscillation, each mode shape will oscillate with its own frequency, with a dispersion relationship describing the connection between them. As stated above, for constrained drops there should be a link between the multiple modal frequencies of bulk oscillation, and the multiple modes of surface oscillation.

We stress again that all of the above framework can be applied to oscillating bubbles as well as drops. However, the slightly different physics (a compressible inner fluid, a possibly incompressible outer fluid, differences in densities, etc.) will change the behaviors seen and the mathematical descriptions of them, as well as the frequencies of oscillations. Also, the existence and occasional presence of a 0^{th} and 1^{st} mode, and the relatedness of drop and bubble oscillation, raises three final comments.

First, some researchers whose work is reviewed in Section 5.2.3 have commented on separate 'Rayleigh modes'[13] and 'rocking (or bending) modes' being present for constrained drops undergoing axisymmetric and non-axisymmetric oscillations, respectively). All of these modes, if driven by a balance between surface tension and inertia, are 'Rayeligh'-type modes and are governed by the same physics and similar equations (Equation 5-1), just different eigenvalues.

Second, some researchers have commented on a 'first Rayleigh mode' for a drop when in fact they mean a drop oscillating in the second axisymmetric mode. This misnomer likely stems from the fact that the 0^{th} mode is forbidden for drops, with the 1^{st} mode is forbidden for the free drops Rayleigh considered (as well as for free bubbles). However, these modes do exist and should not be neglected since they are present for bubbles and constrained drops/bubbles, respectively.

Third, neither the terms 'Rayleigh mode number' nor 'Strani and Sabetta mode number'[18] should be used to define non-axisymmetric modes. The two numbering

systems are identical (if used correctly, as discussed in Section 5.2.2) so no distinction should be made when discussing axisymmetric oscillations. And as stated above, *both* an order and a degree (or mode) number are required to define non-axisymmetric oscillations.

5.4 Experimental Setup and Full Profile Processing

The models described by Equations 5-1 through 5-10 will be considered and tested (as applicable) in comparison to experimental results in Section 5.5. First, the experimental methods and materials will be described for the new data collected for this chapter.

The physical setup of the experiment is given in detail elsewhere[11]. Briefly, a laminar wind tunnel (0-30 m/s measured by an upstream pitot static tube, working cross section of 215.9 mm x 469.9 mm) was fitted with a symmetric streamlined body into which a 2.5 cm x 2.5 cm surface could be mounted flush. The surface was a smooth piece cut from a glass slide, and spin coated with either Teflon or PMMA. The boundary layer Reynolds number at the surface was ≤ ~$2x10^5$, indicating laminar conditions. Drops of 13-100 μl of either DI water (from a Millipore machine) or hexadecane (Sigma Aldrich) were placed on each surface. The drop Reynolds number was ≤ ~3000, again indicating laminar conditions. Calculations indicate that the drop height ranged from approximately 0.9 to 2.5 times the boundary layer thickness. A high-speed camera (Vision Research Inc.) captured 100 frames/s of a backlit side view of the drop oscillation

with a resolution of 42 μm/pixel. Tests involved placing a drop in quiescent conditions and slowly increasing the airspeed until the drop began to move back along the surface. Results presented in this paper were taken before the point of incipient motion, i.e. results correspond to pinned contact lines. A detailed discussion of incipient motion is given elsewhere[11]. It was seen that with increasing airspeed, the drop deformed from its spherical cap shape, and oscillated about this deformed shape.

Processing was performed via several Matlab routines developed in the Surface Engineering and Instrumentation Lab at the University of Alberta (contributed to by Beatriz Defez-Garcia, the thesis author, and several summer students). For each frame of video, the airspeed measurement was synchronized, and image processing algorithms used to identify the drop, calculate the centroid of the side view, and locate the profile view of the drop interface through edge finding. Centroid time traces were binned into bands of airspeed 0.5 m/s wide (i.e. 0-0.5 m/s, 0.5-1m/s, etc.), and an FFT performed for each bin, giving time resolved spectral information (giving frequency of bulk oscillation). The edge traces were also binned in the same manner, and each bin was processed following the schematic shown in Figure 5-4. First, each bin was used to create a reference profile by spline fitting each profile, interpolating points from each fit at a series of identical positions along the curve, averaging these points across all the frames in the bin and performing a single spline fit to all the averaged points (Figure 5-4a and b). This average profile was taken to be the time varying non-spherical equilibrium shape of the drop (time varying since the air velocity was increasing

in time). Each instantaneous profile was compared to the average profile for each bin, and the normal distance between the curves was measured for 32 points along the profile (Figure 5-4c).

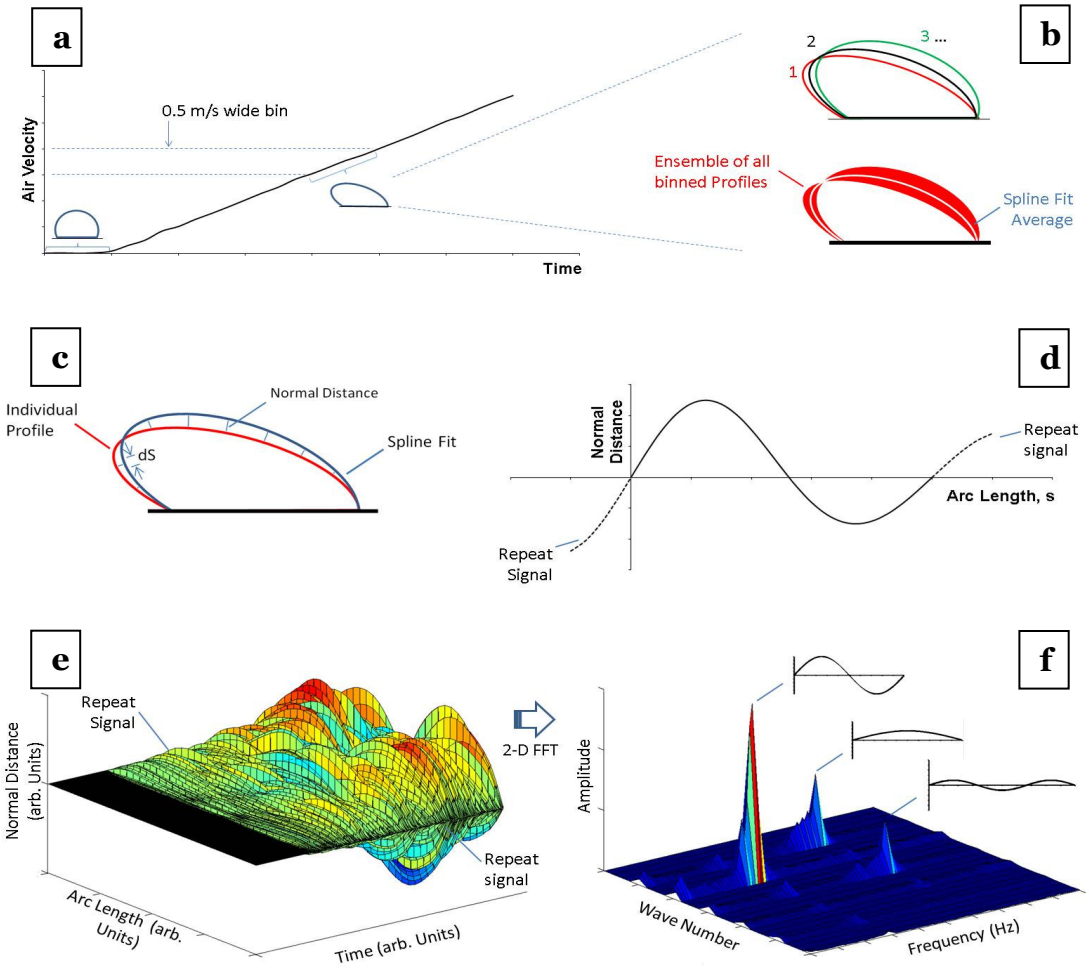

Figure 5-4: Schematic showing surface oscillation processing performed for each frame

A two-dimensional FFT was performed on the stacked normal distance curve, resulting in time resolved spectral information (giving wave number components of surface oscillation and their related frequencies, Figure 5-4e and f). To improve resolution, the normal distance curve was artificially repeated eight times to increase the length of the signal as illustrated in Figure 5-4d and Figure 5-5. Each repeated curve was inverted (i.e. multiplied by negative one) and

flipped along its length, which results in an amplification of all wave forms with any integer number of half-wavelengths along the arc length. Since the drop profile will have nodes at the contact points (since the contact line is pinned), this technique should introduce limited error. It is worth noting here that mode 2-1 (Figure 5-2c) does not present a regular sinusoidal signal component (as illustrated in Figure 5-5c). Performing a Fourier transform of an artificially created and repeated mode 2-1 signal (Figure 5-5l and o) gives a mixture of two sinusoidal signals as shown, one of which corresponds to mode 0-1 (Figure 5-2a and Figure 5-5a). The component in Figure 5-5c cannot be recovered from the non-repeated signal either, so the mixed results shown in Figure 5-5o will be taken as indication of the presence of mode 2-1.

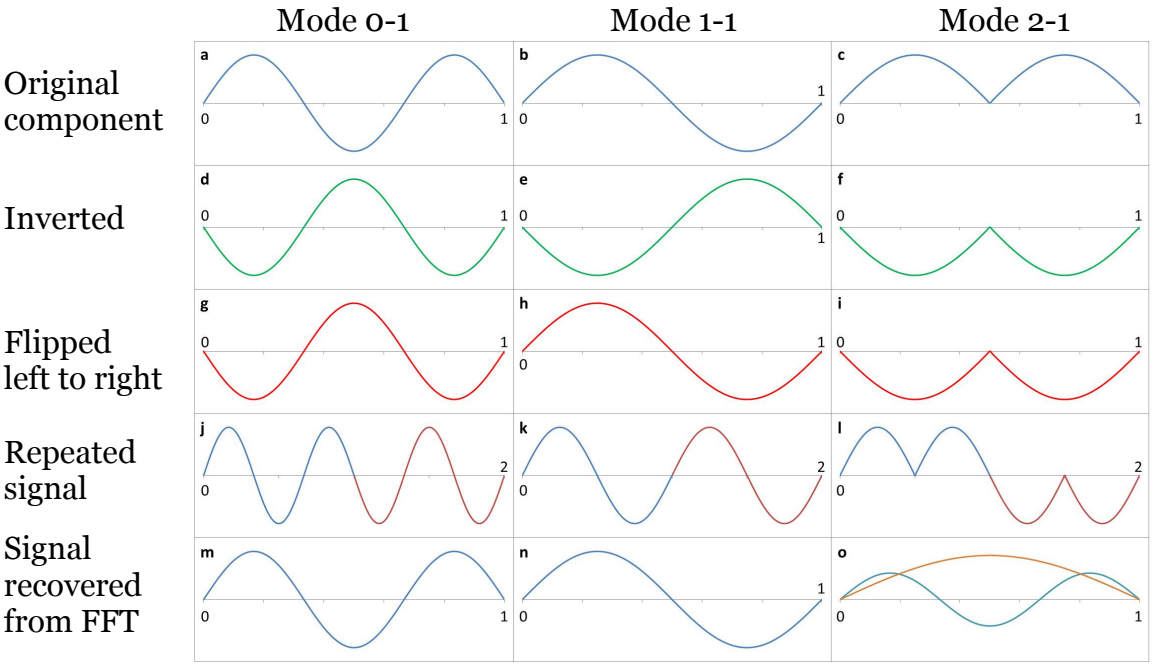

Figure 5-5: Showing the process of inverting and flipping each component of a signal to increase FFT resolution. The original components are a subset of the possible components of the normal distance curve along the drop arc length (as seen in Figure 5-4), and correspond to mode (a) 0-1, (b) 1-1, (c) and 2-1 in Figure 5-2. No error artifacts are introduced for cases a and b, but the individual waveforms are retrieved from the FFT of the repeated signal while they would not be for the original signal alone. Case c cannot be correctly recovered with or without signal repetition, and instead is interpreted by the FFT as two waveforms, one identical to that for mode 0-1 (but with a different magnitude), and one indicating a half wavelength across the arc length of the drop.

The above described processing techniques rely upon a two-dimensional profile view of the three dimensional drop. It therefore depends on an approximation similar to that made by Noblin et al.[48,49] and Sharp et al.[50] in terms of wavenumber analysis, though the frequency analysis is exact. It also measures the oscillations of the profile, rather than assuming their type. As such, it allows for examination of the processed results to determine if the mode shapes and frequencies fit the assumption of Noblin et al.[48,49] and Sharp et al.[50] It can also be used in the future to determine the growth rate of oscillations and as a framework for the processing of a three-dimensional data set if current[74,75] or future three-dimensional drop imaging techniques come to fruition. For now, the processing routine as described has been used to produce the results discussed below.

5.5 Results and Discussion

Following the framework expressed in Figure 5-3, we begin our discussion by examining the source of oscillations for the newly presented experimental results, that of sessile drops under airflow. The constant body force of gravity can be neglected, and there are negligible imposed body displacements (external vibrations). The moving airflow does apply a surface force to the drop, but the free stream air velocity is quasi-steady, slowly increasing with negligible oscillation in time. While this increasing air velocity can easily be understood to deform the equilibrium profile of the drop, it is not immediately clear how the quasi-steady free stream flow could cause drop oscillation.

The source of the oscillation is in fact an applied oscillating surface force induced by the interaction of the quasi-steady airflow with a deformable surface through an aeroelastic, flutter-like instability. The quasi-steady airflow first causes the drop to deform due to air drag, taking a tear drop like shape on the surface with the bulk of the drop pushed downwind. A vortex is then shed from the downwind side of the drop[8] leading to a momentary decrease in the local surface drag force on the drop. The decreased force allows the drop to try and regain its shape, with the bulk of the drop moving upstream. This increases drag force once more, restarting the cycle of oscillation. As will be seen, the vortex shedding couples with the natural frequency of the drop, in that the shedding excites the natural (characteristic) frequency of the drop, which in turn regulates the frequency of vortex shedding.

As discussed above, frequency and mode shape measurements were made for multiple air velocity bins, in order to observe any change in their characteristics with air velocity/due to changes in the equilibrium shape of the drop. No noticeable dependence on air velocity was seen. This is in contradiction to the findings of Lin et al.[76] but in agreement with the findings of Esposito et al.[70] Based on our findings, we will neglect the changing airflow, and present results obtained by taking a single 2-D FFT across all air velocities from near zero to just before the point of incipient motion (while the contact line is still pinned) as illustrated in Figure 5-4e and f. Nonetheless, the normal distance-arc length-time signal was generated using time varying equilibrium profiles determined using the method illustrated in Figure 5-4a through c.

Figure 5-6 shows drop bulk oscillation frequencies versus the reciprocal of the square root of drop volume, for drops of water on Teflon and PMMA, and drops of hexadecane on Teflon. Figure 5-6 shows the raw data, not normalized to account for the differences in fluid properties (surface tension and density) between hexadecane and water. It was taken by performing an FFT of the time trace of centroid position (i.e. it indicates the frequency of the bulk oscillations of the drop, not considering the surface oscillations in any way). Figure 5-6 also shows the linear fit to each data set forced through the origin since in the absence of gravity, an infinitely large drop should approach zero oscillation frequency. The high R^2 value of the fit indicates that the restoring force for these drop oscillations are largely, if not wholly, capillary (see Equation 5-1) rather than capillary-gravity in nature. As further validation, Equations 5-1 through 5-4 can be combined to give a gravity capillary wave formula for free drops in air. Doing so yields Equation 5-11:

$$f_{ml} = \frac{1}{2\pi}\sqrt{\frac{g}{R}\frac{2l+1}{2l(l-1)} + \frac{\gamma l(l-1)(l+2)}{\rho_1 R^3}} \qquad \text{Equation 5-11}$$

For a representative 1 mm drop of water in air, Equation 5-11 yields gravitational effects of only 1%. Disregarding for a moment the concerns in using a one-dimensional equation for three-dimensional drop oscillations, one can also consider the gravity capillary model put forward by Noblin et al.[48,49] in Equation 5-7. In Equation 5-7, the greatest gravitational effect is seen for the lowest mode number. Assuming a drop of water in air, with approximately 1 mm spherical cap

radius, the effect of gravity on the frequency of drop oscillation ranges from 0.02% to only 4.6% as contact angle ranges from 10° to 150°. Based on these order of magnitude arguments, we will neglect the effects of gravity in our drop oscillation analysis from this point forward.

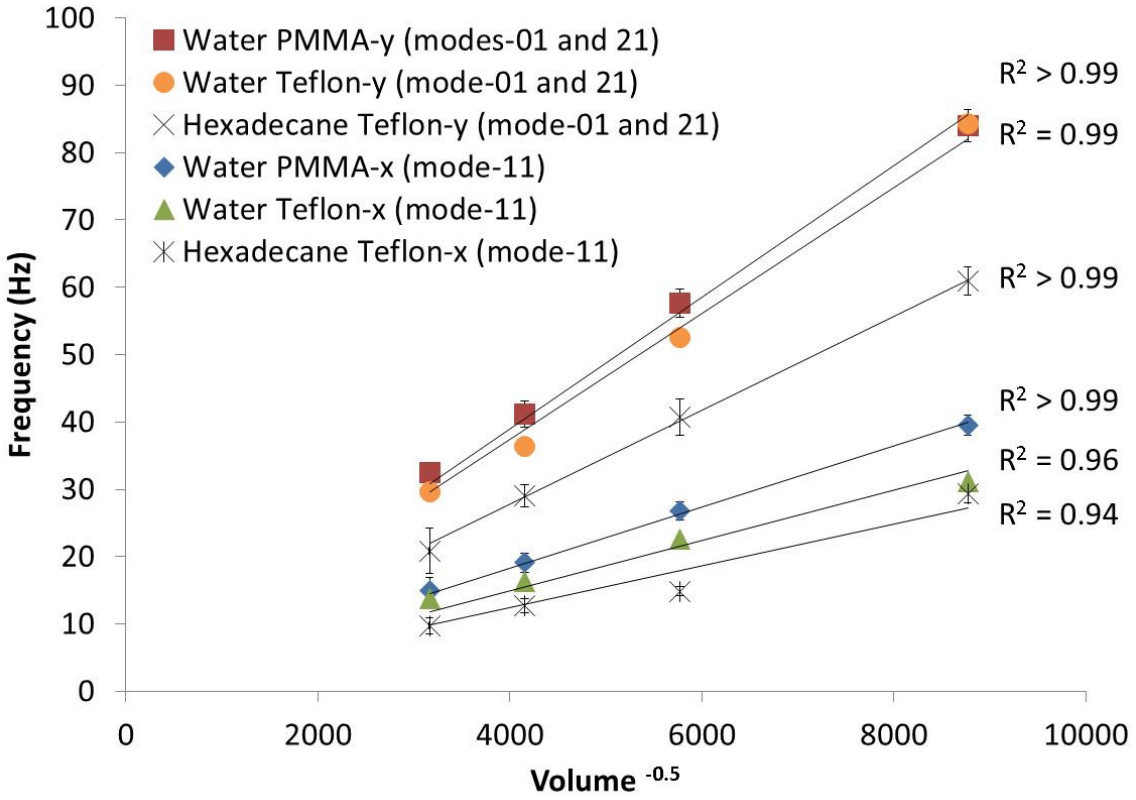

Figure 5-6: Bulk oscillation frequency versus the inverse root of volume for systems of drops of Water on PMMA, Water on Teflon, and Hexadecane on Teflon, with the direction of bulk (centroid) motion denoted in the legend (*x* denoting lateral (horizontal) motion, *y* denoting longitudinal (vertical) motion relative to the flat surface). Surface oscillation degree and order are also listed in the legend based upon matching the frequencies of bulk and surface oscillations. Error bars denote one standard devation.

Each data set in Figure 5-6 has been labeled by its corresponding mode number(s). These mode numbers have been determined based on the whole profile analysis results, a representative sample of which is shown in Figure 5-4. This analysis methodology allows for calculation of both frequency and the two-

dimensional profile of mode shape of each mode of surface oscillation. In general, peaks for mode 0-1, 1-1 and 2-1 were observed, with the 'bending' 1-1 mode generally the strongest, and with the frequency of each model closely matching the frequency of bulk oscillations. The excellent agreement of the frequency of surface oscillation modes with the frequency of bulk oscillation modes indicates that, as stated previously, bulk and surface oscillation modes are related to one another for the case of constrained drops.

As discussed regarding Figure 5-5, mode 2-1 (illustrated in Figure 5-2) is interpreted by an FFT as two separate waveforms, one of which is identical to mode 0-1. According to Chiba et al.[37], modes 0-1 and 2-1 are expected to have nearly identical frequencies for contact angles below 90°, and similar frequencies for contact angles between 90° and 120°. As seen in Figure 5-4, the two lesser peaks indeed have similar frequencies, with wavenumbers that indicate the definite presence of mode 2-1, and the possible presence of mode 0-1. It is difficult to say for certain therefore if both modes are present without additional views of the drop. We believe that both peaks are present since the relative magnitude of the two peaks in FFT is often approximately equal, with some cases for which mode 0-1 shows a stronger peak than the other mode. As Figure 5-5 showed, pure mode 2-1 should present as a mixture of two signals, with a weaker mode 0-1 signal.

5.5.1 Testing Models for Mode 1-1 Oscillations

Having characterized the drop oscillation by its fundamental modes, we now seek to test the various mathematical models (Equations 5-5 through 5-10, and the infinite series results available in literature) that have been suggested as eigenvalue relations between mode number and frequency of drop oscillation for various contact angles (various drop shapes). We start by examining the lowest frequency mode (the 'bending' non-axisymmetric mode 1-1), which is also the least studied of m-1 modes. Equations 5-5 and 5-6 are invalid for modeling mode 1-1, as they are for drops undergoing mode 0-1 oscillations. Equation 5-10 will not be tested as it is for drops oscillating under the effects of gravity, which have been seen to be negligible in this case. Equation 5-9 is neglected as it was already determined to not be generally applicable. This leaves Equations 5-7 and 5-8. Further, the predictions of Lyubimov[36] and of Bauer and Chiba[34] and Chiba et al.[37] have been read from their respective papers for comparison to experimental data.

The experimental data and model predictions are shown in Figure 5-7. Figure 5-7 includes the new experimental data from this work, as well as data from several literature sources, including the extensive work of Sharp et al.[50] The experimental data was collected for sessile drops maintaining pinned contact lines, with different causes of oscillation including an imposed deformation of the surface[50], an imposed oscillating body force from an oscillating substrate[63], and (as in the present work) cross flowing air[70,76]. All data have been cast as eigenvalues to

normalize the effects of varying fluid densities, drop sizes, and surface tensions. The tight clustering of data points in Figure 5-7 shows that sessile drop oscillations are similar for all these cases, suggesting that the deformed equilibrium drop shapes of the drops in the present work have little effect on oscillation characteristics. Other work in our lab (not shown here) confirms this finding for sessile drops forced to oscillate by a vibrating substrate, finding that they have similar frequencies to the drops in cross flow. Altogether, this indicates (as discussed in the second paragraph of Section 5.5) that drops in cross flow undergo natural oscillations, with the frequency of oscillation and vortex shedding determined by the natural frequencies of the drops. Regarding model predictions, while not shown on Figure 5-7, one can surmise that the mode 1-1 eigenvalues for contact angles of 0° and 180° should both be infinite. This is because for a contact angle of 0° the resulting infinitely thin liquid sheet should support no capillary waves. Conversely, a contact angle of 180° indicates a free drop, which forbids observation of any mode with order one (e.g. modes 1-1, 0-1, 2-1, …).

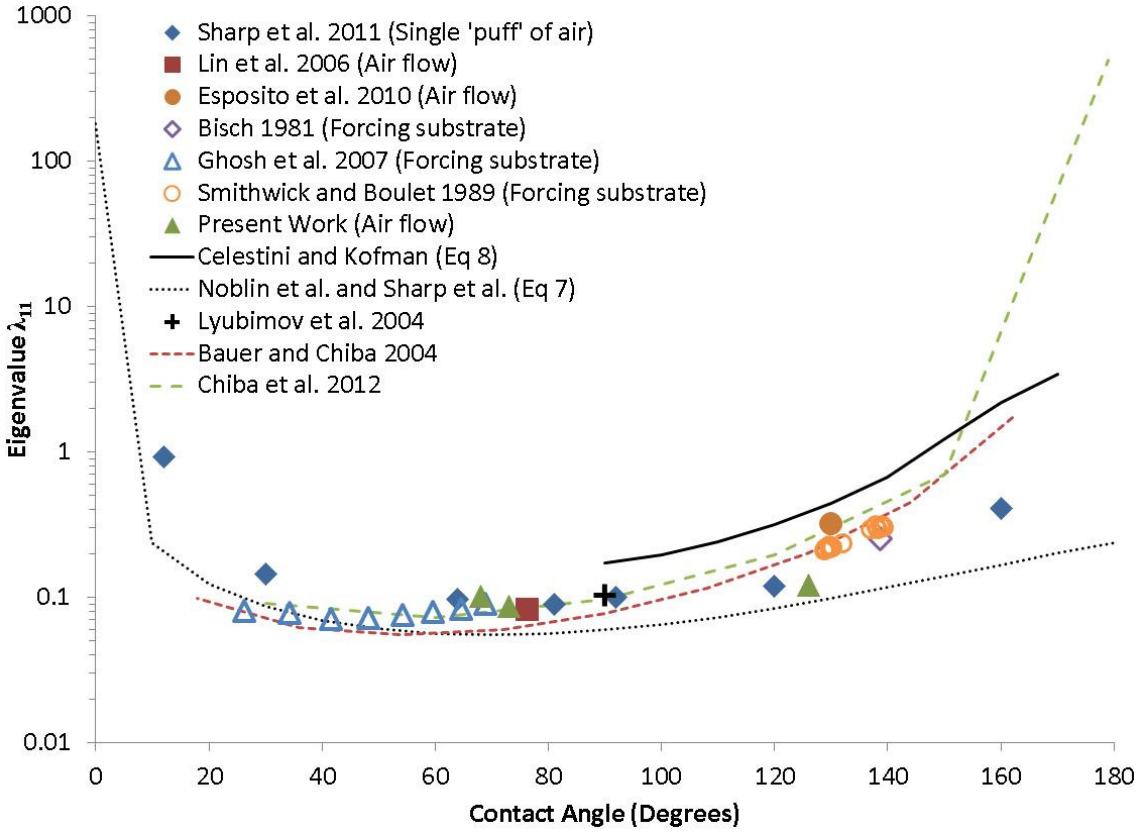

Figure 5-7: Eigenvalue versus contact angle for mode 1-1 oscillations of sessile drops. Experimental data are shown as solid symbols, model predictions were read at discrete points and are connected by straight lines except for the single prediction at 90° made by Lyubimov.

Comparing the model predictions to experimental data, several trends can be seen. The medium order model of Celestini and Kofman[69] consistently overpredicts the eigenvalue (underpredicting oscillation frequency). This indicates that the static drop profiles used to predict dynamic drop oscillation are insufficient. Conversely, the medium order models of Noblin et al.[48] and Sharp et al.[50] consistently underpredict eigenvalues (overpredicting frequency). This was seen by Sharp et al. for mode 1-1[50], while Noblin et al. did not study this mode. Sharp et al.[50] proposed applying a constant correction factor to the predictions. Doing this, one can achieve reasonable agreement with experimental data over the range of contact angles from ~30° to ~120°. However, higher and lower

contact angles then require a varying correction factor, invalidating this approach. The model of Bauer and Chiba[34] (for drops in spherical bowls of the same radius), gives reasonable agreement, as does the model of Chiba et al.[37] (for drops centered on the apex of conical peaks/troughs). Both models are plotted in Figure 5-7 based on the apparent contact angle that would be made between the drop's liquid-vapor interface and the horizontal plane which the contact line intersects (since neither model deals with the experimentally common situation of a drop on a flat plate). The differences between the models indicate that there are effects of the non-planar constraint geometry in modeling drop oscillation. The single prediction of Lyubimov for a contact angle of 90° matches Chiba et al.'s model[37] for the identical case of a contact angle of 90° on a flat plate, and matches experimental data for drops near this contact angle well.

Both the models by Bauer and Chiba[34] and Chiba et al.[37] fail to predict oscillation eigenvalues at low and high contact angles, under- and overpredicting them, respectively. At low contact angles, the difference is likely due to depth effects. Capillary waves decrease in frequency as fluid depth decreases. For the case of sessile drops, low contact angle indicates small fluid depth for a given volume. Both models, on the other hand, have relatively larger fluid depths due to the non-planar geometry they employ to simplify the mathematics. The difference at higher contact angles may be due to the constraint of the drop. For both of the models, there is no surrounding solid surface to interfere with the drop as it oscillates, while a sessile drop on a flat surface can interfere with the surface as the drops interface bends toward it. This would tend to increase the stiffness of

the drop, increasing the frequency and decreasing the eigenvalue, as seen in the comparison between the model predictions and experimental data.

To summarize the above discussion, neither low-order, nor medium-order models can successfully predict modal frequency over the full range of contact angles. While the high-order infinite summation models are close in their predictions, they fail at high and low contact angles. Thus, a more accurate model of mode 1-1 oscillations of constrained drops is necessary. Until such time as such a model exists, the high order model of Chiba et al.[37] can be used, or the collected literature data can be used as an empirical graph of expected eigenvalues. It is worth mentioning here that none of the experimental data for mode 1-1 oscillations are for larger pendant drops (Smithwick and Boulet[40] studied small (low Bond number) pendant drops). Experiments addressing this deficiency would allow for a comparison between sessile and pendant mode 1-1 oscillations (though for sufficiently low gravitational effects (i.e. sufficiently low Bond numbers) there should be no difference seen).

5.5.2 Testing Models for Mode 0-1 and 2-1 Oscillations

A similar analysis to the above can be performed for the mode 0-1 (with mixed mode 2-1 in the newly presented data) oscillations also seen in Figure 5-6. Throughout this section, modes 0-1 and 2-1 are treated as showing identical frequencies, based on literature models[37] and the experimental results given using the whole profile analysis technique. Mode 2-1 was only observed in the newly presented data; however, no other researchers have performed the full

profile analysis technique necessary to identify this mode. Of the models in Equations 5-5 through 5-10, only Equation 5-7 is considered here. Equations 5-5 and 5-6 are neglected since they have no contact angle dependence. Equation 5-8 is neglected since it is for mode 1-1 oscillations, and Equations 5-9 and 5-10 are neglected for the same reasons given in Section 5.5.1. Further, the predictions of Strani and Sabetta[18], Smithwick and Boulet[40] and Yamakita et al.[41] (who each used the model of Strani and Sabetta), of Lyubimov[39], and of Bauer and Chiba[34] and Chiba et al.[37] have been read from their respective papers and compared to experimental data.

The experimental data and model predictions for Mode 0-1 and 2-1 oscillations are shown in Figure 5-8 and Figure 5-9. Figure 5-8 is the prediction of Strani and Sabetta[18] matched to the experimental data given by Rodot et al.[32] for a drop oscillating in a fluid of matched density (it is therefore a reproduction of the result shown in Strani and Sabetta[18], but cast as eigenvalues. It can be seen that there is excellent agreement between experiment and theory at high contact angles, with worse results at lower contact angles. This was noted in the original work[18], and is likely due to the difference between the geometry used in the experiment (a drop on a flat topped pin) versus the geometry of the model (a drop in a spherical bowl), since lower contact angle drops would in effect be a shallower 'pool' leading to decreased frequency and increased eigenvalue.

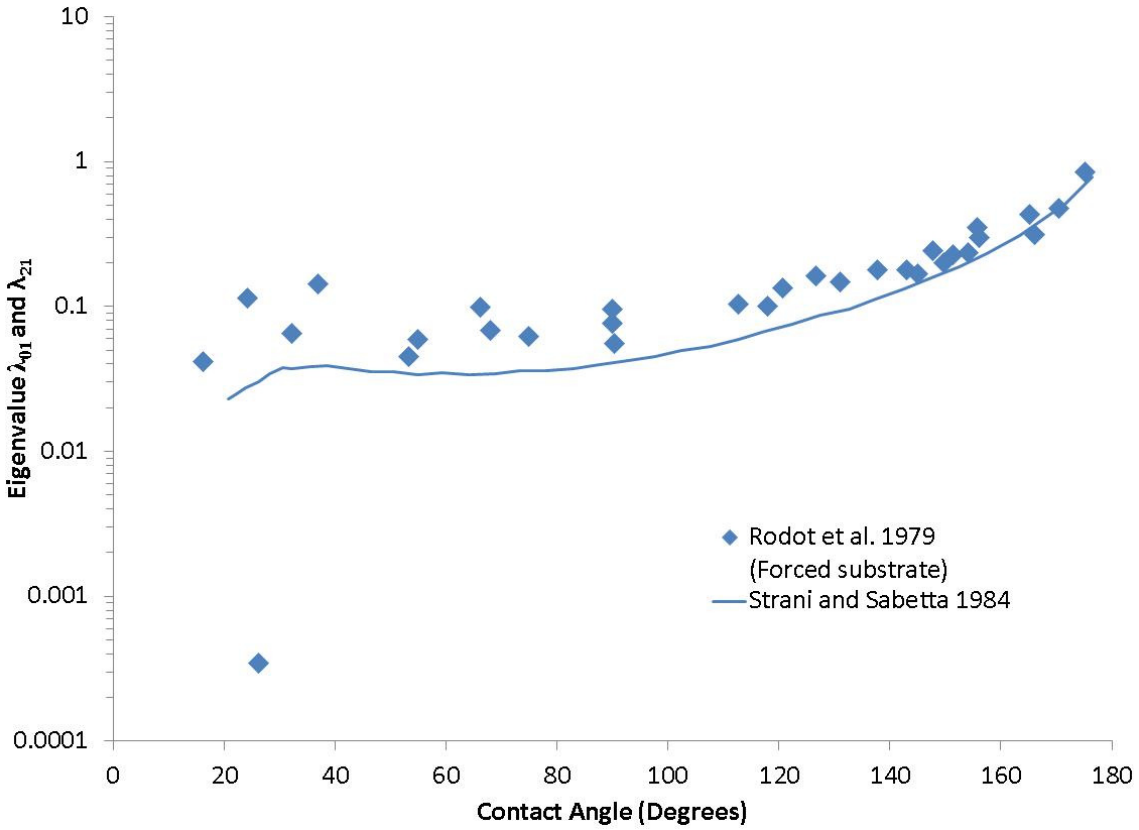

Figure 5-8: Eigenvalue versus contact angle for mode 0-1 oscillations of sessile drops of density matched fluid in a fluid medium. Experimental data are from Rodot et al. 1979, and model predictions are those originally given by Strani and Sabetta 1984. Model predictions were read at discrete points and are connected by straight lines.

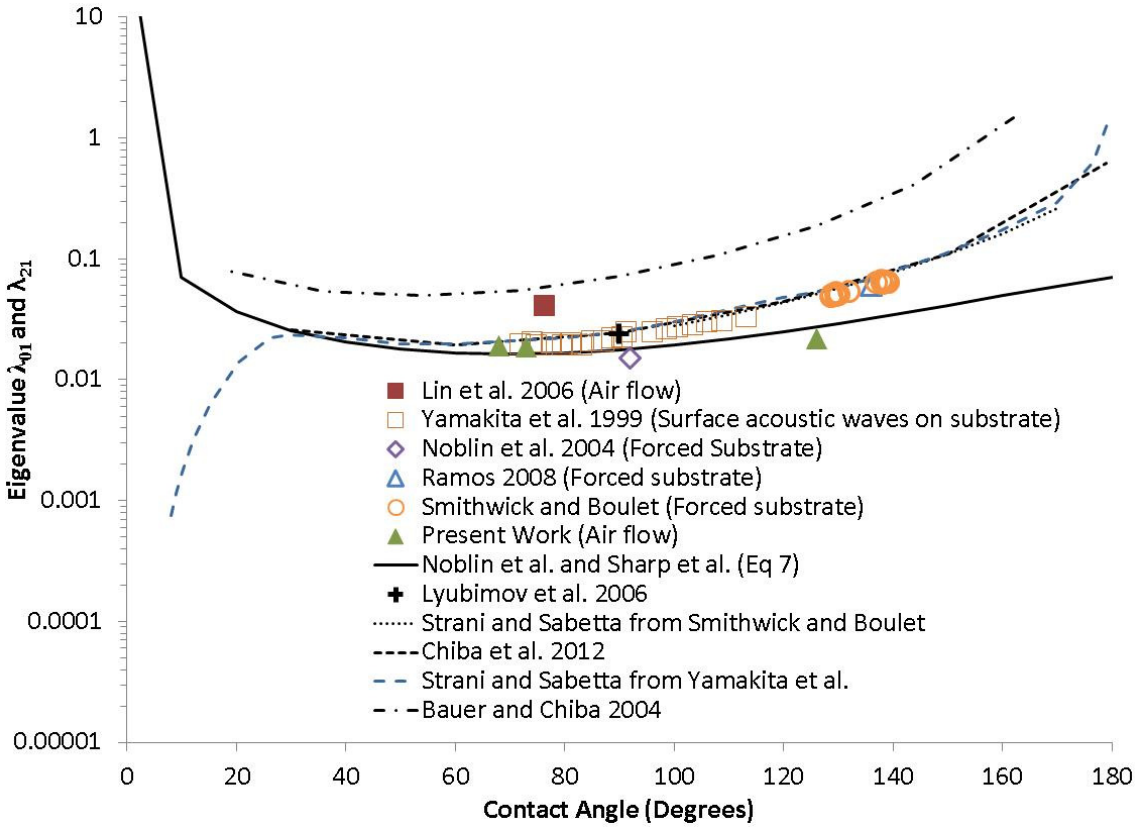

Figure 5-9: Eigenvalue versus contact angle for mode 0-1 and 2-1 oscillations of sessile drops in vapor. Experimental data are shown as solid symbols, model predictions were read at discrete points and are connected by straight lines except for the single prediction at 90° made by Lyubimov.

Figure 5-9 includes the experimental data from this work, as well as data from several literature sources, all for the case of liquid drops oscillating in air with pinned contact lines. Causes of oscillation include surface acoustic wave forcing[41], solid surface oscillation by loudspeaker [40,48,71], and (as in the present work) cross flowing air[76]. All data have been cast as eigenvalues to normalize the effects of varying fluid densities, drop sizes, and surface tensions. The data points in Figure 5-9 are approximately as tightly clustered as those in Figure 5-7 for mode 1-1 oscillations, again suggesting that the (cross flow induced) deformed equilibrium shapes of the drops in the present work have little effect on oscillation characteristics, and indicating (as discussed in the second paragraph of Section

5.5) that drops in cross flow undergo oscillations with the frequency determined by the natural frequencies of the drops. As in Figure 5-7, one can surmise that the mode 0-1 and 2-1 eigenvalues for contact angles of 0° and 180° should both be infinite since the frequency of oscillation in both cases is zero.

Comparing the model predictions to experimental data, it can immediately be seen that the model of Bauer and Chiba[34] fails to predict the eigenvalues. As mentioned previously, the model in that paper gave nearly identical results for mode 1-1 and mode 0-1 oscillations, suggesting that one of the predictions was incorrect. Figure 5-9 shows that Bauer and Chiba's model for mode 0-1 oscillations is incorrect. Otherwise, the high order model predictions of Strani and Sabetta[18] match those from the similar model of Chiba et al.[37], and the single prediction at 90° contact angle by Lyubimov[39]. The models of Strani and Sabetta[18] and Chiba et al.[37], however, do not predict an infinite eigenvalue as they should for a 0° contact angle. This is likely because these models do not accurately capture the vanishing fluid depth as contact angle decreases. Away from these low contact angles, however, the models of Strani and Sabetta[18] and Chiba et al.[37] seem to give satisfactory results for mode 0-1 and 2-1 oscillations. To improve accuracy, it may be possible to add a corrective term for the effects of decreased actual fluid depth.

Considering medium order models, the model of Noblin et al.[48] (subsequently re-derived by Sharp et al.[50]) follows the data relatively well for contact angles below ~80°, but does not follow the data as well at higher contact angles. Further, it is

still not ideal in that while it does approach infinity at zero contact angle (as it should), it does not approach infinity at 180°. As such, it predicts a finite frequency of mode 0-1 oscillation for a free floating drop (contact angle of 180°). This is contrary to the established models for free drops[16], and indicates that the 1-D model of Noblin et al.[48] and Sharp et al.[50] should not be used. Further, the predictions of this model given in Figure 5-9 were for the mode shape of mode 0-1 oscillations (see Figure 5-2). The predictions of this model for mode 2-1 oscillations would be very different, despite the fact that theory and experiments suggests that the frequencies (and thus eigenvalues) would be similar[37].

To summarize the above discussion, the high order model originally proposed by Strani and Sabetta[18] matches experimental data well, except at low contact angles. The high order model of Chiba et al.[37] has the same minor failing as the Strani and Sabetta model, but improves on the previous work by including non-axisymmetric modes (discussed in Section 5.5.1). On the other hand, the medium order models of Noblin et al. (rederived by Sharp et al.) should not be used for mode 0-1 or 2-1 oscillations. Further, an error was made in Bauer and Chiba[34], so their high order model should not be used for mode 0-1 oscillations (they did not present a model for mode 2-1 oscillations). Improvements to the models could include considering the effects of the decreasing depth of the drop as contact angle decreases. Experimental data is also somewhat lacking in the low contact angle range; such data would be necessary to validate improved models.

5.6 Conclusions

Categorizing and collecting diffuse literature, low-order, medium-order, and high-order models for the contact angle dependent eigenvalue describing sessile drop oscillations have been gathered. The eigenvalue is used in the dispersion relationship to relate drop oscillation frequency to mode shape (thus relating bulk oscillation to surface oscillation).

A unifying conceptual framework has also been presented based upon the review of literature. This framework clarifies bulk and surface modes of oscillation, their coupling for constrained drops, and numerates the modes of surface oscillation. Oscillations can be both axisymmetric (requiring a single mode, also known as degree, number) and non-axisymmetric (requiring both an order and degree number to describe the non-axisymmetric spherical harmonic shape).

Using a newly developed full-profile analysis technique, the oscillation of sessile drops in cross flowing air has been investigated for drops of water on smooth PMMA and Teflon, and drops of hexadecane on smooth Teflon. The oscillations are coupled bulk and surface oscillations, driven by a flutter-like aeroelastic coupling in the quasi-steady air flow. The data of mode shape indicated non-axisymmetric mode 1-1 oscillations at lower frequencies, as well as a mix of axisymmetric mode 0-1 oscillations and non-axisymmetric mode 2-1 oscillations at approximately the same higher frequency. Mode 2-1 oscillations could not have been observed in previous literature due to the lack of full profile analysis.

Comparing the dispersion relationship eigenvalues to those seen in literature data, one can conclude that the oscillation of sessile drops in cross flow is similar to drops oscillated by myriad other means (e.g. by oscillating plate or an imposed surface deformation).

With the combined data set, the models available in literature were tested. It is seen that none of the low-order models are sufficient, nor are the medium order models (even those which take into account the 2-D mode shape). High order models (based on the use of Legendre polynomials to decompose the mode shapes) are somewhat successful for mode 1-1 oscillations (seen as a lateral 'bending' mode), and very successful for mode 0-1 and 2-1 oscillations (seen as longitudinal modes), expect for the lowest contact angles. Models could be improved by taking into account the diminishing 'depth' (drop height) of low contact angle drops. Until models are perfected, the collected literature data can serve as an empirical eigenvalue graph, and in the collection of more data or the generation of new models, the conceptual framework may be used to guide analysis and categorization of results.

References for Chapter 5

(1) Della Volpe, C.; Maniglio, D.; Morra, M.; Siboni, S. *Colloids and Surfaces A: Physicochemical and Engineering Aspects* **2002**, *206*, 47–67.
(2) Montes Ruiz-Cabello, F. J.; Rodríguez-Valverde, M. A.; Cabrerizo-Vílchez, M. A. *Langmuir* **2011**, *27*, 8748–8752.
(3) Meiron, T. S.; Marmur, A.; Saguy, I. S. *Journal of Colloid and Interface Science* **2004**, *274*, 637–644.
(4) Decker, E. L.; Frank, B.; Suo, Y.; Garoff, S. *Colloids and Surfaces A: Physicochemical and Engineering Aspects* **1999**, *156*, 177–189.
(5) Andrieu, C.; Sykes, C.; Brochard, F. *Langmuir* **1994**, *10*, 2077–2080.
(6) Smith, T.; Lindberg, G. *Journal of Colloid and Interface Science* **1978**, *66*, 363–366.
(7) Rodríguez-Valverde, M. A.; Montes Ruiz-Cabello, F. J.; Cabrerizo-Vílchez, M. A. *Soft Matter* **2011**, *7*, 53.
(8) Lin, Z.; Peng, X. *Heat Transfer-Asian Research* **2009**, 485–491.
(9) Clift, R.; Grace, J. R.; Weber, M. E. In *Bubbles, drops, and particles*; Dover Publications: Mineola N.Y., 2005.
(10) Montello, A. D. An Experimental Investigation of Water Droplet Growth, Deformation Dynamics and Detachment in a Non-Reacting PEM Fuel Cell via Fluorescence Photometry. MSc, The Ohio State University, 2008.
(11) Milne, A. J. B.; Amirfazli, A. *Langmuir* **2009**, *25*, 14155–14164.
(12) Plateau, J. In *Annual report of the Board of Regents of the Smithsonian Institution*; Government Printing Office: Washington, D. C., 1865; Vol. 1864.
(13) Rayleigh, J. W. S., Baron In *The theory of sound*; Dover: New York, 1945; Vol. 2.
(14) Lord Kelvin (Sir William Thomson) In *Mathematical And Physical Papers*; C. J. Clay and Sons: Cambridge, 1890; Vol. III, pp. 384–386.
(15) Lamb, H. *Proceedings of the London Mathematical Society* **1881**, *1*, 51.
(16) Lamb, H. In *Hydrodynamics*; Cambridge University Press: Cambridge, England, 1906; pp. 451–453.
(17) Landau, L. D.; Lifshitz, E. M. *Course of theoretical physics*; 1st ed.; Pergamon Press Ltd.: London; Paris; Frankfurt; Reading (MA), 1959; Vol. VI, Fluid Mechanics.
(18) Strani, M.; Sabetta, F. *Journal of Fluid Mechanics* **1984**, *141*, 233–247.
(19) Morrison, C. A.; Leavitt, R.; Wortman, D. *Journal of Fluid Mechanics* **1981**, *104*, 295–309.
(20) Miller, C.; Scriven, L. *Journal of Fluid Mechanics* **1968**, *32*, 417–435.
(21) Bauer, H. F.; Chiba, M. *Journal of Sound and Vibration* **2005**, *285*, 51–71.
(22) Beard, K. V. *Journal of the Atmospheric Sciences* **1984**, *41*, 1765–1774.
(23) Kang, I. S.; Leal, L. G. *Journal of Fluid Mechanics* **1988**, *187*, 231–6.
(24) Wang, T. G.; Anilkumar, A. V.; Lee, C. P. *Journal of Fluid Mechanics* **1996**, *308*, 1–14.
(25) Azuma, H.; Yoshihara, S. *Journal of Fluid Mechanics* **1999**, *393*, 309–332.
(26) Natarajan, R.; Brown, R. A. *Physics of Fluids* **1986**, *29*, 2788.
(27) Natarajan, R.; Brown, R. A. *Journal of Fluid Mechanics* **1987**, *183*, 95–121.

(28) Kalechits, V. I.; Nakhutin, I. E.; Poluéktov, P. P. *Soviet Physics. Technical Physics* **1984**, *29*, 934–937.
(29) Shiryaeva, S. O.; Grigor'ev, A. I.; Belonozhko, D. F.; Golovanov, A. S. *Technical Physics Letters* **2001**, *27*, 875–877.
(30) Papoular, M.; Parayre, C. *Physical Review Letters* **1997**, *78*, 2120–2123.
(31) Apfel, R. E.; Tian, Y.; Jankovsky, J.; Shi, T.; Chen, X.; Holt, R. G.; Trinh, E.; Croonquist, A.; Thornton, K. C.; Sacco, Jr, A.; Coleman, C.; Leslie, F. W.; Matthiesen, D. H. *Physical Review Letters* **1997**, *78*, 1912–1915.
(32) Rodot, H.; Bisch, C.; Lasek, A. *Acta Astronautica* **1979**, *6*, 1083–1092.
(33) Watanabe, Y. *Japanese Journal of Applied Physics* **1988**, *27*, 2409–2413.
(34) Bauer, H. F.; Chiba, M. *Journal of Sound and Vibration* **2004**, *274*, 725–746.
(35) Chiba, M.; Miyazawa, T.; Baoyin, H. *Journal of Sound and Vibration* **2006**, *298*, 257–279.
(36) Lyubimov, D. V.; Lyubimova, T. P.; Shklyaev, S. V. *Fluid Dynamics* **2004**, *39*, 851–862.
(37) Chiba, M.; Michiue, S.; Katayama, I. *Journal of Sound and Vibration* **2012**.
(38) Strani, M.; Sabetta, F. *Journal of Fluid Mechanics* **1988**, *189*, 397–421.
(39) Lyubimov, D. V.; Lyubimova, T. P.; Shklyaev, S. V. *Physics of Fluids* **2006**, *18*, 012101.
(40) Smithwick, R. W.; Boulet, J. A. . *Journal of Colloid and Interface Science* **1989**, *130*, 588–596.
(41) Yamakita, S.; Matsui, Y.; Shiokawa, S. *Japanese Journal of Applied Physics* **1999**, *38*, 3127–3130.
(42) Tsukada, T.; Sato, M.; Imaishi, N.; Hozawa, M.; Fujikawa, K. *Journal of Chemical Engineering of Japan* **1987**, *20*, 88–93.
(43) Basaran, O. A.; DePaoli, D. W. *Physics of Fluids* **1994**, *6*, 2923.
(44) Wilkes, E. D.; Basaran, O. A. *Physics of Fluids* **1997**, *9*, 1512.
(45) Vukasinovic, B.; Smith, M. K.; Glezer, A. *Journal of Fluid Mechanics* **2007**, *587*, 395–423.
(46) Fayzrakhmanova, I. S.; Straube, A. V. *Physics of Fluids* **2009**, *21*, 072104.
(47) Perez, M.; Brechet, Y.; Salvo, L.; Papoular, M.; Suery, M. *Europhysics Letters* **1999**, *47*, 189–195.
(48) Noblin, X.; Buguin, A.; Brochard-Wyart, F. *The European Physical Journal E* **2004**, *14*, 395–404.
(49) Noblin, X.; Buguin, A.; Brochard-Wyart, F. *The European Physical Journal Special Topics* **2009**, *166*, 7–10.
(50) Sharp, J. S.; Farmer, D. J.; Kelly, J. *Langmuir* **2011**, *27*, 9367 – 9371.
(51) Ramalingam, S. K.; Basaran, O. A. *Physics of Fluids* **2010**, *22*, 112111.
(52) Jonáš, A.; Karadag, Y.; Tasaltin, N.; Kucukkara, I.; Kiraz, A. *Langmuir* **2011**, *27*, 2150–2154.
(53) Theisen, L. A.; Martin, S. J.; Hillman, A. R. *Analytical Chemistry* **2004**, *76*, 796–804.
(54) Decker, E. L.; Garoff, S. *Langmuir* **1996**, *12*, 2100–2110.
(55) Bormashenko, E.; Pogreb, R.; Whyman, G.; Bormashenko, Y.; Erlich, M. *Applied Physics Letters* **2007**, *90*, 201917–1–201917–2.
(56) Boreyko, J.; Chen, C.-H. *Physical Review Letters* **2009**, *103*, 174502–1–174502–4.

(57) Noblin, X.; Kofman, R.; Celestini, F. *Physical Review Letters* **2009**, *102*, 194504–1–194504–4.
(58) Dong, L.; Chaudhury, A.; Chaudhury, M. K. *The European Physical Journal E* **2006**, *21*, 231–242.
(59) Daniel, S.; Sircar, S.; Gliem, J.; Chaudhury, M. K. *Langmuir* **2004**, *20*, 4085–4092.
(60) John, K.; Thiele, U. *Physical Review Letters* **2010**, *104*, 107801–1–107801–4.
(61) Mettu, S.; Chaudhury, M. K. *Langmuir* **2011**, *27*, 10327–10333.
(62) Daniel, S.; Chaudhury, M. K.; De Gennes, P.-G. *Langmuir* **2005**, *21*, 4240–4248.
(63) Bisch, C. *Comptes rendus de l'Académie des sciences Paris - Série II* **1981**, *293*, 107–110.
(64) Adachi, K.; Takaki, R. *Journal of the Physics Society Japan* **1984**, *53*, 4184–4191.
(65) Takaki, R.; Adachi, K. *Journal of the Physics Society Japan* **1985**, *54*, 2462–2469.
(66) Takaki, R.; Katsu, A.; Arai, Y.; Adachi, K. *Journal of the Physics Society Japan* **1989**, *58*, 129–139.
(67) Takaki, R.; Yoshiyasu, N.; Arai, Y.; Adachi, K. In *Research of pattern formation*; Takaki, R., Ed.; KTK Scientific Publishers: Tokyo, 1994; pp. 363–375.
(68) Yoshiyasu, N.; Matsuda, K.; Takaki, R. *Journal of the Physical Society of Japan* **1996**, *65*, 2068–2071.
(69) Celestini, F.; Kofman, R. *Physical Review E* **2006**, *73*, 041602–1–6.
(70) Esposito, A.; Montello, A. D.; Guezennec, Y. G.; Pianese, C. *Journal of Power Sources* **2010**, *195*, 2691.
(71) Ramos, S. M. M. *Nuclear Instruments and Methods in Physics Research Section B: Beam Interactions with Materials and Atoms* **2008**, *266*, 3143–3147.
(72) Ghosh, S.; Sharma, P.; Bhattacharya, S. *Review of Scientific Instruments* **2007**, *78*, 115110.
(73) Moon, J. H.; Kang, B. H.; Kim, H.-Y. *Physics of Fluids* **2006**, *18*, 021702.
(74) Schmucker, J. A.; Osterhout, J. C.; White, E. B. *Experiments in Fluids* **2011**, *52*, 123–136.
(75) Schmucker, J. A.; White, E. B. *Journal of Fluid Mechanics* **2013**, *In Revisions*, 26 pages.
(76) Lin, Z.; Peng, X.; Wang, X. *Heat Transfer—Asian Research* **2006**, *35*, 13–19.

Chapter 6: Summary Conclusions and Future Directions

6.1 Summary and Conclusions

This thesis has studied some of the interactions of individual sessile drops with cross flowing air, for drops of hexadecane on Teflon coated glass, as well as drops of water on PMMA coated glass, Teflon coated glass, and a Teflon coated etched superhydrophobic surface (SHS) made from aluminum. Drop volumes from 0.5 to 100 μl were tested in a laminar wind tunnel. For the range of volumes tested, the contact angles were not seen to change significantly for a given system of liquid on solid. Drops were monitored by high speed videography and a modified floating element differential drag sensor.

Incipient motion (the onset of shedding) was the main cross flow/sessile drop interaction studied, first in terms of the critical air velocity for shedding (Chapter 2). Using a newly developed floating element differential drag sensor (Chapter 3), the drag forces imposed upon the drop were also studied (Chapter 4). Finally, the air flow induced oscillation of sessile drops was examined (Chapter 5) in relation to the broader, diffuse literature on sessile (or more general surface constrained) drop oscillation. Evaporation, internal circulation, and runback/breakup/(re)entrainment of the drop were not studied.

Critical air velocity, force, and oscillation measurements inform each other in terms of understanding the interactions of sessile drops with a cross flow. Conclusions here centre around the air speed and force for incipient motion, the broader relationship between force and airspeed, and differences due to varying fluid properties.

The wetting properties of drops were seen to have major influences on the airspeed and force necessary for reaching the point of incipient motion at which the drop begins to be shed from a surface by airflow. Adhesion force depends upon wetting parameters such as surface tension, contact angle, and drop shape, as well as drop size (here characterized in terms of length of contact line, with proxy measurement given by baselength measured in profile view). Drag force, which must overcome the maximum adhesion force in order to shed the drop, also depends on drop shape and size (here characterized by cross sectional area). Forces for shedding were comparable in magnitude to the gravitational shedding from a tilted plate and to simplified models for drop adhesion.

Scaling analysis was used to determine that the critical air velocity at which drag overcomes adhesion should scale with the ratio $(L_b/A)^{1/2}$ for any given value of contact angle. It was found, however, that this scaling follows an exponential rather than a linear relation. This indicates that the ratio $(k/C_D)^{1/2}$, also found by the scaling analysis to be important, must grow exponentially with $(L_b/A)^{1/2}$. Force measurements indicated that k

(an empirical parameter related to drop adhesion) is nearly constant with drop volume (i.e. nearly constant with $(L_b/A)^{1/2}$); force measurements also indicated that C_D (drag coefficient) indeed generally grows exponentially with $(L_b/A)^{1/2}$.

It was also found that curves of critical air velocity for shedding for all the water systems can be collapsed to a self similar master curve by means of normalizing by a reference value of $(L_b/A)^{1/2}$. The master curve also captured and explains results from other researchers. This may be related to the finding from force measurements that all systems and volumes follow generally similar relations for drag coefficient versus Reynolds number when Reynolds number is based on drop height. The HD-Teflon system (which also follows a similar C_D versus Re curve), did not collapse onto exactly the same master curve, which will be discussed later in terms of effects of fluid properties.

Measurements of critical airspeed indicated that more hydrophobic surfaces shed drops more easily, but could not indicate whether this was due to decreased adhesion, or increased drag force, due to the drops more spherical shape. Force measurements indicate that decreased adhesion is generally the more important consideration for shedding from SHS, since water drops on such surfaces in fact experience lower drag forces at the point of shedding compared to water on smooth Teflon. Shedding of water

from smooth Teflon is aided both by decreased adhesion and increased drag forces compared to water drops on more hydrophilic PMMA surfaces.

Critical airspeed (and force) for shedding were found not to be affected by wind tunnel vibrational noise. However, minimizing these background vibrations in the future would allow for more accurate measurements of drag force, and of drop oscillation growth rates, which may be important in terms of coupling to vortex shedding/increased wake drag.

The relationship between drag force and airspeed (or drag coefficient and Reynolds number) was found using the floating element differential drag sensor, but is informed by findings from the drop oscillation analysis. It was found that water on Teflon and water on the SHS experiences higher forces at any given value of airspeed. This is understood to be due to the increased cross sectional area/poorly aerodynamic shape of drops for this system. Drops of water on PMMA and hexadecane on Teflon experience similar forces at any given airspeed. Drops of hexadecane are shed at lower forces, while drops of water on PMMA are shed at forces higher than those for any of the other systems due to the increased adhesion of water on PMMA.

Non-dimensionalizing the results, it was found that all four systems follow the same general curve, though the onset of motion limits the range of Reynolds numbers considered for some of the systems, meaning that

behavior could change at the un-probed higher values. The general curve includes a roughly linear Stokesian decrease in drag coefficient at low Reynolds numbers, followed by a brief leveling near C_D~1, followed by an increase in drag coefficient starting at Reynolds numbers around 500-800.

This increase in drag coefficient was hypothesized to be due to aeroelastic coupling of the oscillating drop into the wake, increasing drag in a similar manner to what has been seen for free (non-surface constrained) drops. A slight increase in drag coefficients was also seen with increasing drop volume. As drop shape/contact angles are largely unchanged with volume for a given system, the increase is expected to be due to changes in internal circulation/oscillation with drop size, a theory that should be tested in the future. Increasing contact angle also slightly increases drag coefficient, indicating some effect of drop shape that is not captured by standard non-dimensionalization.

An investigation of fluid properties (such as surface tension, density, and viscosity) was made by studying hexadecane on Teflon along with the three water systems. Hexadecane on Teflon has a similar drop shape to water on PMMA. The Hexadecane-Teflon data (for force and air velocity for shedding) was adjusted by the difference in surface tension and drop shape. This caused the data to reach the same order of magnitude as water-PMMA data. However, the variation of air velocity and force for

shedding with increasing drop size were still dissimilar between the two systems. Similarly adjusted values of oscillation frequency closely match frequencies for water-PMMA, and as mentioned, the relationship between drag coefficient and Reynolds number was also nearly identical for Hexadecane-Teflon and water-PMMA. This indicates that bulk fluid properties, such as density and viscosity, do have an effect on the force/air velocity necessary for shedding.

Aside from measurements of air velocity for shedding and force versus airspeed, the experiments of this thesis have also compared contact angle measurements between air flow shedding tests, tilted plate shedding tests, and quasi-static advancing/receding tests. It was found that the three test types resulted in different contact angles. These differences should impact the adhesion force by which drops resist shedding by, e.g. cross flowing air and gravity, respectively. This was confirmed by subtle differences between measurements of the force for shedding by the two different types of tests. Therefore, it is stressed that models for drop shedding should always use contact angles measured using a suitable experimental methodology (i.e. one that mimics the expected conditions of shedding). Interestingly, the changes in contact angles between cross flow and quasi-static advancing/receding tests does not seem to affect frequency of oscillation, as the measurements presented in this thesis fall in line with data collected from literature.

Categorizing and collecting diffuse literature, low-order, medium-order, and high-order models for the contact angle dependent eigenvalue describing sessile drop oscillations have been gathered. The eigenvalue relates drop oscillation frequency to mode shape (thus relating bulk oscillation to surface oscillation). A unifying conceptual framework has also been presented based upon the literature review, clarifying bulk and surface modes of oscillation, their coupling for constrained drops, and numerating the modes of both axisymmetric and non-axisymmetric surface oscillations.

Full profile analysis techniques were developed and used to identify non-axisymmetric mode 1-1 oscillations at lower frequencies for sessile drops in cross flow, as well as a mix of axisymmetric mode 0-1 oscillations and non-axisymmetric mode 2-1 oscillations at approximately the same higher frequency. As stated above, in both cross flow and quiescent conditions, drops oscillate at similar frequencies, indicating little effect of the deformed drop shape. These new results were combined with collected literature results, with the combined data set used to test the collected models.

It was seen that none of the low-order models are sufficient, nor are the medium order models (even those which take into account the 2-D mode shape). High order models (based on the use of Legendre polynomials to decompose the mode shapes) were somewhat successful for mode 1-1

oscillations (seen as a lateral 'bending' mode), and very successful for mode 0-1 and 2-1 oscillations (seen as longitudinal modes), except at maximum and minimum contact angles. Until models are perfected, the collected literature data can serve as an empirical eigenvalue graph, and can aid in future tests of both the oscillation and shedding of sessile drops by cross flow.

6.2 Future Directions

Several future directions are possible based upon the work of this thesis. Having determined the airspeed and force for shedding, higher airspeeds and forces can be probed with stationary drops by pinning the drop to the surface via heterogeneities and/or roughness variation on the surface. This would allow systems, such as hexadecane on Teflon and water on the SHS, to be tested at higher airspeeds to determine if their behavior continues to follow that of water on PMMA and water on Teflon, respectively. Using a quieter tunnel (e.g. one driven by pressurized air) would allow the growth rate of drop oscillations to be determined, which could lead to greater knowledge of how drop oscillations are linked to the increase in drag force with increasing Reynolds number.

In addition, the possible effects of fluid properties (specifically, viscosity) on shedding and/or oscillation could be probed by testing silicone oils. A wider range of volumes and multiple drops could also be studied. Micro PIV could be used to study the drop's internal flow in such experiments.

PIV measurements could perhaps be made through transparent surfaces to avoid problems with lensing effects through the side of drops.

Improvements to the floating element differential drag sensor are also possible. Temporal and physical resolution of the sensor could be improved by making it an active, rather than passive sensor. Passive shear force sensors rely upon converting measurements of sensor deformation to measurements of force. Active shear force sensors use electronic monitoring and force actuation (through, e.g. magnetic or electrostatic force) to maintain the sensor surface at a fixed position, measuring force on the sensor by monitoring the necessary applied force to fix the sensor in position. The relatively smaller motion of the sensor surface permits a smaller gap in the floating element, which improves the flow characteristics/accuracy. The temporal response is also improved, as it is limited only by the electronic feedback system for active sensors, rather than by the natural frequency of passive sensors. Once these improvements are completed, further calibration tests of the sensor can be made, varying surface size, testing solid particles, etc, to quantify interference drag effects. Drag on other wall bound particles could also be investigated.

Having studied the incipient motion and oscillation of individual sessile drops, run back/breakup and (re)entrainment of drops are logical avenues of future study. Testing the impact of drops onto surfaces under airflow,

and their possible rebound, runback, etc. would also be interesting. Heat transfer and phase change could also be studied, with direct application to, e.g. aircraft icing. Studying sessile drops (or bubbles/other particles) interacting with a fluid outer phase would introduce potentially interesting effects in terms of changes in density and viscosity ratios between the inner and outer fluid. Finally, the 3-D profile measurements techniques currently under development by others could be used in conjunction with the floating element differential drag sensor both to verify measurements between the two systems, and to give further insight into the interactions of sessile drops with crossing flow.

Appendix A

A.1 Annotated Image of Wind Tunnel Setup, Supplemental to Section 2.3.1

Figure A-1 shows an annotated image of the wind tunnel setup. As labeled it shows: a) highspeed camera and lens, b) cold light source, c) diffuser, d) Labview DAQ board, e) laptop, f) fitted surface sample, g) streamlined body, h) cut-out through center of streamlined body for equipment access. Not shown in Figure A-1 are the pitot tubes, mounted just out of frame upstream, and laterally displaced from 'f'. Also not visible is the floating element differential drag sensor (see Chapters 3 and 4), which is mounted below, and connected to, 'f'.

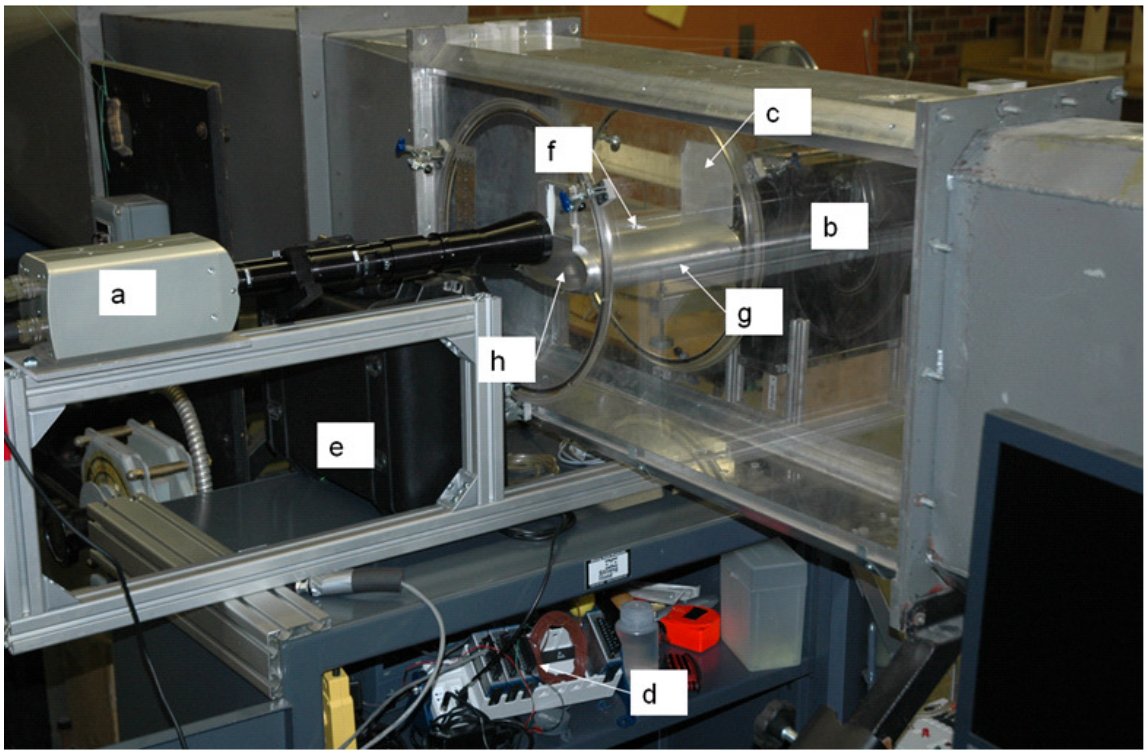

Figure A-1: Annotated image of the wind tunnel setup, with description in the text.

A.2 Illustrative Images from the Image Processing Routine, Supplemental to Section 2.3.4

Representative images from the image processing routine are given below, with descriptions in each images caption.

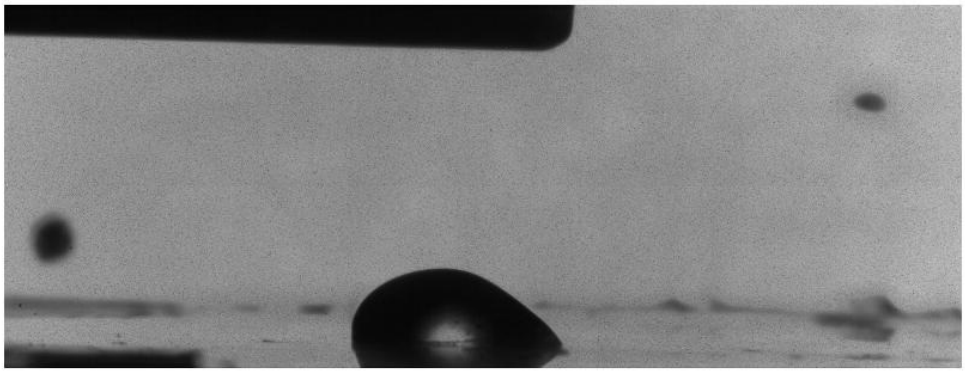

Figure A-2: Raw image (note pitot tube in top left, and registration marks on the wind tunnel side wall in top right and bottom left). Drop is past the point of incipient motion.

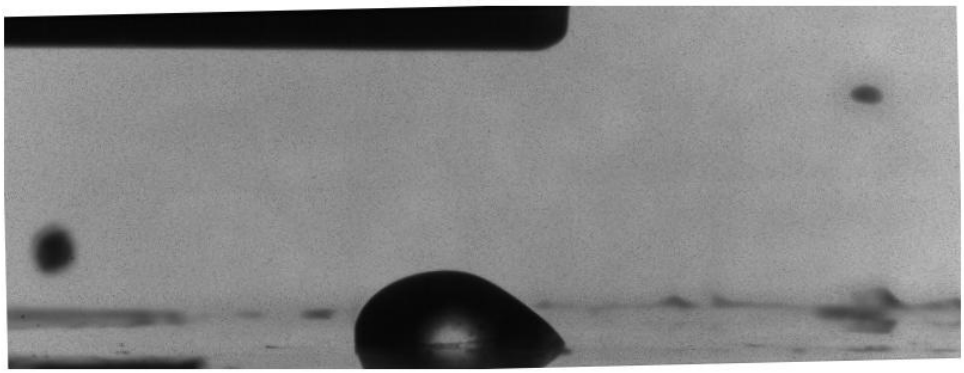

Figure A-3: Registered image (i.e. corrected for tilt/jitter of camera by means of the registration marks and two user input points which define the drop baseline in the original (quiescent) frame.

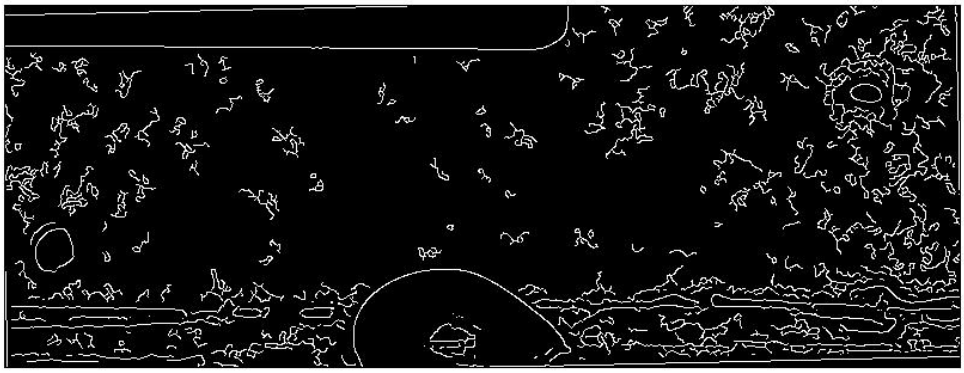

Figure A-4: Edges of registered image found.

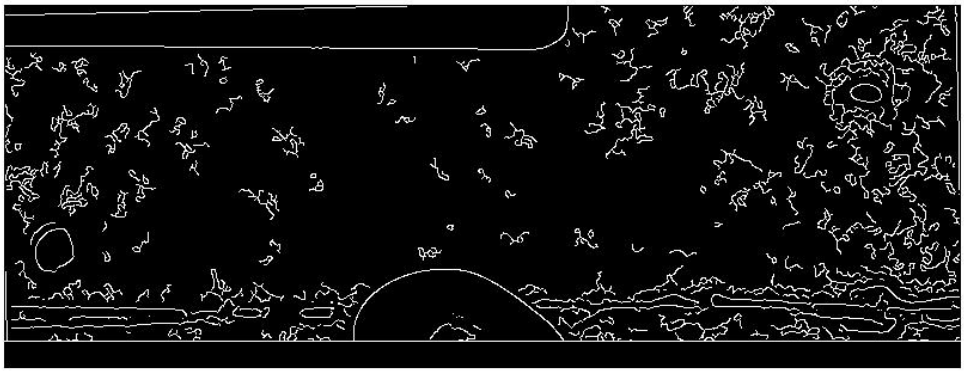

Figure A-5: User defined baseline drawn, and noise below this baseline removed.

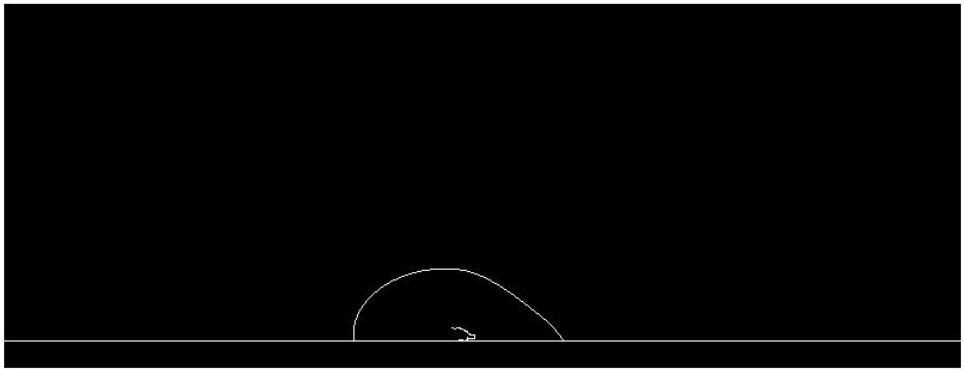

Figure A-6: Edges of drop found by searching outward from a user defined point inside the drop.

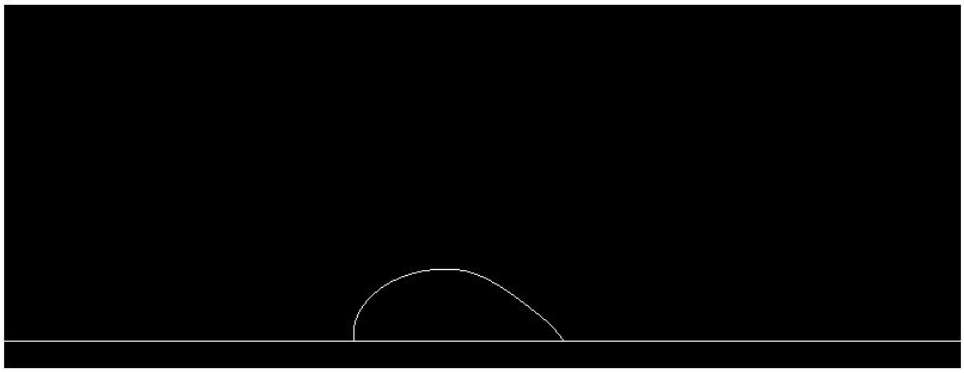

Figure A-7: Edge artifacts inside drop (caused by lensing effect) removed.

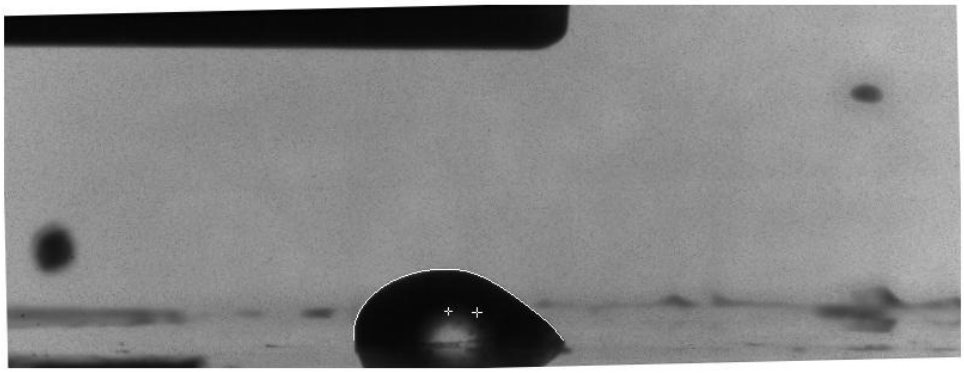

Figure A-8: Final image, drop profile traced in white and ready for determination of, e.g., location of baseline to determine point of incipient motion, or calculation of drop profile oscillation. Small cross inside drop denotes side view centroid. Large cross is user defined point inside drop (but outside light artifact) .

A.3 Reference Measurements (Force with Drop Absent), Supplemental to Section 3.5.2

Figure A-9 corresponds to Figure 3.9, but shows the individual reference measurements that were made for the water-Teflon system tests.

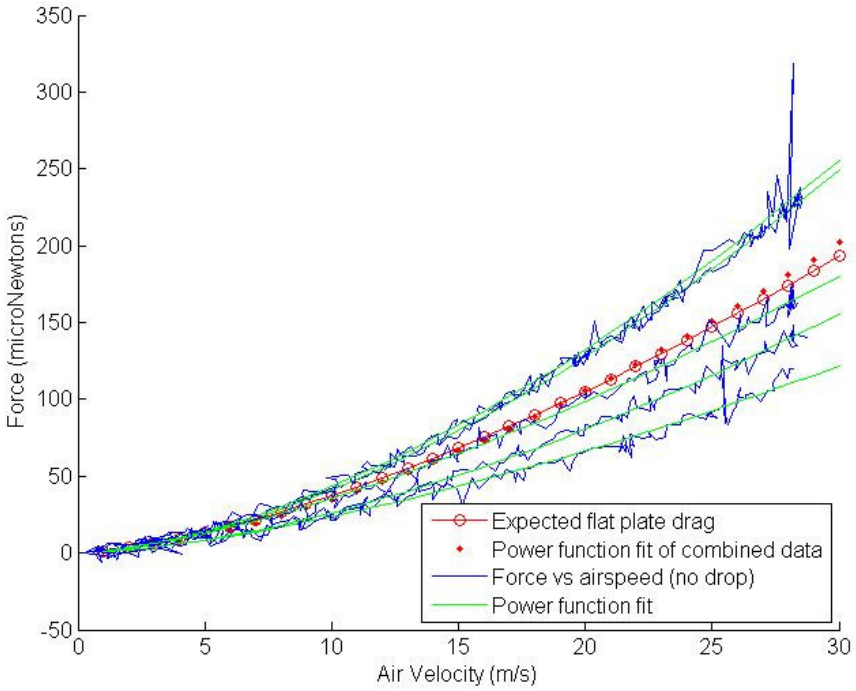

Figure A-9: Force measured by the floating element shear sensor (without drop present) versus airspeed measured 1 cm above surface for five different reference tests prior to water-Teflon tests. Also included are power law fits of each test, a power law fit of the combined data, and the expected force based on flat plate drag theory.

A.4 Force for Shedding, Supplemental to Sections 3.5.4 and 4.3

With the point of incipient motion found from high speed video analysis (see Chapter 2 and 3), the force for shedding can be determined. Figure A-10 shows the averaged results for each repetition for each volume and system. The drag force at the point of incipient motion is just sufficient to overcome the adhesion force between the drop and the surface. Also shown in Figure A-10 for comparison therefore is the gravitation force needed to overcome the adhesion of a drop on a tilted plate measurements for the same systems and similar volume ranges[1] without airflow present. As a proxy model for cross flow shedding, the

Furmidge model[2] for drop adhesion is also shown in Figure A-10. The Furmidge model:

$$F_{adh} = k \cdot L_b \cdot \gamma \cdot (\cos\theta_{\min} - \cos\theta_{\max}) \qquad \text{Equation A-1}$$

contains a fitting parameter, k, and further depends on *a posteriori* measurements of upstream, θ_{min}, and downstream, θ_{max}, contact angles of the drop as it begins to shed, as well as measurements of the drop baselength, L_b, measured in the quiescent state[1]. The fitting parameter was determined by minimizing the error for all measurements of drag force across volume for each system, using average values of maximum and minimum downstream and upstream contact angles. The second highest volume of the HD-Teflon system showed data that was considered to be an outlier. It was not used in determining the fit of the Furmidge model for the HD-Teflon system. As discussed in Chapter 4, the water-Teflon system also shows measurements of the force for shedding which may be an outlier. This data was also not used in the fit of the Furmidge model to that system.

It can be seen that the force for shedding generally increases monotonically with volume. The largest drop volumes for all four systems show a leveling off of force, however. We hypothesis this is due to the increased internal circulation/oscillation of larger drop affecting the external drag necessary to shed the drop. This leveling off could also possibly be caused by the large drops adopting a 'sausage' shape (i.e. a shape elongated along the surface perpendicularly to the direction of airflow) as observed in literature[3]. Some slight lateral elongation of the drop was observed by eye, but the elongation was not as

pronounced as in the previous literature[3], which leads us to forward our first hypothesis.

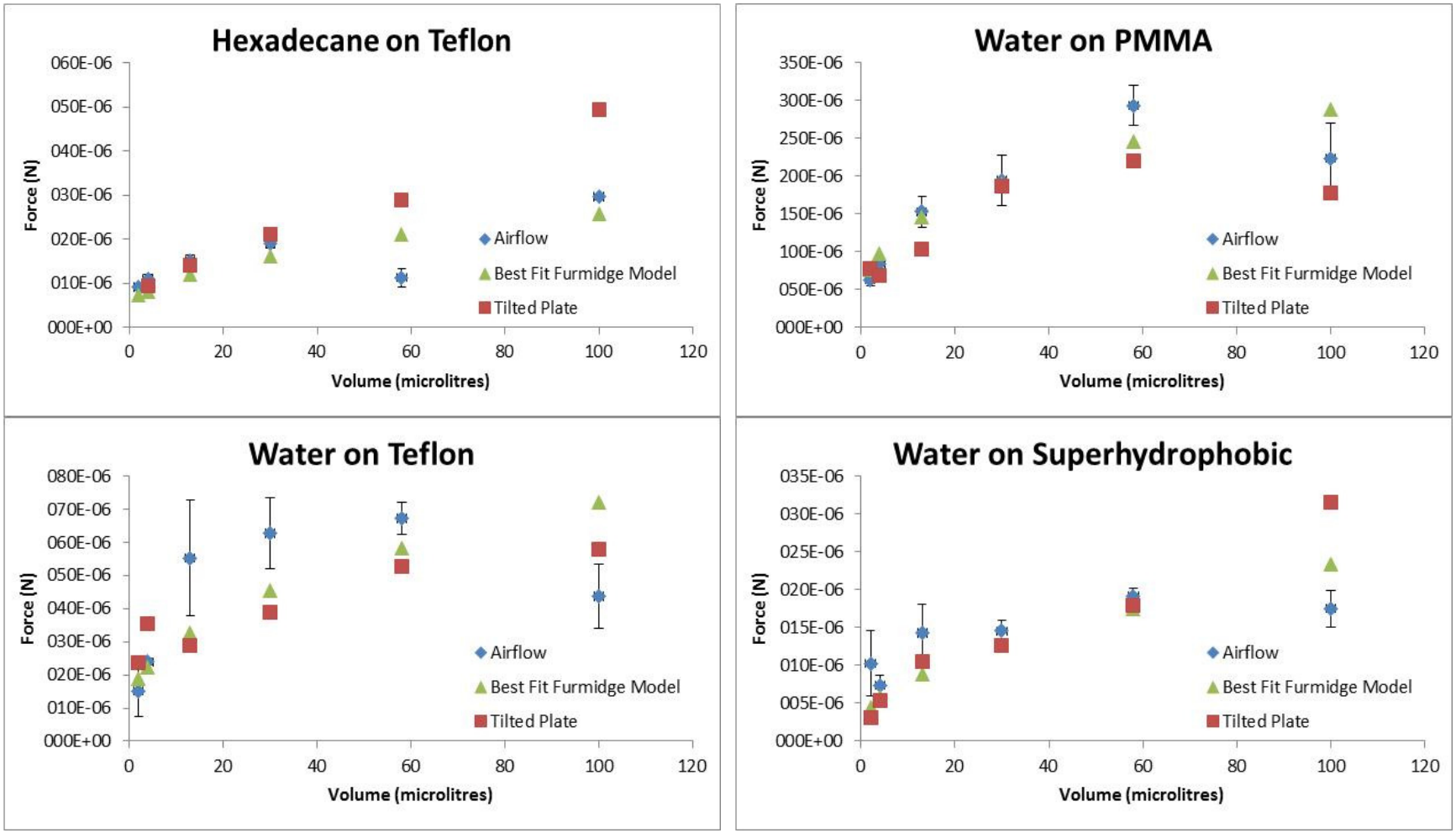

Figure A-10: Force to shed a drop versus drop volume for the four systems tested. Diamond symbols show air drag measured in the present work, triangles show the the Furmidge model[2] as a proxy model for drag measurements, squares are the gravitational force needed to shed a drop from a tilted plate measured previously for the same systems[1]. Error bars denote one standard deviation.

Comparing air drag measurements to gravitation force measurements from tilted plate tests shows that while the forces are of the same order of magnitude and general trend, the tilted plate measurements are almost universally monotonic, unlike for drops in cross flowing air. Drops on a tilted plate do not undergo internal flow, oscillation or inertial effects if the plate is tilted slowly, thus drops on a tilted plate are in a quasi-static state. The difference between the cross flow and tilted plate measurements therefore supports the theory that the interaction of the drops with the airflow changes the shedding conditions, by either or both of changing the shape/contact angle of the drop compared to a tilted plate test (as noted previously[1,4]), or by setting up an internal circulation/oscillation of the drop[5]. Further tests would be necessary to confirm the observation and determine its cause.

Given the tuning and necessary inputs to the Furmidge model, it is of limited utility in *a priori* predicting results in the present case. It was developed to explain the quasi-static gravitational shedding of drops on tilted plates, and the fact that it cannot capture the leveling off of force for shedding as volume increases lends more credence to the idea that air flow interactions do change drop shedding criteria compared to quasi-static cases. The differential drag measurement technique developed in this paper should facilitate further studies into the cause and implications of these changes.

Comparing results between systems, it is seen that more hydrophobic surfaces shed drops at lower forces, as expected[1]. Chapter 4 shows that the water-SHS and

water-Teflon systems experience similar, greater forces compared to the water-PMMA system for any given airspeed. However, the water-SHS requires much lower forces for shedding, followed by water-Teflon and water-PMMA. This change in ranking of forces means that both the adhesion force of the drop to the surface and the drag force experienced by the drop must be considered for their combined effect on shedding by cross flow.

Further comparisons between systems are possible due to the similar drop shape between HD-Teflon and water-PMMA, which permits more direct comparisons between the two. Results must be scaled to account for the difference in surface tensions of water and HD, they should also be scaled for the slight difference in contact angles, which can be approximately accounted for by considering the difference in the cosines of minimum upstream and maximum downstream contact angle[1]. Adjusting the HD-Teflon data by the ratio of water-air/HD-air surface tensions, and by the ratio of $(\cos(\theta_{water\text{-}PMMA\_Upstream})-\cos(\theta_{water\text{-}PMMA\_Downstream}))/(\cos(\theta_{HD\text{-}Teflon\_Upstream})-\cos(\theta_{HD\text{-}Teflon\_Downstream}))$, results in Figure A-11.

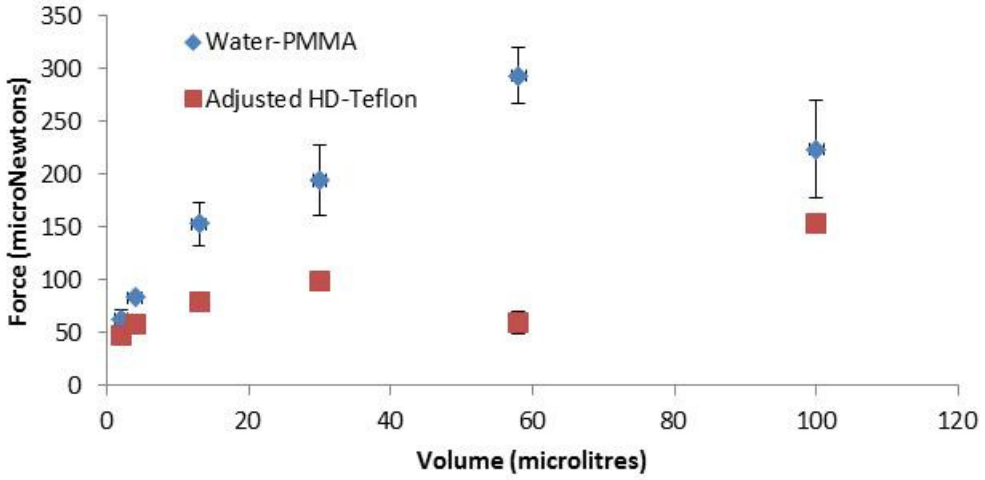

Figure A-11: Drag force to shed a sessile drop versus volume, showing raw data for drops of water on PMMA, and data for drops of Hexadecane on Teflon adjusted by the ratio of surface tensions and the slightly different contact angles as described in the text. Error bars denote one standard deviation.

Figure A-11 shows that the correction brings the HD-Teflon results to the same order of magnitude as the water-PMMA results, but that there are still differences in the trend, with water-PMMA (the less viscous system) showing a greater increase of force with increasing volume, and more of a leveling off/decrease in force at the highest volumes. This suggests that there could be effects of the viscosity and density differences between water and hexadecane, in terms of internal circulation, oscillation, etc., and that these in turn affect the necessary force to overcome adhesion and shed the drop. These topics will be left for future studies which can make use of the floating element differential drag technique for force measurements.

A.5 Force versus Air Velocity Showing All Volumes, Supplemental to Section 4.4

Figure A-12, on the next page, is a graph corresponding to Figure 4-2, showing force versus air velocity for the full range of drop volumes.

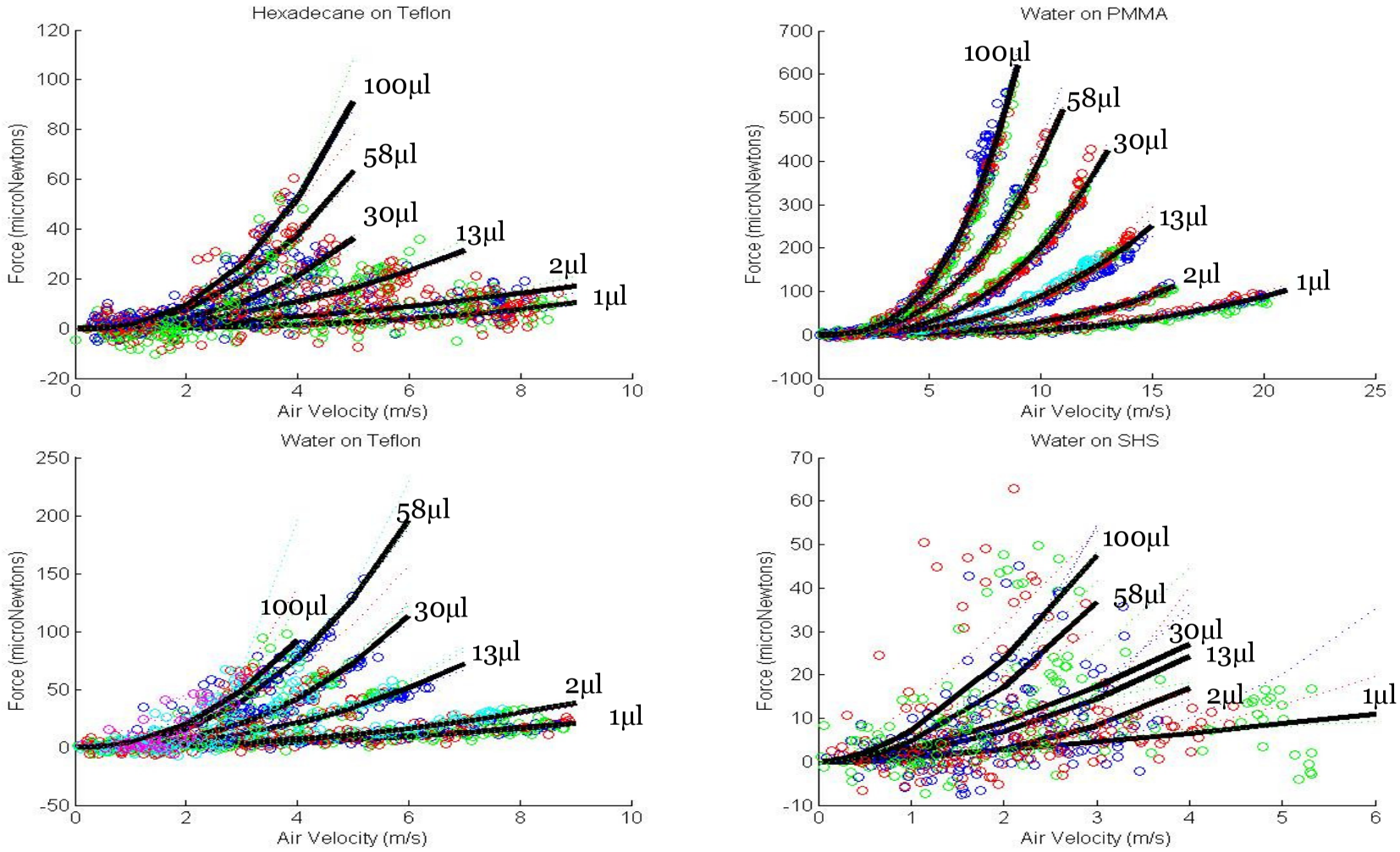

Figure A-12: Force versus air velocity for different drop volumes for each system calculated using the differential drag technique (i.e. corrected to remove the drag on the surface). The differently coloured data points (available in the electronic version) denote different repetitions of the tests. Dotted lines are power law fits to individual tests, solid lines are fits to the collected data for each volume.

A.6 Non-Dimensionalization of Drag versus Air Velocity, Supplemental to Section 4.5

As stated in Section 4.5, the best non-dimensionalizing of the relationship between drag force and air velocity is given by casting the Reynolds number in terms of drop height. Alternatively, air velocity can be non-dimensionalized using drop spherical cap radius as a reference length as is done here. The coefficient of drag, C_D, is still defined by:

$$F_D = \frac{1}{2}\rho U_\infty{}^2 C_D A \qquad \text{Equation A-2}$$

where F_D is the drag force, ρ is air density, U_∞, is the free stream air velocity, and A is a reference area of the drop (here taken to be the cross sectional area of the axisymmetric drop measured in quiescent conditions). The Reynolds number is defined by:

$$\mathrm{Re}_R = \frac{\rho U_\infty R}{\mu} \qquad \text{Equation A-3}$$

where R is the spherical cap radius of the axisymmetric drop measured in quiescent conditions and μ is the viscosity of air.

As in Chapter 4, Equation A-2 and A-3 do not account for drop properties, contact angle, oscillation/internal circulation of the drops, or the deformation of drops away from axisymmetric as velocity increases from quiescent. As discussed in Chapter 4, much knowledge can still be gained from such non-dimensionalizations.

Figure A-13 presents drag coefficient versus Reynolds number for all drop volumes for the four systems tested, for Reynolds numbers corresponding to the range of near quiescent to just past incipient motion (similar to Figure 4-2). As in Chapter 4, point by point calculations of drag coefficient and Reynolds number were made, rather than relying on the power law fits of Figure 4-2.

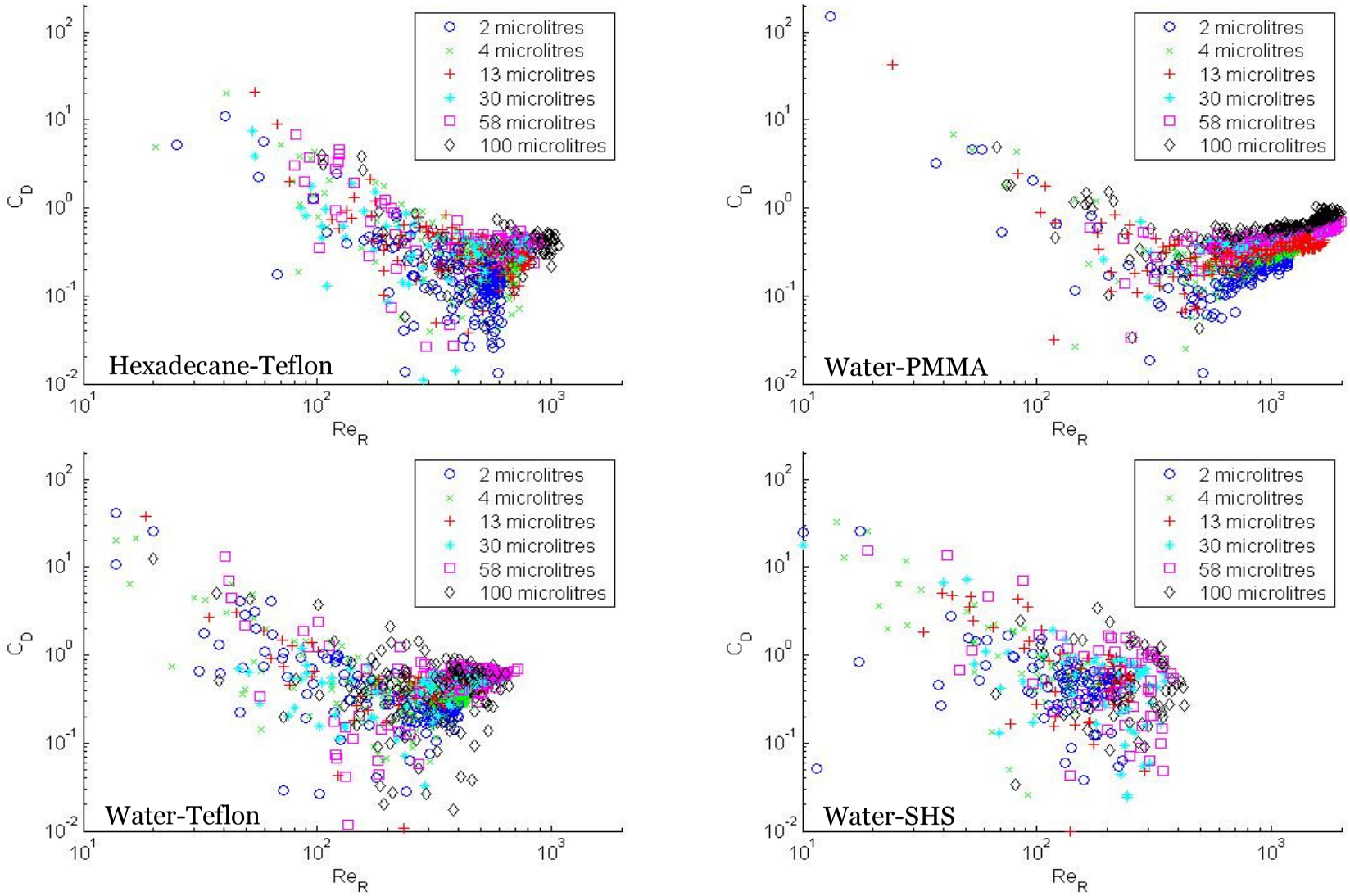

Figure A-13: Coefficient of drag versus Reynolds number based on drop spherical cap radius for sessile drops in cross flowing air for the four liquid-on-solid-surface systems tested.

Considering Figure A-13 in total, it is seen that drag coefficient does not generally level off with Reynolds number, with most relations showing either a roughly linear decrease or more often a decrease followed by brief leveling and then an increase in drag coefficient with Reynolds number. The roughly linear decrease can be ascribed to Stokesian drag behavior for the drops, and as discussed in Chapter 4, the increase is ascribed to aeroelastic coupling between the oscillating drop and the wake causing vortex shedding and increased drag[6,7].

Since Figure A-13 shows the same data as Chapter 4, only recast, it can still be seen that increasing volumes show a shift to higher drag coefficients (most clearly seen for the water-PMMA system, but also seen in general for the other systems). Comparing specific graphs in Figure A-13 it is immediately seen that each system presents somewhat different relationships between drag coefficient and Reynolds number, with the HD-Teflon and water-PMMA systems showing similar results, and the water-Teflon and water-SHS systems likewise showing somewhat similar results to each other, but different results from the other two systems in terms of the slope of the Stokesian region and the Reynolds number for minimum coefficient of drag. This mirrors the finding of similar relationships between force and airspeed for the two sets of systems, and led to the more successful non-dimensionalization by drop height as discussed in detail in Chapter 4.

For the sake of completeness and comparison, Figure A-14 shows the non-dimensionalized relations between drag and air velocity in a manner similar to Figure A-13 but with Reynolds number cast with drop height as the reference

length, as discussed in Section 4.5. It is identical data to that shown in Figure 4-5, organized to show all volumes together on four separate plots (one for each volume). As can be seen, comparing Figure A-14 and Figure A-13, the Reynolds number based on drop height better collapses the results for different systems.

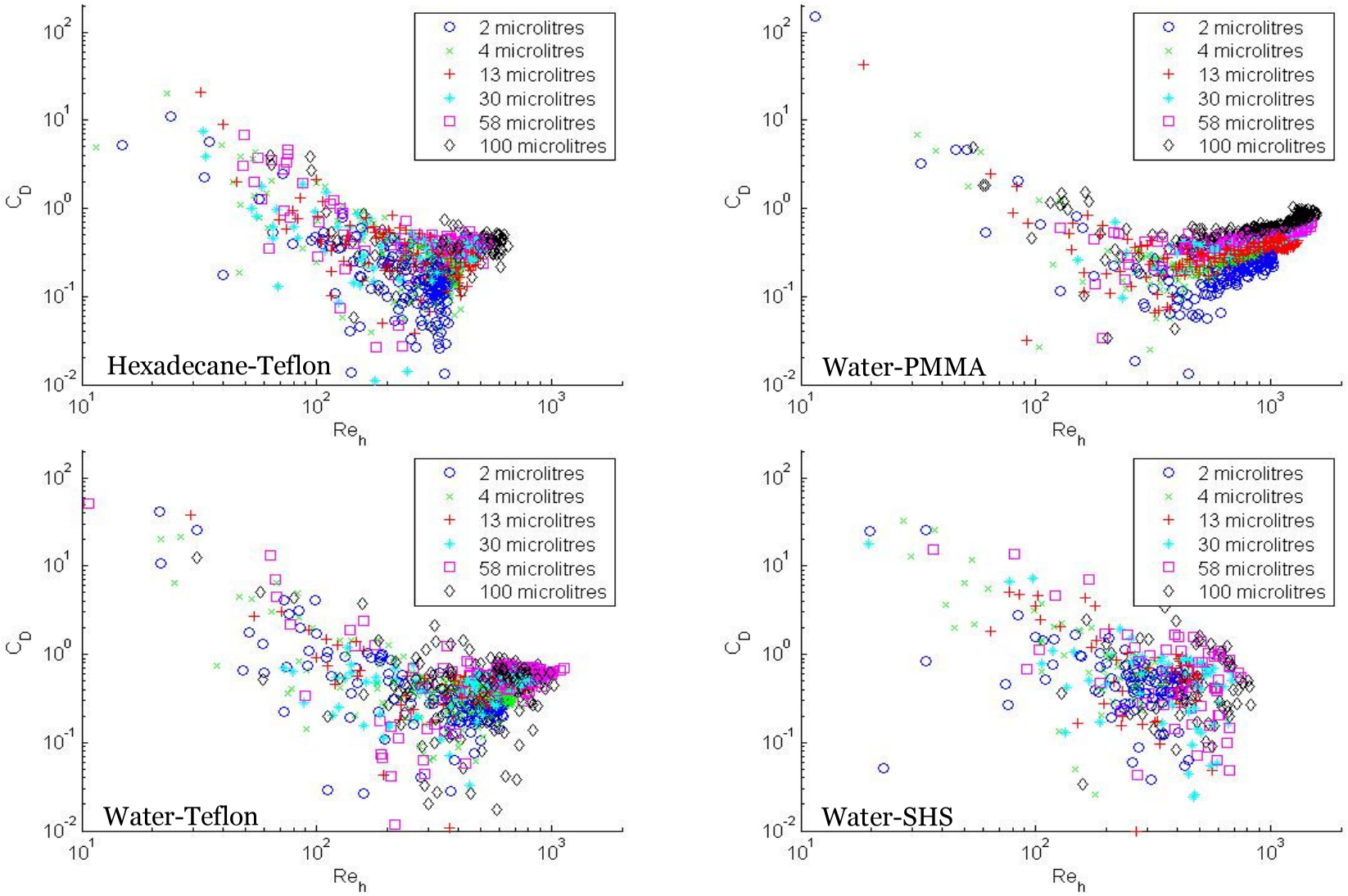

Figure A-14: Coefficient of drag versus Reynolds number based on drop height for sessile drops in cross flowing air for the four liquid-on-solid-surface systems tested.

As mentioned in Section 4.5, quiescent measurements of geometric properties (drop heigh and cross sectional (equal to frontal) area) were used in non-dimensionalizing data. Table A-1 through Table A-4 give these and other geometric parameters, along with averaged measured values of contact angle near the point of incipient motion, and averaged measured values of critical air velocity (measured 1 cm above the streamlined surface) and force at the point of incipient motion.

Table A-1: Geometric and other parameters for tests of hexadecane on Teflon

HD-Teflon Volume (µl)	θ_{max} (°)	θ_{min} (°)	Spherical Cap Drop Radius (m)	Spherical Cap Height (m)	Area (m^2)	Baselength (m)	Critical Air Velocity (m/s)	Standard Deviation of Air Velocity (m/s)	Critical Force (µN)	Standard Deviation of Force (µN)
2	66.0	55.0	1.31E-03	7.78E-04	1.68E-06	2.72E-03	7.69	2.37E-01	9.20E+00	7.34E-01
4	64.2	54.3	1.70E-03	9.61E-04	2.08E-06	3.05E-03	6.89	1.98E-01	1.11E+01	9.41E-01
13	66.0	54.7	2.45E-03	1.45E-03	4.10E-06	4.48E-03	4.95	2.64E-01	1.51E+01	1.21E+00
30	67.8	50.8	3.15E-03	1.96E-03	6.93E-06	6.05E-03	3.97	1.46E-01	1.89E+01	8.42E-01
58	66.8	53.5	3.98E-03	2.41E-03	1.04E-05	7.91E-03	2.74	2.58E-01	1.13E+01	2.05E+00
100	66.7	48.3	4.78E-03	2.89E-03	1.40E-05	9.69E-03	3.11	2.79E-01	2.97E+01	6.34E-01

Table A-2: Geometric and other parameters for tests of water on PMMA

Water-PMMA Volume (μl)	θ_{max} (°)	θ_{min} (°)	Spherical Cap Drop Radius (m)	Spherical Cap Height (m)	Area (m^2)	Baselength (m)	Critical Air Velocity (m/s)	Standard Deviation of Air Velocity (m/s)	Critical Force (μN)	Standard Deviation of Force (μN)
2	82.5	51.0	1.06E-03	9.21E-04	1.48E-06	2.20E-03	17.91	1.89E-01	6.35E+01	8.04E+00
4	73.2	54.2	1.49E-03	1.06E-03	2.33E-06	2.83E-03	14.52	2.93E-01	8.33E+01	3.17E+00
13	76.8	55.5	2.11E-03	1.63E-03	4.60E-06	4.22E-03	12.27	7.02E-01	1.53E+02	2.00E+01
30	77.6	53.2	2.76E-03	2.17E-03	7.41E-06	5.49E-03	9.84	6.00E-01	1.94E+02	3.31E+01
58	76.0	49.8	3.50E-03	2.66E-03	1.16E-05	7.07E-03	8.81	4.69E-01	2.94E+02	2.61E+01
100	78.3	48.5	4.09E-03	3.26E-03	1.53E-05	8.30E-03	6.31	4.66E-01	2.24E+02	4.66E+01

Table A-3: Geometric and other parameters for tests of water on Teflon

Water-Teflon Volume (μl)	θ_{max} (°)	θ_{min} (°)	Spherical Cap Drop Radius (m)	Spherical Cap Height (m)	Area (m^2)	Baselength (m)	Critical Air Velocity (m/s)	Standard Deviation of Air Velocity (m/s)	Critical Force (μN)	Standard Deviation of Force (μN)
2	123.6	110.4	8.18E-04	1.27E-03	1.90E-06	1.64E-03	7.76	4.26E-01	1.52E+01	7.88E+00
4	125.1	111.5	1.03E-03	1.62E-03	2.64E-06	1.94E-03	7.05	3.16E-01	2.39E+01	1.07E+00
13	124.5	106.7	1.52E-03	2.38E-03	5.52E-06	2.86E-03	4.99	3.31E-01	5.54E+01	1.75E+01
30	123.7	106.9	2.02E-03	3.13E-03	9.52E-06	3.99E-03	3.82	2.29E-01	6.28E+01	1.08E+01
58	125.3	105.5	2.50E-03	3.95E-03	1.42E-05	5.08E-03	2.99	7.67E-01	6.73E+01	4.81E+00
100	123.4	102.1	3.01E-03	4.68E-03	2.00E-05	6.29E-03	2.54	7.51E-01	4.38E+01	9.53E+00

Table A-4: Geometric and other parameters for tests of water on the superhydrophobic surface (HCl acid etched, Teflon coated aluminum)

Water-SHS Volume (µl)	θ_{max} (°)	θ_{min} (°)	Spherical Cap Drop Radius (m)	Spherical Cap Height (m)	Area (m^2)	Baselength (m)	Critical Air Velocity (m/s)	Standard Deviation of Air Velocity (m/s)	Critical Force (µN)	Standard Deviation of Force (µN)
2	161.9	142.6	7.82E-04	1.53E-03	2.10E-06	9.38E-04	4.61	1.05E+00	1.10E+01	4.28E+00
4	162.0	133.7	9.85E-04	1.92E-03	2.91E-06	1.22E-03	4.54	3.98E-01	1.03E+01	1.36E+00
13	162.5	125.3	1.46E-03	2.85E-03	5.81E-06	1.86E-03	3.06	4.28E-01	7.40E+00	3.74E+00
30	161.0	116.4	1.93E-03	3.75E-03	9.77E-06	2.66E-03	3.17	4.12E-01	1.43E+01	1.46E+00
58	161.3	123.9	2.40E-03	4.68E-03	1.47E-05	3.64E-03	2.61	2.56E-01	1.46E+01	1.06E+00
100	160.0	129.0	2.88E-03	5.59E-03	2.06E-05	4.89E-03	2.47	4.10E-01	1.92E+01	2.45E+00

A.7 Letters of Permission for Copyrighted or Co-Authored Work

The permission letter on the next page was given related to Figure 4-6, taken from Clift, Grace, and Weber[6]. As a note, Dr. Clift and Dr. Grace gave permission for this use as well through personal communication. Sadly, Dr. Weber passed away in 2008.

UNIVERSITY OF ALBERTA

Andrew Milne <ajmilne@ualberta.ca>

Dover Publications: Permission to use Figure

13 messages

Schwendemann, Joann <jschwendemann@doverpublications.com> Tue, Jan 22, 2013 at 8:58 AM
To: "ajmilne@ualberta.ca" <ajmilne@ualberta.ca>

Dear Andrew,

Dover Publications, Inc., hereby grants you permission to reproduce the following material for your upcoming thesis:

Figure 7.2 of "Bubbles, Drops, and Particles" by R. Clifty, J. R. Grace, and M. E. Weber, ISBN 0-486-44580-1

Please give appropriate credit to the authors, title and publisher of the edition in any standard form.

Sincerely,
Joann Schwendemann

Joann Schwendemann
Contracts/Rights & Permissions
Dover Publications, Inc.
31 East 2nd Street
Mineola, NY 11501
Tel: 516-294-7000 x 164
Fax: 516-746-1821
jschwendemann@doverpublications.com

From: Andrew Milne [mailto:ajmilne@ualberta.ca]
Sent: Monday, January 21, 2013 2:09 PM
To: r.clift@surrey.ac.uk; jgrace@chbe.ubc.ca; Diana_Grey
Subject: Permission to use Figure

Hello,

My name is Andrew Milne, I am a PhD Candidate at the University of Alberta. I am currently writing up my thesis, and am seeking permission to use one of the figures from one of your works as it relates to my research. Specifically, I am seeking permission to use Figure 7.2 of "Bubbles, Drops, and Particles" by R. Clifty, J. R. Grace, and M. E. Weber, ISBN 0-486-44580-1. I would use this figure in my thesis, which would be available to the public through the University of Alberta, through Canada's national library, and through an electronic archive run by the University. I would also, with permission, use this figure in a journal publication based on my thesis chapter.

Please note, I have copied this email both to the surviving original authours, since the bibliographic data indicates it it they who hold copyright to the work, and to Dover Publications, as they are the publishers. My condolences, Professors, on the loss of Dr. Weber.

My use of the figure would be only for illustrative purposes, and would be treated in a positive light. Figure 7.2 describes the difference in drag coefficient for free floating drops compared to solid particles. I have seen a similar behaviour in my research studying sessile (wall contrained) drops, and wish to set my research in the proper context which your excellent book has provided.

I look forward to your response, and would appreciate knowing your decision soon, as I will be defending my thesis in early March.

Many thanks,

Andrew Milne

The permission letter on the following pages was given related to Figure 5.2, taken from Chiba et al.[8]

ELSEVIER LICENSE
TERMS AND CONDITIONS

Feb 02, 2013

This is a License Agreement between Andrew J B Milne ("You") and Elsevier ("Elsevier") provided by Copyright Clearance Center ("CCC"). The license consists of your order details, the terms and conditions provided by Elsevier, and the payment terms and conditions.

All payments must be made in full to CCC. For payment instructions, please see information listed at the bottom of this form.

Supplier	Elsevier Limited The Boulevard,Langford Lane Kidlington,Oxford,OX5 1GB,UK
Registered Company Number	1982084
Customer name	Andrew J B Milne
Customer address	4-9 Mechanical Engineering Building Edmonton, AB T5K 1T4
License number	3081110784761
License date	Feb 02, 2013
Licensed content publisher	Elsevier
Licensed content publication	Journal of Sound and Vibration
Licensed content title	Free vibration of a spherical liquid drop attached to a conical base in zero gravity
Licensed content author	M. Chiba,S. Michiue,I. Katayama
Licensed content date	9 April 2012
Licensed content volume number	331
Licensed content issue number	8
Number of pages	18
Start Page	1908
End Page	1925
Type of Use	reuse in a thesis/dissertation
Portion	figures/tables/illustrations
Number of figures/tables /illustrations	3
Format	both print and electronic
Are you the author of this Elsevier article?	No
Will you be translating?	No
Order reference number	
Title of your thesis/dissertation	Blown Away: The Shedding and Oscillation of Sessile Drops by Shearing Airflow

Expected completion date	Feb 2013
Estimated size (number of pages)	200
Elsevier VAT number	GB 494 6272 12
Permissions price	0.00 USD
VAT/Local Sales Tax	0.0 USD / 0.0 GBP
Total	0.00 USD
Terms and Conditions	

INTRODUCTION

1. The publisher for this copyrighted material is Elsevier. By clicking "accept" in connection with completing this licensing transaction, you agree that the following terms and conditions apply to this transaction (along with the Billing and Payment terms and conditions established by Copyright Clearance Center, Inc. ("CCC"), at the time that you opened your Rightslink account and that are available at any time at http://myaccount.copyright.com).

GENERAL TERMS

2. Elsevier hereby grants you permission to reproduce the aforementioned material subject to the terms and conditions indicated.

3. Acknowledgement: If any part of the material to be used (for example, figures) has appeared in our publication with credit or acknowledgement to another source, permission must also be sought from that source. If such permission is not obtained then that material may not be included in your publication/copies. Suitable acknowledgement to the source must be made, either as a footnote or in a reference list at the end of your publication, as follows:

"Reprinted from Publication title, Vol /edition number, Author(s), Title of article / title of chapter, Pages No., Copyright (Year), with permission from Elsevier [OR APPLICABLE SOCIETY COPYRIGHT OWNER]." Also Lancet special credit - "Reprinted from The Lancet, Vol. number, Author(s), Title of article, Pages No., Copyright (Year), with permission from Elsevier."

4. Reproduction of this material is confined to the purpose and/or media for which permission is hereby given.

5. Altering/Modifying Material: Not Permitted. However figures and illustrations may be altered/adapted minimally to serve your work. Any other abbreviations, additions, deletions and/or any other alterations shall be made only with prior written authorization of Elsevier Ltd. (Please contact Elsevier at permissions@elsevier.com)

6. If the permission fee for the requested use of our material is waived in this instance, please be advised that your future requests for Elsevier materials may attract a fee.

7. Reservation of Rights: Publisher reserves all rights not specifically granted in the combination of (i) the license details provided by you and accepted in the course of this licensing transaction, (ii) these terms and conditions and (iii) CCC's Billing and Payment terms and conditions.

8. License Contingent Upon Payment: While you may exercise the rights licensed immediately upon issuance of the license at the end of the licensing process for the transaction, provided that you have disclosed complete and accurate details of your proposed use, no license is finally effective unless and until full payment is received from you (either by publisher or by CCC) as provided in CCC's Billing and Payment terms and conditions. If full payment is not received on a timely basis, then any license preliminarily granted shall be deemed automatically revoked and shall be void as if never granted. Further, in the event that you breach any of these terms and conditions or any of CCC's Billing and Payment terms and conditions, the license is automatically revoked and shall be void as if never granted. Use of materials as described in a revoked license, as well as any use of the materials beyond the scope of an unrevoked license, may constitute copyright infringement and publisher reserves the right to take any and all action to protect its copyright in the materials.

9. Warranties: Publisher makes no representations or warranties with respect to the licensed material.

10. Indemnity: You hereby indemnify and agree to hold harmless publisher and CCC, and their respective officers, directors, employees and agents, from and against any and all claims arising out of your use of the licensed material other than as specifically authorized pursuant to this license.

11. No Transfer of License: This license is personal to you and may not be sublicensed, assigned, or transferred by you to any other person without publisher's written permission.

12. No Amendment Except in Writing: This license may not be amended except in a writing signed by both parties (or, in the case of publisher, by CCC on publisher's behalf).

13. Objection to Contrary Terms: Publisher hereby objects to any terms contained in any purchase order, acknowledgment, check endorsement or other writing prepared by you, which terms are inconsistent with these terms and conditions or CCC's Billing and Payment terms and conditions. These terms and conditions, together with CCC's Billing and Payment terms and conditions (which are incorporated herein), comprise the entire agreement between you and publisher (and CCC) concerning this licensing transaction. In the event of any conflict between your obligations established by these terms and conditions and those established by CCC's Billing and Payment terms and conditions, these terms and conditions shall control.

14. Revocation: Elsevier or Copyright Clearance Center may deny the permissions described in this License at their sole discretion, for any reason or no reason, with a full refund payable to you. Notice of such denial will be made using the contact information provided by you. Failure to receive such notice will not alter or invalidate the denial. In no event will Elsevier or Copyright Clearance Center be responsible or liable for any costs, expenses or damage incurred by you as a result of a denial of your permission request, other than a refund of the amount(s) paid by you to Elsevier and/or Copyright Clearance Center for denied permissions.

LIMITED LICENSE

The following terms and conditions apply only to specific license types:

15. **Translation**: This permission is granted for non-exclusive world **English** rights only unless your license was granted for translation rights. If you licensed translation rights you may only translate this content into the languages you requested. A professional translator must perform all translations and reproduce the content word for word preserving the integrity of the article. If this license is to re-use 1 or 2 figures then permission is granted for non-exclusive world rights in all languages.

16. **Website**: The following terms and conditions apply to electronic reserve and author websites:
Electronic reserve: If licensed material is to be posted to website, the web site is to be password-protected and made available only to bona fide students registered on a relevant course if:
This license was made in connection with a course,
This permission is granted for 1 year only. You may obtain a license for future website posting,
All content posted to the web site must maintain the copyright information line on the bottom of each image,
A hyper-text must be included to the Homepage of the journal from which you are licensing at http://www.sciencedirect.com/science/journal/xxxxx or the Elsevier homepage for books at http://www.elsevier.com , and
Central Storage: This license does not include permission for a scanned version of the material to be stored in a central repository such as that provided by Heron/XanEdu.

17. **Author website** for journals with the following additional clauses:

All content posted to the web site must maintain the copyright information line on the bottom of each image, and the permission granted is limited to the personal version of your paper. You are not allowed to download and post the published electronic version of your article (whether PDF or HTML, proof or final version), nor may you scan the printed edition to create an electronic version. A hyper-text must be included to the Homepage of the journal from which you are licensing at http://www.sciencedirect.com/science/journal/xxxxx . As part of our normal production process, you will receive an e-mail notice when your article appears on Elsevier's online service ScienceDirect (www.sciencedirect.com). That e-mail will include the article's Digital Object Identifier (DOI). This number provides the electronic link to the published article and should be included in the posting of your personal version. We ask that you wait until you receive this e-mail and have the DOI to do any posting.

Central Storage: This license does not include permission for a scanned version of the material to be stored in a central repository such as that provided by Heron/XanEdu.

18. **Author website** for books with the following additional clauses:
Authors are permitted to place a brief summary of their work online only.
A hyper-text must be included to the Elsevier homepage at http://www.elsevier.com . All content posted to the web site must maintain the copyright information line on the bottom of each image. You are not allowed to download and post the published electronic version of your chapter, nor may you scan the printed edition to create an electronic version.

Central Storage: This license does not include permission for a scanned version of the material to be stored in a central repository such as that provided by Heron/XanEdu.

19. **Website** (regular and for author): A hyper-text must be included to the Homepage of the journal from which you are licensing at http://www.sciencedirect.com/science/journal/xxxxx. or for books to the Elsevier homepage at http://www.elsevier.com

20. **Thesis/Dissertation**: If your license is for use in a thesis/dissertation your thesis may be submitted to your institution in either print or electronic form. Should your thesis be published commercially, please reapply for permission. These requirements include permission for the Library and Archives of Canada to supply single copies, on demand, of the complete thesis and include permission for UMI to supply single copies, on demand, of the complete thesis. Should your thesis be published commercially, please reapply for permission.

21. **Other Conditions**:

v1.6

If you would like to pay for this license now, please remit this license along with your payment made payable to "COPYRIGHT CLEARANCE CENTER" otherwise you will be invoiced within 48 hours of the license date. Payment should be in the form of a check or money order referencing your account number and this invoice number RLNK500948643.
Once you receive your invoice for this order, you may pay your invoice by credit card. Please follow instructions provided at that time.

Make Payment To:
Copyright Clearance Center
Dept 001
P.O. Box 843006
Boston, MA 02284-3006

For suggestions or comments regarding this order, contact RightsLink Customer Support: customercare@copyright.com or +1-877-622-5543 (toll free in the US) or +1-978-646-2777.

Gratis licenses (referencing $0 in the Total field) are free. Please retain this printable license for your reference. No payment is required.

The following permission was given by the co-authors of Chapter 5, Dr. Miguel Cabrerizo Vilchez and Dr. Beatriz Defez Garcia. As co-supervisors of my theis, Dr. Alidad Amirfazli and Dr. Brian Fleck have not included letters, and have instead approved of the entire thesis through the examination process of the University of Alberta.

UNIVERSITAT POLITÈCNICA DE VALÈNCIA

Valencia, 1 February 2013

To whom it may concern:

As a co-author with Andrew James Milne on a work submitted for publication in an academic journal, I, **Beatriz Defez García**, hereby grant permission for Andrew James Milne to include our combined work on sessile drop oscillation in his thesis as he sees fit. Andrew is the main author/investigator in this work, warranting its inclusion in the main body of his thesis as a testament to the work he has completed during his degree.

Yours faithfully,

Beatriz Defez
Professor of the Department of Graphics Engineering
Universitat Politècnica de Valencia

Universitat Politècnica de València, Camino de Vera S/N, 46022, Valencia.
+34963879518; bdefez@degi.upv.es

Miguel Cabrerizo Vílchez
Departamento de Física Aplicada
Facultad de Ciencias
Universidad de Granada

To whom it may concern:

As a co-author with Andrew James Milne on a work submitted for publication in an academic journal, I, Miguel Cabrerizo Vilchez, hereby grant permission for Andrew James Milne to include our combined work on sessile drop oscillation in his thesis as he sees fit. Andrew is the main author/investigator in this work, warranting its inclusion in the main body of his thesis as a testament to the work he has completed during his degree.

Sincerely,

Miguel C.
Professor
University of Granada

Fuentenueva sn 18071 Granada (Spain) mcabre@ugr.es Telf./fax (34) 958243211/4

References to Appendix A

(1) Milne, A. J. B.; Amirfazli, A. *Langmuir* **2009**, *25*, 14155–14164.
(2) Furmidge, C. G. . *Journal of Colloid Science* **1962**, *17*, 309–324.
(3) Bico, J.; Basselièvre, F.; Mermigier, M. In *Bulletin of the American Physical Society*; American Physical Society: Chicago, IL, 2005.
(4) Schmucker, J. A.; White, E. B. *Journal of Fluid Mechanics* **2013**, *In Revisions*, 26 pages.
(5) Minor, G. Experimental Study of Water Droplet Flows in a Model PEM Fuel Cell Gas Microchannel. MASc, University of Victoria, 2007.
(6) Clift, R.; Grace, J. R.; Weber, M. E. In *Bubbles, drops, and particles*; Dover Publications: Mineola N.Y., 2005.
(7) Lin, Z.; Peng, X. *Heat Transfer-Asian Research* **2009**, 485–491.
(8) Chiba, M.; Michiue, S.; Katayama, I. *Journal of Sound and Vibration* **2012**.